Olefin Oligomerization on Nickel-Based Metal Organic Framework Catalysts

A DISSERTATION
SUBMITTED TO THE FACULTY OF THE
UNIVERSITY OF MINNESOTA
BY

Benjamin Yeh

IN PARTIAL FULFILLMENT OF THE REQUIREMENTS
FOR THE DEGREE OF
DOCTOR OF PHILOSOPHY

Advised by Professors Aditya Bhan and Laura Gagliardi

July 2023

Acknowledgements

I would like to first thank my advisors, Professor Aditya Bhan and Professor Laura Gagliardi. Aditya has mentored me and taught me the technical and soft skills required to be a competent researcher. He has also been extremely patient in my personal growth and career path, often believing in me when I didn't believe in myself. Laura reminded me to look at the big picture when it comes to science, and I thank her for her constant encouragement and positive feedback and allowing me to pursue my interests in research without limitations.

I would like to thank my collaborators involved in the multidisciplinary projects over the past five years. First, I want to thank Saumil Chheda for his helpful discussions in the oligomerization projects and assisting me with my density functional theory calculations. I also want to thank Jian Zheng, Julian Schmid, Laura Löbbert, Ricardo Bermejo-Deval, Oliver Gutiérrez, and Johannes Lercher for synthesizing and characterizing the materials discussed in Chapter 2 and 3 and offering insights into the research described herein. I would like to thank Professor Matthew Neurock for giving his insight into the mechanism in Chapter 2, for allowing me to be a recitation instructor, and for caring about my wellbeing as a researcher as well as my career during graduate school. I would like to thank Professor Rachel Getman and Stephen Vicchio for providing me with knowledge with ab initio thermodynamic analysis calculations and assisting our conclusions in Chapter 2. I would like to acknowledge Professor Connie Lu and Steven Prinslow for synthesizing and characterizing the materials in Chapter 4 and providing their insights and knowledge about MOFs and organometallic chemistry. And lastly, I would like to thank Adam Hoffman, Jiyun Hong, Jorge Perez-Aguilar, and Simon Bare for teaching me X-ray absorption spectroscopy and for their openness and thoughtfulness to different research directions.

I thank the Bhan and Gagliardi group members for their insight into my projects while supporting me throughout graduate school. I would like to thank Jenny, Carlo, Navneet, Meagan, Thais, Riddhish, Hung, Debmalya, and Daniel for always making me feel welcome and for assisting me with computations. I would like to thank Brandon and Jake for being like big brothers to me in the group while believing in my ability to grow as

a scientist. I would like to acknowledge Matt S. who developed the MOF projects and set the rigor and foundation for science in this area. I would like to thank Jane for her friendship, putting up with me in lab, and being there to complain about anything even after she graduated and especially at Dow. I would like to thank Krishna who joined the lab at the same time as me and commiserated with me in our experiences in graduate school. I would like to thank Thomas for helping me with scientific questions and equipment in the lab. I am grateful for Brian for his friendship where he always encouraged me to live my truth. I would like to thank Joseph for his friendship and helpful technical discussions with no judgement. I thank Matt J. for his ability to hold space for me to be vulnerable to become great friends and for being a great beamtime travel partner.

I would like to thank the friends that I have made before graduate school for keeping me grounded during graduate school. To my friends back home in Pennsylvania, Jess, Teena, Cindy, and Tyler, whenever I would go home during winter break, you reminded me of the growth and the resilience I gained over the years. To my undergraduate chemical engineering friends, Harry, Naomi, and Brian, who I Facetimed with on a monthly basis, we supported each other on our graduate school journey, and you all believed that I was still one of the smartest people you all knew even when I didn't see it for myself anymore. And lastly, to Najiba, you supported me during my darkest and fragile times while always knowing what to say to make me feel better. To those mentioned here, you always showed me there was more than just school and held space for me to be myself even after years apart.

I would like to thank Alchemy 365 Northeast for giving me a community outside of graduate school. To the present and past coaches at Alchemy 365, Hannah, Evelyn, Monica, Matt, Zach, Jo, Leah, Whitney, Ben and many more, you pushed me physically but also showed me the kind of positive encouragement I needed to push myself further in all aspects of life. To the community and friends, Vicki, Devin, Tamara, Dale, Maddie, Ian, Justin, and many more, I am thankful for camaraderie, which pushed me during the insane workouts at 6:30 AM. This community provided me a safe space to destress and take care of my mind and body while showing me the growth mindset to "Pursue Your Legend."

I am grateful for the friendships that I made in the cohort and more broadly in the CEMS community, especially those during the tumultuous times of COVID-19. To my quarantine friend group, Kathleen, Patrick, AJ, Beth, Isaac, and Paul, you all helped make times in graduate school feel normal and safe during uncertain times. To Nathan, Matt, Erin, Teli, Ela, John, Demetra, and others, I am thankful for the support during the first and second years of graduate school when we were taking classes. I am thankful for the friends in CEMS, Choongsze, Diana, Kristine, Tyler, Geetha, EJ, and many more, who were willing to build authentic friendships with me beyond their year. And lastly, I thank my roommate, Justin, for spending countless hours providing friendship and support throughout my journey as a scientist but also as a person. To those mentioned here, your presence in the department brightened my day and reminded me that I was never truly alone in graduate school.

I would like to acknowledge the outside-the-department friendships made on my graduate school journey. To Haley, Emily, and Neel, you all provided support for me during graduate school even though none of us ended up together after our visit to UT Austin. I am grateful for the friendships of Melanie, Rishabh, Minju, and Daniel from Dow who wanted the best for me in my career and provided me comfort and security in Michigan.

I would like to thank the people who taught me the skills to live authentically. I am forever grateful to my therapists, Athena and Jeremy, who listened to me complain but also taught me how to set boundaries for myself and to take agency over myself and my decisions to empower myself in the hardest of times. I want to thank my faculty mentor, Professor Michelle Calabrese, for providing an excellent example of living authentically and fearlessly and for showing empathy and compassion for me in graduate school. I would like to thank Alex for his patience and acceptance of me and for inspiring me to not be fearful of living my truth and of being my authentic self.

I am forever grateful for my parents and my sister, who provided me with unconditional support over my entire academic career. Even through the failures and setbacks academically and emotionally, they were always there for me. I would not be here at this point without their encouragement.

Dedication

To *Myself*

For the Strength, Courage, Perseverance, Empathy, Compassion, Mindfulness, and Personal Growth that was gained over the past five years

Table of Contents

List of Tables

List of Figures

Chapter 1. Introduction

1.1. Motivation

Shale gas reserves have doubled within the past decade, motivating interest in valorization of light alkanes.[1,2] Steam cracking is a method to convert these saturated hydrocarbons into light olefins, such as ethylene and propylene.[1–8] Light olefins can be upgraded via oligomerization to synthesize transportation fuels and other petrochemical intermediates. Specifically, linear alpha olefins (LAOs), such as 1-butene, 1-hexene, and 1-octene, from light olefin oligomerization are sought industrially due to the high reactivity of the terminal double bond.[9] In 2021, the global market for LAOs was estimated to be about 8.5 metric million tons per year.[10] The increased demand for LAOs is due to the increased demand for high density polyethylene (HDPE) and linear low-density polyethylene (LLDPE), where LAOs function as comonomers in the polymerization process to give HDPE and LLDPE their desired structural and mechanical properties.[10,11]

Industrially, the production of LAOs employs transition metal homogeneous catalysts.[5] For example, the Ziegler process utilizes a trialkylaluminum catalyst to oligomerize ethylene at high temperatures (389 – 405 K) and pressures (18 – 21 MPa) to make a wide range of LAOs in a Poisson distribution.[6,9,12,13] The largest process for the production of LAOs is the Shell Higher Olefin Process (SHOP), which accounted for ~36% of the world's production of LAOs in 2010.[9] SHOP utilizes a homogeneous nickel-based catalyst with bidentate chelating ligands, which selectively produces LAOs in a Schulz-Flory distribution favoring the production of dimers during ethylene oligomerization at moderate temperatures (353 – 393 K) and pressures (6 – 14 MPa) with the flexibility to convert alpha olefins to internal alkenes.[6,9,12,14–16] Other homogeneous nickel-based catalysts similar to the SHOP catalyst have been investigated by fine tuning the ligands on the nickel active site to improve selectivity toward linear alpha olefins and desired oligomer product distributions, but these catalysts require the use of alkylaluminum activators and cocatalysts which inhibit environmental feasibility of these catalysts for olefin oligomerization.[5,17,18] Furthermore, homogeneous catalysts for oligomerization

chemistries often require solvents and the catalyst cannot be readily recycled or separated from the products.[19]

Heterogeneous catalysts, such as solid phosphoric acid (SPA) catalysts,[20,21] and zeolites[19,22] have been implemented industrially as alternative catalysts for light olefin oligomerization. Since the 1930s, UOP designed a process with SPA catalysts to produce branched products with high octane numbers from C_3-C_5 olefins.[5,23–25] The intolerance of SPA catalysts to water and their low thermal stability has necessitated the study of other heterogeneous catalysts for olefin oligomerization.[5,26] Propylene oligomerization is used to make higher molecular weight distillate fuels via the Mobil Olefins to Gasoline and Distillates (MOGD) process, which utilizes a ZSM-5 catalyst.[27] Brønsted acid-catalyzed propylene oligomerization on zeolites creates a distribution of higher molecular weight olefins and does not produce simple oligomers from the reacting olefin, due to the occurrence of cracking side reactions, which causes significant coking and catalyst deactivation.[27–30] Thus, both industrially practiced olefin oligomerization process with heterogeneous catalysts are unable to selectively produce LAOs.

Motivated by the high selectivity toward LAOs and dimers for olefin oligomerization for SHOP, nickel based heterogenous catalysts with the nickel active site supported on zeolite materials (Ni-Beta,[31–34] Ni-M-X,[35,36] Ni-M-LTA,[37–39] Ni-SSZ-24[40,41] and Ni-FAU[42]) and mesoporous materials (Ni-MCM-22,[22] Ni-MCM-36,[22] Ni-MCM-41,[43–45] Ni-MCM-48,[43] and Ni-SBA-15[43]) have been formulated and researched in recent years with attempts to evaluate catalytic performance and understand the active site and mechanism at elevated temperatures and pressures.[19,46] To date, there is no industrial process which incorporates nickel heterogeneous catalysts, as their catalytic activity is often lower than their homogeneous counterparts and the catalysts experience significant deactivation due to the formation of higher molecular weight oligomer products.[19,46,47] Additionally, zeolite and mesoporous materials often have residual acid sites which can form polyconjugated aliphatic compounds and/or polycondensed aromatics from H-transfer and cyclization reactions.[32,48] This further convolutes the study of the activity of

the nickel site and olefin oligomerization mechanisms, as simple oligomers are not the sole products produced from these catalysts.

To obtain catalytic activity similar to the SHOP catalyst, nickel based metal organic framework (MOF) catalysts (Ni-MFU-4l[49–51], Ni-CFA-1,[52] Ni-NU-1000,[53] Ni-MIL-125,[54] and Ni-DUT-8[55]) have been synthesized with isolated nickel active sites covalently bound to the MOF framework similar to liganded nickel species in the organometallic SHOP catalyst. MOFs are hybrid materials that include inorganic nodes consisting of metal ions or metal oxide clusters and organic linkers, both of which can be tuned for selective olefin oligomerization[56,57] during- or post-synthesis through atomic layer deposition,[57–59] solvothermal synthesis,[49–51,60] and grafting of molecular complexes[54] to generate metal-oxo species with active sites (i) supported on the framework,[53,60] (ii) embedded in the framework,[49–51] or (iii) attached to the organic ligand,[54] which manifest different reactivity for reactions.[56,61,62] MOFs with active sites supported on the framework have larger pore sizes than zeolites[63] and contain structural defects, such as missing cluster and missing linker defects,[64–66] which create open metal sites,[64] both of which have been shown to enhance reaction rates per active site.[64] These defects can be quantified with thermogravimetric analysis (TGA) and proton nuclear magnetic resonance (^{1}H NMR) spectroscopy to estimate the amount of organic content between defective and pristine MOF samples.[67,68] Additionally, MOFs can be synthesized with various topologies by varying the inorganic node and linkers to tailor the structure of the active site to those similar to their homogeneous equivalents, which provides countless possibilities in MOF structures.[69,70] Computational methods have been employed to design and evaluate a variety of MOF structures and their reactivity as catalysts.[70,71]

Currently, nickel MOFs generally have higher reactivity for olefin oligomerization and higher selectivity toward dimers and LAOs compared to other heterogeneous catalysts with Ni-MFU-4l, a MOF with nickel incorporated in the node, having the highest reported activity for a heterogeneous catalyst at 11.5 $mol_{C4=}$ mol_{Ni}^{-1} s^{-1} with a 91% selectivity for 1-butene in C_4 products during ethylene oligomerization at 5 MPa and 298 K with methylaluminoxane (MAO) activators.[49] Ni-NU-1000, a MOF with nickel supported on

the zirconium oxide framework, deactivates with time on stream during ethylene oligomerization in the presence of an $(CH_3CH_2)_2AlCl$ activator.[58] The use of cocatalysts with these heterogeneous nickel MOF catalysts is proposed to initiate and facilitate olefin oligomerization in a mechanism similar to that of homogeneous nickel based catalysts; nevertheless, operating olefin oligomerization with this method requires the use of excess solvents and activators.[46] A nickel framework-based MOF, Ni-MOF-74, has been studied for propylene oligomerization in the absence of cocatalysts, but similar to other heterogeneous catalysts, the catalyst deactivates with time on stream.[72]

Through a concerted experimental and computational effort, this work aims to (i) identify and enumerate the nickel active site and (ii) determine reaction kinetics and mechanism on nickel-based MOFs with nickel (i) incorporated in and (ii) supported on the inorganic node in the absence of activators during stable olefin oligomerization catalysis. The remainder of Chapter 1 details the speciation of the nickel active site and the mechanisms for olefin oligomerization on nickel-based heterogeneous catalysts and the challenges in measuring intrinsic rates and kinetics on these materials. Chapter 2 reports Ni/UiO-66, a zirconium-oxide based MOF with nickel supported on the inorganic node through a missing linker defect, which oligomerizes ethylene devoid of cocatalysts with unprecedented stability of >17 days on stream at 500 kPa and 473 K. Enhancement in reaction rates observed are due to the in-situ generation of active sites from elevated ethylene pressures. Active site enumeration at various pressures is employed to deconvolute the effect of active site generation and increased ethylene pressures on reaction rate to obtain intrinsic reaction rates and apparent activation energies, which were used to corroborate the Cossee-Arlman mechanism for ethylene oligomerization through comparisons with experimental and computed activation enthalpies. Chapter 3 outlines the use of Ni/UiO-66 for propylene oligomerization and highlights a new method to assess the Cossee-Arlman and metallacycle mechanism for olefin oligomerization by comparing steady state product selectivities at various pressures and demonstrating that the former and latter are characteristic of hexene isomer selectivities that are pressure-dependent and pressure-independent, respectively. Chapter 4 describes Ni-MIL-127, a bimetallic oxo-

trimer based MOF with nickel and iron incorporated in the inorganic node, which oligomerizes propylene and is stable for ~24 hours on stream at 500 kPa and 473 K in the absence of activators after thermal treatment in helium at 493 K, which generates a missing linker defect and an open coordination site on nickel as evinced by temperature programmed oxidation, proton nuclear magnetic resonance spectroscopy, and X-ray absorption spectroscopy with the defect density verified with infrared spectroscopy and in-situ titrations. Density functional theory calculations were employed to corroborate the structure of the active site and the propylene oligomerization mechanism from characterization of the catalyst and steady state kinetics, respectively. Chapter 5 investigates the effect of elevated pressures (>1500 kPa) and subambient temperatures (<273 K) during ethylene and propylene oligomerization in attempts to alleviate catalyst deactivation on Ni-MOF-74, a nickel-framework based MOF.

1.2. Mechanisms, Active Site, and Kinetics for Olefin Oligomerization

The Cossee-Arlman mechanism, also known as the coordination-insertion mechanism and shown in Figure 1.1a, is proposed on the homogeneous SHOP catalyst and homogeneous nickel catalysts with P,O chelators.[14,73–75] The catalytic cycle is proposed to start with a nickel-hydride (***A***) or nickel-alkyl species (***C***), with the latter being formed from the inclusion of cocatalysts during the reaction as shown from (***G***).[31,32,40,45,46,76,77] The nickel species is proposed to remain the 2+ oxidation state throughout the entire catalytic cycle. Starting with a nickel-hydride species (***A***), an olefin molecule binds to form ***B*** and is inserted to form a nickel-alkyl species (***C***). A subsequent olefin molecule binds to form ***D*** and is inserted to generate nickel-alkyl species that is double in carbon chain length (***E***). The nickel-alkyl complex undergoes a β-hydride elimination to regenerate the nickel-hydride species and the resulting oligomer (***F***).

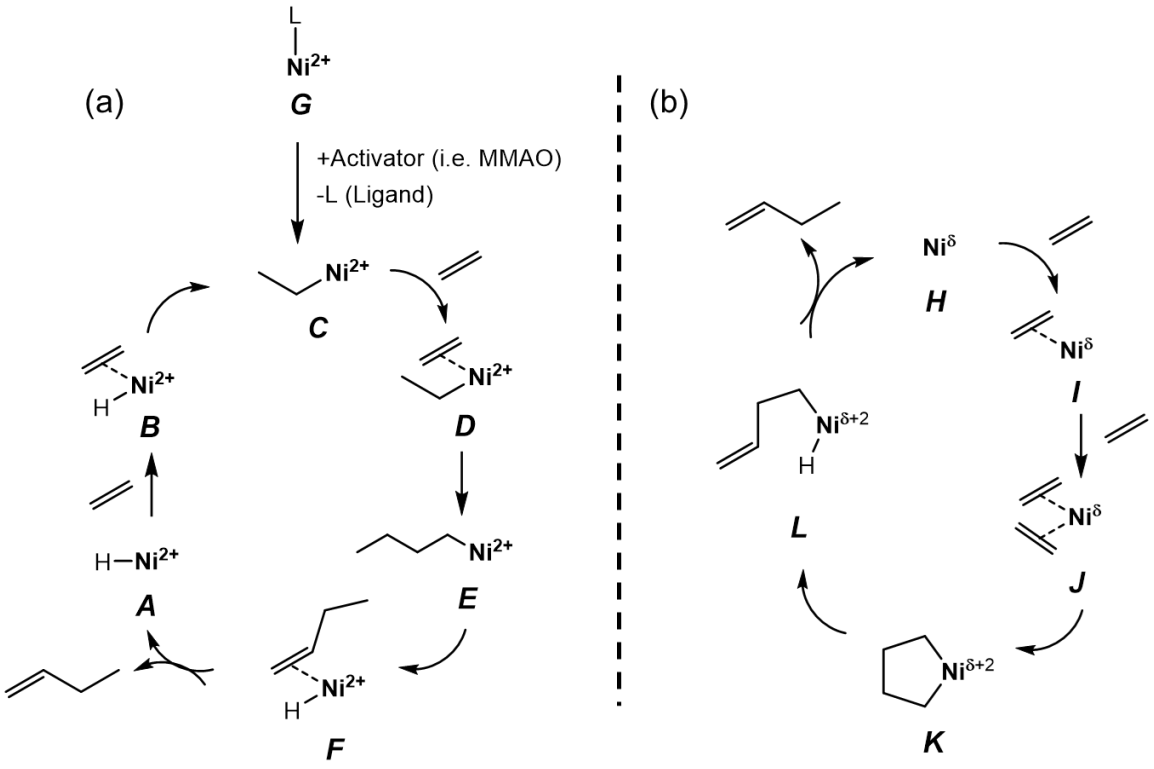

Figure 1.1. (a) Cossee-Arlman and (b) metallacycle mechanisms on nickel catalysts for ethylene oligomerization.

Prior to the catalytic cycle, heterogeneous catalysts often undergo an induction period in the absence of cocatalysts which involves a stoichiometric reaction attributed to the in-situ generation of catalytically relevant Ni-alkyl or Ni-hydride species for the Cossee-Arlman mechanism.[32,40,41] The putative initiation mechanisms are postulated based on the speciation of nickel in the precatalyst state and products formed during the induction period. In Figure 1.2a, the starting nickel state is a Ni^{2+} species, ***A1***, that binds to two olefin molecules, shown as ***A2*** and ***A3***. Heterolytic cleavage of a C-H bond on one olefin molecule forms a [Ni-alkenyl-alkene]$^{-}$ complex and a Brønsted acid site (***A4***). The alkene inserts into the Ni-alkenyl to form a Ni-alkenyl species double in carbon chain length (***A5***). The resulting Ni-alkenyl species undergoes β-hydride elimination to generate a diene species double in carbon chain length (***A6***) and a nickel-hydride species after the desorption of the diene molecule (***A7***). In Figure 1.2b, the starting species of Ni is a [Ni-OH]$^{+}$ complex (***B1***), and an olefin molecule binds to form ***B2*** and inserts to form a [Ni-alkanol]$^{+}$ species

(***B3***). A subsequent olefin molecule inserts (**B4**) and eliminates water to generate a [Ni-alkenyl-alkene]$^-$ complex (**B5**) and produces a Ni-hydride species similar to the mechanism described above without the presence of a Brønsted acid site.

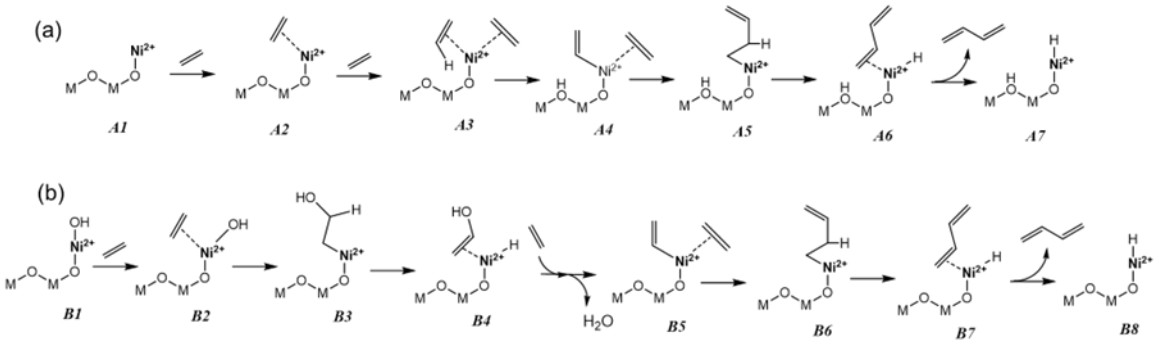

Figure 1.2. Initiation mechanism prior to the steady state Cossee-Arlman mechanism for ethylene oligomerization on (a) Ni^{2+} and (b) $[Ni\text{-}OH]^+$ species.

In nickel-based homogeneous catalysts, the addition of an activator to create a Ni-alkyl species provides evidence for Cossee-Arlman mechanism, as the Ni-alkyl species is an intermediate in the mechanism.[12,17] Additionally, evidence for the Cossee-Arlman mechanism on homogeneous nickel catalysts includes the observation of internal alkenes, which are formed upon the reinsertion and subsequent β-hydride elimination of the resulting oligomer product.[78,79] In nickel-based heterogeneous catalysts, hydrogen cofeeds during ethylene oligomerization on Ni-Beta have been used to probe the involvement of a nickel-hydride species as rates with and without hydrogen cofeeds converge with time on stream.[31] In-situ infrared spectroscopy on Ni-Ca-LTA formulations demonstrate the presence of a nickel-butyl species during 1-butene oligomerization to validate the Cossee-Arlman mechanism.[37] Analysis of isotopomer product distributions during ethylene oligomerization on Ni-MFU-4l reveal H/D scrambling with mixtures of deuterated ethylene and ethylene which is consistent with the β-hydride elimination step and insertion of the hydrogen or deuterium into a subsequent olefin molecule.[50] In the same body of work, 1,6-heptadiene was fed on Ni-MFU-4l, and the presence of 1,5-heptadiene and its carbon-carbon coupling product, 1-methyl-2-methylene-cyclopentane, was observed via chain walking to evince the possibility of coordination, insertion, and β-hydride elimination, characteristic of the Cossee-Arlman mechanism.[50] The use of DFT

calculations to determine the lowest free energy barrier for the Cossee-Arlman mechanism and the metallacycle mechanisms on Ni-SSZ-24 and Ni-NU-1000 has shown that the Cossee-Arlman mechanism is more favorable with the lower free energy barriers.[41,53,80]

The metallacycle mechanism presented in Figure 1.1b is proposed on homogeneous nickel(II) bis-phosphine catalysts, specifically in the absence of activators.[81,82]The metallacycle mechanism is posited on the observation of solely LAOs as the major products for olefin oligomerization on nickel homogeneous catalysts.[17,81,82] On nickel heterogeneous catalysts, the evidence for the metallacycle mechanism include the absence of cocatalysts and induction periods.[83] On Ni-MCM-41, Ni-AlSBA-15, and Ni-Ca-Y materials, the presence of Ni^{+} species are observed, similar to those observed in homogeneous catalysts that can form nickellacyclopentane complexes, validating the metallacycle mechanism.[83,84] However, in these studies, Ni^{2+} species and internal alkenes were observed where the latter was attributed to the isomerization of LAOs via Brønsted acid sites, and the catalysts constantly deactivate with time on stream, convoluting elucidation of the mechanism.[84,85] The active species for the metallacycle mechanism has been proposed to be either a Ni^{+} or Ni^{2+} ion, denoted as Ni^{δ} (***H*** in Figure 1.1b) that successively coordinates two olefin molecules, shown as ***I*** and ***J***.[41,46] The complex, ***J***, undergoes oxidative coupling, where the nickel ion becomes $Ni^{\delta+2}$ and is bound to a metallacyclopentane intermediate. (***K***) The metallacyclopentene intermediate undergoes β-hydride elimination and then reductive elimination to regenerate the Ni^{δ} species and the oligomer molecule (***L***).

The active site for olefin oligomerization on heterogeneous catalysts has been disputed in the literature with reports on the same catalysts reporting different active species for oligomerization. On Ni-AlSBA-15[83] and Ni-Ca-Y zeolites,[86,87] the active site was proposed to be Ni^{+} species, where the oxidation state on the latter material was evinced by electron spin resonance spectroscopy during ethylene oligomerization.[86,87] In Ni-MCM-41, Ni^{+} ions and dehydrated Ni^{2+} species were postulated to be active for ethylene oligomerization due to the reduction of Ni^{2+} species to Ni^{+} species after thermal treatment in nitrogen at 823 K as determined by in-situ CO adsorption experiments.[88] On the same material, $[Ni\text{-}OH]^{+}$ complexes were proposed to be the active species which were

characterized by 2,6-di-tert-butylpyridine and CO titration experiments with Ni^{+} ions proposed to be spectator species.[44,45,89] From probe molecule infrared spectroscopy experiments with CO, X-ray absorption spectroscopy (XAS), and diffuse reflectance UV−vis spectroscopy on Ni-Beta zeolites, only Ni^{2+} species are observed and proposed to be the relevant species for ethylene oligomerization.[31,33] The speciation of the nickel species is crucial for validating the olefin oligomerization mechanism as Ni^{2+} species are involved in the Cossee-Arlman mechanism while Ni^{+} species are involved in the metallacycle mechanism.[31,83]

The various active nickel species on the same catalyst complicate the measurement of kinetics for olefin oligomerization as each nickel species can have different intrinsic reactivities. While multiple nickel species can exist in the catalyst, residual acid site activity in zeolites and catalyst deactivation in heterogeneous catalysts often obscure the measurement of rates, kinetics, and product selectivities.[32,48] Furthermore, normalization of oligomerization rates, which is required to measure intrinsic kinetics, rely on the quantification of relevant active sites, which depend on the areal density of nickel sites in the catalyst[43,44,76] and the amount of cocatalyst used.[49,90] Nevertheless, reaction rates are reported to have a second order dependence on ethylene pressures on Ni-SSZ-24,[40] Ni-MCM-41,[44] and Ni-Beta[32] with the catalysts deactivating with time on stream at elevated temperatures and with residual acid site reactivity on Ni-Beta forming branched butene isomers as opposed to linear isomers. Ethylene dimerization rates on Ni-MFU-4l with a methylaluminoxane activator show a first order dependence in ethylene pressure at ethylene pressures less than 2.5 MPa and a zero order dependence in ethylene pressures at ethylene pressure greater than 2.5 MPa.[49] Propylene oligomerization rates are first order in propylene pressure on Ni-Na-X from 125 kPa to 500 kPa but the catalyst deactivates with time on stream.[35] In general, the variety of nickel species in catalysts, side reactions, and deactivation complicate the measurement of reaction kinetics and mechanisms for olefin oligomerization.

In this thesis, normalized oligomerization rates per nickel active site are reported after enumeration of active sites with in-situ titrations in the absence of cocatalysts and

deactivation to determine reaction kinetics and to validate the mechanism for olefin oligomerization. The mechanism for olefin oligomerization was validated on Ni-based MOFs by (i) analyzing transient rates, (ii) determining the nickel speciation with infrared spectroscopy and X-ray absorption spectroscopy, (iii) investigating the most abundant surface intermediate through steady state reaction orders, in-situ spectroscopic measurements, and *ab initio* thermodynamic analysis calculations (iv) calculating reaction enthalpies for various mechanisms on cluster models of MOFs and comparing experimental and computed activation energies, and (v) evaluating rate and product selectivity expressions for the Cossee-Arlman and metallacycle mechanisms. This combined experimental and computational effort will provide active site characterization and mechanistic information on nickel-based MOFs for olefin oligomerization to generally synthesize and logically design new nickel-based heterogeneous catalysts for stable olefin oligomerization reactions selective for linear alpha olefins.

Chapter 2. Site Densities, Rates, and Mechanism of Stable Ni/UiO-66 Ethylene Oligomerization Catalysts

This material has been adapted from a previously published work.[76] Contributions of other authors is noted in the footnotes of the experimental and computational methods.

2.1. Introduction

Linear alpha olefins (LAOs), specifically 1-butene, 1-hexene, and 1-octene, are consumed as co-monomers for polyethylene production and are produced following a Schulz-Flory-type distribution through the Shell Higher Olefin Process (SHOP) at 1.1 million tons a year with a homogeneous nickel catalyst.[3,14,91] Nickel functionalized metal organic frameworks (MOFs)[49–51,80] designed with active sites to mimic the catalytic properties of the homogeneous SHOP catalyst[12] for oligomerization rely on alkyl-aluminum co-catalysts, while nickel-zeolite catalysts viz. Ni/LTA,[37] Ni/H-Beta,[32] Ni/SSZ-24,[40] and Ni/MCM-41[44] deactivate with time on-stream. We report a nickel-functionalized UiO-66 MOF formulation that after an induction period, exhibits >15 days on-stream stability unprecedented in framework or supported heterogeneous catalytic materials for ethylene oligomerization in the absence of activators and co-catalysts. The Ni/UiO-66 material in this study exhibits first-order kinetics in ethylene pressure after accounting for generation of active sites to validate a Cossee-Arlman mechanism[32,37,40,49–51,80] that prescribes physisorbed ethylene in the pores of the MOF framework for ethylene oligomerization. These distinctive characteristics and correspondent mechanisms on Ni/UiO-66 are detailed through transient and steady-state reaction kinetics and density functional theory (DFT) calculations, and the effect of ethylene pressure on rates of reaction is deconvoluted through *in-situ* chemical titration experiments to determine the site density and reaction order and apparent activation energy for selective 1-butene synthesis.

2.2. Experimental and Computational Methods

2.2.1. Synthesis of Ni/UiO-66[1]

Parent UiO-66 metal organic framework (MOF) was synthesized following a procedure reported by Katz *et al.*,[92] where 8.39 g of $ZrCl_4$ (>99.5%, Alfa Aesar, 36 mmol) were charged into a glass-lined 2000 cm^3 stainless steel Parr autoclave and dissolved in 400 cm^3 of a mixture of N,N-dimethyl formamide (DMF) and HCl (37% aqueous solution) (v/v=5/1). Separately, 8.31 g of 1,4-benzendicarboxylic acid (BDC) (98%, Sigma Aldrich, 50 mmol) was immersed in 660 cm^3 DMF and sonicated until dissolved. The solution of BDC was added to the autoclave, which was sealed and kept at 353 K under stirring for 18 h. The obtained UiO-66 MOF was filtered under vacuum and washed with DMF and with methanol.

Prior to the deposition of Ni, UiO-66 MOF (typically 1 g) was treated under vacuum (< 1 Pa) at 473 K for 4 hours. Then the treated UiO-66 powder was immersed in 80 cm^3 of hexane (Fisher Chemical), minimizing the contact with air, and dispersed by sonication for 20 minutes. $Ni(NO_3)_2{\cdot}6H_2O$ (99.9985%, Strem Chemicals) was dissolved in a volume of H_2O corresponding to the pore volume of the MOF (V_{pore}= 0.6 $cm^3\ g^{-1}$). The amount of Ni precursor was calculated based on the targeted Ni content. The solution of the precursor was added dropwise to the suspension of UiO-66 in hexane under vigorous stirring and was stirred for 6 h. The resulting material was filtered and heated in He flow for 3 hours at 523 K to decompose the nitrates.

2.2.2. Catalytic Testing

Ni/UiO-66 was pressed (<6.9 MPa), pelletized, and sieved to obtain 180-420 μm (40-80 mesh) aggregates. The sample (20-100 mg) was physically mixed with sand (~200 mg, subjected prior to an overnight wash in 2 M HNO_3 solution followed by DI water rinse until pH ~7, and a final thermal treatment in flowing dry air (0.83 $cm^3\ s^{-1}$) at 1273 K (0.083 K s^{-1} ramp rate from RT) for 16 h; 10 < $wt_{diluent}/wt_{cat}$ < 15), before being loaded into a tubular glass-lined stainless-steel reactor (6.35 mm O.D. and 4 mm I.D., SGE Analytical

[1] Synthesis was performed by Jian Zheng and Julian Schmid with Oliver Y. Gutiérrez and Johannes Lercher at Pacific Northwest National Laboratory (PNNL) and Technical University of Munich (TUM).

Science) packed between two quartz wool plugs (Technical Glass Products). The free volume in the reactor tube was filled with quartz rods (3 mm O.D.; Technical Glass Products) to prevent any vertical displacement of the catalyst bed. The tubular reactor was then placed inside a resistively heated furnace (Applied Test Systems). The temperature was measured and regulated using a K-type thermocouple (Omega) wrapped around the periphery of the stainless-steel reactor with the tip placed at the center of the catalyst bed and an electronic controller (Watlow), respectively. The catalyst was pretreated in helium (Matheson, 99.997%, 0.83 $cm^3\ s^{-1}$) from ambient temperature to 573 K (0.08 K s^{-1}) for 4 hours and then cooled to reaction temperature (443-503 K) in flowing helium (Matheson, 99.997%, 0.83 $cm^3\ s^{-1}$). Ethylene (Matheson, 99.999%, 0.2-1.5 $cm^3\ s^{-1}$) was introduced to the reactor with flow controlled by mass flow controllers (Brooks 5850E Series). The gas-phase pressure was measured using a pressure transducer (Omega) placed upstream of the reactor and controlled using a back-pressure regulator (TESCOM Series 44-2300) placed downstream of the reactor. The composition of the reactor effluent was quantified using a gas chromatograph (Agilent GC 7890A) equipped with a dimethylpolysiloxane HP-1 column (50 m × 320 μm × 0.52 μm) connected to a flame ionization detector (FID).

2.2.3. In-situ NO Titration Experiments

The reactor setup is identical to the one described above. A nitric oxide/argon mixture (Matheson, 1% NO, 1% Ar, balance helium, 0.05-0.33 $cm^3\ s^{-1}$) was introduced in the ethylene gas stream at elevated pressures (100-1800 kPa) with a mass flow controller (Brooks 5850E Series). An online mass spectrometer (MKS Cirrus 2) was utilized to quantify the effluent ethylene, butene, NO, and Ar flowrates (m/z: 27, 56, 30, and 40, respectively). The Ar flow was used as a tracer to determine the average residence time of NO over the catalyst bed,[93] which was used to calculate the amount of NO reacted/absorbed on nickel sites to suppress the rate of oligomerization.

2.2.4. Ex-situ NO Titration Experiments

A nitric oxide/nitrogen mixture (Airgas, 1% / 99%, 0.17 $cm^3\ s^{-1}$) was cofed with ethylene (Matheson, 99.999%, 0.83 $cm^3\ s^{-1}$) with mass flow controllers (Brooks 5850E Series). An online mass spectrometer (MKS Cirrus 2) was utilized to measure the signals of ethylene and NO (m/z: 27, 30, respectively). Once the flows of the NO/N_2/ethylene

mixture stabilized in the bypass (106 kPa), the stream was introduced into the reactor (473 K).

2.2.5. Powder X-Ray Diffraction (PXRD)[2]

PXRD patterns were collected over a 2θ range of 5-50° at 0.04° resolution with a Bruker-AXS (Siemens) D5005 diffractometer with 2.2 kW Cu-Kα radiation (λ=1.5418 Å), diffracted beam monochromator, and a scintillation counter detector. Data analysis was performed using JADE 8.0 (Materials Data Incorporated) software package.

2.2.6. N_2 Isotherms

Nitrogen adsorption isotherms were measured at 77 K using an ASAP 2020 surface area and porosity analyzer (Micromeritics) after removing water by degassing the samples at <150 Pa at 333 K for one hour and then 423 K for two hours.[67] Surface areas were determined by fitting a Langmuir isotherm between P/P_0 values of 0.05 and 0.30.

2.2.7. ^{1}H NMR Spectroscopy

The MOF samples (~20 mg) were dissolved with a 600 μL solution of 1 M NaOH (Fisher Chemical) in D_2O (Cambridge Isotope Laboratories) in 7-inch nuclear magnetic resonance (NMR) sample tubes (Wilmad). The resulting mixture was inverted three times and left overnight to digest the MOF. ^{1}H NMR spectra were recorded using a Bruker Avance III HD Nanobay AX-400 (400 MHz) with a relaxation delay of 20 seconds and 32 scans.[67]

2.2.8. Thermogravimetric Analysis (TGA)[3]

TGA measurements were obtained using a Shimadzu TGA-50 instrument loaded with 6-10 mg of the material in flowing air (0.83 $cm^3\ s^{-1}$). The temperature was ramped (0.17 $K\ s^{-1}$) from ambient temperature to 393 K and held at 393 K for 1 hour to remove excess water. Then the temperature was ramped (0.05 $K\ s^{-1}$) from 393 K to 1023 K and held at 1023 K for 1 hour.

[2] PXRD was collected by Xinyu Li at the Characterization Facility at the University of Minnesota
[3] TGA was collected by Matheus Dorneles de Mello and Michael Tsapatsis at the University of Minnesota.

2.2.9. Scanning transmission electron microscopy-energy-dispersive X-ray spectroscopy (STEM-EDS)[4]

The MOF samples were loaded onto 300-mesh lacey carbon/Cu TEM grids by drop-casting a dilute suspension of each sample in acetone. STEM-EDS was performed using an FEI Tecnai G2 field emission STEM at an accelerating voltage of 80 kV. High-angle annular dark-field (HAADF) images were collected on an E. A. Fischione annular detector using an inner collection semiangle of 25.5 mrad. Energy-dispersive X-ray spectroscopy (EDS) spectra were obtained using the ChemiSTEM EDX spectrometer. EDS maps were collected while rastering the beam over the sample. A probe current of ~0.8 nA was used, and maps were collected over a minimum of 5 min. Data were analyzed using ESPRIT software (version 1.9.4).[94]

2.2.10. Infrared (IR) Spectroscopy

Wafers of MOF samples for IR spectroscopy were pressed (<6.9 MPa) and placed in a quartz IR cell with KBr (Sigma-Aldrich) windows. Spectra from 400-4000 cm^{-1} at a resolution of 2 cm^{-1} with an average of 32 scans were measured with a Nicolet 6700 spectrometer. The IR spectra were taken after the IR cell was heated from ambient temperature to 523 K (0.067 K s^{-1}) in helium (Matheson, 99.997%) and held for 4 hours at 523 K.

2.2.11. Inductively Coupled Plasma – Atomic Emission Spectroscopy (ICP-AES)[5]

MOF samples (~50 mg) were dissolved and sealed in a digestion vessel (CEM) with a mixture of HNO_3/HF/H_2O (v:v = 2/1/1). The vessel was heated to 483 K using a 20 minute ramp and held for 30 minutes. The vessel was cooled, and 5 cm^3 of saturated H_3BO_3 was added to the mixture. The vessel was resealed and heated at 453 K using a 20 minute ramp and held for 30 minutes. The vessel was cooled, and the mixture was transferred, and rinsed with water in a 50 cm^3 centrifuge tube. The Ni and Zr content of the Ni/UiO-66

[4] STEM-EDS was performed by Rebecca Combs and Lee R. Penn at the Characterization Facility at the University of Minnesota.
[5] ICP-AES was performed by Jian Zheng, Julian Schmid, Oliver Y. Gutiérrez, and Johannes Lercher at PNNL and TUM.

MOF was determined by inductively coupled plasma-atomic emission spectroscopy (ICP-AES, Perkin Elmer 7300DV).

2.2.12. Temperature Programmed Oxidation (TPO)

Powder samples were loaded in tubular reactor described above. The samples were heated (0.067 K s^{-1}) from ambient temperature to 723 K and then ramped again (0.05 K s^{-1}) from 723 K to 923 K with a gaseous mixture of oxygen (Matheson, 99.999%, 0.33 cm^3 s^{-1}), helium (Matheson, 99.997%, 1.17 cm^3 s^{-1}), and argon (Matheson, 99.999%, 0.17 cm^3 s^{-1}, internal standard). The effluent stream composition was quantified using an online mass spectrometer (MKS Cirrus 2) with signals from the mass spectra for oxygen, argon, and carbon dioxide assigned m/z values of 32, 40, and 44, respectively.

2.2.13. X-Ray Adsorption (XAS) Spectroscopy[6]

Ni/UiO-66 samples, as-synthesized and after reaction (473 K, 1000 kPa), were loaded into glass capillaries (1.0 mm, Charles Supper Company) in an N_2 glove box. The capillaries were sealed with wax (Charles Supper Company) and shipped for XAS measurements at the bending-magnet beamline at Sector 20 of the Advanced Photon Source (APS) at Argonne National Laboratory (ANL), or at beamlines 2–2 at Stanford Synchrotron Radiation Light source (SSRL). All experiments were carried out in transmission mode. A harmonic rejection mirror was used to reduce the effects of harmonics. A Ni foil was placed downstream of the sample cell, as a reference to calibrate the photon energy of each spectrum.

The XAS data were processed using ATHENA, as part of the XAFS software package, to remove the background from the $\chi(k)$ oscillations. The Fourier transform of the k-space EXAFS data were fit to X-ray determined structures using Artemis. For the fitting, alpha-$Ni(OH)_2$ and nickel foil were used as the crystallographic models. The fits to the Ni K-edge EXAFS $\chi(k)$ data were weighted by k^2 and windowed between 2.0 $Å^{-1} < k < 12.0$ $Å^{-1}$ using a Hanning window with dk = 1.0 $Å^{-1}$.

[6] XAS measurements were taken by Adam Hoffman and Simon R. Bare at SSRL, a division of SLAC National Accelerator Laboratory, and by Mahalingam Balasubramanian at ANL and data analysis was performed by Julian Schmid, Oliver Y. Gutiérrez, and Johannes Lercher at PNNL and TUM.

2.2.14. Cluster Models of Ni/UiO-66 and Kohn-Sham Density Functional Theory (DFT) Calculations

A cluster model of the Zr_6 node of UiO-66 was truncated from an optimized periodic structure of UiO-66 with formate groups capping the inorganic linker.[70] One carbon atom on the formate group was displaced with nickel, as nickel is hypothesized to persist on the Zr_6 node through missing linker defects,[80,95,96] to give the cluster model formula of $[NiZr_6(\mu_3\text{-}OH)_3(\mu_3\text{-}O)_4(OH)_2]^{11+}11(CHO_2^{-1})$.[97] Kohn-Sham DFT calculations were performed with the M06-L density functional[98] implemented in the *Gaussian 16* software package.[99] The def2-SVP basis set and def2-TZVPP basis sets were used for C, H, and O atoms and Zr and Ni atoms, respectively,[100,101] and the SDD effective core potential was implemented for Zr atoms.[102] All atoms for cluster molecules and individual gas phase molecules were optimized, except for C atoms capping the Zr_6 node to mimic framework rigidity.[70] Zero-point energies and thermal contributions to enthalpies and Gibbs free energies were calculated from vibrational frequency calculations at 298.15 K and 1 atm pressure. Previous reports show that this level of theory on other nickel functionalized zirconium based MOFs reproduces the electronic structure and predicts reaction enthalpies for ethylene oligomerization.[53,59,95]

2.2.15. *Ab initio* Thermodynamic Analysis[7]

We utilize *ab initio* thermodynamic analysis[103–106] to capture the influence of reaction conditions on the thermodynamic stability of different Ni/UiO-66 clusters. In our model, thermodynamic stability of the Ni/UiO-66 cluster is assessed according to Eq. 2.1:

$$\Delta F^{(2)}\left(T, \mu_{C_2H_4}, \mu_{C_4H_6}\right) = \left(\Delta F^{(0)}\right) - \mu_{C_2H_4}\left(\Delta N_{C_2H_4}\right) - \mu_{C_4H_6}\left(\Delta \mathrm{N}_{C_4H_6}\right) \quad \text{Eq. 2.1}$$

where $\Delta F^{(2)}$ is the second Legendre transformation of the Helmholtz free energy $\Delta F^{(0)}$. Specifically, to transform $\Delta F^{(0)}$ into $\Delta F^{(2)}$, $N_{C_2H_4}$ and $N_{C_4H_6}$ are transformed into $\mu_{C_2H_4}$ and $\mu_{C_4H_6}$, respectively using Eq. 2.1. $\Delta F^{(2)}$ is calculated as a function of T, $\mu_{C_2H_4}$, and

[7] *Ab initio* thermodynamic analysis calculations were performed by Stephen Vicchio and Rachel Getman at Clemson University.

$\mu_{C_4H_6}$ to explore compositionally distinct Ni/UiO-66 clusters. We construct the chemical reaction, Eq. 2.2, to describe Eq. 2.1:

$$\frac{Ni(OH)_2(O)}{UiO66} + xC_2H_4\ (g) \xrightarrow{\Delta F^{(2)}} Ni(OH)_3\left(C_{2x-4y}H_{4x-6y-1}\right)/\text{UiO66} + y\ C_4H_6 \quad \text{Eq. 2.2}$$

where x is the number of C_2H_4 molecules that adsorb and y is the number of C_4H_6 molecules that desorb with respect to the reference catalyst $Ni(OH)_2(O)$/UiO-66. The Δ symbols in Eq. S1 denote quantities taken with respect to the reference catalyst. ΔN values indicate a change in composition of C and H relative to the reference catalyst. Values of $\Delta F^{(0)}$ in Eq. S1 are calculated according to Eq. 2.3:

$$F^{(0)} = E^{DFT} + E^{ZPE} + \mathrm{G_{corr}} \quad \text{Eq. 2.3}$$

where E^{DFT} and E^{ZPE} are the electronic (from DFT) and zero-point energies, and $\mathrm{G_{corr}}$ is the free energy correction term which comprises thermal contributions to the internal energy (E_{tot}) and entropy (S_{tot}):

$$\mathrm{G_{corr}} = E_{tot} + k_B T - TS_{tot} \quad \text{Eq. 2.4}$$

where $E_{tot} = E_{elec} + E_{trans} + E_{rot} + E_{vib}$ and $S_{tot} = S_{elec} + S_{trans} + S_{rot} + S_{vib}$ (noting that $E_{elec} = 0$ and $S_{elec} \sim 0$ for all structures). Values for the electronic, translational, and rotational contributions to E_{tot} and S_{tot} are taken directly from the Gaussian16 log files. E^{ZPE}, E_{vib}, and S_{vib} are calculated by hand using the method described in detail by Ochterski.[107] In these calculations, we replace all frequencies below 50 cm^{-1} with 50 cm^{-1}, which is typically done when computing vibrational entropies.[108] All contributions to $\mathrm{G_{corr}}$ are computed with T = 298 K.

By assuming equilibrium between the adsorbed and gaseous species, i.e., $C_2H_4(g) \leftrightarrow C_2H_4*$ and $C_4H_6(g) \leftrightarrow C_4H_6*$, adsorbate and gas phase chemical potential terms can be equated, i.e., $\mu_{C_2H_4} = \mu^g_{C_2H_4}(T, P_{C_2H_4})$ and $\mu_{C_4H_6} = \mu^g_{C_4H_6}(T, P_{C_4H_6})$. Both $\mu^g_{C_2H_4}(T, P_{C_2H_4})$ and $\mu^g_{C_4H_6}(T, P_{C_4H_6})$ are influenced by the reaction conditions, e.g,

$$\mu^g_{C_2H_4}(T, P_{C_2H_4}) = E^{DFT}_{C_2H_4} + E^{ZPE}_{C_2H_4} + \left[G_{C_2H_4}(T, P^o) - G_{C_2H_4}(0\ K, P^o) + RTln\left(\frac{P_{C_2H_4}}{P^o}\right)\right] \quad \text{Eq. 2.5}$$

where G is the Gibbs Free energy computed using the NASA Polynomials[109]in the pMuTT[110] Python package, P is the partial pressure, and P^o is the standard pressure (1 bar). In Eq. 2.5, $G_{C_2H_4}(0\ K, P^o)$ is approximated with $G_{C_2H_4}(10\ K, P^o)$, which is calculated by extrapolating the NASA Polynomials.[105,111]An analogous expression is generated for $\mu^g_{C_4H_6}(T, P_{C_4H_6})$. Phase diagrams show the thermodynamic landscape of the Ni/UiO-66 structure as a function of T, $P_{C_2H_4}$, and $P_{C_4H_6}$ by plotting the structures that exhibit the lowest free energy at the given conditions.

2.3. Results and Discussion

An ideal UiO-66 material has Zr_6O_8 nodes connected with twelve terephthalate ligands, or benzene dicarboxylic (BDC) acid linkers.[92,112–115] Zirconium oxide based MOFs, such as UiO-66 and NU-1000, are characterized with missing linker defects, and single metal atoms and metal oxide complexes can be anchored on the zirconium oxide node in lieu of the missing linker defect.[59,96,116,117]

2.3.1. Characterization of parent UiO-66 and Ni/UiO-66

From PXRD in Figure 2.1a, we observe that Ni/UiO-66 maintains crystallinity with nickel functionalization and appears to be more porous than the parent MOF as indicated by N_2 adsorption isotherms shown in Figure 2.1b and by measured BET surface area reported in Table 2.1. The MOFs are stable in oxygen (20% by volume) up to 623 K as indicated with TGA and TPO in Figures 2.1c and 2.1d, respectively, consistent with the thermal stability of UiO-66 MOFs prevoiusly reported.[67,118] BDC linkers in nickel functionalized UiO MOF samples remain unchanged, as denoted by the relative intensity of the BDC peak (7.7 ppm) in ^{1}H NMR spectra as shown in Figure 2.1e.[67] Figure 2.1f presents the loss of physisorbed water in the MOF framework with flowing helium (Matheson, 99.997%, 0.83 $cm^3\ s^{-1}$) at various temperatures temperatures (5 K min^{-1}, 573 K for 4 hours), consistent with the procedure of pretreating the catalyst prior to ethylene oligomerization, and that the structural integrity of the framework is unchanged with heating in helium as denoted by the bands at ~3675 cm^{-1}, 2850-3100 cm^{-1}, and 1300-1600 cm^{-1}, which correspond to isolated OH groups, aromatic and aliphatic ν(C-H) modes in the BDC linker, and the carboxylate stretching modes, respectively.[119] From STEM-EDS,

nickel is dispersed homogeneously throughout the MOF framework (Figure 2.2). Elemental analysis in Table 2.2 from EDS maps from Figure 2.2 and results from ICP-AES in Table 2.3 yield 0.75 Ni atoms per Zr_6 node and 0.71 Ni atoms per Zr_6 node (Eq. 2.7 and Eq. 2.8), calculated on a 100 atom basis per EDS map or 100 gram basis per sample, respectively, assuming one inorganic node has six zirconium atoms.

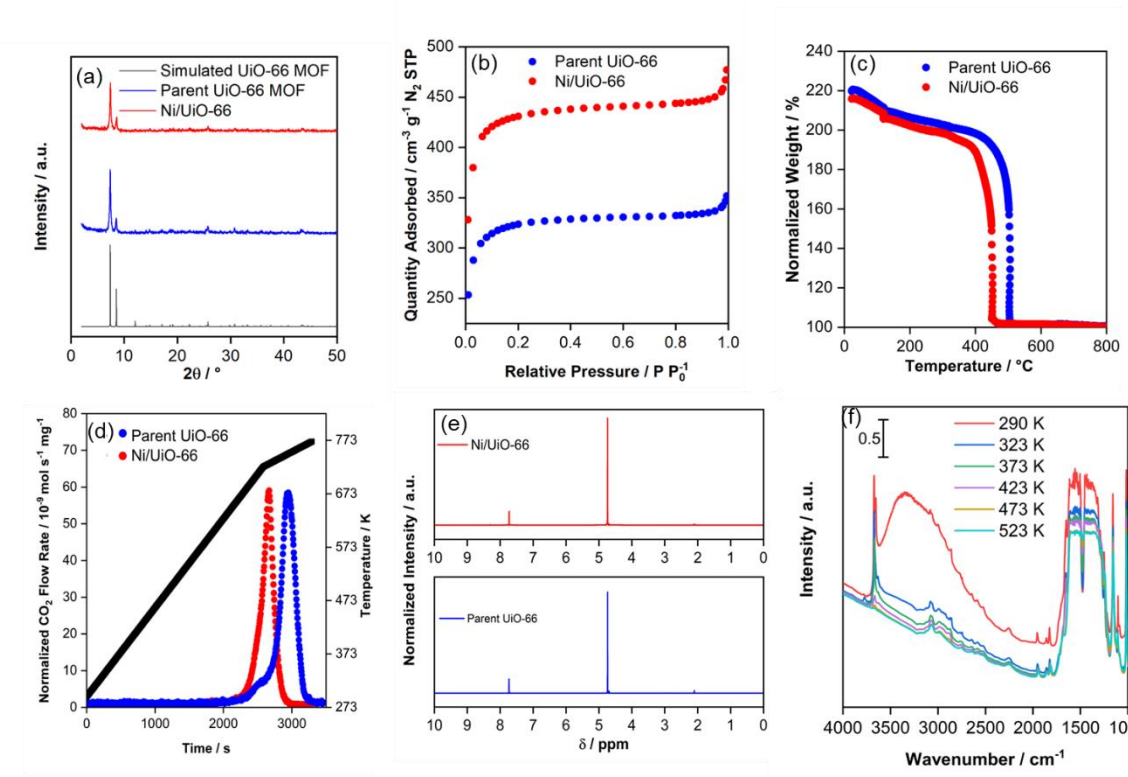

Figure 2.1. (a) PXRD pattern (b) N_2 isotherms, (c) TGA, (d) TPO, and (e) ^{1}H NMR spectra of digested MOFs for parent UiO-66 (blue) and Ni/UiO-66 (red) and (f) IR spectra in flowing helium (0.83 cm^3 s^{-1}) at various temperatures

Table 2.1. BET surface areas and micropore volumes for parent UiO-66 and Ni/UiO-66 MOF

Sample	BET Surface Area / m^2 g^{-1}	Micropore Volume / cm^3 g^{-1}
Parent UiO-66	982	0.63
Ni/UiO-66	1301	0.58

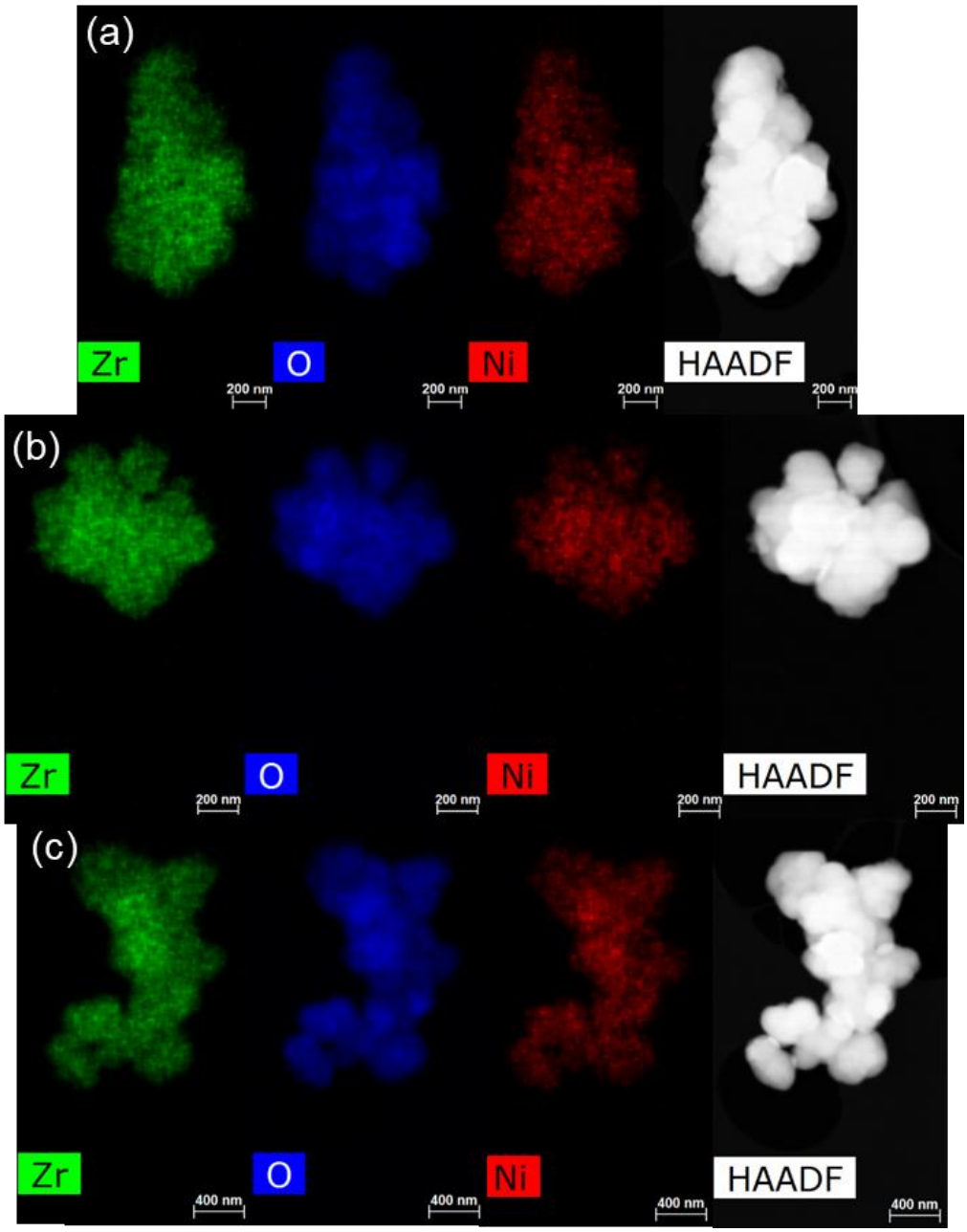

Figure 2.2. Representative high-angle annular dark-field images and energy-dispersive X-ray spectroscopy maps for (a) region 1, (b) region 2, and (c) region 3 of Ni/UiO-66 for Zr, O, and Ni.

Table 2.2. Atomic percentages of Ni, Zr, and O for Ni/UiO-66 MOF as determined by energy-dispersive X-ray spectroscopy

Atom	Region 1 / atomic %	Region 2 / atomic %	Region 3 / atomic %	Average / atomic %
Ni	2.2	1.9	2.7	2.27
Zr	17.1	16.8	20.5	18.17
O	80.7	81.2	76.9	79.60

$$\frac{2.27\ Ni\ atoms\ per\ region}{18.7\ Zr\ atoms\ per\ region\ \left(\frac{1\ node}{6\ Zzr\ atoms}\right)} = 0.75\frac{Ni\ atoms}{node} \qquad \text{Eq. 2.7}$$

Table 2.3. Weight percentages of Ni and Zr for Ni/UiO-66 MOF as determined by inductively coupled plasma-atomic emission spectroscopy

Sample	Ni Content / weight %	Zr Content / weight %	Average Ni per node / $mol_{Ni}\ mol_{node}^{-1}$
Sample 1	2.55	33.44	0.071
Sample 2	2.51	32.95	0.071

$$\frac{\left(\frac{2.55\ g\ Ni}{100\ g\ sample}\right)}{\left(\frac{33.44\ g\ Zr}{100\ g\ sample}\right)} * \frac{\left(91.244\ \frac{g\ Zr}{mol\ Zr}\right)}{\left(58.692\ \frac{g\ Ni}{mol\ Ni}\right)} * \left(\frac{6\ mol\ Zr}{1\ mol\ node}\right) = 0.71\ \frac{mol\ Ni}{mol\ node} \qquad \text{Eq. 2.8}$$

2.3.2. Creation of Active Sites on Ni/UiO-66

The catalytic behavior of Ni/UiO-66 was probed by examining ethylene oligomerization after treating the material in 0.83 $cm^3\ s^{-1}$ of helium (Matheson, 99.997%) at 573 K for 4 hours. The nascent Ni/UiO-66 is a precatalyst that activates on-stream at various ethylene pressures (106 – 2500 kPa) and in the absence of co-catalysts, as shown in Figure 2.3a. The catalyst reaches a steady state at ethylene pressures ≤1000 kPa and, atypically for heterogeneous Ni-based ethylene oligomerization catalysts, maintains stable rates. We observe shorter induction periods for ethylene oligomerization as ethylene pressure is increased, which suggests that ethylene pressures impact the rate at which surface species necessary for attaining steady state rates are formed.

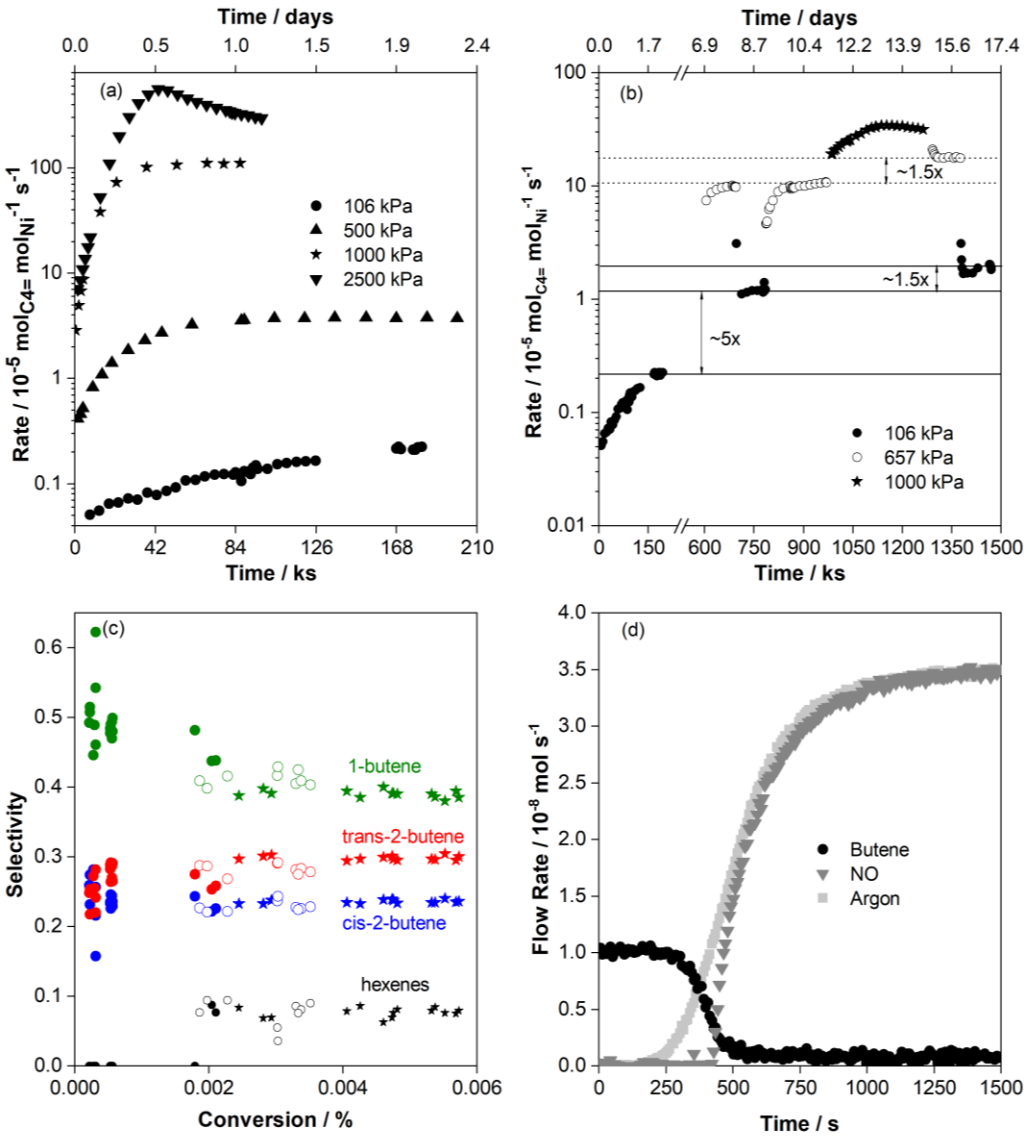

Figure 2.3. Ethylene oligomerization rates with pure ethylene at (a) 106 kPa, 500 kPa, 1000 kPa, and 2500 kPa at 0.83 cm^3 s^{-1} STP and (b) 106 kPa, 657 kPa, and 1000 kPa on the same catalyst with (c) the corresponding 1-butene (—), *cis*-2-butene (—), *trans*-2-butene (—), and hexene (—) selectivity and conversion profiles initially at 106 kPa (●) and after exposure to 657 kPa (○) and 1000 kPa (★) ethylene pressures with an ethylene flow rate of 0.25-1.5 cm^3 s^{-1} STP and 102 mg Ni/UiO-66; (d) Butene, Ar, and NO flowrates during *in-situ* NO titration for ethylene oligomerization at 500 kPa total pressure, 0.83 cm^3 s^{-1} ethylene and 8.3 mm^3 s^{-1} of Ar and NO. Total flow: 0.92 cm^3 s^{-1}. All data shown at 473 K.

The effect of ethylene pressure, shown in Figure 2.3b, was explored further by increasing the ethylene pressure on-stream once the catalyst had reached steady state at 106 kPa, with the rate characteristics for 150-600 ks time-on-stream shown in Figure 2.5a. Using a reference condition of 106 kPa ethylene pressure, increasing ethylene pressure to 657 kPa and lowering ethylene pressure back to 106 kPa (~0-150 ks; ~600-750 ks) increases the rate of oligomerization by 5×. However, a step change in ethylene pressure from 106 kPa back to 657 kPa (~750-900 ks) reveals that the same intrinsic rate is observed at 657 kPa. After exposing the catalyst to 1000 kPa ethylene pressure (~900-1200 ks) and decreasing the ethylene pressure to 657 kPa and 106 kPa (~1200-1500 ks), the intrinsic rate of oligomerization at each condition increased by 50% from the reaction rates at ~600-900 ks. Remarkably, the catalyst is stable for 17 days on-stream, which stands in marked contrast to other nickel supported[59] and framework-based[72] MOFs and nickel functionalized zeolites[31,32,37,40] for oligomerization. We surmise the increase in reaction rates at the same ethylene partial pressures after subsequent exposure to higher ethylene pressures can be attributed to either a change in the nature of the active site or an increase in the number of active sites.

Enhancement in catalytic rates on-stream by generation or alteration of active sites can be reasoned by plotting selectivities at isoconversion, as illustrated in methanol-to-hydrocarbons[120] and methane dehydroaromatization[121] catalysis. In Figure 2.3c, we present steady state product selectivities at 106 kPa after exposing the catalyst to ethylene pressures of 657 kPa and 1000 kPa with the flow rate of ethylene (0.25-1.5 $cm^3\ s^{-1}$ STP) regulated to maintain isoconversion. Product selectivities overlay at isoconversion, indicating that only one type of active site is relevant and formed during ethylene oligomerization by exposure to higher ethylene pressures.

Observations in Figures 2.3a and 2.3b present initiation periods that are plausibly stoichiometric with ethylene pressure, where higher ethylene pressures induce an increase in the number of active sites. Thus, we employed NO titration experiments to enumerate the number of nickel active sites *in-situ* during ethylene oligomerization, with the flow rates for butene, Ar, and NO shown in Figure 2.3d. An equimolar mixture of Ar and NO

was introduced to the catalyst bed after steady state time-on-stream rates were observed, and a decrease in butene flow rate was observed upon introduction of NO. The Ar flow achieves breakthrough while NO has a delayed breakthrough response attributed to the adsorption of NO on the nickel active sites that in turn impedes butene formation. The total number of active sites can be estimated by mathematical integration between the Ar and NO breakthrough curves, normalized by the amount of catalyst loaded (50-200 mg) at various ethylene pressures (110-1800 kPa) and is reported in Table 2.3. An *ex-situ* NO titration on the pristine UiO-66 MOF (Figure 2.18) is reported to demonstrate that NO binds to the nickel active site as opposed to the inactive MOF framework. The tabulated values illustrate that the number of active sites indeed increases with increasing ethylene pressures. At 1800 kPa, it appears only ~12% of the nickel sites are active for oligomerization from ~430 μmol g_{cat}^{-1} calculated from ICP-AES (Table 2.3), assuming one NO binds to one nickel atom to suppress the rate of oligomerization. Prior reports on Ni/NU-1000, a zirconium based MOF,[59,95,122] show isolated nickel atoms and clusters are supported on the MOF framework, and thus, we postulate that only some of the Ni species present are relevant for ethylene oligomerization.

Table 2.4. Experimental conditions and Ni titrated for *in-situ* NO titrations for ethylene oligomerization on Ni/UiO-66 at 473 K.

Ethylene Pressure / kPa	**NO Flow Rate / 10^{-8} mol s^{-1}**	**Ni Titrated / μmol g_{cat}^{-1}**
110	3.48	4.1
111	3.48	5.5
200	2.09	13
500	3.48	15
500	3.48	16
500	3.48	24
1000	6.96	21
1000	13.9	23
1800	13.9	51

2.3.3. Ethylene Oligomerization Kinetics and Mechanism on Ni/UiO-66

On-stream generation of nickel sites with increasing ethylene pressures requires enumeration of active sites formed during reaction and then normalization of rates per mole of nickel to determine correct oligomerization reaction orders with respect to ethylene pressure. After accounting for the increase in the number of active sites formed upon exposure to high ethylene pressures, rates are first order in ethylene pressure as shown in Figure 2.4a, whereas rates appear second order in ethylene pressure when active site densities are not enumerated (Figure 2.5b). An Arrhenius plot, shown in Figure 2.4b, from temperatures of 443–503 K yields an apparent activation enthalpy of 80.9 ± 2.3 kJ mol^{-1}. We note that the number of active sites is unchanged with changing temperatures (Figure 2.11).

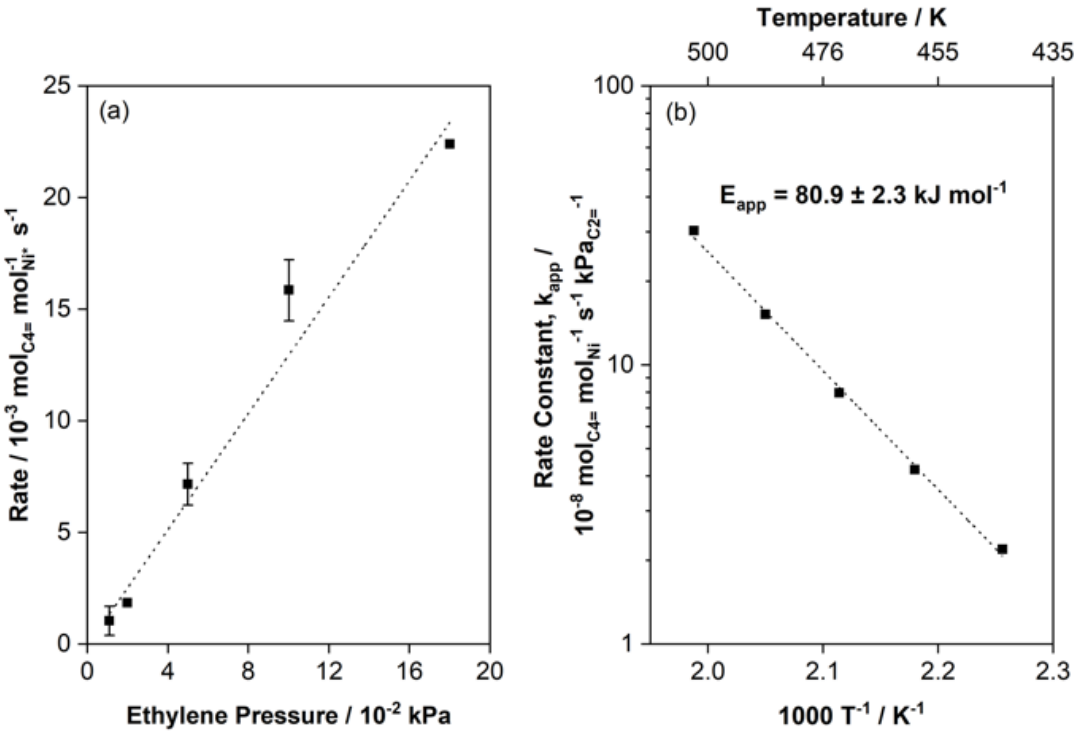

Figure 2.4. (a) Butene formation rate versus ethylene partial pressures (110-1800 kPa) at 473 K (b) Arrhenius plot at 500 kPa on 40.0 mg Ni/UiO-66 and 0.83 cm^3 s^{-1} STP for ethylene oligomerization from 443-503 K.

Active site enumeration and normalization of reaction rates is required as incorrect reaction orders are obtained without active site enumeration. For ethylene oligomerization on Ni/UiO-66, reaction rates are conflated after exposing the catalyst to higher ethylene pressures due to an increase in the number of active sites and the effect of ethylene pressures, as shown in Figures 2.3d and 2.3b, respectively. Figure 2.5a presents a systematic increase in ethylene pressure from 106 kPa to 657 kPa to demonstrate that increases in rate are observed and maintain steady state. However, as noted in Figure 2.3b, returning to 106 kPa (750-900 ks), increases the intrinsic rate of oligomerization (on a per gram basis) is caused by an increase in the number of active sites inferred from overlaying selectivity-conversion profiles at the same pressure (106 kPa) of ethylene (Figure 2.3c). Using the steady state rates presented in Figure 2.5a and without enumerating the active sites, second order kinetics in Figure 2.5b are acquired as opposed to first order kinetics in Figure 2.4b that were obtained by accounting for the increase in site density due to an increase in ethylene pressures.

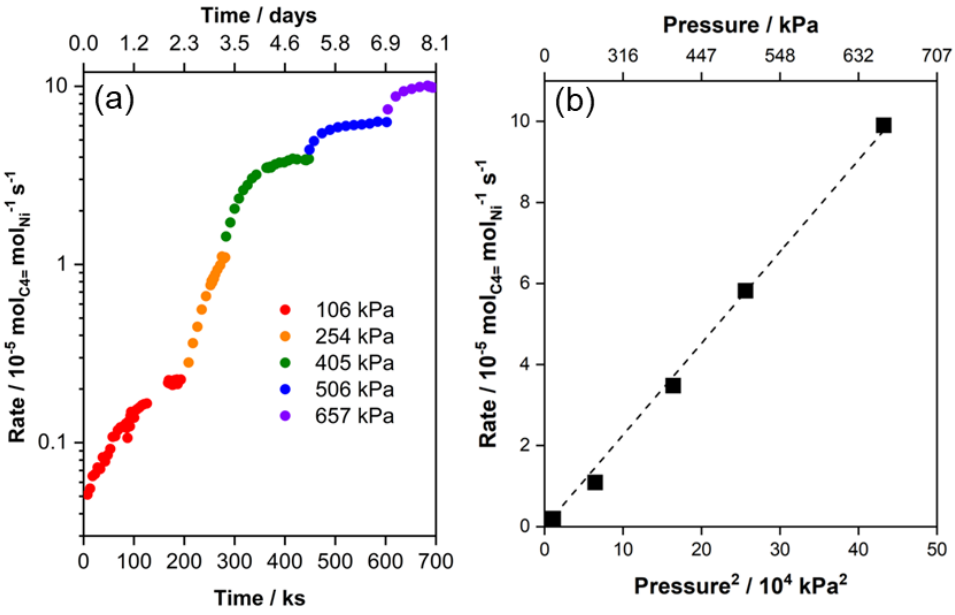

Figure 2.5. Butene formation rates (a) with time on stream with pure ethylene (0.83 cm^3 s^{-1}) during systematic increases in pressure at 106 kPa, 254 kPa, 405 kPa, 506 kPa, and 657 kPa at 473 K and (b) from 106-657 kPa at 473 K with systematic increases in pressure and without enumeration of active sites on Ni/UiO-66.

We report a mechanistic sequence for ethylene oligomerization to rationalize our observed induction periods and reaction kinetics utilizing DFT calculations on cluster models of Ni/UiO-66. The initiation mechanism[32,40,41] (**A** to **H** in Figure 2.6) involves a series of stoichiometric reactions with the first step involving heterolytic activation of a C-H bond in ethylene to form a [Ni-vinyl]$^-$ (**C**) and an acidic [μ_3-OH]$^+$ complex, which is similar to initiation mechanisms proposed on Ni-containing zeolites where a proton from ethylene is abstracted to form a [Ni-vinyl-H]$^+$ complex.[32,33,40,41] After the formation of **C**, another ethylene molecule is adsorbed (**D**) and inserts into the Ni-vinyl bond to form a [Ni-$CH_2CH_2CH{=}CH_2$]$^-$ species (**E**). Species **E** undergoes β-hydride elimination to form butadiene bound to the active site (**F**), and a nickel hydride species (**G**) is formed upon subsequent desorption of butadiene.[32,40,41]

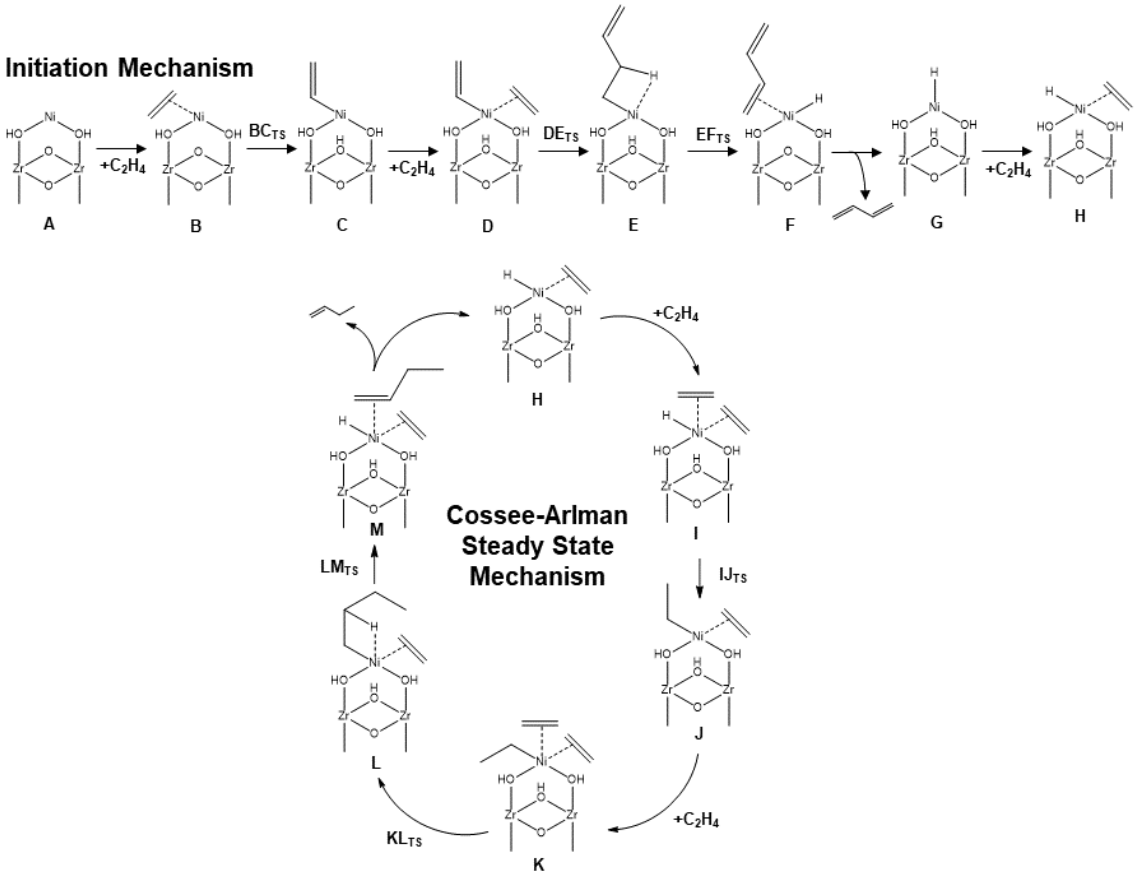

Figure 2.6. Initiation Mechanism and Cossee-Arlman mechanism for ethylene Oligomerization on Ni/UiO-66. Note the entire node is omitted for clarity.

Steady-state oligomerization kinetics are proposed to follow the Cossee-Arlman mechanism which typically initiates with the formation of a nickel hydride species (**G** in Figure 2.6 and **CA-1** in Figure 2.23).[6,7,8,10,12–14,22,24,29,31] DFT calculations carried out using cluster models of Ni/UiO-66 result in near zero apparent activation energies that are inconsistent with first-order kinetics and activation energies observed experimentally (Table 2.7 and Figure 2.25). Hence, we employed *ab initio* thermodynamic analysis[103–106] to probe the active site composition under reaction conditions. Thermodynamic modeling suggests among candidate structures plausible at steady state conditions (Figures 2.6 and 2.23), a nickel-ethyl species (**CA-3** in Figure 2.23) requires the presence of an additional ethylene adsorbate for ethylene pressures greater than ~100 kPa (Figure 2.7). Thus, we employ a more representative model of the active site environment that accounts for physisorbed ethylene in the pores of the MOF at the experimental operating conditions (110 – 1800 kPa) in cluster model DFT calculations throughout the catalytic cycle. This model incorporates one extra adsorbed ethylene molecule to influence the reaction energetics and nature of the active site. A similar model on Ni-SSZ-24 with physisorbed ethylene molecules was able to replicate experimentally determined activation energies with DFT calculations.[40] Experimentally, catalytic stability for ethylene oligomerization on Ni-MCM-41 is reported at 1500 kPa and sub-ambient temperatures and attributed to solvation of ethylene molecules but the Ni-MCM-41 is observed to deactivate at pressures <900 kPa.[44] In the Ni/UiO-66 system reported herein, we observe catalytic stability at lower ethylene pressures (<1000 kPa) and elevated temperatures (443-503 K) to plausibly suggest physisorbed ethylene stabilizes nickel active site at our process conditions.[44] Furthermore, previous studies on homogeneous nickel catalysts have suggested that an additional olefin facilitates the formation of a five-coordinated transition state which in turn enables β-hydride elimination required to desorb the resultant oligomer and enable subsequent chain growth during oligomerization.[123] Along the same lines, we posit that solvation by ethylene facilitates olefin insertion into the Ni-C bond for chain growth. Co-adsorbed ethylene prevents the formation of a stable, unreactive surface-bound intermediate (**K**) and destabilizes the transition state for this step ($\mathbf{KL}_{TS}$) relative to a four coordinated nickel-ethyl-ethylene complex (**J**).[123,124] For these reasons, we postulate that

structure **H**, a nickel hydride species with ethylene adsorbed on the active site, is relevant for the Cossee-Arlman mechanism operative in our system.

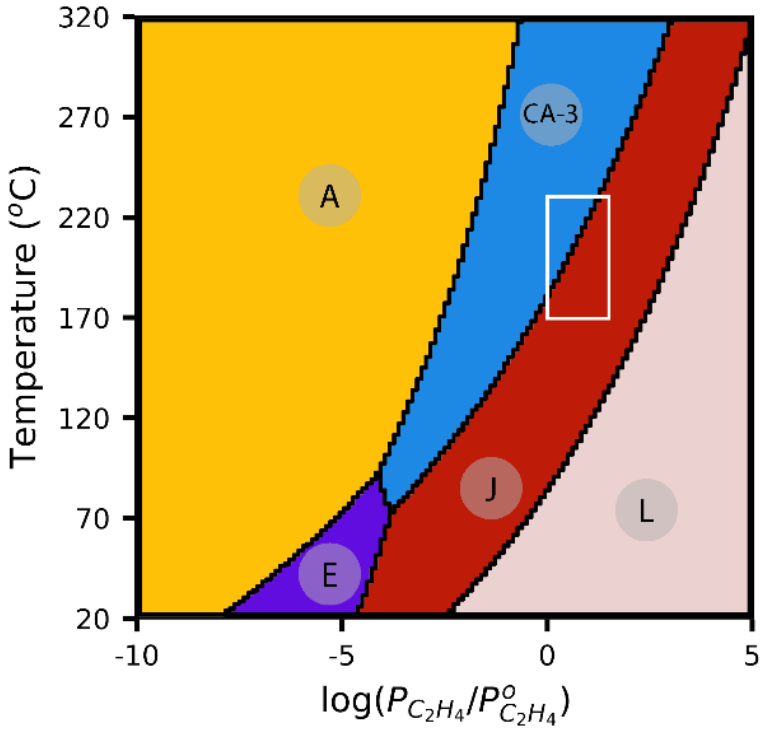

Figure 2.7. Phase diagram for the Ni/UiO-66 catalyst model calculated as a function of $P_{C_2H_4}$ (relative to standard pressure) and temperature at a constant 1,3-butadiene partial pressure of 0.05 Pa. Candidate structures were those utilized in Figures 2.6 and 2.23; thermodynamically stable structures are those indicated in the phase diagram.

From H, another ethylene molecule is adsorbed to yield structure **I**. A migratory hydride insertion transforms species **I** to a nickel-ethyl species (**J**). From species **J**, another ethylene molecule is adsorbed (**K**) and inserts into the Ni-C bond to produce a nickel-butyl species (**L**). The nickel butyl species undergoes β-hydride elimination to produce 1-butene adsorbed on the surface (**M**) and regenerate the nickel hydride active site with ethylene adsorbed (**H**).

Enthalpy (red) and free energy (blue) diagrams for ethylene oligomerization on Ni/UiO-66 are presented in Figure 2.24 and Figure 2.8 for the initiation mechanism and the Cossee-Arlman mechanism, respectively. We examined various spin states of Ni and

report here the lowest energy spin state structures ($S^2 = 0$) with results from other spin states reported in the SI along with optimized reaction coordinates. The intrinsic free energy barrier for the C-H activation of the bound olefin (**BC**$_{TS}$) during the initiation mechanism is 141 kJ mol^{-1} at 298 K and ambient pressure, which is consistent with the 153 kJ mol^{-1} intrinsic free energy barrier calculated on Ni-AIM+NU-1000 for C-H activation.[53] Olefin insertion into the Ni-vinyl bond (**DE**$_{TS}$) and the β-hydride elimination step (**EF**$_{TS}$) have intrinsic free energy barriers of 15 kJ mol^{-1} and 31 kJ mol^{-1}, respectively. The free energy of adsorption of an ethylene molecule from G to H is -49 kJ mol^{-1}. From experiment, butadiene is observed at all ethylene pressures during the first 100 minutes on stream (Figure 2.8), which is consistent with the β-hydride elimination step (**EF**$_{TS}$) where butadiene is formed. Additionally, shorter induction periods and an increase in the number of active sites are observed with increasing ethylene pressures (Figure 2.3 and Table 2.4), which is congruous with the stoichiometric formation of active sites dependent on ethylene pressure proposed in the initiation mechanism.

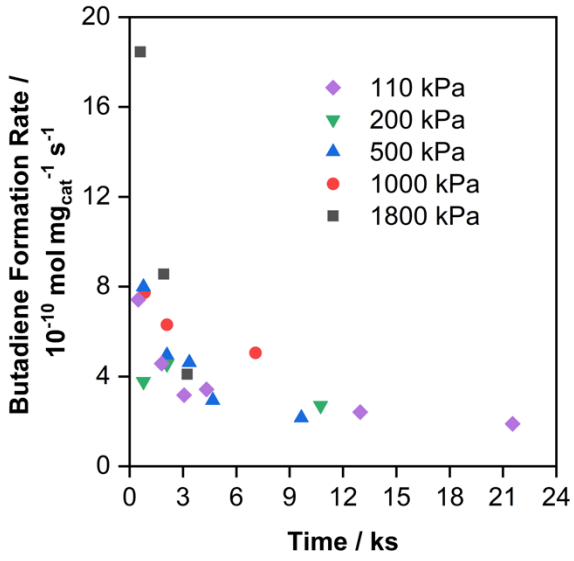

Figure 2.8. Butadiene formation rate during ethylene oligomerization at 110 kPa, 200 kPa, 500 kPa, 1000 kPa, and 1800 kPa at 473 K and 0.83 cm^3 s^{-1} STP.

The steady state Cossee-Arlman mechanism begins with species **H** followed by adsorption of an ethylene molecule (**I**), resulting in a free energy of adsorption of 17 kJ

mol^{-1}. The migratory insertion of the hydride and adsorbed ethylene molecule (**IJ**$_{TS}$) has a barrier of 22 kJ mol^{-1}. From species **J**, the free energy for adsorbing another ethylene molecule is 18 kJ mol^{-1}. The olefin insertion step (**KL**$_{TS}$), the kinetically relevant step in the Cossee-Arlman mechanism, transpires with a free energy barrier of 80 kJ mol^{-1}. The β-hydride elimination step (**LM**$_{TS}$) yields a free energy barrier of 48 kJ mol^{-1}. Calculated free energy barriers for the migratory insertion, olefin insertion, and β-hydride elimination step for ethylene oligomerization on a model of Ni/NU-1000, where physisorbed ethylene was not incorporated, are 15 kJ mol^{-1}, 55 kJ mol^{-1}, 48 kJ mol^{-1}, respectively, and are consistent with calculated free energy barriers on Ni/UiO-66 reported here.[53,80] With ethylene insertion into the Ni-C bond as the kinetically relevant step, experimentally determined first order kinetics with respect to ethylene (Figure 2.4a), and thermodynamic modeling results indicating additional adsorbed ethylene under reaction conditions (Figure 2.7), we propose J as the most abundant surface intermediate which results in a calculated apparent activation enthalpy of 49 kJ mol^{-1}. This value is somewhat lower than the experimentally determined activation enthalpy of 81 kJ mol^{-1}. However, this mechanistic sequence and model are consistent with experimentally observed first-order kinetics in ethylene concentrations, induction periods that decrease with higher ethylene pressures, and stoichiometric events that form active sites on-stream.

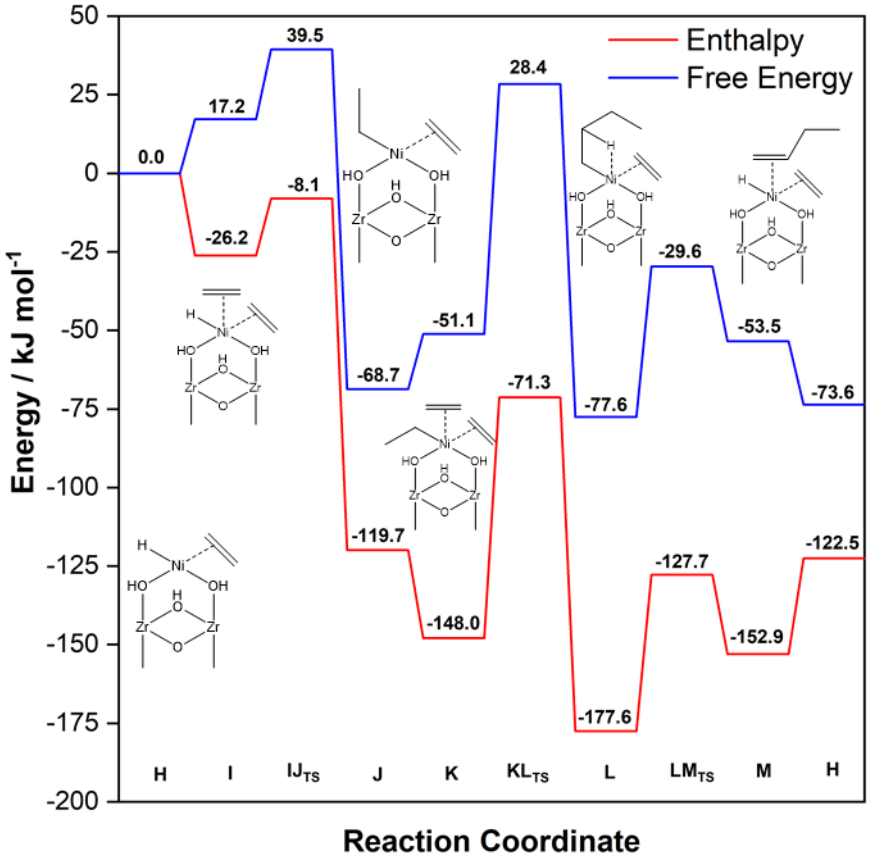

Figure 2.9. Enthalpy (—) and free energy (—) diagram for the Cossee-Arlman mechanism with an extra ethylene molecule on the nickel for ethylene oligomerization on Ni/UiO-66 at 298 K and 101.3 kPa. All structures in the singlet spin state ($S^2 = 0$).

2.4. Conclusion

In summary, we report a nickel supported UiO-66 MOF that uniquely engenders active sites on-stream and exhibits >15-day time-on-stream stability devoid of co-catalysts unprecedented in heterogeneous catalytic systems for ethylene oligomerization. Active site densities are enumerated *in-situ* with NO titration experiments to disambiguate the effect of increased reaction rates with increasing ethylene pressures to appropriately determine first-order kinetics in ethylene pressure. A cluster model of Ni/UiO-66 that captures the effect of physisorbed ethylene is determined with *ab initio* thermodynamic modeling and comparisons between experimental and computed apparent activation enthalpies validate the Cossee-Arlman mechanism for ethylene oligomerization on Ni/UiO-66 MOFs.

2.5. Supplemental Information

2.5.1. Ethylene Oligomerization Time on Stream and Kinetics on Ni/UiO-66

In Figure 2.10, space velocity measurements (0.25-1.5 $mol_{C2=}$ mol_{Ni}^{-1} s^{-1}) demonstrate that the rate is invariant with space velocity and thus is not influenced by product inhibition or external mass transfer limitations at 106 kPa and 500 kPa.

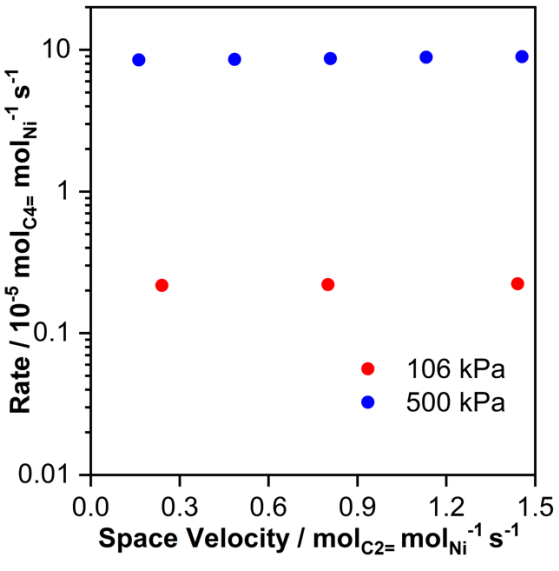

Figure 2.10. Rate versus space velocity at 106 kPa and 500 kPa for ethylene oligomerization at 473 K with ethylene flow rates ranging from 0.083-1.49 cm^3 s^{-1}.

We attempted to explore if increases in temperature increases the number of active sites. Using 473 K as a reference condition, changing the reaction temperature does not change the intrinsic rate of oligomerization at the same reference condition at 473 K, as shown in Figure 2.11. To verify if an increase in intrinsic rate is still obtained with higher pressures, after this experiment, we exposed the catalyst to 1000 kPa ethylene (Figure 2.12) and observe a ~1.5x increase in rate. This increase in rate is consistent with what was seen previously after exposure to higher ethylene pressures in Figure 2.4b, where a ~1.5× increase in rate was observed at 657 kPa ethylene pressure when the catalyst was exposed to 1000 kPa ethylene pressure. In Figure 2.13, we observe that selectivities and conversions overlay at 500 kPa to indicate that there is only one type of active site generated during

ethylene oligomerization and the increase in rate is caused by the inception of active sites at high ethylene pressures.

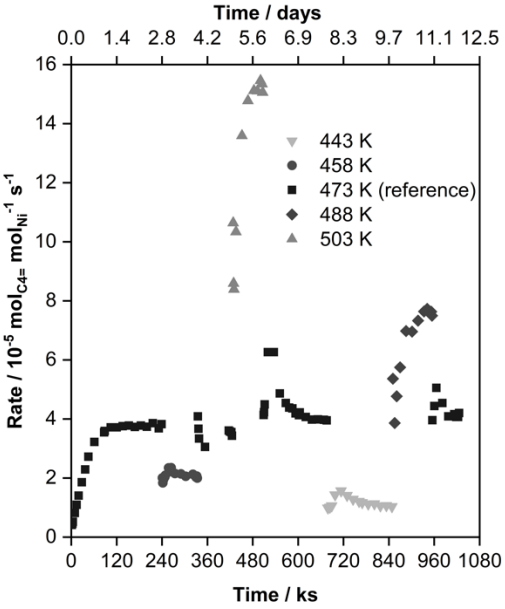

Figure 2.11. Rates of ethylene oligomerization as a function of time on stream at 500 kPa and 0.83 cm^3 s^{-1} from 443-503 K.

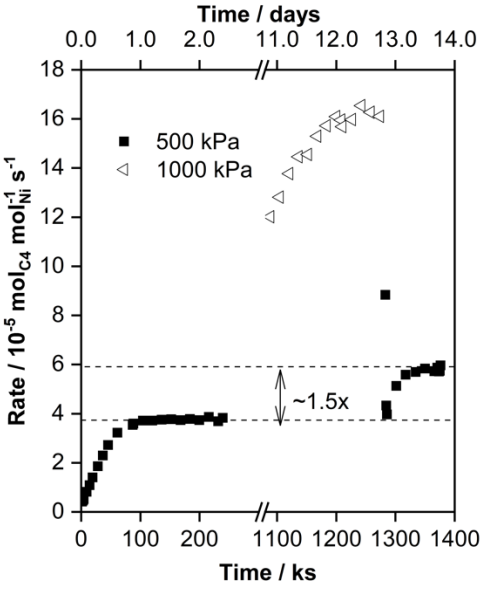

Figure 2.12. Rates of ethylene oligomerization as a function of time on stream at 473 K at 500 kPa and 1000 kPa.

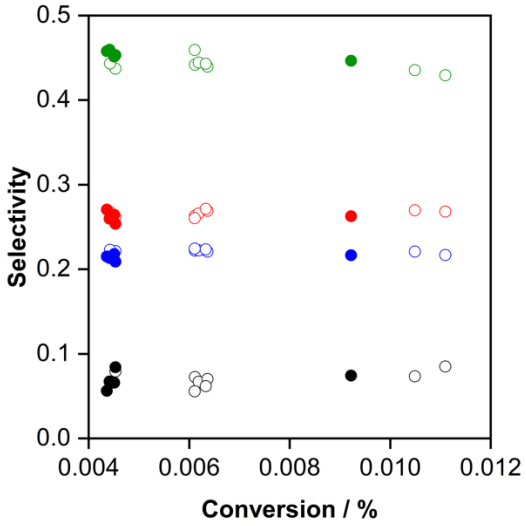

Figure 2.13. 1-butene (▲), cis-2-butene (▲), trans-2-butene (▲), and hexene (▲) selectivity versus conversion at 500 kPa before (●) and after exposure (○) to 1000 kPa with an ethylene flow rate of 0.25 -1.5 cm^3 s^{-1} STP and 40 mg Ni/UiO-66

2.5.2. Supplemental NO Titrations

This section presents NO titration experiments at various ethylene pressures presented in Table 2.4 during ethylene oligomerization once that catalyst had reached steady state. The quantification of NO required to titrate active Ni species is achieved by the mathematical integration of the Ar and NO breakthrough curves, normalized by the amount of catalyst loaded (50-200 mg).

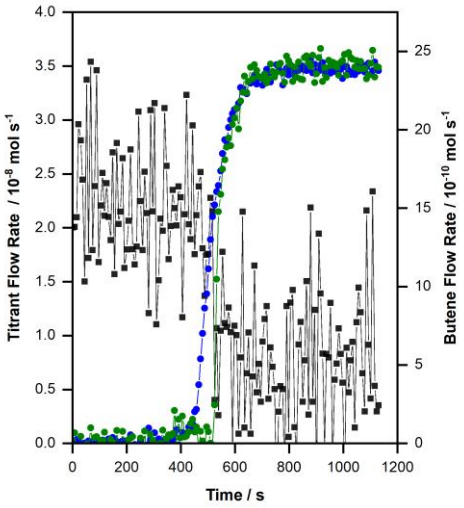

Figure 2.14. Butene (■), Ar (●), and NO (●) flowrates during in-situ NO titration for ethylene oligomerization at 110 kPa total pressure, 0.83 cm^3 s^{-1} ethylene, 8.3 mm^3 s^{-1} of Ar, and 8.3 mm^3 s^{-1} NO. Total flow: 0.92 cm^3 s^{-1} at 473 K. Catalyst weight: 178.5 mg Ni/UiO-66.

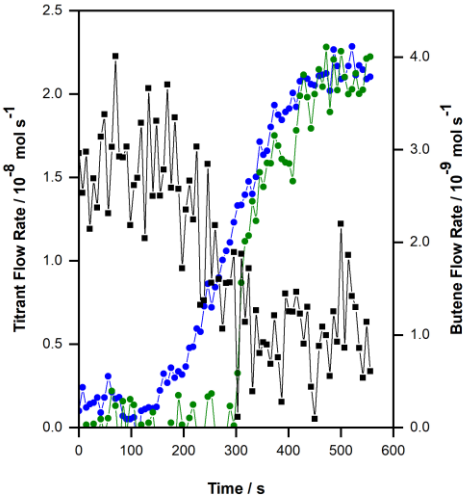

Figure 2.15. Butene (■), Ar (●), and NO (●) flowrates during in-situ NO titration for ethylene oligomerization at 200 kPa total pressure, 0.83 cm^3 s^{-1} ethylene, and 5.0 mm^3 s^{-1} Ar, and 5.0 mm^3 s^{-1} NO. Total flow: 0.88 cm^3 s^{-1} at 473 K. Catalyst weight: 76.5 mg Ni/UiO-66.

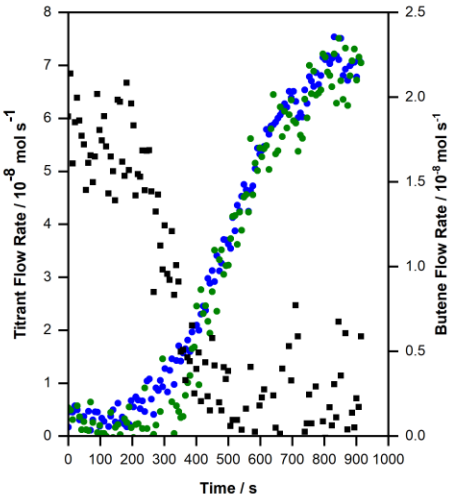

Figure 2.16. Butene (■), Ar (●), and NO (●) flowrates during in-situ NO titration for ethylene oligomerization at 1000 kPa total pressure, 0.83 cm^3 s^{-1} ethylene, 16.8 mm^3 s^{-1} Ar, and 16.8 mm^3 s^{-1} NO. Total flow: 1.0 cm^3 s^{-1} at 473 K. Catalyst weight: 60.8 mg Ni/UiO-66.

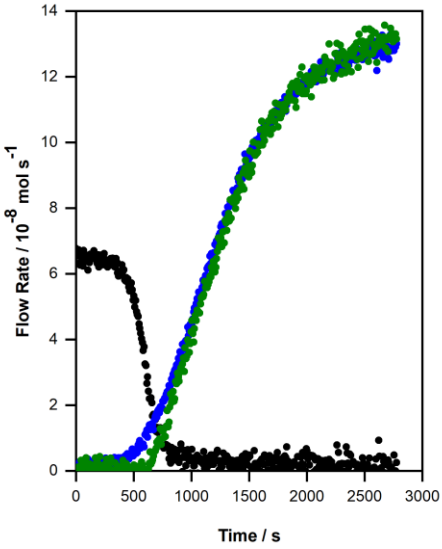

Figure 2.17. Butene (■), Ar (●), and NO (●) flowrates during in-situ NO titration for ethylene oligomerization at 1800 kPa total pressure, 0.83 cm^3 s^{-1} ethylene, 16.8 mm^3 s^{-1} Ar, and 16.8 mm^3 s^{-1} NO. Total flow: 1.0 cm^3 s^{-1} at 473 K. Catalyst weight: 60.8 mg Ni/UiO-66.

The pristine UiO-66 MOF was inactive for ethylene oligomerization (500 kPa ethylene, 473 K, 0.83 cm^3 s^{-1}). However, an *ex-situ* titration was performed on the pristine UiO-66 MOF to determine if the NO adsorbed/reacted on Ni/UiO-66 is on nickel active site or on the UiO-66 MOF. Titration experiments in an empty reactor and with UiO-66 are shown in Figure 2.18.

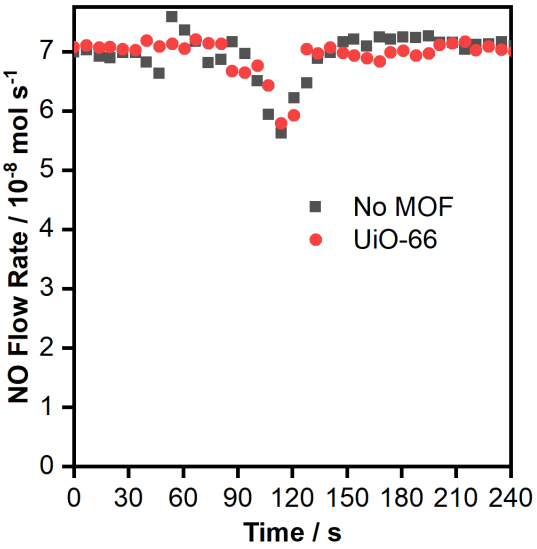

Figure 2.18. Ex situ titration with and without UiO-66 at 106 kPa, 473 K and 0.17 cm^3 s^{-1} of 1% NO and 99% N2 and 0.83 cm^3 s^{-1} ethylene with 56 mg UiO-66.

From observations reported in Figure 2.18, there is no difference in the NO flow rates through an empty reactor and a loaded reactor with UiO-66. Thus, we surmise that NO does not titrate the UiO-66 MOF, and all NO titrated from the *in-situ* titration experiment binds to the nickel active site.

2.5.3. Supplemental XAS

X-ray absorption spectra were collected on Ni/UiO-66 as-synthesized, after helium pretreatment (573 K, ambient pressure, 4 hours), and after ethylene oligomerization (1000 kPa, 473 K, and 0.83 cm^3 s^{-1} for 24 hours) as shown in Figures 2.19-2.22.

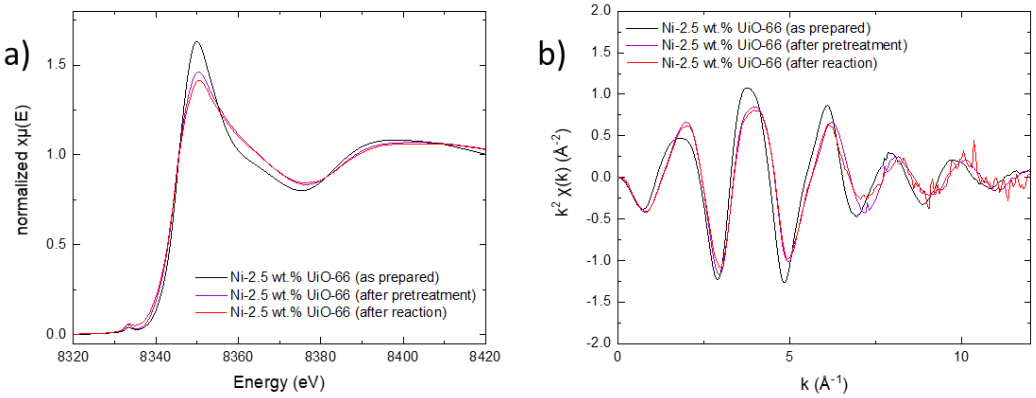

Figure 2.19. Comparison of k2-weighted Ni K-edge normalized XANES spectra (a) and χ(k) plots (b) of the as prepared Ni/UiO-66, the sample after pretreatment in He flow at 573 K for 4 hours and the sample after reaction in ethylene flow at 1000 kPa and 473 K for 24 hours.

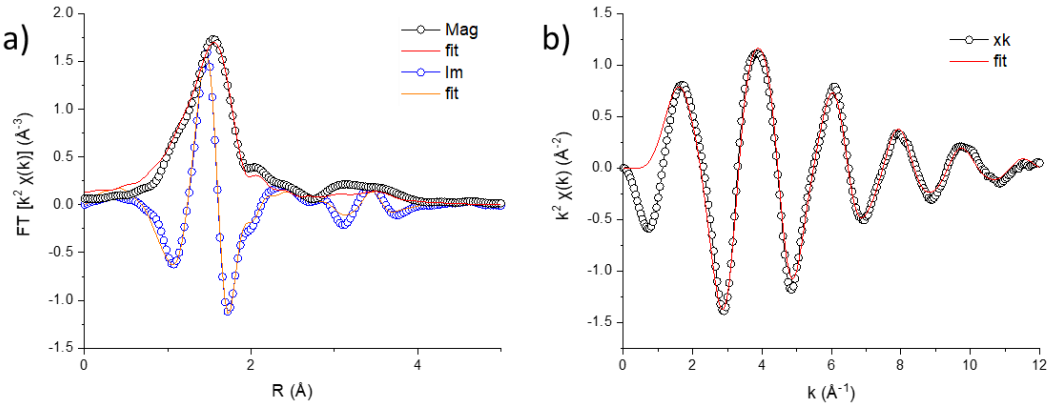

Figure 2.20. k2-weighted Ni K-edge (a) Magχ(R) and Imgχ(R) spectra, and (b) xk plots of as prepared Ni/UiO-66, and the corresponding FEFF fits.

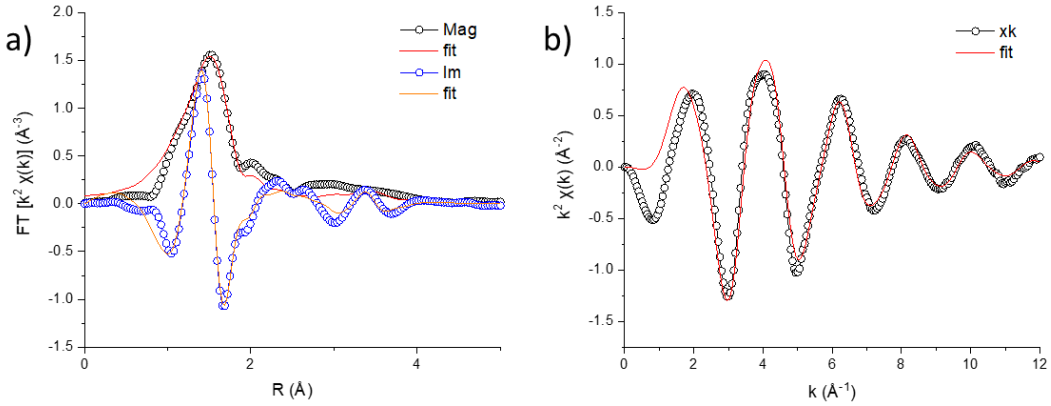

Figure 2.21. k2-weighted Ni K-edge (a) Magχ(R) and Imgχ(R) spectra, and (b) xk plots of Ni/UiO-66 after pretreatment in He flow at 573 K for 4 hours, and the corresponding FEFF fits.

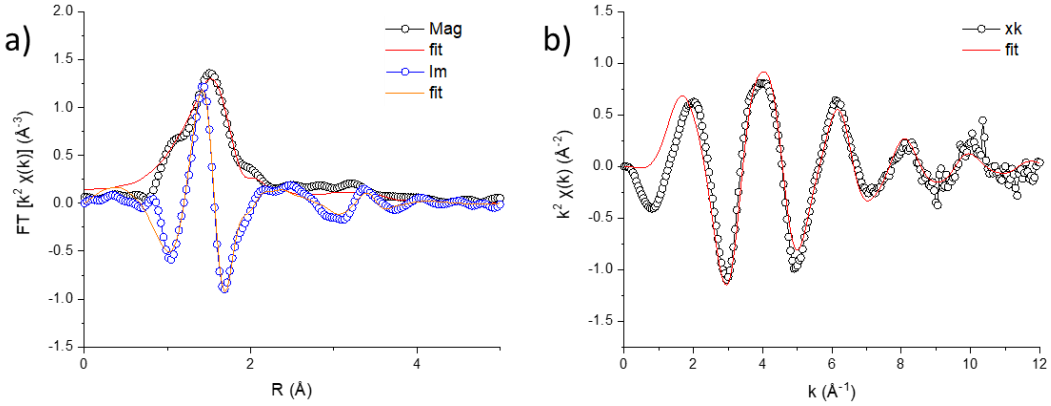

Figure 2.22. k2-weighted Ni K-edge (a) Magχ(R) and Imgχ(R) spectra, and (b) xk plots of Ni/UiO-66 after reaction in ethylene flow (0.83 cm^3 s^{-1}) at 1000 kPa and 473 K for 24 hours, and the corresponding FEFF fits.

From our EXAFS fitting in Table 2.5, we do not observe any Ni-Ni interactions, indicating that nickel does not form clusters and suggesting that nickel atoms are isolated on Ni/UiO-66 in as-synthesized materials, after pretreatment, and after reaction. The Ni-O coordination decreases from 6 to 5 after pretreatment in helium at 573 K. We surmise this is caused by loss of adsorbed water on the active metal after activating the material at elevated temperatures.[96]

Table 2.5. EXAFS fitting results of as synthesized, thermally treated (He flow at 573 K for 4 hours) and post reaction (ethylene flow of 0.83 cm^3 s^{-1} at 1000 kPa and 473 K for 24 hours) structures of Ni/UiO-66.

Condition	Back scatters	Coordination number	Interatomic distances / Å	Debye-Waller factor, $\Delta\sigma^2$ / $Å^2$
As Synthesized	Ni-O	6.1 ± 0.3	2.045 ± 0.0057	0.0077 ± 0.0009
	Ni-Ni	-	-	-
Thermal Treated	Ni-O	5.2 ± 0.4	1.997 ± 0.0036	0.0080 ± 0.0012
	Ni-Ni	-	-	-
Post Reaction	Ni-O	4.8 ± 0.3	2.010 ± 0.0037	0.0086 ± 0.0012
	Ni-Ni	-	-	-

2.5.4. The Cossee-Arlman Mechanism and Supplemental DFT Calculations

The initiation and Cossee-Arlman mechanisms without an adsorbed ethylene molecule during the catalytic cycle are presented in Figure 2.23.[31,32,40,41,49–51,53,80,95] The initiation mechanism is similar up to structure **G**, a nickel hydride species, in Figure 2.6 and will be denoted here as **CA-1** in Figure 2.23. From the nickel hydride species, one ethylene molecule is adsorbed to generate **CA-2**, which is identical to **H** in Figure 2.6. **CA-2** undergoes a migratory insertion into the Ni-H bond to generate a nickel ethyl species, **CA-3.** Another ethylene molecule is adsorbed on nickel to yield structure **CA-4**, which is identical to **J** in Figure 2.6. The nickel-ethyl-ethylene complex undergoes an olefin insertion into the Ni-alkyl intermediate to generate a nickel-butyl species, **CA-5**. The nickel-butyl species subsequently undergoes a β-hydride elimination step to generate **CA-6**, and then butene desorbs to regenerate **CA-1**.

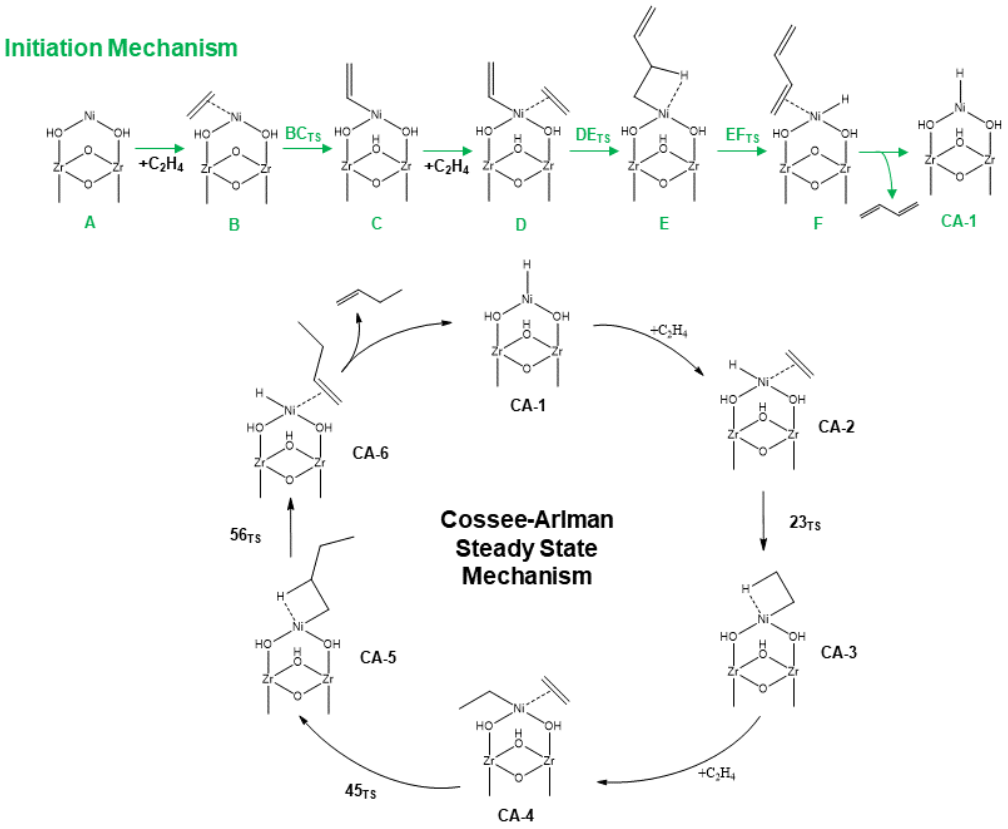

Figure 2.23. Initiation (green arrows) and Cossee-Arlman mechanisms[31,32,40,41,49–51,53,80,95] (black arrows) for ethylene oligomerization on Ni/UiO-66 without an additional physisorbed ethylene molecule. The entire node is not shown for clarity.

Below in Tables 2.6 - 2.8 reports electronic energies, enthalpies, and Gibbs free energies at 298 K and 101.3 kPa for intermediate and transition state structures reported in Figures 2.6 and 2.23 using DFT calculations. The error with the M06-L functional for calculating reaction barriers is 10-20 kJ mol^{-1} and has been benchmarked against the BH76 database,[125] which contains a variety of hydrogen transfer, association, nucleophilic substitution, and unimolecular reactions.[126,127] The lowest energy spin state is used to formulate the free energy and enthalpy diagrams below. The bare cluster model, $[[NiZr_6(\mu_3\text{-}OH)_3(\mu_3\text{-}O)_5(OH)_2]^{11+} \bullet 11(CHO_2^{-1})$, is represented as species **A.**[97]

Table 2.6. Electronic energy, enthalpy, and Gibbs free energy (hartree) for all intermediates and TS structures in the initiation mechanism for the Cossee-Arlman mechanism at 298 K and 101.3 kPa as well as the corresponding spin state. Absolute energies with the lowest spin state energy for intermediates are italicized and the relative enthalpies and free energies (kJ mol^{-1}) with respect to **A** and three ethylene molecules are reported.

Species	Spin	E	H^0	G^0	ΔH	ΔG
A	*2*	*-4626.751987*	*-4626.327234*	*-4626.46564*	*0.0*	*0.0*
B	0	-4705.256383	-4704.776584	-4704.917809	-	-
B	*2*	*-4705.299851*	*-4704.818624*	*-4704.963478*	*-86.4*	*-34.6*
BC_{TS}	*2*	*-4705.242282*	*-4704.766155*	*-4704.909761*	*51.3*	*106.4*
C	0	-4705.265736	-4704.785254	-4704.929369	-	-
C	*2*	*-4705.274215*	*-4704.792441*	*-4704.937545*	*-17.8*	*33.5*
D	*0*	*-4783.821381*	*-4783.282879*	*-4783.43410*	*-101.7*	*2.2*
D	2	-4783.803113	-4783.264683	-4783.419532	-	-
DE_{TS}	*0*	*-4783.816713*	*-4783.279656*	*-4783.428309*	*-93.3*	*17.4*
E	*0*	*-4783.857469*	*-4783.316806*	*-4783.465687*	*-119.2*	*-17.2*
EF_{TS}	0	-4783.816401	-4783.280631	-4783.429742	*-95.8*	*13.6*
F	*0*	*-4783.827841*	*-4783.289472*	*-4783.438726*	*-119.1*	*-10.0*
G	*0*	*-4627.939253*	*-4627.494089*	*-4627.632369*	*-28.1*	*25.6*
G	2	-4627.932957	-4627.489498	-4627.630864	-	-
H	*0*	-4706.494099	-4705.991418	-4706.135487	*-130.2*	*-22.9*

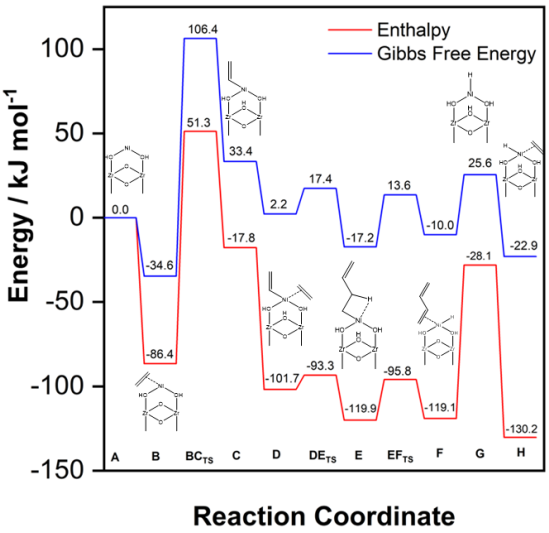

Figure 2.24. Enthalpy (–) and free energy (–) diagram for the initiation mechanism prior to the Cossee-Arlman mechanism for ethylene oligomerization on Ni/UiO-66 at 298 K and 101.3 kPa.

Table 2.7. Electronic energy, enthalpy, and Gibbs free energy (hartree) for all intermediates and TS structures in the Cossee-Arlman mechanism presented in Figure 2.26 at 298 K and 101.3 kPa. The singlet spin state was determined to yield the lowest spin state energies[95] (S^2 = 0) and only those values are reported here. Absolute energies with the lowest spin state energy for intermediates are italicized and the relative enthalpies and free energies (kJ mol^{-1}) with respect to **CA-1** and two ethylene molecules.

Species	E	H^0	G^0	ΔH	ΔG
CA-1	-4627.939253	-4626.327234	-4627.632369	0	0
CA-2	-4706.494099	-4705.991418	-4706.135487	-102.1	-48.5
23_{TS}	-4706.485922	-4705.984675	-4706.127945	-84.4	-28.7
CA-3	-4706.509280	-4706.004491	-4706.149222	-136.4	-84.6
CA-4	-4785.058461	-4784.495528	-4784.64629	-222.0	117.2
45_{TS}	-4785.028086	-4784.465436	-4784.615701	-143.0	-36.9
CA-5	-4785.072166	-4784.507926	-4784.658104	-254.5	-148.2
45_{TS}	-4785.051440	-4784.491163	-4784.641413	-224.5	-116.0
CA-6	-4785.060744	-4784.498403	-4784.648126	-243.6	-41.7
CA-1 + C_4H_8	--4785.017093	-4784.457656	-4784.629694	-138.1	-90.2

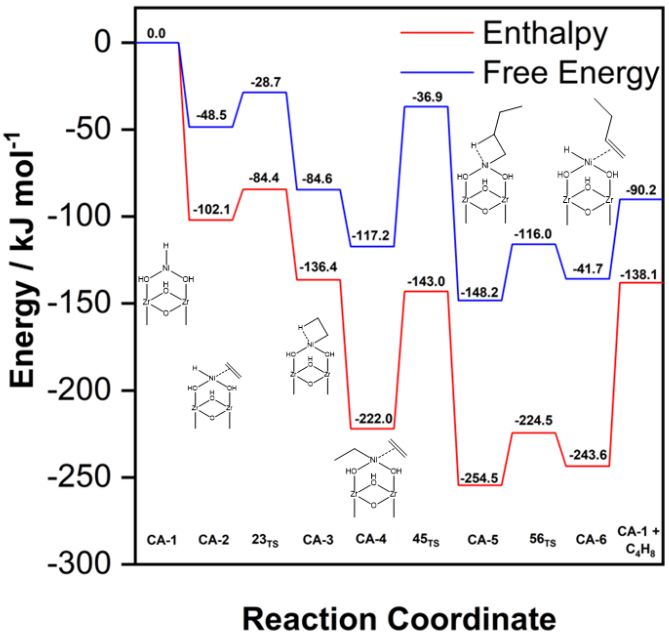

Figure 2.25. Enthalpy (–) and free energy (–) diagram for Cossee-Arlman mechanism for ethylene oligomerization on Ni/UiO-66 at 298 K and 101.3 kPa. All structures in the singlet spin state (S^2 = 0).

The olefin insertion step (**45**$_{TS}$) is reported to be the kinetically relevant step in the Cossee-Arlman mechanism on Ni/NU-1000 as well as our DFT study on Ni/UiO-66.[59,80,95] From the first order kinetics presented in Figure 2.4a, it suggests that ethylene adsorbed on the nickel hydride active site or a nickel-ethyl species (**CA-2** or **CA-3**, respectively) is the most abundant surface intermediate to afford computational activation enthalpies of -40.9 or -6.6 kJ mol^{-1}, respectively. The value is greatly underestimated from the experimentally measured activation energy of 81 kJ mol^{-1} (Figure 2.4b). Thus, we added an ethylene molecule in our computational cluster model to mimic the effects of solvation from physisorbed ethylene in the MOF pores relevant for high operating pressures (100 – 1800 kPa).

Table 2.8. Electronic energy, enthalpy, and Gibbs free energy (hartree) for all intermediates and TS structures in the Cossee-Arlman mechanism with an additional ethylene molecule presented in Figure 2.6 at 298 K and 101.3 kPa. The singlet spin state was determined to yield the lowest spin state energies[95] ($S^2 = 0$) and only those values are reported here. Absolute energies with the lowest spin state energy for intermediates are italicized and the relative enthalpies and free energies (kJ mol^{-1}) with respect to **H** and two ethylene molecules.

Species	E	H^0	G^0	ΔH	ΔG
H	-4706.494099	-4705.991418	-4706.135487	0	0
I	-4785.018991	-4784.459828	-4784.61359	-26.2	17.2
IJ_{TS}	-4785.010683	-4784.452934	-4784.605106	-8.1	39.5
J	-4785.058461	-4784.495528	-4784.64629	-119.9	-68.7
K	-4863.584124	-4862.964671	-4863.124229	-148.0	-51.2
KL_{TS}	-4863.554575	-4862.935458	-4863.09398	-71.3	28.4
L	-4863.617176	-4862.975941	-4863.134327	-177.6	-77.6
LM_{TS}	-4863.574256	-4862.956953	-4863.116069	-127.7	-29.6
M	-4863.597071	-4862.966558	-4863.125164	-152.9	-53.5
H+ C_4H_8	-4863.571939	-4862.954985	-4863.132812	-122.5	-73.6

2.5.5. Influence of 1,3-butadiene partial pressure on *ab initio* thermodynamic analysis results

Based on Equation 2.2 and 1,3-butadiene formation observed at various partial pressures as shown in Figure 2.8, we attempted to explore if 1,3-butadiene concentration affected the phase space and dominate surface species for ethylene oligomerization as

shown in Figure 2.26. At 1800 kPa ethylene pressure, the greatest concentration of butadiene observed during the induction period is 0.05 Pa, or $10^{-6.3}$ kPa (Figure 2.26a). The phase space at this condition is presented in Figure 2.7. As the reaction periods, butadiene is not observed after ~100 minutes (Figure 2.9) and is represented in the model as 10^{-20} kPa butadiene pressure (Figure 2.26d). Despite changes in the phase space as a function of 1,3-butadiene partial pressure, Figure 2.26 demonstrates that under operating conditions the dominant surface intermediates are **CA-3** and **J**.

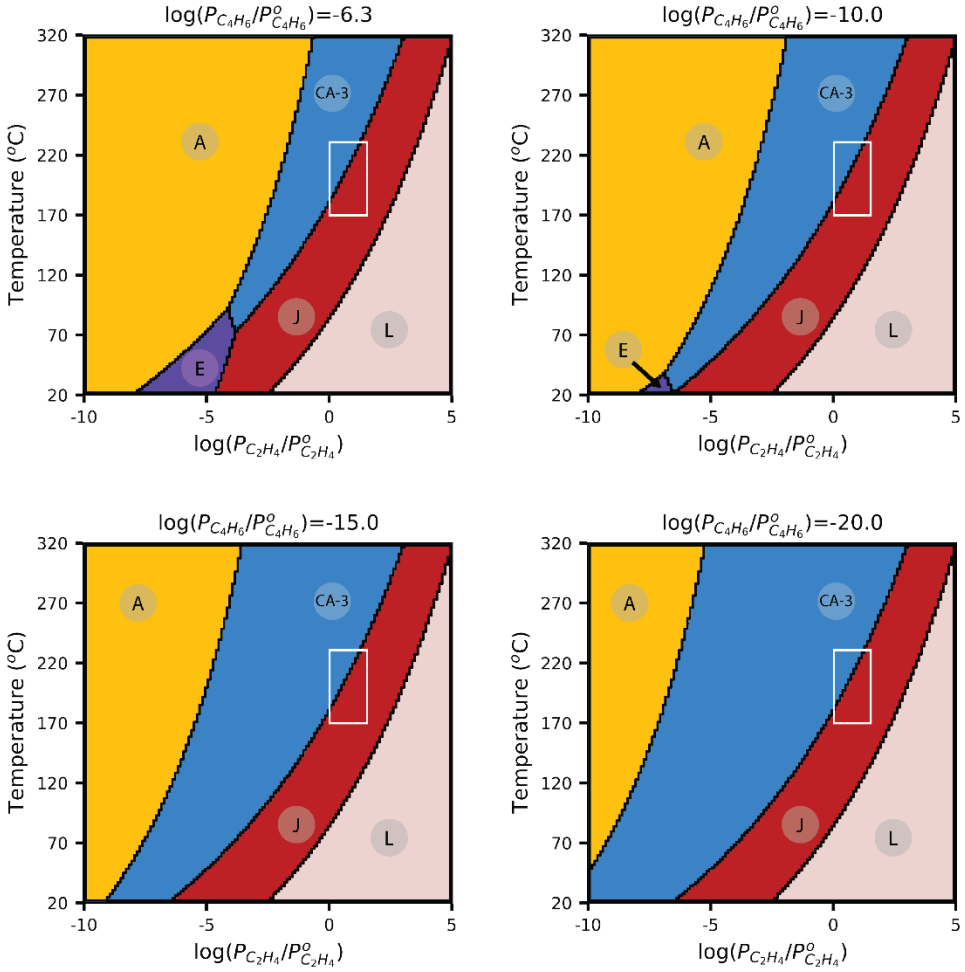

Figure 2.26. The Ni/UiO-66 cluster thermodynamic stability under different reaction conditions from *ab initio* thermodynamic analysis. The 1,3-butadiene partial pressure is decreased from the maximum observed partial pressure (a) $10^{-6.3}$ kPa to (b) $10^{-10.0}$ kPa to (c) $10^{-15.0}$ kPa to (d) $10^{-20.0}$ kPa. The partial pressure standard state for ethylene ($P^o_{C_2H_4}$) and ($P^o_{C_4H_6}$) is 101.3 kPa. The white box represents the experimental operating conditions.

Chapter 3. Validation of the Cossee-Arlman Mechanism for Propylene Oligomerization on Ni/UiO-66

This material has been adapted from published work.[128] Contributions of other authors is noted in the footnotes of the experimental and computational methods.

3.1. Introduction

The Shell Higher Olefin Process (SHOP) that is practiced industrially accomplishes homologation of ethylene to linear alpha olefins (LAOs) on nickel-based homogeneous catalysts .[3,10,46] The coordination-insertion mechanism, also known as the Cossee-Arlman mechanism, and the metallacycle mechanism have been proposed on these homogeneous nickel catalysts to describe oligomer chain growth on these materials. The Cossee-Arlman mechanism involves coordination and subsequent insertion of olefin molecules and has been postulated on nickel-based homogeneous catalysts for ethylene oligomerization through comparisons of external and internal oligomer selectivities from reinsertion and the inclusion of an alkylaluminium cocatalyst to form Ni-alkyl intermediates posited in the mechanism.[12,14,15,17,78,79,123] On the other hand, the metallacycle mechanism for ethylene oligomerization on nickel, chromium, titanium, and tantalum transition metal catalysts is associated with successive coordination of olefin molecules prior to carbon-carbon coupling and is proposed to produce LAOs, such as 1-butene and 1-hexene.[17,81,82] formula

Motivated by the high selectivity for LAOs in homogeneous nickel catalysts for olefin oligomerization, heterogeneous nickel-based catalysts have been formulated for this chemistry as they typically do not use cocatalysts or activators.[19,46] Prior work on heterogeneous nickel catalysts has supported the Cossee-Arlman mechanism for olefin oligomerization/dimerization based on comparisons of the Cossee-Arlman and metallacycle mechanisms from density functional theory (DFT) calculations,[41,50,53,76,77,80,95,129,130] infrared (IR) spectroscopy to illustrate kinetically relevant Ni-alkyl surface intermediates for olefin oligomerization,[37,77] analysis of isotopomer product distributions with ethylene and perdeuteroethylene mixtures,[50] use of nonconjugated diene probe molecules to evince coordination and insertion,[50] and hydrogen cofeeds to suggest a Ni-hydride intermediate.[31,33] Nevertheless, analysis of olefin

oligomerization reactivity and mechanisms on heterogeneous nickel catalysts are often convoluted because typically only a fraction of nickel sites are active with[49,90] or without[43,44,76] the use of an activator, the catalyst deactivates on-stream,[32,35,37,40,88,129] and/or residual acid site reactivity.[22,31,131]

While DFT, molecular cofeeds and probes, and spectroscopic methods can be used to elucidate the Cossee-Arlman mechanism for olefin oligomerization, analysis of the product selectivities at various process conditions is seldom performed to validate the mechanism. For ethylene oligomerization on nickel catalysts, both sequential coordination-insertion and successive coordination of ethylene in the Cossee-Arlman and metallacycle mechanisms, respectively, yield butene product selectivities that are invariant with process conditions, as only one kinetic pathway occurs before the rate-limiting carbon-carbon coupling steps.[41,50,53,80,95] However, propylene can insert on nickel through either the α or β carbon in the Cossee-Arlman mechanism, which generates two distinct mechanistic pathways prior to the kinetically relevant step.[51,132,133] In contrast, successive coordination of propylene in the metallacycle mechanism invokes only one pathway prior to the kinetically relevant step. The distinct mechanistic pathways lead to pressure-dependent and pressure-independent hexene product selectivities that can be examined to differentiate the Cossee-Arlman and metallacycle mechanisms.

In our previous work, a nickel functionalized zirconium oxide-based metal organic framework (MOF) catalyst, Ni/UiO-66, was synthesized with isolated nickel atoms deposited on the zirconium oxide node through a missing linker defect, as evinced from comparisons between DFT-optimized cluster models and extended X-ray absorption fine structure analysis (EXAFS) data. [129] This material was active for ethylene and 1-butene oligomerization devoid of cocatalysts.[76,129] Unprecedented stability for >10 days on-stream was observed during ethylene oligomerization, and only oligomers were detected to suggest absence of residual acid sites.[76] After undergoing an induction period and reaching steady state, butene formation rates increased after exposing the catalyst to higher ethylene pressures when comparing rates at the lower reference partial pressure.[76] This increase in rate was ascribed to an increase in nickel active site density, as higher ethylene pressures

were proposed to facilitate a stoichiometric reaction to generate the catalytically relevant nickel-hydride species during the induction period.[76,129] The nickel species for ethylene oligomerization were enumerated with in-situ NO titration experiments to normalize reaction rates, and steady state kinetics were measured to compare experimental and DFT-computed activation energies to validate the Cossee-Arlman mechanism.[76]

The unique stability for ethylene oligomerization on Ni/UiO-66, the ability to titrate active sites and normalize reaction rates, and the production of only oligomers proffers Ni/UiO-66 as a platform to study propylene oligomerization and the reaction mechanism. In the work presented herein, we report propylene oligomerization rates in the absence of a cocatalyst to measure steady state kinetics and hexene product selectivities. From steady state product selectivities, the Cossee-Arlman mechanism can be validated through analysis of the steady state rates and ratio of hexene product selectivities that are a function of pressure.

3.2. Experimental and Computational Details

3.2.1. Catalyst Synthesis and Characterization

An ideal UiO-66 material is a zirconium oxide (Zr_6O_8) based MOF connected with twelve terephthalate ligands.[67,92,112,114,115] Nickel can be functionalized on the Zr_6O_8 node through a missing linker defect to form Ni/UiO-66.[59,76,96,116,117,129] The detailed synthesis of UiO-66 and deposition of nickel onto the inorganic node to generate Ni/UiO-66 is described elsewhere.[76,92,129] Powder X-ray diffraction (PXRD), N_2 isotherms, thermal gravimetric analysis (TGA), temperature programmed oxidation (TPO), proton nuclear magnetic resonance (^{1}H NMR) spectroscopy on the digested Ni/UiO-66 MOF, scanning transmission electron microscopy−energy dispersive X-ray spectroscopy (STEM-EDS), inductively coupled plasma−atomic emission spectroscopy (ICP-AES), IR spectroscopy, and X-ray adsorption spectroscopy (XAS) data for the as-synthesized Ni/UiO-66 were reported previously.[76,129] Briefly, the as-synthesized Ni/UiO-66 had a surface area of 1301 $m^2\ g^{-1}$ with ~0.7 nickel atoms per zirconium oxide node.[76]

3.2.2. Catalytic Testing

Ni/UiO-66 was pressed (<6.9 MPa), pelletized, and sieved to obtain particle sizes of 180-420 μm (40-80 mesh). The sample (10-80 mg) was physically mixed with sand (~200 mg, subjected prior to an overnight wash in 2 M HNO_3 solution followed by DI water rinse until pH ~7, and a final thermal treatment in flowing dry air (0.83 $cm^3\ s^{-1}$) at 1273 K (0.083 K s^{-1} ramp rate from ambient temperature) for 16 h; $10 < wt_{diluent}/wt_{cat} < 15$) and then packed between two quartz wool plugs (Technical Glass Products) in a tubular glass-lined stainless-steel reactor (6.35 mm O.D. and 4 mm I.D., SGE Analytical Science). The free volume of the reactor was filled with quartz rods (3 mm O.D.; Technical Glass Products) to prevent vertical displacement of the catalyst bed. The temperature was measured using a K-type thermocouple (Omega) wrapped around the periphery of the stainless-steel reactor with the tip placed at the center of the catalyst bed and regulated with an electronic controller (Watlow), respectively. The catalyst was pretreated in helium (Matheson, 99.997%, 0.83 $cm^3\ s^{-1}$) from ambient temperature to 573 K (0.08 K s^{-1}) for 4 hours and then cooled to reaction temperature (473 K) in flowing helium. Propylene (Matheson, 99.83%, 0.08-0.83 $cm^3\ s^{-1}$) was introduced to the reactor with mass flow controllers (Brooks 5850E Series) and pressurized (105-550 kPa) using a back-pressure regulator (TESCOM Series 44-2300) placed downstream of the reactor with the gas-phase pressure measured using a pressure transducer (Omega) placed upstream of the reactor. Propylene gas phase pressures less than 105 kPa were obtained by feeding a mixture of helium (Matheson, 99.997%) and propylene at ambient pressure. The composition of the reactor effluent was quantified using a gas chromatograph (Agilent GC 7890A) equipped with a dimethylpolysiloxane HP-1 column (50 m × 320 μm × 0.52 μm) connected to a flame ionization detector (FID).

3.2.3. In-Situ NO Titrations

The reactor setup is identical to the one described above. A nitric oxide/nitrogen mixture (Airgas, 1% NO, balance N_2, 0.083-0.17 $cm^3\ s^{-1}$) was introduced in the propylene gas stream at various pressures (500 – 550 kPa) with a mass flow controller (Brooks 5850E Series). An online mass spectrometer (MKS Cirrus 2) was utilized to determine the effluent

propylene, hexene, NO, and N_2 signals (m/z: 42, 84, 30, and 28, respectively). The N_2 flow was used as a tracer to determine the average residence time of NO over the catalyst bed, which was normalized and used to calculate the amount of NO reacted/absorbed on nickel sites to suppress the rate of propylene oligomerization.

3.2.4. X-Ray Absorption Spectroscopy (XAS)[8]

All XAS spectra were collected at beamline 9-3 at Stanford Synchrotron Radiation Light source (SSRL). All experiments were carried out in fluorescence mode with a passivated implanted planar silicon (PIPS) detector and with a water cooled double-crystal monochromator with Si (220) crystals. Six inch long, nitrogen-filled, ion chambers were used to measure the relative intensity of the X-ray beam before and after the sample, and before and after the nickel reference foil, which was used as an internal reference to calibrate the photon energy of each spectrum. The as synthesized Ni/UiO-66 (~3 mg) was loaded in an *in-situ* XAS cell[134] forming an approximately 1 cm long catalyst bed located in between two quartz wool plugs inside the 1 mm OD, 0.96 mm ID, quartz capillary.

Continuous extended X-ray absorption fine structure (EXAFS) spectra at the Ni-K edge (8333 eV) were collected for the as-synthesized sample in helium (0.33 $cm^3\ s^{-1}$) at ambient temperature. Continuous EXAFS spectra were collected while the temperature was ramped at 0.083 K s^{-1} until 573 K and held for 4 hours where continuous EXAFS spectra for the Ni-K edge were obtained. After 4 hours, the reactor was allowed to cool to reaction temperature (473 K) before propylene (0.17 $cm^3\ s^{-1}$) was introduced. Continuous EXAFS spectra were collected for 3 hours, where the catalyst was assumed to be at steady state (Figure 3.1 in the main text). Each continuous EXAFS spectrum took approximately 2 minutes to collect, and nine EXAFS spectra were merged to improve signal to noise.

3.2.5. Cluster Models of Ni/UiO-66 and Kohn-Sham Density Functional Theory (DFT) Calculations

Cluster models of Ni/UiO-66 were derived from a truncated Zr_6 node of an optimized periodic structure of UiO-66 with formate groups capping the inorganic linker.[70]

[8] XAS measurements were taken by Adam Hoffman, Jiyun Hong, and Simon R. Bare at SSRL.

One formate group was removed and replaced with a $[Ni(OH)_2)]^{-1}$ group as nickel is deposited on the zirconium oxide node through missing linker defects,[80,95,96] to give the cluster model formula of $[NiZr_6(\mu_3\text{-}OH)_3(\mu_3\text{-}O)_5(OH)_2]^{11+} \bullet 11(CHO_2^{-1})$.[97] Kohn-Sham DFT calculations were performed with the M06-L density functional[98] implemented in the Gaussian 16 software package.[99] The def2-SVP and def2-TZVPP basis sets were used for C, H, and O atoms and Zr and Ni atoms, respectively,[100,101] and the SDD effective core potential was implemented for Zr atoms.[102] All cluster models and the individual gas phase olefin molecules were optimized, except the C atoms capping the Zr_6 node to maintain the framework structure and rigidity.[70] Zero-point energies and thermal contributions to enthalpies and Gibbs free energies were calculated from vibrational frequency calculations at 298.15 K and 101.3 kPa.

3.3 Results and Discussion

3.3.1 Catalyst Performance and Active Site Enumeration

Figure 3.1 presents propylene oligomerization rates normalized by the total amount of nickel in Ni/UiO-66 with time on stream at 473 K and 5 kPa, 106 kPa, and 500 kPa devoid of cocatalysts. The induction periods on Ni/UiO-66 for propylene oligomerization at 106 kPa and 500 kPa are ~2 ks and ~8 ks which are significantly shorter than the induction periods of ~150 ks and ~85 ks, respectively, for ethylene oligomerization on the same material at the same partial pressures.[76] It is postulated that induction periods are controlled by a heterolytic C-H dissociation step to generate a [Ni-ethenyl]$^-$ species and [µ-OH]$^+$ complex for ethylene dimerization and are necessary to form the kinetically relevant Ni-alkyl species.[32,40,41,46,76] In our previous work, the induction period was attributed to the in-situ generation of relevant Ni-ethyl species during ethylene oligomerization, and higher ethylene pressures were required to create these active sites, as reference reaction rates increased after exposing the catalyst to higher ethylene pressures.[76] However, for propylene oligomerization, as shown in Figure 3.10, the catalyst returns to the same reaction rates at 5 kPa after exposing the catalyst to 500 kPa of propylene, suggesting that no additional active sites are formed at higher propylene pressures. The observed invariance in the induction period with propylene pressure shown in Figure 3.1 and in the number of Ni-

alkyl species at different propylene pressures (Figure 3.10) plausibly arises because propylene has a weaker allylic C-H bond compared to the vinylic C-H bond of ethylene, where the former more readily forms the relevant Ni-alkyl species.[135] While there are slight variations in the length of induction period when changing propylene pressures from 5 – 500 kPa as shown in Figure 3.1, these changes are minor compared to the days-long transients observed with ethylene oligomerization at similar ethylene pressures as relevant Ni-alkyl species are much more more rapidly formed during propylene oligomerization. The catalyst appears to be stable for propylene oligomerization, with the reaction rate decreasing <5% over 150 minutes. The steady state rates that are reported hereafter are those that are examined with a reference condition and do not change within 10% (Figure 3.11).

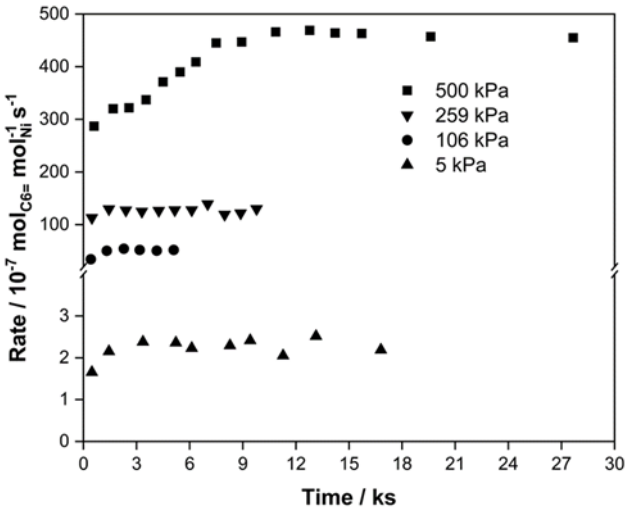

Figure 3.1. Propylene oligomerization rates as a function of time on stream on Ni/UiO-66 at 500 kPa (■), 259 kPa (▼)106 kPa (●) and 5 kPa (▲) at 473 K.

Normalization of reaction rates is required to study reaction kinetics, as not all nickel species are active or yield the same reactivity during olefin oligomerization.[43,44,76] In a prior report, we noted that incorrect reaction orders are obtained when nickel active site densities are not enumerated because active site densities increase with increasing pressure, resulting in conflated reaction rates from an increase in site densities and ethylene pressures. In-situ NO titrations were able to deconvolute this effect because the number of

Ni species relevant for catalysis could be precisely determined and reaction rates could be normalized by measured site densities to determine the reaction orders for ethylene oligomerization.[76] Following the same experimental protocols, the number of nickel active sites were assessed with in-situ NO titration experiments during propylene oligomerization as shown in Figure 3.2. Once the catalyst reached steady state at 493 K and 550 kPa, a mixture of 1% NO and 99% N_2 was introduced to the reactant gas stream. A decrease in the hexene flowrate is observed when N_2 appears to break through the catalyst bed. The NO flow has a delayed breakthrough response, suggesting that NO titrates the nickel active sites on Ni/UiO-66 to impede the rate of hexene formation. The number of nickel active sites can be enumerated by mathematical integration between the NO and normalized N_2 breakthrough curves.[136,137] The number of nickel active sites enumerated during propylene oligomerization on Ni/UiO-66 is ~20 μmol g_{cat}^{-1}, which is about 5% of nickel active sites from the ~430 μmol g_{cat}^{-1} of nickel in the MOF, as determined by ICP-AES, assuming one NO molecule binds to one nickel atom.[76] This value is consistent with prior work that show that not all active sites are active for catalysis on Ni/UiO-66 MOFs during ethylene oligomerization.[76] Another in-situ NO titration is presented in Figure 3.14 at 500 kPa and 473 K to affirm that ~5% of nickel sites are active for propylene oligomerization.

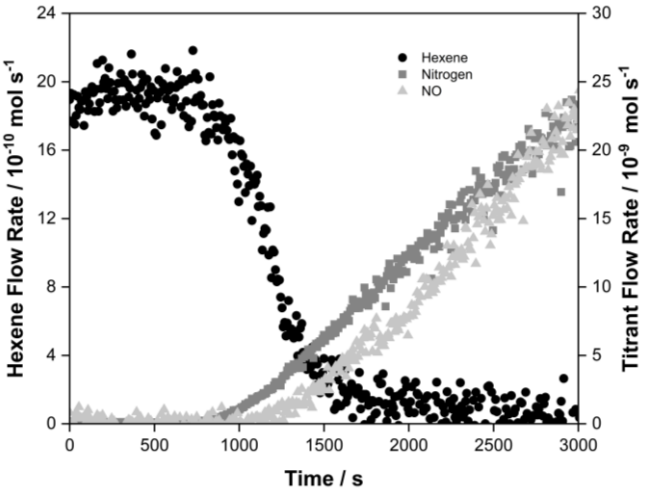

Figure 3.2. In situ NO titration showing a decrease in the rate of hexene formation (●) upon introduction of 0.083 $cm^3\ s^{-1}$ of 1% NO (▲, light grey) and 99% N_2 (■, dark gray) in 0.83 $cm^3\ s^{-1}$ at a total pressure of 550 kPa at 493 K on 90.8 mg of Ni/UiO-66

3.3.2. Mechanisms and Kinetics for Propylene Oligomerization

The Cossee-Arlman and metallacycle mechanisms are proposed on heterogeneous nickel-based catalysts for olefin oligomerization.[31,41] In Figure 3.3, we present the Cossee-Arlman mechanism for propylene oligomerization, showing the formation of all possible hexene isomers with nickel proposed to remain in the 2+ oxidation state throughout the entire cycle.[51,77] This mechanism is often posited on the basis of the inclusion of alkylaluminum cocatalysts that form Ni-alkyl species.[49–51,59] However, observed induction periods in the absence of activators during olefin oligomerization are often attributed to the creation of relevant nickel-hydride or nickel-alkyl species during catalysis.[31,32,40,45,46,76,77] The mechanism is proposed to start with a nickel-hydride species (**A**) that binds to a propylene molecule (**B**). Species **B** can undergo two distinct regioselective hydride insertions to either form a 2,1-propyl species (**C**) or a 1,2-propyl species (**D**). Another propylene molecule can coordinate to **C** and **D** to yield species **E** and **F**, respectively. Regioselective 2,1 and 1,2 olefin insertions, which are proposed to be the kinetically relevant steps, proceed on species **E** and **F** to generate four distinct Ni-hexyl species.[41,50,53,80,95,129] The Ni-hexyl species undergo β-hydride elimination to generate a nickel hydride species and the resulting hexene product that desorbs to regenerate **A** and form 4-methylpentenes (**4MP**), 2,3-dimethylbutenes (**DMB**), linear hexenes (**LH**), and 2-methylpentenes (**2MP**), respectively.

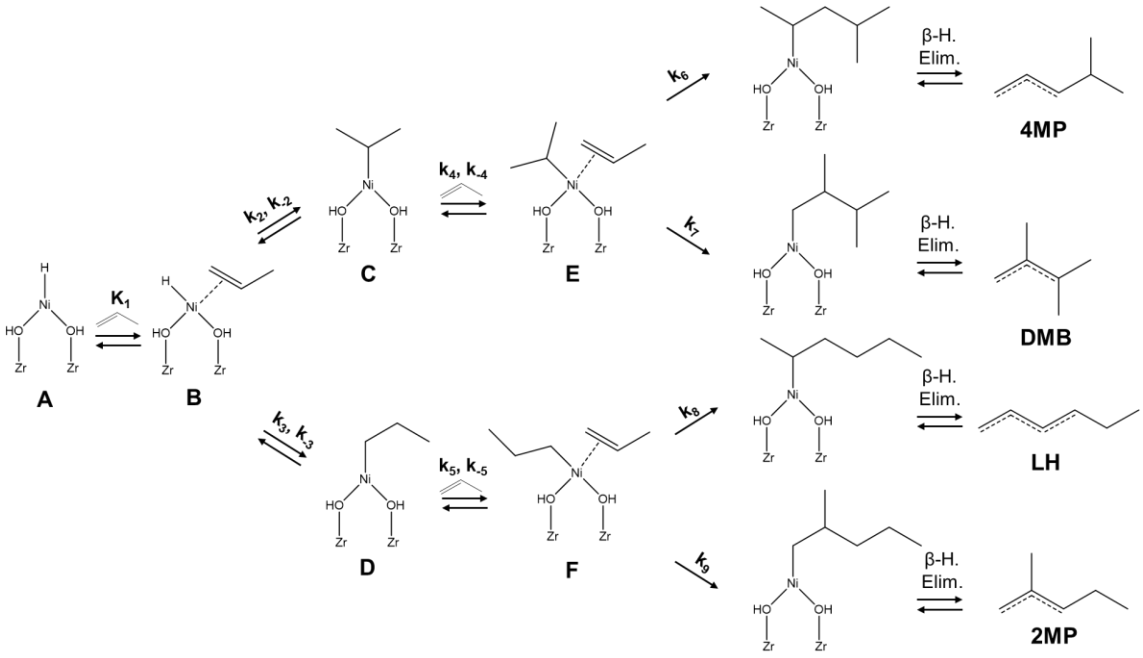

Figure 3.3. Schematic for the Cossee-Arlman mechanism for propylene oligomerization on Ni/UiO-66. Note the entire node is omitted for clarity.

The metallacycle mechanism for propylene oligomerization on Ni/UiO-66, shown in Figure 3.4, is also proposed on heterogeneous catalysts.[17,31,41,84,88] This mechanism is postulated on catalysts for olefin oligomerization without the use of cocatalysts or observed induction periods due to the direct successive insertion of olefin molecules.[46] The active species for the metallacycle mechanism is proposed to be Ni^{+} or Ni^{2+} ions (**G**) that undergo successive coordination of two propylene molecules, where the catalytic moieties with one and two propylene molecules coordinated to the nickel site are denoted as **H** and **I**, respectively.[41,46] Species **I** undergoes oxidative coupling, which is the slow step of the catalytic sequence, to form three distinct metallacyclopentane intermediates.[41,53] The metallacyclopentane intermediates undergo successive β-hydride and reductive elimination steps to regenerate **G** and produce **4MP**, **DMB**, **LH**, and **2MP**.

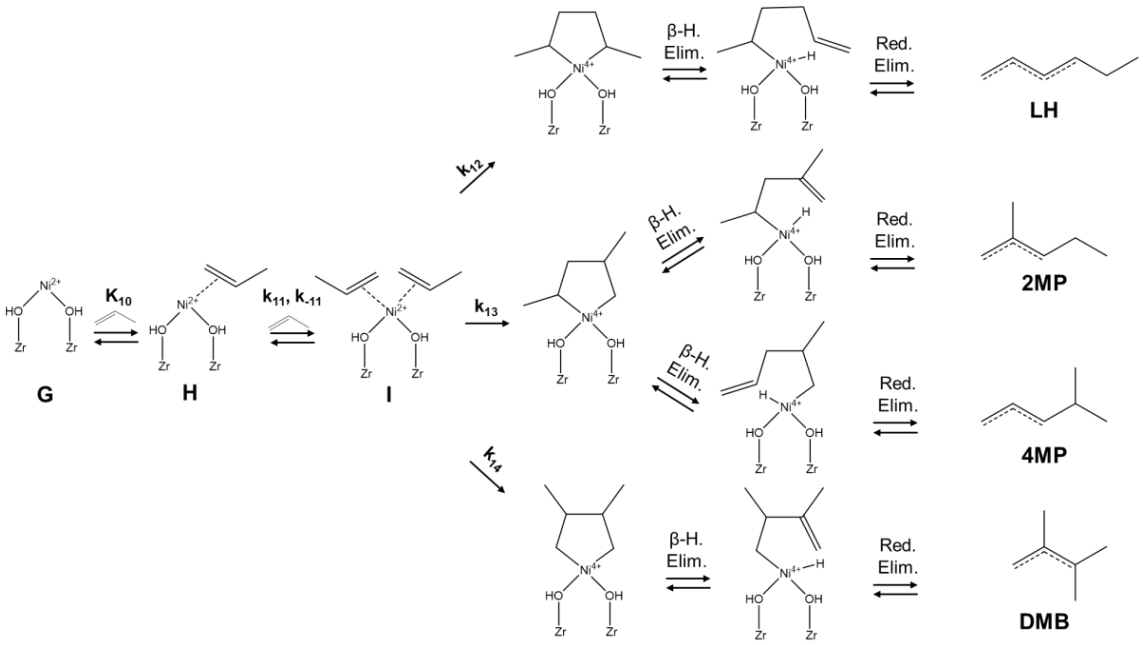

Figure 3.4. Schematic for the metallacycle mechanism for propylene oligomerization on Ni/UiO-66. Note the entire node is omitted for clarity.

The Cossee-Arlman mechanism on Ni/UiO-66 is considered to propagate olefin oligomerization over the metallacycle mechanism for ethylene and butene oligomerization due to observed induction periods in the absence of cocatalysts, persistence of Ni species in the 2+ oxidation state before and after reaction as determined by X-ray adsorption near edge structure (XANES) analysis, and agreement of apparent activation energies between experiment and computation with DFT.[76,129] In Figure 3.1, short induction periods are observed to indicate that in-situ generation of kinetically relevant Ni-hydride or Ni-propyl are relevant for propylene oligomerization devoid of activators. Previous work has suggested that these induction periods are accompanied with in-situ generation of dienes,[40,41,76,77] which is consistent with the observed hexadiene formation in this study as shown in Figure 3.5. When comparing the XANES spectra for the Ni/UiO-66 after thermal treatment and at steady state during propylene oligomerization (Figure 3.6a), no change in the pre-edge region is observed. The peak at 8333 eV persists and is consistent with nickel(II) species using a α-$Ni(OH)_2$ reference from our previous work[129] to suggest that nickel remains as 2+ during reaction, in line with the Cossee-Arlman mechanism.

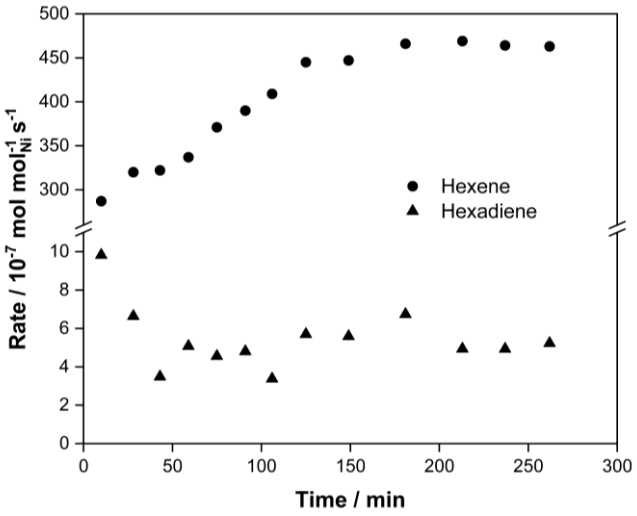

Figure 3.5. Time on stream showing hexene (●) and hexadiene (▲) formation on 80.6 mg of Ni/UiO-66 at 500 kPa of 0.83 cm^3 s^{-1} of propylene at 473 K.

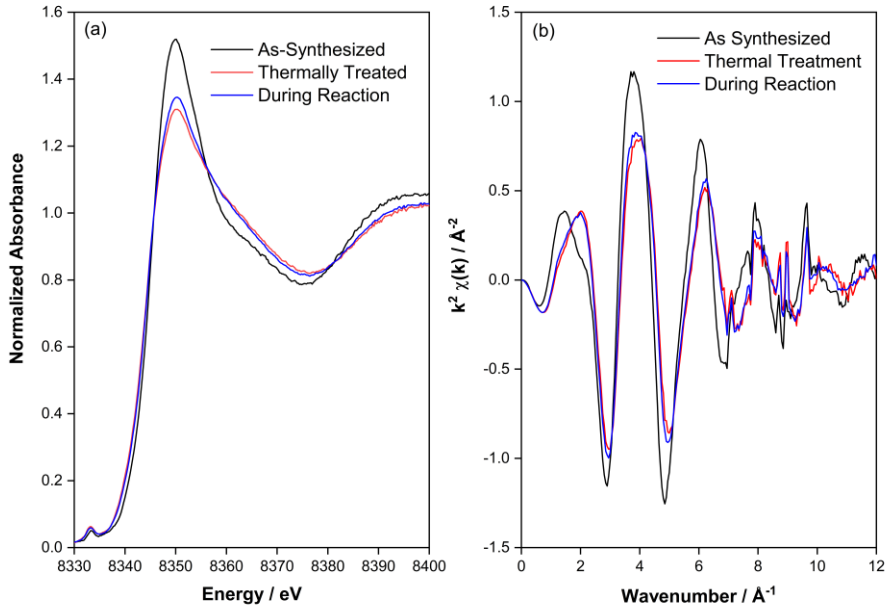

Figure 3.6. (a) XANES and (b) EXAFS data for Ni/UiO-66 as synthesized (black), after thermal treatment (red, 573 K, 0.33 cm^3 s^{-1} of helium) and during propylene oligomerization (blue, 473 K, 0.17 cm^3 s^{-1} of propylene)

Steady state reaction orders and comparisons among experimental and computed activation energies can be examined to validate the Cossee-Arlman mechanism on Ni/UiO-66 for olefin oligomerization after normalization of reaction rates by the number of relevant active sites.[76,129] The reaction was determined to be first order in propylene pressure from

5 kPa to 500 kPa at 473 K on Ni/UiO-66, as shown Figure 3.7a in line with observations ethylene and 1-butene oligomerization being first order in olefin pressure on Ni/UiO-66.[76,129] Assuming only two propylene molecules are required to make hexene products, this suggests that a singly-coordinated propylene species on the nickel active site is the most abundant surface intermediate (MASI). From 453 K to 493 K, an Arrhenius plot in Figure 3.7b reveals an apparent activation energy of 21.0 ± 3.4 kJ mol^{-1}, 24.6 ± 3.8 kJ mol^{-1}, 15.7 ± 2.2 kJ mol^{-1}, and 17.5 ± 2.8 kJ mol^{-1} for **4MP**, **DMB**, **LH**, and **2MP**, respectively. These activation energies are lower than experimentally measured activation energies of 81 kJ mol^{-1} and 58 kJ mol^{-1} for ethylene and butene oligomerization on Ni/UiO-66 and lower than those measured on Ni-Na-X and Ni-MIL-127 for propylene oligomerization at 35 kJ mol^{-1} and ~60 kJ mol^{-1}, respectively.[35,76,77,129] From the computed Gibbs free energy diagrams of the Cossee-Arlman mechanism using DFT on cluster models of Ni/UiO-66 shown in Figures 3.17 to 3.20, the olefin insertion steps have the highest barriers of 88 kJ mol^{-1} to 143 kJ mol^{-1} depending on the hexene product being formed, and thus, C-C bond formation is the kinetically relevant step. For **LH**, the intrinsic free energy barrier for the olefin insertion is 96 kJ mol^{-1} which is in good agreement with the olefin insertion barriers for ethylene and butene oligomerization for the formation of linear dimers on Ni/UiO-66 of 80 kJ mol^{-1} and 87 kJ mol^{-1}.[76,129] From the first order kinetics determined in Figure 3.7a that suggests the resting state of the catalyst is a Ni-propyl species, the calculated apparent activation barrier from the Ni-propyl MASI, **D**, and the olefin insertion step for **LH**, is 21 kJ mol^{-1}, as shown in Figure 3.19, which is in good agreement with the apparent activation energy of 15.7 kJ mol^{-1} obtained from experiment to corroborate the Cossee-Arlman mechanism. Energy diagrams for all other products and thermodynamic values for intermediates for the Cossee-Arlman mechanism are reported in Section 3.5.3.

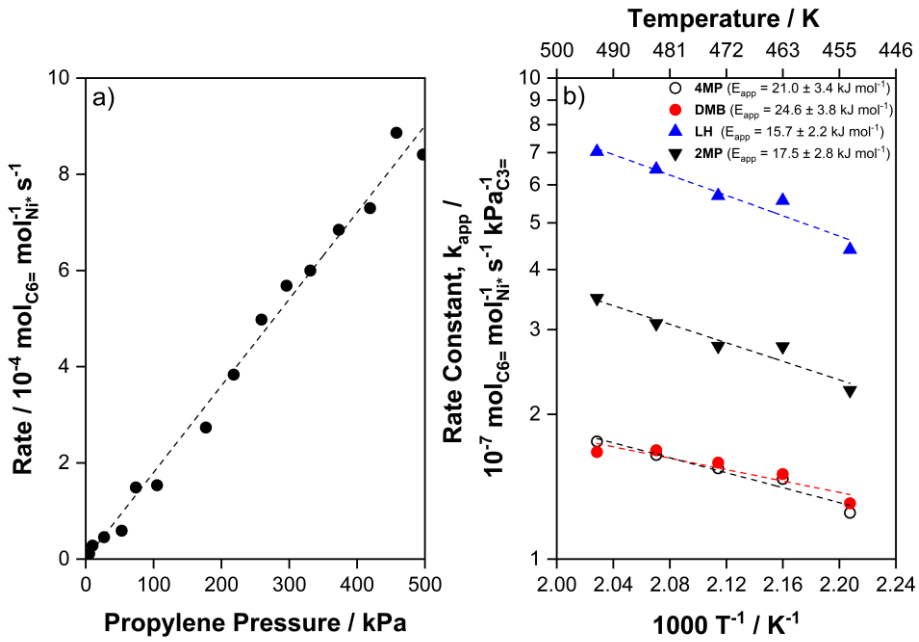

Figure 3.7. (a) Hexene formation rate versus propylene partial pressure (5−500 kPa) at 473 K and (b) Arrhenius plot at 259 kPa for propylene oligomerization from 453 K to 493 K for **4MP** (○), **DMB** (●), **LH** (▲), and **2MP** (▼) on Ni/UiO-66.

3.3.3 Hexene Product Selectivities for Propylene Oligomerization

While previous work on Ni/UiO-66 has presented evidence for the Cossee-Arlman mechanism for olefin oligomerization, we propose that the Cossee-Arlman and metallacycle mechanisms can be more broadly evinced through analysis of hexene product selectivity ratios derived from rate expressions for the proposed mechanisms. The rate expression and selectivities for species i is denoted as r_i and s_i, respectively with rate constants and equilibrium constants for each elementary step denoted as k_j and K_j, respectively, from Figures 3.3 and 3.4 for the Cossee-Arlman and metallacycle mechanisms, respectively. From DFT calculations, the kinetically relevant step for the Cossee-Arlman mechanism is the olefin insertion step on heterogeneous nickel catalysts.[41,50,53,80,95,129] In our system, the proposed rate expressions for **4MP**, **DMB**, **LH**, and **2MP** assuming the olefin insertion step is kinetically limiting for the Cossee-Arlman mechanism are shown in Equations 3.1-3.4 respectively, based on Figure 3.3.

$$r_{\mathbf{4MP}} = k_6[\mathrm{E}] \qquad \text{Eq. 3.1}$$

$$r_{\boldsymbol{DMB}} = k_7[E] \quad \text{Eq. 3.2}$$

$$r_{\boldsymbol{LH}} = k_8[F] \quad \text{Eq. 3.3}$$

$$r_{\boldsymbol{2MP}} = k_9[F] \quad \text{Eq. 3.4}$$

Assuming the first adsorption step between **A** and **B** is quasi-equilibrated and all surface-bound species before the kinetically relevant step are at pseudo-steady state, the rate expressions for **4MP**, **DMB**, **LH**, and **2MP** can be derived to only be expressed in terms of propylene pressures and the density of unoccupied nickel sites **A**, as shown in Equations 3.5-3.8 (See Section 3.5.2 for derivation).

$$r_{\boldsymbol{4MP}} = \frac{k_6 k_4 k_2 K_1 [A] P_{C_3H_6}^2}{(k_{-4} + k_6 + k_7)\left(k_{-2} - \frac{k_{-4} k_4 P_{C_3H_6}}{k_{-4} + k_6 + k_7} + k_4 P_{C_3H_6}\right)} \quad \text{Eq. 3.5}$$

$$r_{\mathbf{DMB}} = \frac{k_7 k_4 k_2 K_1 [A] P_{C_3H_6}^2}{(k_{-4} + k_6 + k_7)\left(k_{-2} - \frac{k_{-4} k_4 P_{C_3H_6}}{k_{-4} + k_6 + k_7} + k_4 P_{C_3H_6}\right)} \quad \text{Eq. 3.6}$$

$$r_{\mathbf{LH}} = \frac{k_8 k_5 k_3 K_1 [A] P_{C_3H_6}^2}{(k_{-5} + k_8 + k_9)\left(k_{-3} - \frac{k_{-5} k_5 P_{C_3H_6}}{k_{-5} + k_8 + k_9} + k_5 P_{C_3H_6}\right)} \quad \text{Eq. 3.7}$$

$$r_{\mathbf{2MP}} = \frac{k_9 k_5 k_3 K_1 [A] P_{C_3H_6}^2}{(k_{-5} + k_8 + k_9)\left(k_{-3} - \frac{k_{-5} k_5 P_{C_3H_6}}{k_{-5} + k_8 + k_9} + k_5 P_{C_3H_6}\right)} \quad \text{Eq. 3.8}$$

The selectivity for **4MP**, **DMB**, **LH**, and **2MP** for the Cossee-Arlman mechanism can be derived from Equations 3.5-3.8 (see Section 3.5.2 for derivation) and these expressions are shown in Equations 3.9-3.12 with α, β, γ, δ, and ε defined in Equation 3.13-3.17. The selectivity for all hexene isomers is a function of propylene pressure as shown in equations 3.9-3.12.

$$s_{\boldsymbol{4MP}} = \frac{\frac{k_6}{k_6 + k_7}(\beta + \delta P_{C_3H_6})}{\varepsilon(\alpha + \gamma P_{C_3H_6}) + (\beta + \delta P_{C_3H_6})} \quad \text{Eq. 3.9}$$

$$s_{\mathbf{DMB}} = \frac{\frac{k_7}{k_6 + k_7}\,(\beta + \delta P_{C_3H_6})}{\varepsilon(\alpha + \gamma P_{C_3H_6}) + (\beta + \delta P_{C_3H_6})} \qquad \text{Eq. 3.10}$$

$$s_{\boldsymbol{LH}} = \frac{\frac{k_8}{k_8 + k_9}\,(\alpha + \gamma P_{C_3H_6})}{(\alpha + \gamma P_{C_3H_6}) + \frac{1}{\varepsilon}(\beta + \delta P_{C_3H_6})} \qquad \text{Eq. 3.11}$$

$$s_{\mathbf{2MP}} = \frac{\frac{k_9}{k_8 + k_9}\,(\alpha + \gamma P_{C_3H_6})}{(\alpha + \gamma P_{C_3H_6}) + \frac{1}{\varepsilon}(\beta + \delta P_{C_3H_6})} \qquad \text{Eq. 3.12}$$

$$\alpha = k_{-2} \qquad \text{Eq. 3.13}$$

$$\beta = k_{-3} \qquad \text{Eq. 3.14}$$

$$\gamma = k_4 - \frac{k_{-4}k_4}{k_{-4} + k_6 + k_7} \qquad \text{Eq. 3.15}$$

$$\delta = k_5 - \frac{k_{-5}k_5}{k_{-5} + k_8 + k_9} \qquad \text{Eq. 3.16}$$

$$\varepsilon = \frac{(k_8 + k_9)k_5k_3(k_{-4} + k_6 + k_7)}{(k_6 + k_7)k_4k_2(k_{-5} + k_8 + k_9)} \qquad \text{Eq. 3.17}$$

Based on the Cossee-Arlman mechanism (Figure 3.3), products **4MP** and **DMB** are both formed from **C**, while products **LH** and **2MP** are both formed from **D**. Consequently, the ratio between **4MP** and **DMB** and the ratio between **LH** and **2MP** should only be a function of the olefin insertion rate constants, as shown in Equations 3.18 and 3.19. This ratio arises simply from the possibility of propylene undergoing a 2,1- or 1,2- insertion for both intermediates **E** and **F**, which can be clearly seen from Equations 3.1-3.4. The two branching mechanistic pathways prior to the kinetically relevant step can be evaluated from the products derived from **C**, **4MP** + **DMB**, and **D**, **LH** + **2MP**, as shown in Equation 3.20, which shows that the selectivity ratio of **LH** + **2MP** to **4MP** + **DMB** is pressure dependent due to adsorption of a propylene molecule to form **E** and **F** from **C** and **D**, respectively. Thus, Equations 3.9-3.12 and 3.18-3.20 can be used to assess the coordination of propylene and insertion characteristics that would result from the Cossee-Arlman mechanism, which suggest that product selectivities and selectivity ratios are a function of propylene pressure.

$$S_{\frac{\mathbf{4MP}}{\mathbf{DMB}}} = \frac{k_6}{k_7} \quad \text{Eq. 3.18}$$

$$S_{\frac{\mathbf{LH}}{\mathbf{2MP}}} = \frac{k_8}{k_9} \quad \text{Eq. 3.19}$$

$$S_{\frac{\mathbf{LH+2MP}}{\mathbf{4MP+DMB}}} = \frac{\left(\alpha + \gamma \, \boldsymbol{P_{C_3H_6}}\right)}{\left(\beta + \delta \, \boldsymbol{P_{C_3H_6}}\right)} * \varepsilon \quad \text{Eq. 3.20}$$

Selectivity characteristics of hexene isomers are distinct when considering the metallacycle mechanism and can be determined by deriving rate expressions for the mechanism shown in Figure 3.4. The oxidative coupling step has been proposed to be the kinetically relevant step for olefin oligomerization via the metallacycle mechanism based on previous DFT calculations.[41,53,129] The proposed rate expressions from **4MP**, **DMB**, **LH**, and **2MP** following the metallacycle mechanism (See Section 3.5.2) are shown in Equations 3.21-3.24. Assuming the first adsorption from **G** to **H** is quasi-equilibrated and the formation of species **I** is at pseudo-steady state, the rate expression can be derived and only expressed in terms of propylene pressure and unoccupied nickel sites **G**.

$$r_{\mathbf{4MP}} = \mathrm{k}_{13}[I] = \frac{k_{13}k_{11}K_{10}[\mathrm{G}]P_{C_3H_6}^2}{k_{-11} + k_{12} + k_{13} + k_{14}} \quad \text{Eq. 3.21}$$

$$r_{\mathbf{DMB}} = \mathrm{k}_{14}[I] = \frac{k_{14}k_{11}K_{10}[\mathrm{G}]P_{C_3H_6}^2}{k_{-11} + k_{12} + k_{13} + k_{14}} \quad \text{Eq. 3.22}$$

$$r_{\mathbf{LH}} = \mathrm{k}_{12}[I] = \frac{k_{12}k_{11}K_{10}[\mathrm{G}]P_{C_3H_6}^2}{k_{-11} + k_{12} + k_{13} + k_{14}} \quad \text{Eq. 3.23}$$

$$r_{\mathbf{2MP}} = \mathrm{k}_{13}[I] = \frac{k_{13}k_{11}K_{10}[\mathrm{G}]P_{C_3H_6}^2}{k_{-11} + k_{12} + k_{13} + k_{14}} \quad \text{Eq. 3.24}$$

From the rate expressions shown in Equations 3.21-3.24, product selectivities for **4MP**, **DMB**, **LH**, and **2MP** can be derived as shown in Equations 3.25-3.28 for the metallacycle mechanism. Additionally, the ratio of product selectivities are only a ratio of rate constants and are not pressure dependent (Equation 3.29). Uniquely, the ratio of product selectivities for **2MP** and **4MP** is proposed to be unity in the metallacycle mechanism (Equations 3.21 and 3.24), as these two products share the same oxidative

coupling step, and the distinct isomers are formed from the β-hydride elimination step after the kinetically relevant step. Thus, individual product selectivities (Equations 3.25-3.28) and the ratio of product selectivities (Equation 3.29) are pressure-independent for the metallacycle mechanism.

$$s_{\boldsymbol{4MP}} = \frac{k_{13}}{k_{12} + 2k_{13} + k_{14}} \quad \text{Eq. 3.25}$$

$$s_{\mathbf{DMB}} = \frac{k_{14}}{k_{12} + 2k_{13} + k_{14}} \quad \text{Eq. 3.26}$$

$$s_{\boldsymbol{LH}} = \frac{k_{12}}{k_{12} + 2k_{13} + k_{14}} \quad \text{Eq. 3.27}$$

$$s_{\boldsymbol{2MP}} = \frac{k_{13}}{k_{12} + 2k_{13} + k_{14}} \quad \text{Eq. 3.28}$$

$$s_{\frac{(\boldsymbol{LH+2MP})}{(\boldsymbol{4MP+DMB})}} = \frac{k_{12} + k_{13}}{k_{13} + k_{14}} \quad \text{Eq. 3.29}$$

From the selectivity expressions and ratios derived from the Cossee-Arlman (Equations 3.9-3.12 and 3.18-3.20) and metallacycle mechanisms (Equations 3.25-3.29), the former and latter are pressure-dependent and pressure-independent respectively. These differences in product selectivities being pressure-dependent or pressure-independent arise from the inherent mechanistic pathways, where the metallacycle mechanism is characteristic of successive coordination before the kinetically relevant olefin coupling while the Cossee-Arlman mechanism coordinates and inserts an olefin molecule before coordinating and inserting a second olefin molecule. Thus, only one pathway occurs before the kinetically relevant step in the metallacycle mechanism, while two pathways arise via a 2,1- or 1,2- hydride insertion step to form **C** and **D** in the Cossee-Arlman mechanism.

In Figure 3.8, individual product selectivities for **4MP**, **DMB**, **LH**, and **2MP** are shown as a function of propylene pressure from 5-220 kPa to evaluate the verisimilitude of the Cossee-Arlman or metallacycle mechanism for propylene oligomerization on Ni/UiO-66. At low propylene pressures (<50 kPa), the selectivities of **LH** and **2MP**

increase with increasing propylene pressure while the selectivities of **4MP** and **DMB** decrease with increasing propylene pressure until all product selectivities become invariant with propylene pressure (> 50 kPa). These selectivity characteristics are consistent with selectivity expressions derived in Equation 3.9-3.12 for the Cossee-Arlman mechanism where all product selectivities are a function of propylene pressure. Furthermore, the selectivities of **4MP** and **DMB** decrease together while the selectivities of **LH** and **2MP** increase together, which is consistent with the products of **4MP** and **DMB** forming from intermediate **C** and with products **LH** and **2MP** forming from intermediate **D**, where **C** and **D** are two distinct Ni-propyl intermediates posited in the Cossee-Arlman mechanism.[51]

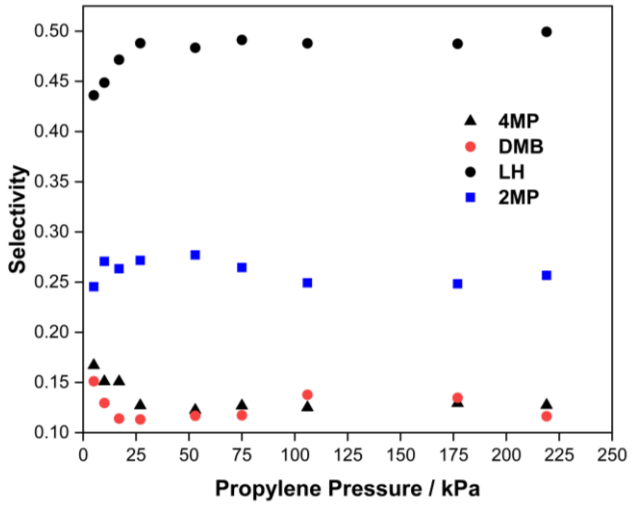

Figure 3.8. Selectivity of **4MP** (▲), **DMB** (●), **LH** (●), and **2MP** (■) as a function of propylene pressure at 473 K on Ni/UiO-66.

In Figure 3.9a, ratios of **4MP** to **DMB** (Equation 3.18), of **LH** to **2MP** (Equation 3.19), and of **2MP** to **4MP** (Equations 3.21 and 3.24) are plotted as a function of propylene pressure at 473 K from 5 to 220 kPa to further assess the plausibility of the Cossee-Arlman or metallacycle mechanism on Ni/UiO-66. Comparing the ratio of selectivities of **4MP** to **DMB** (blue) and of **LH** to **2MP** (black) as shown in Figure 3.9a, the two distinct product ratios are unaffected by propylene pressure, which are consistent with Equation 3.18 and Equation 3.19, respectively, for the Cossee-Arlman mechanism. However, when comparing the selectivity ratio of **2MP** to **4MP**, the ratio increases as a function of pressure

at low propylene pressures (<50 kPa) and approaches a value of ~2. The latter observation is incongruous with the metallacycle mechanism as the expected ratio should be pressure independent and be a value of unity (Equations 3.21 and 3.24). In Figure 3.9b, the ratio of **LH** + **2MP** to **4MP** + **DMB** is plotted against propylene partial pressure from 5 kPa to 220 kPa at 473 K. At low propylene pressures (<50 kPa), the ratio of **LH** + **2MP** to **4MP** + **DMB** is function of propylene pressure before it becomes invariant with propylene pressure, consistent with the selectivity expression derived in Equation 3.20 from the Cossee-Arlman mechanism. The individual product selectivities and ratios of selectivities from Figures 3.8 and 3.9 are all consistent with Equations 3.9-3.12 and 3.18-3.20, respectively, to suggest propylene oligomerization occurs via the Cossee-Arlman mechanism on Ni/UiO-66. The Cossee-Arlman and metallacycle mechanisms can be distinguished based on sequential coordination and insertion branching pathways, which give unique product selectivities as a function of propylene pressure.

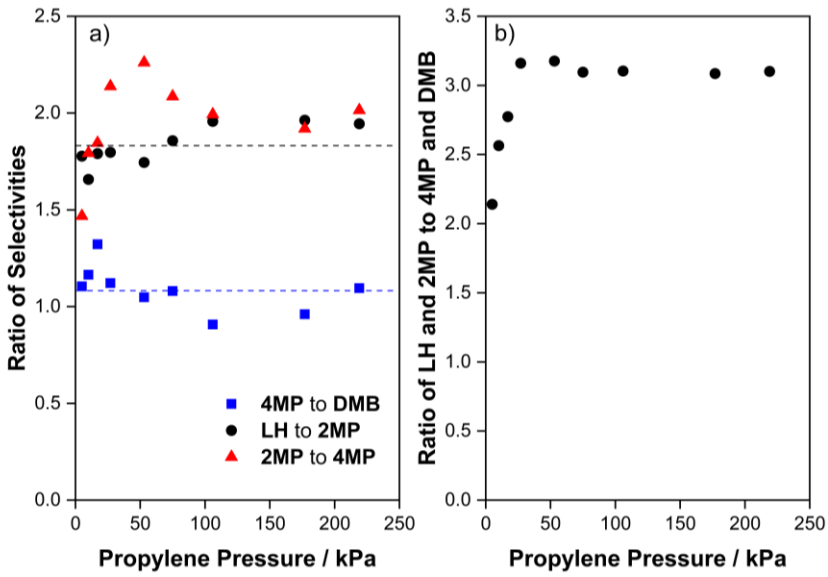

Figure 3.9. Ratio of selectivities for (a) **4MP** to **DMB** (■), **LH** to **2MP** (●), **2MP** to **4MP** (▲), where the dashed lines are meant to guide the eye and (b) **LH** + **2MP** to **4MP** + **DMB** at 473 K on Ni/UiO-66

3.4. Conclusion

This work affirms propagation of the Cossee-Arlman mechanism over the metallacycle mechanism on Ni/UiO-66 for olefin oligomerization, specifically for

propylene oligomerization, through observations of induction periods in the absence of cocatalysts, analysis of the nickel(II) oxidation state through XANES, and comparison of apparent activation energies through experiment and DFT. This study also illustrates a new method to discriminate between the Cossee-Arlman and metallacycle mechanisms based on ratios of hexene product selectivities derived from rate expressions for each mechanism. The former shows that the ratios of products are a function of olefin pressure, consistent with observations reported herein to confirm the Cossee-Arlman mechanism.

3.5. Supplemental Information

3.5.1. Propylene Oligomerization Time on Stream, Selectivities, Kinetics, and NO Titration on Ni/UiO-66

Previously, we reported enhancements in rate on Ni/UiO-66 on-stream during ethylene oligomerization. This observation was attributed to the increase in the density of nickel sites upon exposing the catalyst to higher ethylene pressures.[76] We sought to determine if this phenomena occurred during propylene oligomerization to correctly normalize reaction rates. In Figure 3.10, the propylene pressure was increased from 5 kPa to 500 kPa and the pressure was returned to 5 kPa. No enhancement in rate was determined at 5 kPa after exposing the catalyst to higher propylene pressures (0 – 250 minutes and 750 – 1500 minutes) to suggest that nickel site densities do not increase after exposing the catalyst to high propylene pressures.

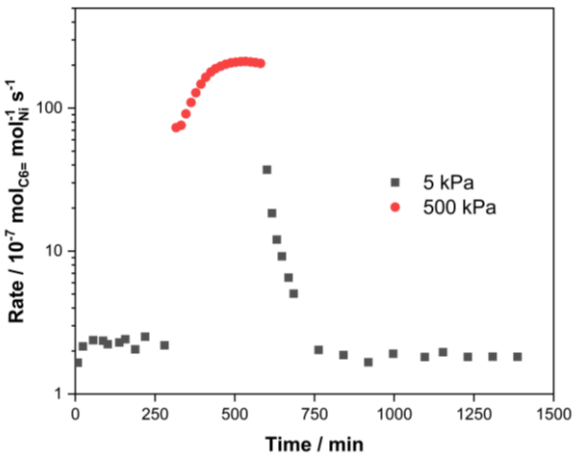

Figure 3.10. Time on stream after increasing propylene partial pressure from 5 kPa to 500 kPa and then decreasing the pressure back 5 kPa on Ni/UiO-66 at 473 K.

The stability of Ni/UiO-66 was examined further by changing propylene partial pressures with time on stream on the same catalyst at 473 K. In Figure 3.11, the reaction rate decreases by ~10% with time on stream at 420 kPa initially (~0-6 ks). However, after changing the propylene partial pressure to 249 kPa, 331 kPa, and returning to 420 kPa (~6-24 ks), the reference pressure, the catalyst is stable at 420 kPa, with the reaction rate at 420 kPa ~30% lower than the initial rate at 420 kPa (~0-6 ks). The partial pressure of propylene was decreased to 331 kPa (~24-30 ks) which yielded reaction rates within 10% of the previous condition at 331 kPa. After increasing partial pressure of propylene back to 420 kPa (~30-36 ks), the rate was within 10% of the reaction rate at 420 kPa at ~21-24 ks. Subsequently, after changing partial pressures of propylene to 497 kPa and 177 kPa, the rates of reaction at the reference partial pressure of 420 kPa were within 10%. In this case, we consider that rates from ~15-42 ks to be steady state rates. We note that although the catalyst appears to be stable initially (Figure 3.1 in the main text), changes in process conditions and returning to the same reference process conditions shows a decrease in the rate of reaction initially, and thus, is not the steady state rate for propylene oligomerization.

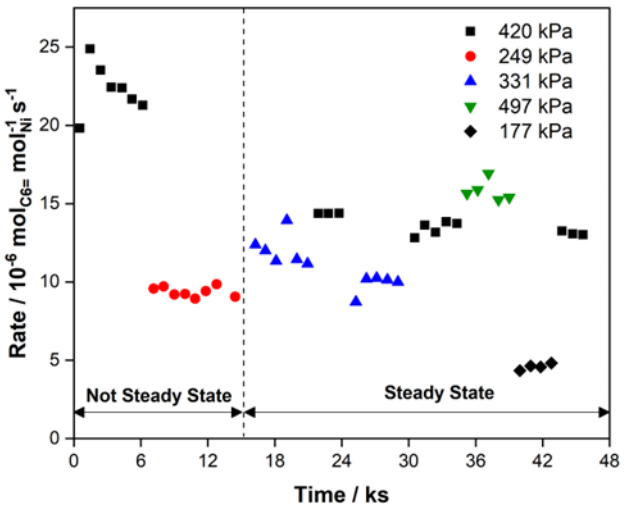

Figure 3.11. Propylene oligomerization rates as a function of time on stream on 18.2 mg of Ni/UiO-66 at 420 kPa (■), 249 kPa (●) 331 kPa (▲), 497 kPa (▼), and 177 kPa (◆) of 0.83 cm^3 s^{-1} of propylene at 473 K.

In Figure 3.12, no effect on oligomerization rates at 259 kPa and 473 K are observed with changes in propylene flowrate (0.17 – 0.83 cm^3 s^{-1}) to suggest kinetics were not measured in the presence of external mass transfer limitations or product inhibition. We note that the rate decreases by ~10% over 700 minutes. The individual hexene product selectivities are tabulated in Table 3.1.

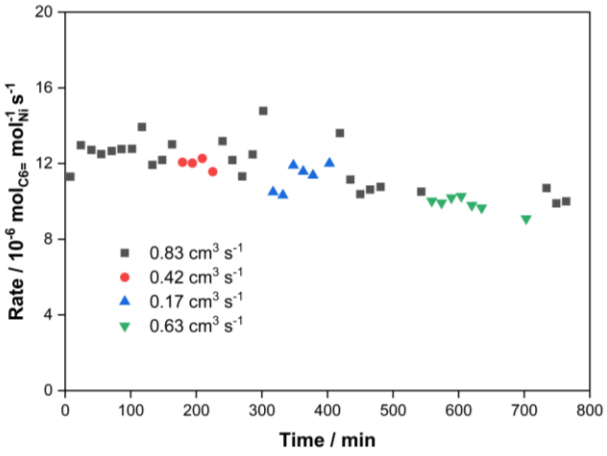

Figure 3.12. Time on stream after changing propylene flow rate (0.17 – 0.83 cm^3 s^{-1}) at 259 kPa and 473 K on 13.5 mg of Ni/UiO-66

Table 3.1. Individual hexene product selectivities at 259 kPa and 473 K at 0.002% conversion on Ni/UiO-66

Product	Selectivity / %
4-methyl-1-pentene	12.3
4-methyl-2-pentene	2.7
2,3-dimethyl-1-butene	6.1
2,3-dimethyl-2-butene	9.6
1-hexene	7.6
2-hexene	22.0
3-hexene	16.9
2-methyl-1-pentene	15.6
2-methyl-2-pentene	7.4

Rates of propylene oligomerization recorded at varying times-on-stream while changing temperature (453 - 493 K) at 259 kPa and 0.42 cm^3 s^{-1} propylene are shown in Figure 3.13. The rates decrease by <10% when returning the temperature back to the reference temperature (483 K). These data were used to extract the Arrhenius plot in Figure 3.7b in the main text.

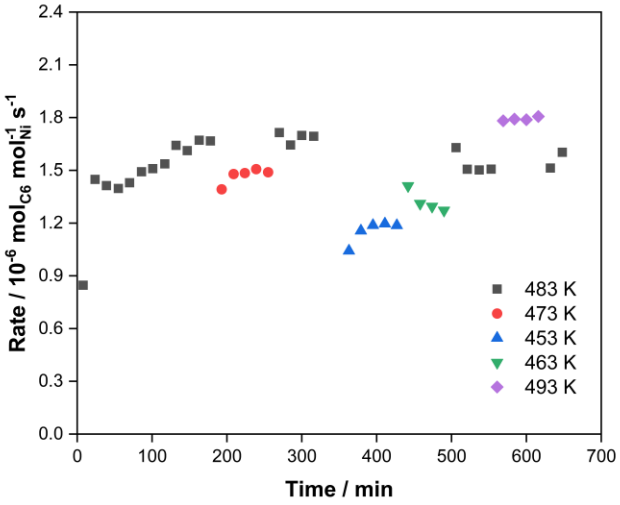

Figure 3.13. Time on stream with changes in temperature (453 – 493 K) on 259 kPa of 0.42 cm^3 s^{-1} of propylene on 18.8 mg of Ni/UiO-66

In Figure 3.14 below, we present a supplemental in-situ NO titration at 500 kPa and 473 K on Ni/UiO-66 during propylene oligomerization This titration gives ~15 $\mu mol_{Ni}\ g_{cat}^{-1}$, which is in good agreement with the NO titration shown in Figure 3.2 in the main text.

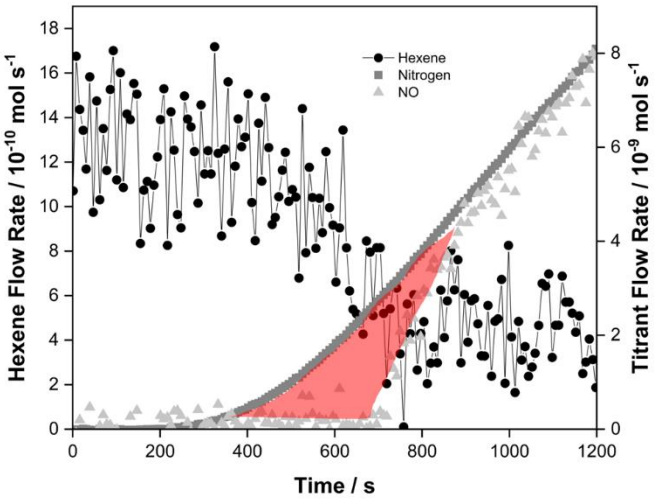

Figure 3.14. In situ NO titration showing a decrease in the rate of hexene formation (●) upon introduction of 0.083 $cm^3\ s^{-1}$ of 1% NO (▲, light grey) and 99% N_2 (■, dark gray) in 0.83 $cm^3\ s^{-1}$ at a total pressure of 500 kPa at 473 K on 80.6 mg of Ni/UiO-66. The amount of nickel titrated is calculated by integration of the red shaded area.

3.5.2. Cossee-Arlman and Metallacycle Mechanisms and Rate Expressions

The Cossee-Arlman has been proposed for olefin oligomerization and is shown in Figure 3.15. The nomenclature is the same as the main text up until the Ni-hexyl species, and additional designation is made for Ni-hexyl species (**J**, **K**, **L**, and **M**) and the Ni-hydride species with the absorbed hexene product (**N**, **O**, **P**, and **Q**) for products **4MP**, **DMB**, **LH**, and **2MP**, respectively, in the Cossee-Arlman mechanism. This designation is made for identification of intermediates in Section 3.5.3.

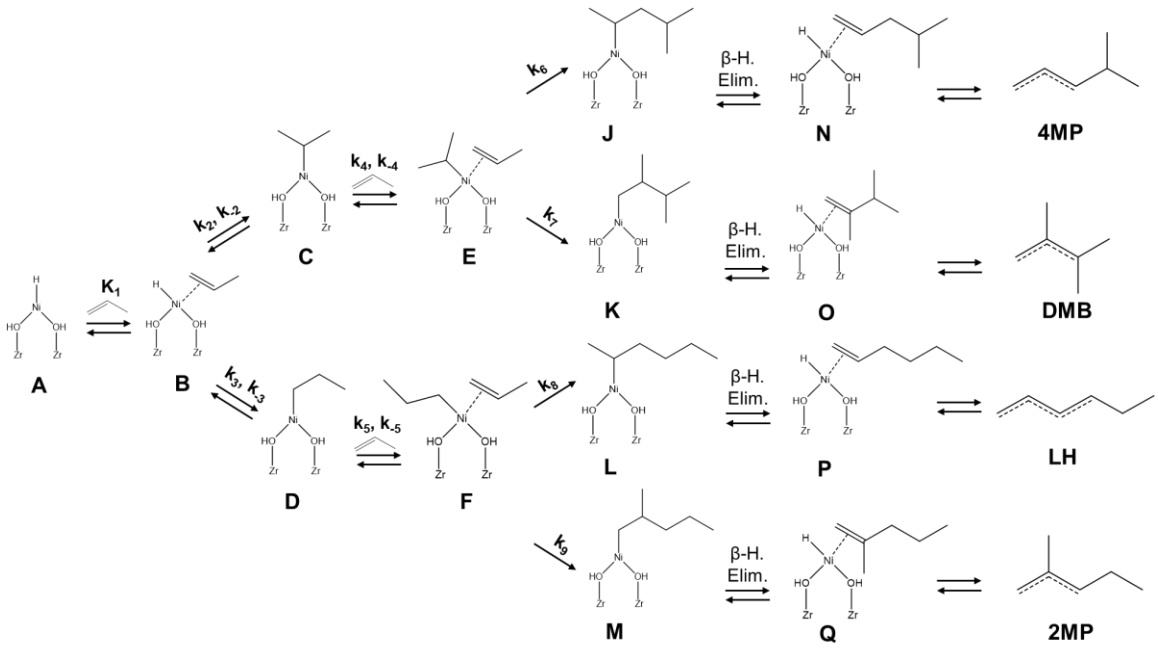

Figure 3.15. Cossee-Arlman mechanism for propylene oligomerization on Ni/UiO-66. Entire node omitted for clarity.

For the Cossee-Arlman mechanism, the rate limiting step is the olefin insertion step (k_6, k_7, k_8, and k_9).[41,50,53,80,95,129] Thus, the rate expressions are for **4MP**, **DMB**, **LH**, and **2MP** are shown below in Equations 3.30-3.33

$$r_{4MP} = k_6[E] \quad \text{Eq. 3.30}$$

$$r_{DMB} = k_7[E] \quad \text{Eq. 3.31}$$

$$r_{LH} = k_8[F] \quad \text{Eq. 3.32}$$

$$r_{2MP} = k_9[F] \quad \text{Eq. 3.33}$$

The rate expressions for the products can be written in terms of propylene pressure by assuming that the first adsorption step is quasi-equilibrated and all other intermediates are at pseudo-steady state. Assuming species **E** and **F** are at steady state, the rate expression for **E** and **F** is shown in Equation 3.34 and 3.35, respectively, with the concentration of **E** and **F** solved for in terms of concentrations of species **C** and **D**, respectively, and propylene pressure, as shown in Equations 3.36 and 3.37.

$$r_E = 0 = k_4[C]\,P_{C_3H_6} - k_{-4}[E] - k_6[E] - k_7[E] \quad \text{Eq. 3.34}$$

$$r_F = 0 = k_5[D]\,P_{C_3H_6} - k_{-5}[F] - k_8[F] - k_9[F] \quad \text{Eq. 3.35}$$

$$[E] = \frac{k_4[C]P_{C_3H_6}}{k_{-4} + k_6 + k_7} \quad \text{Eq. 3.36}$$

$$[F] = \frac{k_5[D]P_{C_3H_6}}{k_{-5} + k_8 + k_9} \quad \text{Eq. 3.37}$$

The concentration of **C** and **D** can be solved for by assuming steady state on these species by solving the rate expressions shown in Equations 3.38 and 3.39, respectively. The concentrations of **C** and **D**, shown in Equations 3.40 and 3.41 respectively, are solved for by substituting Equations 3.36 and 3.37 into Equations 3.38 and 3.39, respectively.

$$r_C = 0 = k_2[B] - k_{-2}[C] + k_{-4}[E] - k_4[C]P_{C_3H_6} \quad \text{Eq. 3.38}$$

$$r_D = 0 = k_3[B] - k_{-3}[D] + k_{-5}[F] - k_5[D]P_{C_3H_6} \quad \text{Eq. 3.39}$$

$$[C] = \frac{k_2[B]}{k_{-2} - \dfrac{k_{-4}k_4P_{C_3H_6}}{k_{-4} + k_6 + k_7} + k_4P_{C_3H_6}} \quad \text{Eq. 3.40}$$

$$[D] = \frac{k_3[B]}{k_{-3} - \dfrac{k_{-5}k_5P_{C_3H_6}}{k_{-5} + k_8 + k_9} + k_5P_{C_3H_6}} \quad \text{Eq. 3.41}$$

The concentration of species **B** can be solved by assuming the first adsorption of the propylene molecule from **A** to **B** to be quasi-equilibrated, as shown in Equation 3.42.

$$[B] = K_1[A]P_{C_3H_6} \quad \text{Eq. 3.42}$$

By substituting Equations 3.42, 3.40, and 3.36 into Equations 3.30 and 3.31 and by substituting Equations 3.42, 3.41, and 3.37 into Equations 3.32 and 3.33, the rate expressions for the hexene products for the Cossee-Arlman mechanism can be written in

terms of propylene pressure and **A**, unoccupied nickel sites, as shown in Equations 3.43, 3.44, 3.45, and 3.46, for **4MP**, **DMB**, **LH**, and **2MP**.

$$r_{\mathbf{4MP}} = \frac{k_6 k_4 k_2 K_1 [A] P_{C_3H_6}^2}{(k_{-4} + k_6 + k_7)\left(k_{-2} - \frac{k_{-4} k_4 P_{C_3H_6}}{k_{-4} + k_6 + k_7} + k_4 P_{C_3H_6}\right)} \quad \text{Eq. 3.43}$$

$$r_{\mathbf{DMB}} = \frac{k_7 k_4 k_2 K_1 [A] P_{C_3H_6}^2}{(k_{-4} + k_6 + k_7)\left(k_{-2} - \frac{k_{-4} k_4 P_{C_3H_6}}{k_{-4} + k_6 + k_7} + k_4 P_{C_3H_6}\right)} \quad \text{Eq. 3.44}$$

$$r_{\mathbf{LH}} = \frac{k_8 k_5 k_3 K_1 [A] P_{C_3H_6}^2}{(k_{-5} + k_8 + k_9)\left(k_{-3} - \frac{k_{-5} k_5 P_{C_3H_6}}{k_{-5} + k_8 + k_9} + k_5 P_{C_3H_6}\right)} \quad \text{Eq. 3.45}$$

$$r_{\mathbf{2MP}} = \frac{k_9 k_5 k_3 K_1 [A] P_{C_3H_6}^2}{(k_{-5} + k_8 + k_9)\left(k_{-3} - \frac{k_{-5} k_5 P_{C_3H_6}}{k_{-5} + k_8 + k_9} + k_5 P_{C_3H_6}\right)} \quad \text{Eq. 3.46}$$

The ratio of selectivities for **4MP** to **DMB** and **LH** to **2MP**, shown in Equations 3.47 and 3.48, respectively, can be solved for by either dividing Equation 3.43 by 3.44 or dividing 3.30 by 3.31 and by either dividing Equation 3.45 by 3.46 or dividing 3.32 by 3.33, respectively.

$$S_{\frac{\mathbf{4MP}}{\mathbf{DMB}}} = \frac{k_6}{k_7} \quad \text{Eq. 3.47}$$

$$S_{\frac{\mathbf{LH}}{\mathbf{2MP}}} = \frac{k_8}{k_9} \quad \text{Eq. 3.48}$$

The ratio of selectivities for **LH** and **2MP** to **4MP** and **DMB** shown in Equation 3.51 can be solved for by adding Equations 3.45 and 3.46 and by adding 3.43 and 3.44, respectively, as shown in Equations 3.49 and 3.50, and dividing Equation 3.49 by 3.50. Equation 3.51 shows that if propylene oligomerization occurs via the Cossee-Arlman mechanism, the ratio of **LH** and **2MP** to **4MP** and **DMB** is pressure dependent.

$$r_{LH} + r_{2MP} = \frac{(k_8 + k_9)k_5k_3K_1[A]P_{C_3H_6}^2}{(k_{-5} + k_8 + k_9)\left(k_{-3} - \frac{k_{-5}k_5P_{C_3H_6}}{k_{-5} + k_8 + k_9} + k_5P_{C_3H_6}\right)} \quad \text{Eq. 3.49}$$

$$r_{4MP} + r_{DMB} = \frac{(k_6 + k_7)k_4k_2K_1[A]P_{C_3H_6}^2}{(k_{-4} + k_6 + k_7)\left(k_{-2} - \frac{k_{-4}k_4P_{C_3H_6}}{k_{-4} + k_6 + k_7} + k_4P_{C_3H_6}\right)} \quad \text{Eq. 3.50}$$

$$S_{\frac{(LH+2MP)}{(4MP+DMB)}} = \frac{(k_{-2} - \frac{k_{-4}k_4P_{C_3H_6}}{k_{-4} + k_6 + k_7} + k_4P_{C_3H_6})}{\left(k_{-3} - \frac{k_{-5}k_5P_{C_3H_6}}{k_{-5} + k_8 + k_9} + k_5P_{C_3H_6}\right)} * \frac{(k_8 + k_9)k_5k_3(k_{-4} + k_6 + k_7)}{(k_6 + k_7)k_4k_2(k_{-5} + k_8 + k_9)} \quad \text{Eq. 3.51}$$

The individual product selectivity expressions for **4MP**, **DMB**, **LH**, and **2MP** in Equations 3.52-3.55 can be determined from Equations 3.43-3.46

$$s_{\mathbf{4MP}} = \frac{\frac{k_6k_4k_2K_1[A]P_{C_3H_6}^2}{(k_{-4} + k_6 + k_7)\left(k_{-2} - \frac{k_{-4}k_4P_{C_3H_6}}{k_{-4} + k_6 + k_7} + k_4P_{C_3H_6}\right)}}{\frac{(k_6 + k_7)k_4k_2K_1[A]P_{C_3H_6}^2}{(k_{-4} + k_6 + k_7)\left(k_{-2} - \frac{k_{-4}k_4P_{C_3H_6}}{k_{-4} + k_6 + k_7} + k_4P_{C_3H_6}\right)} + \frac{(k_8 + k_9)k_5k_3K_1[A]P_{C_3H_6}^2}{(k_{-5} + k_8 + k_9)\left(k_{-3} - \frac{k_{-5}k_5P_{C_3H_6}}{k_{-5} + k_8 + k_9} + k_5P_{C_3H_6}\right)}} \quad \text{Eq. 3.52}$$

$$s_{\mathbf{DMB}} = \frac{\frac{\mathrm{k}_7k_4k_2K_1[A]P_{C_3H_6}^2}{(k_{-4} + k_6 + k_7)\left(k_{-2} - \frac{k_{-4}k_4P_{C_3H_6}}{k_{-4} + k_6 + k_7} + k_4P_{C_3H_6}\right)}}{\frac{(k_6 + k_7)k_4k_2K_1[A]P_{C_3H_6}^2}{(k_{-4} + k_6 + k_7)\left(k_{-2} - \frac{k_{-4}k_4P_{C_3H_6}}{k_{-4} + k_6 + k_7} + k_4P_{C_3H_6}\right)} + \frac{(k_8 + k_9)k_5k_3K_1[A]P_{C_3H_6}^2}{(k_{-5} + k_8 + k_9)\left(k_{-3} - \frac{k_{-5}k_5P_{C_3H_6}}{k_{-5} + k_8 + k_9} + k_5P_{C_3H_6}\right)}} \quad \text{Eq. 3.53}$$

$$s_{\mathbf{LH}} = \frac{\frac{k_8k_5k_3K_1[A]P_{C_3H_6}^2}{(k_{-5} + k_8 + k_9)\left(k_{-3} - \frac{k_{-5}k_5P_{C_3H_6}}{k_{-5} + k_8 + k_9} + k_5P_{C_3H_6}\right)}}{\frac{(k_6 + k_7)k_4k_2K_1[A]P_{C_3H_6}^2}{(k_{-4} + k_6 + k_7)\left(k_{-2} - \frac{k_{-4}k_4P_{C_3H_6}}{k_{-4} + k_6 + k_7} + k_4P_{C_3H_6}\right)} + \frac{(k_8 + k_9)k_5k_3K_1[A]P_{C_3H_6}^2}{(k_{-5} + k_8 + k_9)\left(k_{-3} - \frac{k_{-5}k_5P_{C_3H_6}}{k_{-5} + k_8 + k_9} + k_5P_{C_3H_6}\right)}} \quad \text{Eq. 3.54}$$

$$s_{\mathbf{2MP}} = \frac{\frac{k_8k_5k_3K_1[A]P_{C_3H_6}^2}{(k_{-5} + k_8 + k_9)\left(k_{-3} - \frac{k_{-5}k_5P_{C_3H_6}}{k_{-5} + k_8 + k_9} + k_5P_{C_3H_6}\right)}}{\frac{(k_6 + k_7)k_4k_2K_1[A]P_{C_3H_6}^2}{(k_{-4} + k_6 + k_7)\left(k_{-2} - \frac{k_{-4}k_4P_{C_3H_6}}{k_{-4} + k_6 + k_7} + k_4P_{C_3H_6}\right)} + \frac{(k_8 + k_9)k_5k_3K_1[A]P_{C_3H_6}^2}{(k_{-5} + k_8 + k_9)\left(k_{-3} - \frac{k_{-5}k_5P_{C_3H_6}}{k_{-5} + k_8 + k_9} + k_5P_{C_3H_6}\right)}} \quad \text{Eq. 3.55}$$

Using the parameters α, β, γ, δ and ε from the main text and defined below in Equations 3.56-3.60, Equations 3.52-3.55 can be simplified, as shown in Equations 3.61-3.64.

$$\alpha = k_{-2} \quad \text{Eq. 3.56}$$

$$\beta = k_{-3} \quad \text{Eq. 3.57}$$

$$\gamma = k_4 - \frac{k_{-4}k_4}{k_{-4} + k_6 + k_7} \quad \text{Eq. 3.58}$$

$$\delta = k_5 - \frac{k_{-5}k_5}{k_{-5} + k_8 + k_9} \quad \text{Eq. 3.59}$$

$$\varepsilon = \frac{(k_8 + k_9)k_5k_3(k_{-4} + k_6 + k_7)}{(k_6 + k_7)k_4k_2(k_{-5} + k_8 + k_9)} \quad \text{Eq. 3.60}$$

$$s_{\mathbf{4MP}} = \frac{\frac{\mathrm{k}_6}{k_6 + k_7}\,(\beta + \delta P_{C_3H_6})}{\varepsilon(\alpha + \gamma P_{C_3H_6}) + (\beta + \delta P_{C_3H_6})} \quad \text{Eq. 3.61}$$

$$s_{\mathbf{DMB}} = \frac{\frac{\mathrm{k}_7}{k_6 + k_7}\,(\beta + \delta P_{C_3H_6})}{\varepsilon(\alpha + \gamma P_{C_3H_6}) + (\beta + \delta P_{C_3H_6})} \quad \text{Eq. 3.62}$$

$$s_{\mathbf{LH}} = \frac{\frac{\mathrm{k}_8}{k_8 + k_9}\,(\alpha + \gamma P_{C_3H_6})}{(\alpha + \gamma P_{C_3H_6}) + \frac{1}{\varepsilon}(\beta + \delta P_{C_3H_6})} \quad \text{Eq. 3.63}$$

$$s_{\mathbf{2MP}} = \frac{\frac{k_9}{k_8 + k_9}\,(\alpha + \gamma P_{C_3H_6})}{(\alpha + \gamma P_{C_3H_6}) + \frac{1}{\varepsilon}(\beta + \delta P_{C_3H_6})} \quad \text{Eq. 3.64}$$

From Equations 3.61-3.64, the individual product selectivities for **4MP**, **DMB**, **LH**, and **2MP** are a function of propylene pressure. This is consistent with Figure 3.8 in the main text where the individual product selectivities of **4MP**, **DMB**, **LH**, and **2MP** are a function of propylene pressure.

While the Cossee-Arlman mechanism has been proposed for olefin oligomerization, the metallacycle mechanism, as shown in Figure 3.16, has also been proposed for olefin oligomerization on nickel-based catalyst.

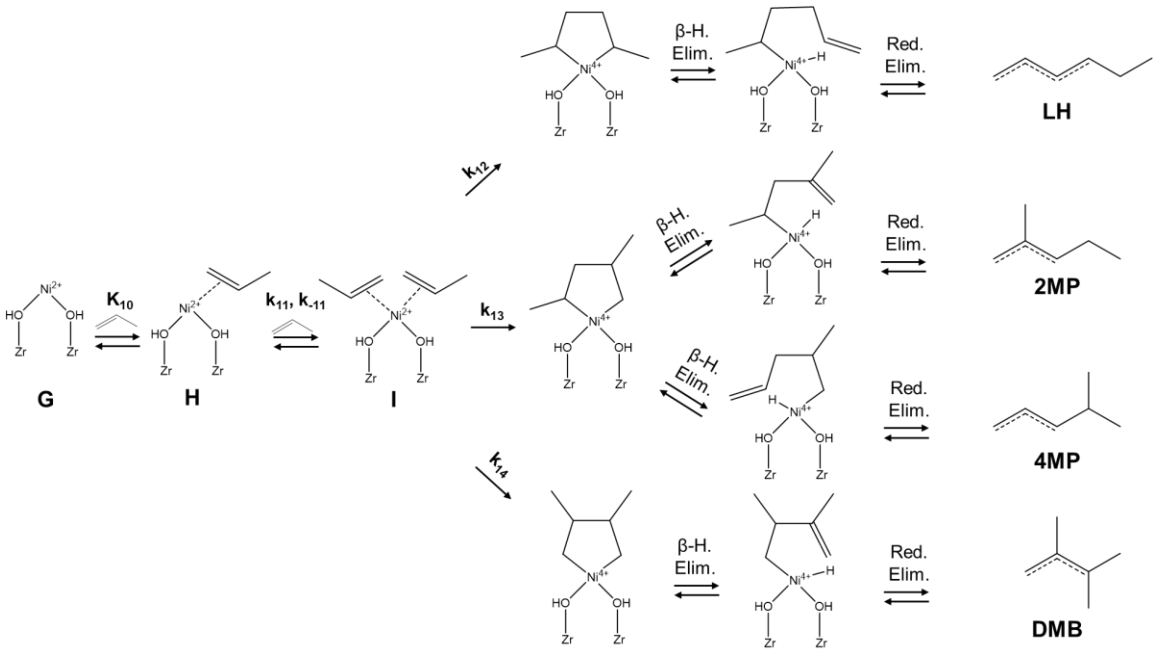

Figure 3.16. Metallacycle mechanism for propylene oligomerization on Ni/UiO-66. Entire node omitted for clarity.

The kinetically relevant step in the metallacycle mechanism is the oxidative coupling step (k_{12}, k_{13}, and k_{14}).[41,53,129] The rate expressions for products **4MP**, **DMB**, **LH**, and **2MP** for the metallacycle mechanism are shown in Equations 3.65-3.68.

$$r_{\boldsymbol{4MP}} = k_{13}[I] \qquad \text{Eq. 3.65}$$

$$r_{\mathbf{DMB}} = k_{14}[I] \qquad \text{Eq. 3.66}$$

$$r_{\boldsymbol{LH}} = k_{12}[I] \qquad \text{Eq. 3.67}$$

$$r_{\boldsymbol{2MP}} = k_{13}[I] \qquad \text{Eq. 3.68}$$

The rate expressions for the products can be written in terms of propylene pressure by assuming that the first adsorption step is quasi-equilibrated, and all other intermediates are at pseudo-steady state. Assuming that species **I** is at pseudo-steady state (Equation 3.69), the concentration of **I** can be solved for as shown in Equation 3.70.

$$r_I = 0 = k_{11}[H]P_{C_3H_6} - k_{-11}[I] - k_{12}[I] - k_{13}[I] - k_{14}[I] \quad \text{Eq. 3.69}$$

$$[I] = \frac{k_{11}[H]P_{C_3H_6}}{k_{-11} + k_{12} + k_{13} + k_{14}} \quad \text{Eq. 3.70}$$

The concentration of species **H** can be solved by assuming the first adsorption of the propylene molecule from **G** to **H** to be quasi-equilibrated, as shown in Equation 3.71.

$$[H] = K_{10}[G]P_{C_3H_6} \quad \text{Eq. 3.71}$$

By substituting Equations 3.70 and 3.71 into Equations 3.65-3.68, the rate expressions for the hexene products for the metallacycle mechanism can be written in terms of propylene pressure and **G**, unoccupied nickel sites, as shown in Equations 3.72, 3.73, 3.74, and 3.75, for **4MP**, **DMB**, **LH**, and **2MP**.

$$r_{\boldsymbol{4MP}} = \mathrm{k}_{13}[I] = \frac{k_{13}k_{11}K_{10}[\mathrm{G}]P_{C_3H_6}^2}{k_{-11} + k_{12} + k_{13} + k_{14}} \quad \text{Eq. 3.72}$$

$$r_{\mathbf{DMB}} = \mathrm{k}_{14}[I] = \frac{k_{14}k_{11}K_{10}[\mathrm{G}]P_{C_3H_6}^2}{k_{-11} + k_{12} + k_{13} + k_{14}} \quad \text{Eq. 3.73}$$

$$r_{\boldsymbol{LH}} = \mathrm{k}_{12}[I] = \frac{k_{12}k_{11}K_{10}[\mathrm{G}]P_{C_3H_6}^2}{k_{-11} + k_{12} + k_{13} + k_{14}} \quad \text{Eq. 3.74}$$

$$r_{\boldsymbol{2MP}} = \mathrm{k}_{13}[I] = \frac{k_{13}k_{11}K_{10}[\mathrm{G}]P_{C_3H_6}^2}{k_{-11} + k_{12} + k_{13} + k_{14}} \quad \text{Eq. 3.75}$$

The ratio of selectivities for the metallacycle mechanism can be found by either dividing any of the rate expressions from Equations 3.65-3.68 by one other or dividing any of the rate expressions from Equations 3.72-3,75 by one another. This yields ratios of selectivities that are solely a function of rate constants. This arises from **4MP**, **DMB**, **LH**, and **2MP** originating from the same intermediates, and the ratio of selectivities comes from the kinetically relevant olefin insertion step, where the metallacycle mechanism branches

off. The ratio of **LH** + **2MP** to **4MP** + **DMB** for the metallacycle mechanism is shown in Equation 3.76.

$$S_{\frac{(LH+2MP)}{(4MP+DMB)}} = \frac{k_{12} + k_{13}}{k_{13} + k_{14}} \quad \text{Eq. 3.76}$$

The selectivity expressions shown in Equations 3.77-3.80 derived from the metallacycle mechanism for **4MP**, **DMB**, **LH**, and **2MP** from the rate expressions shown in Equations 3.65-3.68.

$$s_{\mathbf{4MP}} = \frac{k_{13}}{k_{12} + 2k_{13} + k_{14}} \quad \text{Eq. 3.77}$$

$$s_{\mathbf{DMB}} = \frac{k_{14}}{k_{12} + 2k_{13} + k_{14}} \quad \text{Eq. 3.78}$$

$$s_{\mathbf{LH}} = \frac{k_{12}}{k_{12} + 2k_{13} + k_{14}} \quad \text{Eq. 3.79}$$

$$s_{\mathbf{2MP}} = \frac{k_{13}}{k_{12} + 2k_{13} + k_{14}} \quad \text{Eq. 3.80}$$

In contrast to the pressure-dependent ratio of selectivities in Equation 3.51 and selectivity expressions in Equation 3.61-3.64, the ratio of selectivities shown in Equation 3.76 and selectivity expressions in Equations 3.77-3.80 are pressure-independent. Observations from Figures 3.8 and 3.9 in the main text suggest that propylene oligomerization does not proceed via the metallacycle mechanism on Ni/UiO-66.

The curvature of the ratio of product selectivities described in Equation 3.51 or Equation 3.20 in the main text is determined by the parameters α, β, γ, and δ (Equations 3.13-3.16 in the main text). By taking the first derivative of Equation 3.20 as shown in Equation 3.81, an increase in the ratio of **LH** and **2MP** to **4MP** and **DMB** arises when the product of β and γ is greater than the product of α and δ and a decrease in the ratio of **LH** and **2MP** to **4MP** and **DMB** arises when the product of β and γ is less than the product of α and δ.

$$\frac{d}{dP_{C_3H_6=}}\left(\frac{\left(\alpha+\gamma\,\boldsymbol{P_{C_3H_6}}\right)}{\left(\beta+\delta\,\boldsymbol{P_{C_3H_6}}\right)}*\varepsilon\right)=\frac{(\beta*\gamma-\alpha*\delta)}{\left(\beta+\delta\,\boldsymbol{P_{C_3H_6}}\right)^2}*\varepsilon \qquad \text{Eq. 3.81}$$

3.5.3. Supplemental DFT Calculations

The enthalpy and free energy diagrams for **4MP**, **DMB**, **LH**, and **2MP** for the Cossee-Arlman mechanism (Figure 3.15 and Figure 3.3) are shown in Figures 3.17-3.20, respectively. In all cases, the kinetically relevant step for each hexene product is the olefin insertion step with free energies ranging from 88 kJ mol^{-1} to 143 kJ mol^{-1}. The apparent activation energy for each hexene product is calculated from the difference in enthalpy between the nickel-propyl species and the kinetically relevant olefin insertion step. A comparison of apparent activation energies from experiment and computation are tabulated in Table 3.2. The differences in the calculated energy barriers and those from experiment are 5-27 kJ mol^{-1} and are within the range of 8-23 kJ mol^{-1}, consistent with differences in experimental and computed enthalpy barriers found in olefin oligomerization on Ni/UiO-66 and Ni/NU-1000 MOF materials using the M06L functional.[76,80,129] Electronic energy, enthalpy, and Gibbs free energy (hartree) for all intermediates and TS structures for species in Figure 3.15 are reported in Table 3.3. The spin state in all species is in the singlet spin state (2S+1 = 0) based on previous calculations on Ni/UiO-66.[76,129]

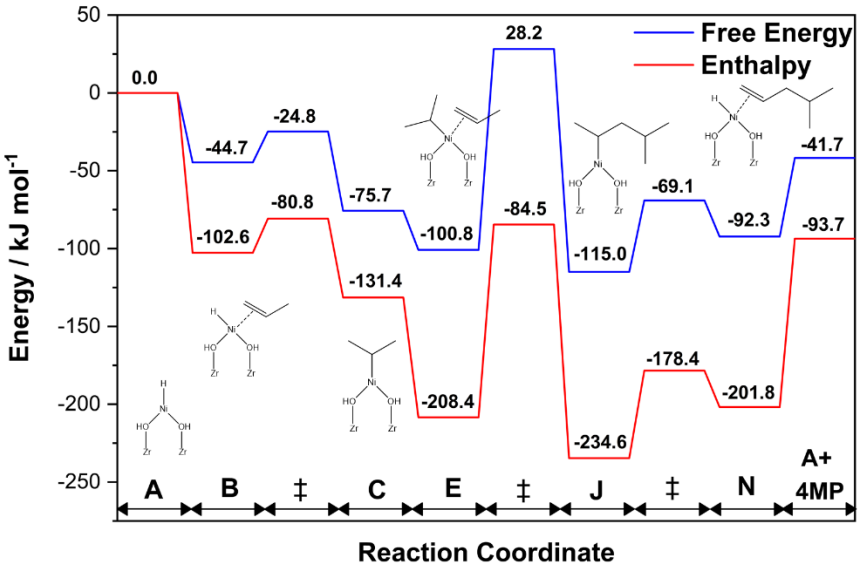

Figure 3.17. Free energy (blue) and enthalpy (red) diagram for **4MP** following the Cossee-Arlman mechanism on cluster models during propylene oligomerization of Ni/UiO-66 at 101.3 kPa and 298 K.

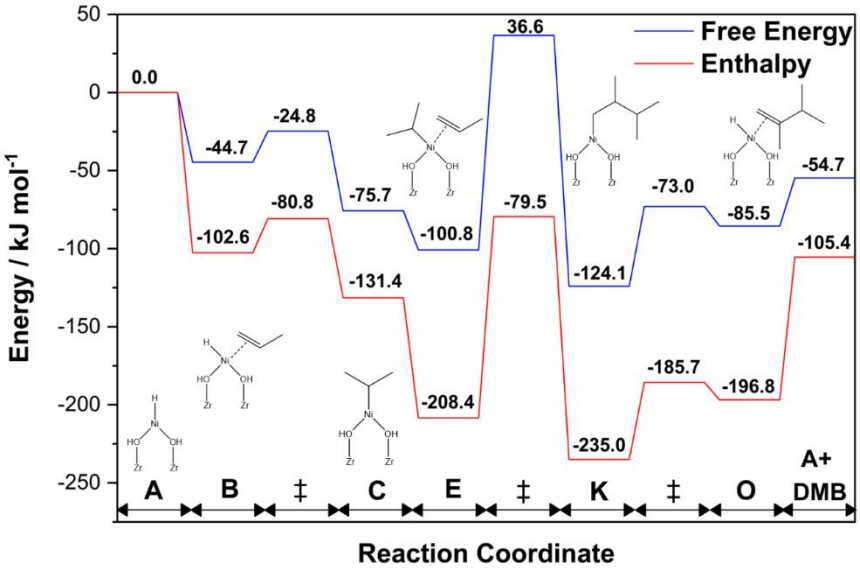

Figure 3.18. Free energy (blue) and enthalpy (red) diagram for **DMB** following the Cossee-Arlman mechanism on cluster models during propylene oligomerization of Ni/UiO-66 at 101.3 kPa and 298 K.

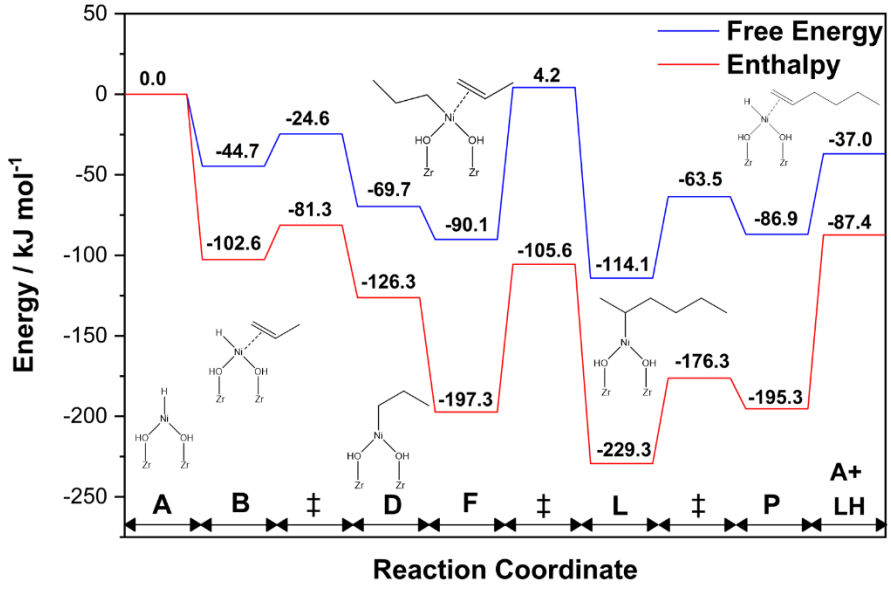

Figure 3.19. Free energy (blue) and enthalpy (red) diagram for **LH** following the Cossee-Arlman mechanism on cluster models during propylene oligomerization of Ni/UiO-66 at 101.3 kPa and 298 K.

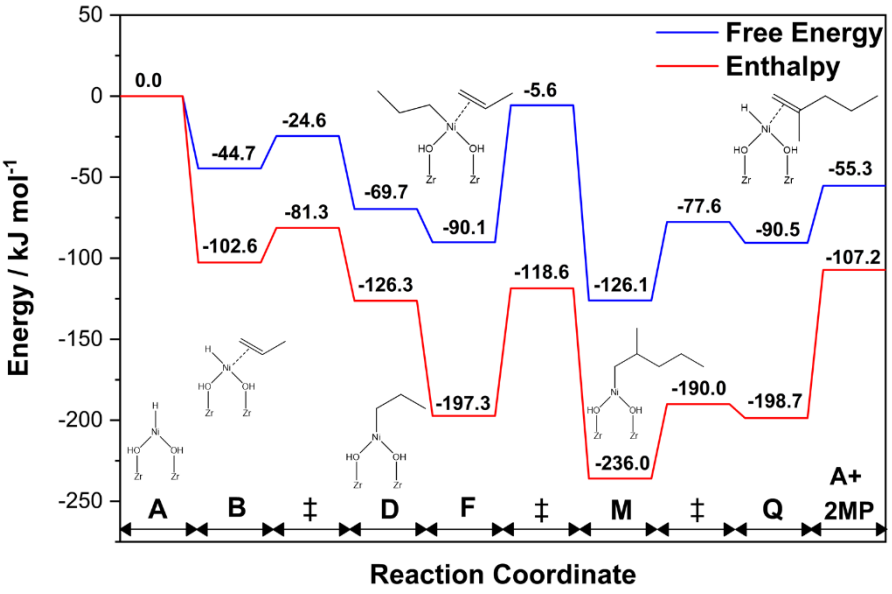

Figure 3.20. Free energy (blue) and enthalpy (red) diagram for **2MP** following the Cossee-Arlman mechanism on cluster models during propylene oligomerization of Ni/UiO-66 at 101.3 kPa and 298 K.

Table 3.2. Apparent activation energies from experiment and DFT for 4MP, DMB, LH, and 2MP on Ni/UiO-66 during propylene oligomerization at 259 kPa.

Hexene Product	Experimental Activation Energy / kJ mol^{-1}	Computed Activation Energy / kJ mol^{-1}
4MP	21.0 ± 3.4	46.9
DMB	24.6 ± 3.8	51.9
LH	15.7 ± 2.2	20.7
2MP	17.5 ± 2.8	7.7

Table 3.3. Electronic energy, enthalpy, and Gibbs free energy (hartree) for all intermediates and transition state TS structures for the Cossee-Arlman mechanism in Figure 3.15 at 298 K and 101.3 kPa. The relative enthalpies and free energies (kJ mol^{-1}) with respect to **A** and two propylene molecules are reported.

Structure	E / hartree	H / hartree	G / hartree	△H / kJ mol^{-1}	△G / kJ mol^{-1}
Propylene	-117.71998	-117.714938	-117.744969	-	-
4MP	-235.4743	-235.465555	-235.505839	-	-
DMB	-235.47893	-235.470026	-235.510782	-	-
LH	-235.472	-235.463178	-235.504029	-	-
2MP	-235.47948	-235.470712	-235.51099	-	-
Production of 4-methylpentenes (4MP)					
A	-4627.5525	-4627.494089	-4627.632369	0.0	0.0
B	-4745.3099	-4745.248111	-4745.394354	-102.6	-44.7
B to C TS	-4745.3025	-4745.239784	-4745.386784	-80.8	-24.8
C	-4745.3219	-4745.259092	-4745.406182	-131.4	-75.7
E	-4863.0708	-4863.00334	-4863.160706	-208.4	-100.8
E to J TS	-4863.0229	-4862.956152	-4863.111564	-84.5	28.2
J	-4863.0777	-4863.011623	-4863.166105	-203.7	-115.0
J to N TS	-4863.0587	-4862.991937	-4863.148625	-178.5	-69.1
N	-4863.0677	-4863.000829	-4863.157453	-201.83	-92.3
A + 4MP	-4863.0268	-4862.959644	-4863.138208	-93.7	-41.7
Production of 2,3-dimethylbutenes (DMB)					
A	-4627.552	-4627.4941	-4627.632	0.0	0
B	-4745.31	-4745.2481	-4745.394	-102.6	-44.7
B to C TS	-4745.302	-4745.2398	-4745.387	-80.8	-24.8
C	-4745.322	-4745.2591	-4745.406	-131.4	-75.7
E	-4863.071	-4863.0033	-4863.161	-208.4	-100.8
E to K TS	-4863.021	-4862.9542	-4863.108	-79.5	36.6
K	-4863.08	-4863.0135	-4863.17	-235.0	-124.1
Kto O TS	-4863.061	-4862.9947	-4863.15	-185.7	-73.0
O	-4863.066	-4862.9989	-4863.155	-196.8	-85.5
A + DMB	-4863.031	-4862.9641	-4863.143	-105.4	-54.7
Production of linear hexenes (LH)					

A	-4627.5525	-4627.494	-4627.632369	0	0.0
B	-4745.3099	-4745.248	-4745.394354	-102.6	-44.7
B to C TS	-4745.3026	-4745.24	-4745.3867	-81.3	-24.6
C	-4745.3198	-4745.257	-4745.403871	-126.3	-69.7
E	-4863.0665	-4862.999	-4863.156638	-197.3	-90.1
E to J TS	-4863.031	-4862.964	-4863.120695	-105.6	4.2
J	-4863.0759	-4863.009	-4863.165782	-223.4	-114.1
J to N TS	-4863.0575	-4862.991	-4863.146506	-176.3	-63.5
N	-4863.0652	-4862.998	-4863.155421	-195.3	-86.9
A + LH	-4863.0245	-4862.957	-4863.136398	-87.4	-37.0
Production of 2-methylpentenes (2MP)					
A	-4627.55	-4627.4941	-4627.63	0	0.0
B	-4745.31	-4745.2481	-4745.39	-102.6	-44.7
B to C TS	-4745.3	-4745.24	-4745.39	-81.3	-24.6
C	-4745.32	-4745.2571	-4745.4	-126.3	-69.7
E	-4863.07	-4862.9991	-4863.16	-197.3	-90.1
E to J TS	-4863.04	-4862.9691	-4863.12	-118.6	-5.6
J	-4863.08	-4863.0139	-4863.17	-236.0	-126.1
J to N TS	-4863.06	-4862.9963	-4863.15	-190.0	-77.6
N	-4863.07	-4862.9996	-4863.16	-198.7	-90.5
A + 2MP	-4863.03	-4862.9648	-4863.14	-107.2	-55.3

Chapter 4. Structure and Site Evolution of Framework Ni Species in MIL-127 MOFs for Propylene Oligomerization Catalysis

This material has been adapted from a previously published work.[77] Contributions of other authors is noted in the footnotes of the experimental and computational methods.

4.1. Introduction

Metal-organic frameworks (MOFs) contain a variety of structural defects which can be beneficial for catalysis.[65,138–141] These defects can be engendered from missing linkers in the framework to expose relevant catalytic active sites and can be tuned based on the choice of modulators used in synthesis to change the electronic properties of the catalytic site.[140,142–144] UiO-66 and NU-1000, zirconium-oxide based MOFs, for example, have been shown to facilitate cyclization of (+)-citronellal to isopulegol and epoxide-ring opening reactions, respectively, through a coordinately unsaturated zirconium Lewis acid site derived from a missing linker defect, and up to 25% of linkers can be missing in UiO-66 to generate these unsaturated zirconium Lewis acid sites.[119,145,146] The strength of coordinately unsaturated zirconium Lewis acid sites on UiO-66 can be tuned with acetic acid, formic acid, difluoroacetic acid, or trifluoroacetic acid modulators used in synthesis while maintaining the structure of the MOF as these modulators have similar chemical functionalities as the organic linker.[67,144] Thermal treatment of MOF-5, a zinc-based MOF, below its decomposition temperature exposes zinc sites through partial decomposition of the bridging carboxylate in the organic linker.[147] Iron oxo-trimer MOF catalysts, such as MIL-100 and PCN-250/MIL-127, have been proposed to develop an unsaturated Fe(II) site from a saturated Fe(III) through the loss of an OH species or a decarboxylation mechanism to lose CO_2 on the organic linker to expose relevant catalytic sites for alkane oxidation reactions after thermal activation.[143,148,149] Missing linker defects and the coordination environment of unsaturated metal sites in MOFs have been probed using techniques such as thermogravimetric analysis (TGA), ^{1}H nuclear magnetic resonance (NMR) spectroscopy, and X-ray absorption spectroscopy (XAS).[65,67,119,150] Upon generation of missing linker defects, metal centers can be exposed for their respective chemistry, but a major challenge in MOF catalysis involves identifying and quantifying relevant open

coordination catalytic sites from the formation of defects as nonuniformities exist in the MOF structure.[65]

An open coordination site is purportedly required to facilitate the Cossee-Arlman mechanism for olefin oligomerization on nickel-based catalysts after the reactant olefin molecule binds to a vacant nickel site to undergo a stoichiometric reaction to generate nickel-alkyl or nickel-hydride species.[14,31,32,40,41,44–46,76] Heterogeneous nickel-zeolite catalysts for propylene oligomerization such as Ni-Na-X,[35] Ni-SiO_2,[35] Ni-Na-MOR,[35] and Ni-M-MCM-41[43] inherently have an open coordination site but deactivate with time on stream at elevated temperatures. Nickel-framework MOF catalysts for propylene oligomerization such as Ni-MOF-74[72] are proposed to generate a Ni-propyl species during the induction period through the loss of a Ni-O ligand and deactivate with time on stream, while Ni-MFU-4l[51] inherently has an open coordination site but uses cocatalysts to promote propylene oligomerization. Due to the lack of catalyst stability for propylene oligomerization on these materials, few reports elucidate either the mechanism or the kinetics devoid of deactivation for this chemistry, while the Cossee-Arlman mechanism has been proposed for ethylene oligomerization on nickel catalysts.[14,31,32,40,41,44–46,76]

Herein, we report a stable trimeric bimetallic Ni-MIL-127 MOF, with a fully coordinated nickel atom and two iron atoms in the inorganic node as synthesized, that engenders a coordinately unsaturated nickel site upon thermal treatment (493 K) in flowing helium through the loss of a linker, as determined from temperature programmed oxidation (TPO), ^{1}H NMR spectroscopy, and XAS. Upon thermal treatment, the catalyst undergoes an induction period and oligomerizes propylene in the absence of activators and cocatalysts and is stable for ~1000 minutes on stream, distinct from other catalysts for this chemistry. The Cossee-Arlman mechanism for propylene oligomerization is affirmed by comparisons of apparent activation enthalpies through steady state kinetic measurements and density functional theory (DFT) calculations on cluster models of Ni-MIL-127 to contend that light olefin oligomerization occurs via the Cossee-Arlman mechanism regardless of the length and carbon number of the reacting linear olefin. Our investigation of Ni-MIL-127 not only highlights that as-synthesized MOF materials can be pre-catalysts that generate defects to

engender active sites for catalysis but also allows us to formulate catalysts with isolated metal centers with varying coordination and electronic structure environments that can be probed and tuned through a combination of experiment and computation.

4.2. Experimental and Computational Methods

4.2.1. Synthesis of Ni-MIL-127[9]

The 3,3',5,5'-azobenzenetetracarboxylic acid (ABTC), the organic linker in Ni-MIL-127, was synthesized with modifications to a previously reported procedure.[151] NaOH (50 g, 1.25 mol) was added to 250 cm^3 of deionized water. 5-Nitroisophthalic acid (19 g, 0.09 mol) was added and the slurry was allowed to stir at 333 K for 1 hour. An aqueous solution of glucose (100 g, 0.56 mol) in 150 cm^3 deionized water was then added slowly to the slurry. The reaction immediately turned dark brown and was allowed to cool to ambient temperature before air was bubbled into the stirring solution for 16 hours. The reaction was then cooled with an ice bath and the sodium salt of ABTC was recovered by filtration. This solid was then dissolved in 200 cm^3 of deionized water and acidified to approximately pH = 1 with concentrated HCl. A bright orange solid was isolated on a fine porosity glass frit, washed with deionized water, and dried under vacuum at 353 K. Yield: 11.7 g, 73%. ^{1}H NMR (400 MHz, DMSO-d_6) δ 13.63 (s, 4H), 8.62 (s, 6H).

The Ni-MIL-127 cluster, $Fe_2Ni(\mu_3\text{-}O)(CH_3CO_2)_6$, was synthesized with modifications to a previously reported procedure.[152] Sodium acetate (25.43 g, 0.31 mol) was dissolved in 70 cm^3 deionized water. Simultaneously, $Fe(NO_3)_3 \cdot 9H_2O$ (8.08 g, 0.02 mol) and $Ni(NO_3)_2 \cdot 6H_2O$ (29.08 g, 0.1 mol) were dissolved in 70 cm^3 deionized water. The sodium acetate solution was then added to the stirring $Fe(NO_3)_3$ and $Ni(NO_3)_2$ solution. A brown precipitate immediately formed and was collected on a medium porosity glass frit, washed with deionized water and EtOH, and dried in air.

Ni-MIL-127/PCN-250 (Fe_2Ni) was synthesized with modifications according to a previously reported procedure.[152] ABTC (500 mg, 1.40 mmol), $Fe_2Ni(\mu_3\text{-}O)(CH_3CO_2)_6$ (500 mg), acetic acid (50 cm^3) and DMF (100 cm^3) were added to a 350 cm^3 Ace Glass

[9] Ni-MIL-127 was synthesized by Steven Prinslow and Connie Lu at the University of Minnesota

pressure flask. The mixture was sonicated for 10 minutes and then placed in an oven at 413 K for 16 hours. The flask was removed from the oven and allowed to cool to ambient temperature before the brown crystalline material was separated on a medium porosity glass frit and washed with DMF. To activate the material, the PCN-250 was soaked in DMF (100 cm^3) at 333 K for 2 days. It was then soaked in MeOH (100 cm^3) at 333 K for 2 days. The MOF was then soaked in CH_2Cl_2 (100 cm^3) at 313 K for 3 days. Throughout this entire process, the solvent was exchanged every 8 hours. Lastly, the material was dried under vacuum at 423 K for 8 hours.

4.2.2. Catalytic Testing

Ni-MIL-127 was (5-20 mg) was physically mixed with sand (~100 mg, subjected prior to an overnight wash in 2 M HNO_3 solution followed by DI water rinse until pH ~7, and a final thermal treatment in flowing dry air (0.83 $cm^3\ s^{-1}$) at 1273 K (0.083 K s^{-1} ramp rate from RT) for 16 h; $10 < wt_{diluent}/wt_{cat} < 15$), before being loaded into a tubular glass-lined stainless-steel reactor (6.35 mm O.D. and 4 mm I.D., SGE Analytical Science) packed between two quartz wool plugs (Technical Glass Products). The free volume in the reactor tube was filled with quartz rods (3 mm O.D.; Technical Glass Products) to prevent any vertical displacement of the catalyst bed. The tubular reactor was then placed inside a resistively heated furnace (Applied Test Systems). The temperature was measured and regulated using a K-type thermocouple (Omega) wrapped around the periphery of the stainless-steel reactor with the tip placed at the center of the catalyst bed and an electronic controller (Watlow), respectively. The catalyst was pretreated in helium (Matheson, 99.997%, 0.83 $cm^3\ s^{-1}$) from ambient temperature to 493 K (0.08 K s^{-1}) for 4 hours and then cooled to reaction temperature (443-493 K) in flowing helium (Matheson, 99.997%, 0.83 $cm^3\ s^{-1}$). Propylene (Matheson, 99.83%, 0.17-83 $cm^3\ s^{-1}$) was introduced to the reactor with flow controlled by mass flow controllers (Brooks 5850E Series). The gas-phase pressure was measured using a pressure transducer (Omega) placed upstream of the reactor and controlled using a back-pressure regulator (TESCOM Series 44-2300) placed downstream of the reactor. The composition of the reactor effluent was quantified using a gas

chromatograph (Agilent GC 7890A) equipped with a dimethylpolysiloxane HP-1 column (50 m × 320 μm × 0.52 μm) connected to a flame ionization detector (FID).

4.2.3. In-situ NO Titration Experiments

The reactor setup is identical to the one described above. A nitric oxide/nitrogen mixture (Airgas, 1% NO, balance N_2, 0.083-0.17 $cm^3\ s^{-1}$) was introduced in the propylene gas stream at 500 kPa with a mass flow controller (Brooks 5850E Series). An online mass spectrometer (MKS Cirrus 2) was utilized to determine the effluent propylene, hexene, NO, and N_2 signals (m/z: 42, 84, 30, and 28, respectively). The N_2 flow was used as a tracer to determine the average residence time of NO over the catalyst bed,[93] which was used to calculate the amount of NO reacted/absorbed on nickel sites to suppress the rate of oligomerization.

4.2.4. Liquid Co-feed Experiments

Liquid reactants of 1-hexene (≥99%, Sigma Aldrich, ~330,000 $\mu m^3\ s^{-1}$), 2,3-dimethylbutene (97%, Sigma Aldrich, ~330,000 $\mu m^3\ s^{-1}$), or 1-nonene (≥99.5%, Sigma Aldrich, ~0.001 $mm^3\ s^{-1}$) were delivered using a syringe pump (Legato 100, KD Scientific), vaporized in heat traced lines (~388 K), and mixed with the propylene gas feed that bypassed the reactor before the gas stream was introduced to the reactor in a configuration described above.

4.2.5. Powder X-Ray Diffraction (PXRD)[10]

PXRD patterns were collected over a 2θ range of 5-50° at 0.01° resolution with a Smartlab SE (Rigaku) diffractometer with Cu-Kα radiation (λ=1.54414 Å).

4.2.6. N_2 Isotherms

Nitrogen adsorption isotherms were measured at 77 K using an ASAP 2020 surface area and porosity analyzer (Micromeritics) after removing water by degassing the samples at <150 Pa at 333 K for one hour and then 423 K or 493 K for four hours. Surface areas were determined by fitting a Langmuir isotherm between P/P_0 values of 0.05 and 0.30.

[10] PXRD was collected by Xinyu Li at the Characterization Facility at the University of Minnesota.

4.2.7. ^{1}H NMR Spectroscopy

The MOF samples (~20 mg) and organic linker (~5 mg) were dissolved with a ~600 mm^3 solution of 1 M NH_4OH (ACS) in D_2O (Cambridge Isotope Laboratories) in 7-inch nuclear magnetic resonance (NMR) sample tubes (Wilmad). The resulting mixture was inverted three times before a 100 mm^3 acetonitrile (ACS) internal standard was added to the sample tube. The resulting mixture was inverted three more times and left overnight. ^{1}H NMR spectra were recorded using a Bruker Avance III HD Nanobay AX-400 (400 MHz) with a relaxation delay of 20 seconds and 32 scans.

4.2.8. Scanning electron microscopy-energy-dispersive X-ray spectroscopy (SEM-EDS)[11]

Ni-MIL-127 samples were prepared via mounting on a stub with conductive carbon tape, then coating with a thin (5 nm) layer of carbon by evaporative deposition under vacuum to engender sample conductivity. Samples were analyzed using a JEOL-6500.

4.2.9. Infrared (IR) Spectroscopy

Wafers of MOF samples for IR spectroscopy were pressed (<1.4 MPa) and placed in a quartz IR cell with KBr (Sigma-Aldrich) windows. Spectra from 400-4000 cm^{-1} at a resolution of 2 cm^{-1} with an average of 32 scans were measured with a Nicolet 6700 spectrometer. The IR spectra were taken after the IR cell was heated from ambient temperature to 493 K (0.067 K s^{-1}) in flowing helium (Matheson, 99.997%) and held for 4 hours at 493 K. After 4 hours, the helium flow was switched to propylene flow (Matheson, 99.83%) for 2 days. Vacuum (<3 Pa) was pulled on the sample and the spectra were collected.

4.2.10. Low temperature IR spectroscopy

Wafers of MOF samples were pressed (<1.4 MPa) and were encapsulated around gold foil (Beantown Chemical, 0.1 mm). The foil was cut with a slit so the IR beam can pass through the sample. The sample was placed into a custom-made IR cell (Disa Milano) and was under vacuum (<3 Pa) for four hours. Spectra from 400-4000 cm^{-1} at a resolution of 2 cm^{-1} with an average of 32 scans were measured with a Nicolet 6700 spectrometer.

[11] SEM-EDS was collected by Brian Bayer at the Characterization Facility at the University of Minnesota.

After degassing, the cell was cooled with liquid nitrogen (77 K). Nitric oxide (Matheson, CP Grade) was dosed from a 23.71 cm^3 dosing volume after the pressure stabilized after each dose, and the pressure was monitored with a pressure transducer (Kurt J. Lesker).

4.2.11. Temperature Programmed Oxidation (TPO)

Powder samples (2-7 mg) were loaded in tubular reactor described above. The as synthesized samples were heated (0.05 K s^{-1}) from ambient temperature to 873 K, while the activated material was treated in helium (Matheson, 99.999%, 0.17 cm^3 s^{-1}) for four hours at 493 K before allowing the material to cool to 323 K before the temperature was increased (0.05 K s^{-1}) to 823 K. While the temperature was increased during the TPO experiment, the reactant stream was a mixture of oxygen (Matheson, 99.999%, 0.17 cm^3 s^{-1}), helium (Matheson, 99.997%, 0.83 cm^3 s^{-1}), and argon (Matheson, 99.999%, 0.17 cm^3 s^{-1}, internal standard). The effluent stream composition was determined using an online mass spectrometer (MKS Cirrus 2) with signals from the mass spectra for oxygen, argon, and carbon dioxide assigned m/z values of 32, 40, and 44, respectively.

4.2.12. ^{57}Fe Mössbauer spectroscopy[12]

Powder samples (~20 mg) of Ni-MIL-127 as synthesized and after thermal activation in helium (Matheson, 99.997%, 0.83 cm^3 s^{-1}, 493 K for four hours) were diluted with Spectroblend and pressed between two Delcron cups (12.7 mm in diameter and 10 mm deep). ^{57}Fe Mössbauer spectra were collected at 25 K with liquid helium with a MS4 Mössbauer spectrometer (SEE Co.) equipped with a Janis closed-cycle refrigerator.

4.2.13. X-Ray Absorption (XAS) Spectroscopy[13]

All XAS spectra were collected at beamline 4-1 at Stanford Synchrotron Radiation Light source (SSRL). All experiments were carried out in transmission mode and with a water cooled double-crystal monochromator with Si (220) crystals. Six inch long, nitrogen-filled, ion chambers, operated with an 1800 VDC bias, were used to measure the relative intensity of the X-ray beam before and after the sample, and before and after the reference

[12] Mössbauer spectra were collected and analyzed by Peter Solheid at the Institute of Rock Magnetism at the University of Minnesota.
[13] XAS spectra were collected in collaboration with Adam Hoffman, Jiyun Hong, Jorge Perez-Aguilar, and Simon R. Bare at SSRL.

foil. A Ni and Fe foil located downbeam of the sample was used as an internal reference to calibrate the photon energy of each spectrum. For the *in-situ* measurements the as synthesized Ni-MIL-127 was diluted with SiO_2 in a 1:1 ratio by mass to obtain a total absorption length of 2.5, determined at 50 eV above the Ni and Fe K-edge. The sample (~4 mg mixed) was loaded in an *in-situ* XAS cell[134] forming an approximately 1 cm long catalyst bed located in between two quartz wool plugs inside the 1 mm OD, 0.96 mm ID, quartz capillary.

Extended X-ray absorption fine structure (EXAFS) spectra at the Ni-K edge (8333 eV) and Fe-K edge (7112 eV) were collected for the as-synthesized sample in helium (0.25 $cm^3\ s^{-1}$) at 309 K. X-ray absorption near edge structure (XANES) spectra were collected while the temperature was ramped at 0.05 K s^{-1} until 513 K and held for 4 hours where EXAFS spectra for the Ni-K edge and Fe-K edge were obtained. Propylene (0.14 $cm^3\ s^{-1}$) was introduced to the sample while the helium flow was set at 0.02 $cm^3\ s^{-1}$ while XANES spectra were continuously being collected. After ~12 hours, EXAFS spectra for the Ni-K and Fe-K edge were obtained, where the catalyst was assumed to be at steady state (Figure 4.11a). Each XANES and EXAFS spectrum took approximately 5 and 15 minutes, respectively, to collect.

The XAS data were processed using ATHENA, as part of the XAFS software package,[153] to remove the background from the $\chi(k)$ oscillations. Four EXAFS spectra were merged to improve signal to noise. The spectra for Ni-MIL-127 were calibrated and aligned to the largest inflection point of the first derivative of the spectra for the nickel reference foil (8333 eV). The Fourier transform of the k-space EXAFS data were fit to X-ray determined structures using Artemis. For the fitting, NiO was used as the crystallographic models.[154] The single scattering Ni-O path in NiO, which had a rank of 100, was used to fit the coordination of first coordination shell in Ni-MIL-127. The amplitude reduction factor, S_0^2, (0.77 ± 0.02) was fit by determining the amplitude factor for the reference nickel foil and multiplying the amplitude factor by a fitted Ni-O coordination number. The fits to the Ni K-edge EXAFS $\chi(k)$ data were weighted by k^2 and windowed between 3.0 $Å^{-1}$ < k < 13.0 $Å^{-1}$ using a Hanning window with dk = 1.0 $Å^{-1}$ and in r between 1.0 Å < r < 2.8 Å.

4.2.14. Cluster Models of Ni-MIL-127 and Kohn-Sham Density Functional Theory (DFT) Calculations[14]

A cluster model encompassing a single $Ni(II)Fe(III)_2O(COO)_6$ node of Ni-MIL-127 from Barona *et al.*[155] was employed for investigating the favorability for linker decarboxylation and the Cossee-Arlman reaction mechanism for propylene oligomerization. The ABTC linkers of Ni-MIL-127 were truncated with benzene rings (*Model I*, see Figure 4.34) for modeling the proposed linker decarboxylation upon thermal activation of the sample. A cluster model where the ABTC linkers were further truncated as formate groups (*Model II,* see Figure 4.34) was used to investigate the Cossee-Arlman mechanism for propylene oligomerization. The *para* C of the benzene rings in *Model I* and the C atom of the formate groups in *Model II* were spatially frozen during all DFT optimizations to mimic the structural rigidity of the framework while all other atoms were relaxed. Note that frequency calculations for a molecule in *Gaussian* include the translational and rotational contributions to the free energy which is correct for gas phase molecules. However, since the MOF is a crystalline material which does not rotate or translate, translational and rotational contributions should not be included in the free energy calculated for the intermediates (or TS) of the MOF. However, since the translational and rotational partition functions depend on the mass of the full MOF cluster model, which is much larger than the mass of the reactants and products, the contributions to the free energies due to the translational and rotational partition functions of the MOF are expected to be cancelled in the computed relative energies between the optimized intermediate (or TS) and the reference node MOF structure, thus accounting for the translational and rotational contributions to the calculated free energy otherwise included a Gaussian calculation

Kohn-Sham density functional theory (KS-DFT) calculations were performed on the cluster models described above in the *Gaussian 16* software package[99] using the M06-L[98]exchange-correlation density functional. The def2TZVP[100,101] basis was used for the Ni, Fe, and O atoms while the def2SVP basis set was used for the C and H atoms. Vibrational

[14] DFT calculations were performed by Saumil Chheda at the Minnesota Supercomputing Institute at the University of Minnesota.

frequency calculations for the optimized cluster models were performed to determine the nature of the intermediate and transition state (TS), and to calculate the zero-point energies and thermal corrections to enthalpies and free energies at 493 K (unless otherwise specified) and 101.3 kPa. All intermediates had all real vibrational frequencies while the transition states had one imaginary frequency corresponding to the reaction coordinate. Vibrational frequencies below 50 cm^{-1} were corrected to 50 cm^{-1} to account for anharmonicity.[108,156] Since Ni^{2+} (E.C. = $[Ar]3d^8$) and Fe^{3+} (E.C. = $[Ar]3d^5$) have 8 and 5 valence electrons respectively, the overall spin state of a single node can vary from $2S + 1 = 1$ (zero unpaired electrons) to $2S + 1 = 13$ (12 unpaired electrons). The $2S + 1 = 11$ spin state was found to be most stable along the reaction coordinate with negligible spin contamination ($|S^2$ deviation$| < 0.01$) while the electronic energy generally increased upon decreasing $2S + 1$ spin state. Thus, the reported energy diagrams correspond to $2S + 1 = 11$ spin state unless otherwise specified. For intermediates in which propylene or product hexene are adsorbed on Ni-H species as well as transition states for their corresponding hydride insertion step and β-hydride elimination step in Figure 4.29-4.32, stable optimized geometries could not be isolated in the $2S + 1 = 11$ spin state in some cases. In such instances, the electronic energies for such intermediates and transition states in the $2S + 1 = 11$ spin state were obtained from single point energy calculations on stable optimized geometry of the $2S + 1 = 13$ spin state. The spin state having the lowest electronic energy is reported as the ground state. The spin states for the lowest electronic energy structures and the calculated absolute and relative zero-point energies (ZPE), electronic energies (E), enthalpies (H), and free energies (G) for all the DFT-optimized structures are tabulated in Section S8.

The thermodynamic energies for the intermediates and TS along the reaction mechanism are referenced to bare Ni-H species (intermediate A) and isolated gas phase propylene molecules (Equation 4.1).

$$\Delta Y_{\mathrm{int/TS}}\,(Y = E, H, G) = Y_{\mathrm{int/TS}} - Y_{\mathrm{A}} - \left(n_{\mathrm{ads}} Y_{\mathrm{gas}}\right)_{\mathrm{propylene}} \qquad \text{Eq. 4.1}$$

where $Y_{\mathrm{int/TS}}$, Y_{A}, and $Y_{\mathrm{gas,propylene}}$ are the absolute energies of the intermediate or TS, vacant Ni-H species, and isolated propylene molecules in the gas phase. $n_{\mathrm{ads,propylene}}$ are the number of propylene molecules adsorbed in the intermediate or TS, respectively.

4.3. Results and Discussion

Ni-MIL-127 is a mixed metal MOF consisting of [$Fe_2Ni(\mu_3\text{-}O)$] nodes and 3,3′,5,5′-azobenzenetetracarboxylate (ABTC) linkers (Figure 4.1a).[152,157] Powder X-ray diffraction (PXRD) and nitrogen isotherms, shown in Figures 4.1b and 4.1c respectively, were used to confirm the crystallinity and porosity of the as synthesized material. The pore size distribution is presented Figure 4.2a to demonstrate that mesopores and missing cluster vacancies are not created upon thermal treatment.[158] The average pore size based on the BJH desorption isotherm is 1.73 nm and 1.76 nm for the as synthesized and thermally treated samples, respectively. The IR spectra for Ni-MIL-127 as synthesized and after thermal activation in Figure 4.2b to show that the structural integrity of the MOF is unchanged with heating in flowing helium (0.05 K s^{-1} to 493 K for 4 hours) as denoted by bands between 1300-1700 cm^{-1} which correspond to the ABTC linker.[90,159] Mössbauer spectra (Figure 4.2c) and fitting parameters (Table 4.1) acquired at 25 K affirm that the iron species are Fe(III) in as synthesized samples. Scanning electron microscopy – energy dispersive spectroscopy (SEM-EDS) was conducted to determine the nickel to iron ratio was 1 : 2.7 (Figure 4.2d, Table 4.2, and Equation 4.2) assuming 100 grams of Ni-MIL-127 per EDS map.

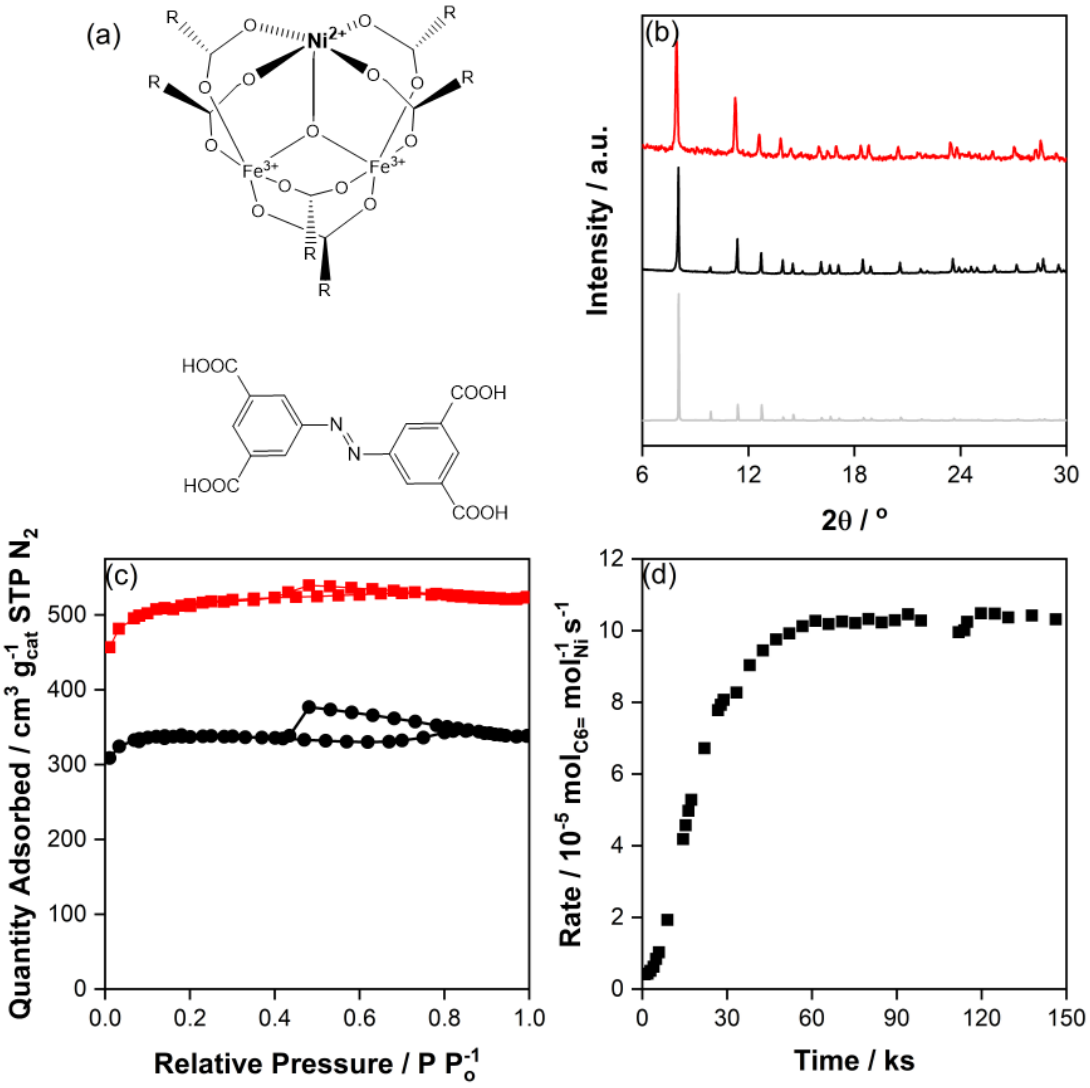

Figure 4.1. (a) Modular building blocks for Ni-MIL-127 consisting of [$Fe_2Ni(\mu_3\text{-}O)$] nodes and 3,3′,5,5′-azobenzenetetracarboxylate (ABTC) linkers. (b) PXRD for computed (grey), as synthesized (black), and thermally treated (red) structures of Ni-MIL-127 and (c) N_2 isotherms for Ni-MIL-127 as synthesized (black) and after thermal treatment (red). (d) Time on stream for propylene oligomerization at 0.83 $cm^3\ s^{-1}$ propylene at 500 kPa and 473 K on 26.3 mg Ni-MIL-127

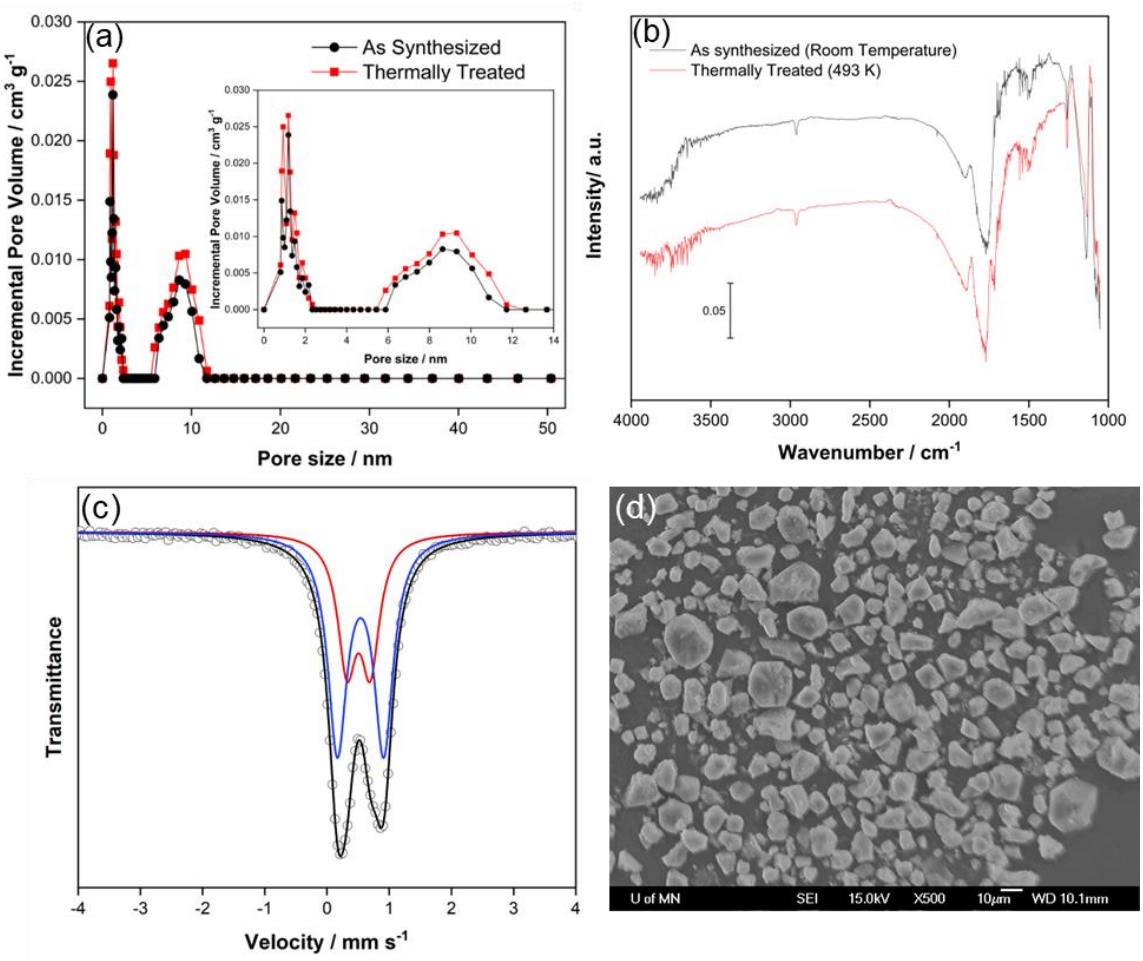

Figure 4.2. (a) Pore size distribution of Ni-MIL-127 as synthesized (black) and after thermal treatment at 493 K (red), (b) IR spectra for as-synthesized and thermally treated Ni-MIL-127 after 4 hours in flowing helium at 493 K, (c) Raw data (○) ^{57}Fe Mössbauer spectra for as synthesized Ni-MIL-127 the fit to the raw data (black) with the Fe(III) fitted doublets (blue and red), and (d) SEM image of as synthesized Ni-MIL-127

Table 4.1. Tabulated values for the isomer shift, quadrupole splitting, and line widths by deconvoluting the Mössbauer spectra for as synthesized Ni-MIL-127 into Lorentzian doublets

Species	**Isomer Shift (δ) / mm s^{-1}**	**Quadrupole Splitting (ΔE_Q) / mm s^{-1}**	**Width / mm s^{-1}**
Doublet 1 (red)	0.51	0.38	0.36
Doublet 2 (blue)	0.54	0.74	0.37

Table 4.2. Weight percentages of Ni, Fe, and O for Ni-MIL-127 MOF as synthesized as determined by energy-dispersive X-ray spectroscopy

Atom	Region 1 / weight %	Region 2 / weight %	Region 3 / weight %	Average / weight %
Ni	13.22	13.63	13.64	13.50
Fe	34.44	34.88	35.34	34.89
O	50.92	50.01	49.71	50.21

$$\frac{\left(\frac{13.50\ g\ Ni}{100\ g\ MOF}\right) * \left(\frac{1\ mol\ Ni}{58.69\ g\ Ni}\right)}{\left(\frac{50.21\ g\ Fe}{100\ g\ MOF}\right) * \left(\frac{1\ mol\ Fe}{55.685\ g\ Fe}\right)} = \left(\frac{1\ mol\ Ni}{2.7\ mol\ Fe}\right) \quad \text{Eq. 4.2}$$

4.3.1. Reactivity, Structure, and Active Sites of Ni-MIL-127 for Propylene Oligomerization

After thermally activating Ni-MIL-127 in 0.83 $cm^3\ s^{-1}$ of helium at 493 K (0.05 K s^{-1}) for 4 hours, the catalytic behavior of the material was examined for propylene oligomerization in 0.83 $cm^3\ s^{-1}$ propylene at 500 kPa and 473 K in the absence of activators, as shown in Figure 4.1d. As a reference, the pure iron trimer MIL-127 material was tested for propylene oligomerization at the same process conditions to reveal hexene formation rates three orders of magnitude lower than Ni-MIL-127, as shown in Figure 4.3. Similar to other olefin oligomerization systems on heterogeneous catalysts devoid of cocatalysts and activators, an induction period (~60 ks) is observed[35,129] on Ni-MIL-127 and has been attributed to the formation of the catalytically relevant surface species for oligomerization.[32,40,41,76] We note that Ni-MIL-127 is stable for propylene oligomerization after the induction period for another ~60 ks, which is unprecedented for propylene oligomerization on heterogeneous catalysts at elevated temperatures and pressures. Stable propylene oligomerization rates were obtained on Ni-Al-MCM-41 but at sub-ambient temperatures.[45] Prior work on Ni-Na-X shows stable propylene oligomerization rates after the catalyst is activated in 500 kPa of propylene at 493 K and the temperature is subsequently decreased to 393-453 K; however, the catalyst deactivates at 453 K and 493 K without prior activation.[35] The Ni-MIL-127 system for propylene oligomerization

reported herein showcases a Ni-based catalyst that is stable at elevated temperatures without prior exposure to propylene. Our disquisition demonstrates how framework atoms in Ni-MIL-127 enable site isolation and provide opportunities to tailor unique coordination and electronic environments to enhance oligomerization reactivity. As reference a comparison of heterogeneous nickel catalysts for propylene oligomerization and their respective turnover frequencies and linear hexene selectivities are reported in Table 4.3.

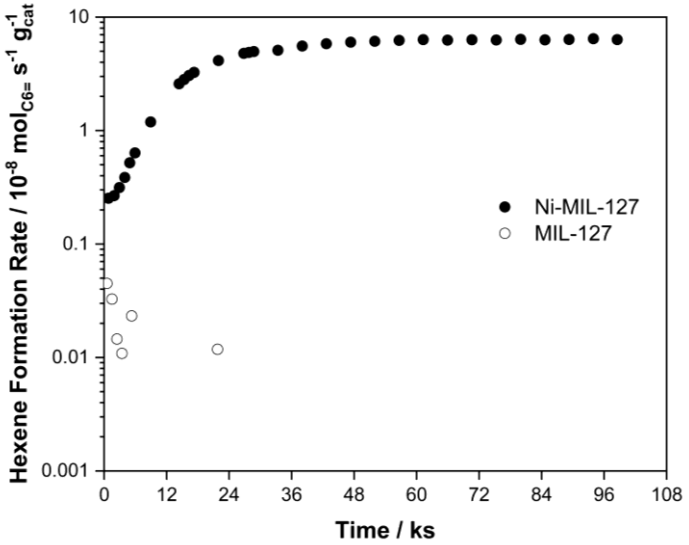

Figure 4.3. Time on stream for propylene oligomerization on 25.0 mg Ni-MIL-127 (●) and 28.9 mg MIL-127 (○) at 500 kPa, 473 K, and 0.83 cm^3 s^{-1} of propylene.

Table 4.3. Turnover frequencies and linear hexene selectivity on various nickel-based heterogeneous catalysts for propylene oligomerization

Material	Pressure / kPa	Temperature / K	TOF / $mol_{C6=}$ mol_{Ni}^{-1} h^{-1}	Linear Hexene Selectivity / %	Phase	Reference
Ni-MFU-4l	600	294	460	26	Liquid	[51]
Ni-MOF-74	500	453	0.04	38	Gas	[72]
Ni_2(dobpdc)	500	453	0.01	37	Gas	[72]
Ni-MIL-127	500	473	0.6	47	Gas	This work
Ni-Li-X	500	453	50	45	Gas	[36]
Ni-Na-X	500	453	30	53	Gas	[35,72]
Ni-K-X	500	453	6	59	Gas	[36]
Ni-Mg-X	500	453	15	41	Gas	[36]
Ni-Ca-X	500	453	20	45	Gas	[36]
Ni-Sr-X	500	453	50	31	Gas	[36]
Ni-Na-MCM-41	500	453	260	51[a]	Gas	[43]
Ni-Al-MCM-41	230	248	1200	20	Liquid	[45]

[a] The linear hexene selectivity is reported at 101.3 kPa and 453 K

Olefin oligomerization on heterogeneous nickel catalysts requires an open coordination site to bind a gas phase olefin molecule, as has been noted for Ni-Na-X[35] and Ni-SSZ-24[40] for propylene and ethylene oligomerization, respectively.[46] We sought to explain the reactivity of Ni-MIL-127 for propylene oligomerization as Ni-MIL-127 appears to be fully coordinated with four ABTC linkers, a bridging oxo species, and an aqua ligand.[152,160] Prior work on PCN-250/MIL-127 and their bimetallic analogs has shown that these materials undergo decarboxylation to open a coordination site on Fe(II) or M(II) as evinced by thermogravimetric analysis-mass spectrometry (TGA-MS) after thermal treatment.[143,160] These studies focused on nature of the iron species, determined by ^{57}Fe Mössbauer and Fe K-edge XAS but do not investigate the nature of M(II) species.[143,160] Because nickel is the active species for propylene oligomerization as opposed to iron (Figure 4.3), we sought to quantify the number of missing linkers in both as synthesized and thermally treated (493 K in 0.83 cm^3 s^{-1} helium for 4 hours) samples to determine the fraction of missing linkers on these samples, and the effect they have on nickel active sites for propylene oligomerization.

Temperature programmed oxidation (TPO) enumerates the number of ABTC linkers in as synthesized and thermally treated samples by quantifying carbon dioxide from the combustion of the ABTC linker. The materials were heated at 0.05 K s^{-1} starting from 423 K in 0.83 cm^3 s^{-1} He, 0.17 cm^3 s^{-1} Ar, and 0.17 cm^3 s^{-1} O_2 until 723 K. The thermally treated sample (493 K in 0.83 cm^3 s^{-1} for 4 hours) was cooled to 423 K before ramping the temperature at 0.05 K s^{-1}. As depicted in Figure 4.4a, carbon dioxide is observed at temperatures >523 K, consistent with the thermal stability of MIL-127 type materials.[90] The amount of CO_2 can be quantified by integration of the flow rate of CO_2 over the time duration when CO_2 is observed in the effluent and this amount of CO_2 can be normalized by the mass of the material to determine 28.7 ± 3.7 mmol g_{cat}^{-1} and 22.4 ± 4.0 mmol g_{cat}^{-1} of CO_2 evolved for the as synthesized and thermally treated samples, respectively. Based on the stoichiometry of the ABTC linker, there are 16 carbon atoms per organic linker, there are 1.79 ± 0.23 and 1.40 ± 0.25 mmol g_{cat}^{-1} of organic linkers in as synthesized and

thermally treated samples, respectively. From TPO, ~22% of linkers are lost upon thermal treatment.

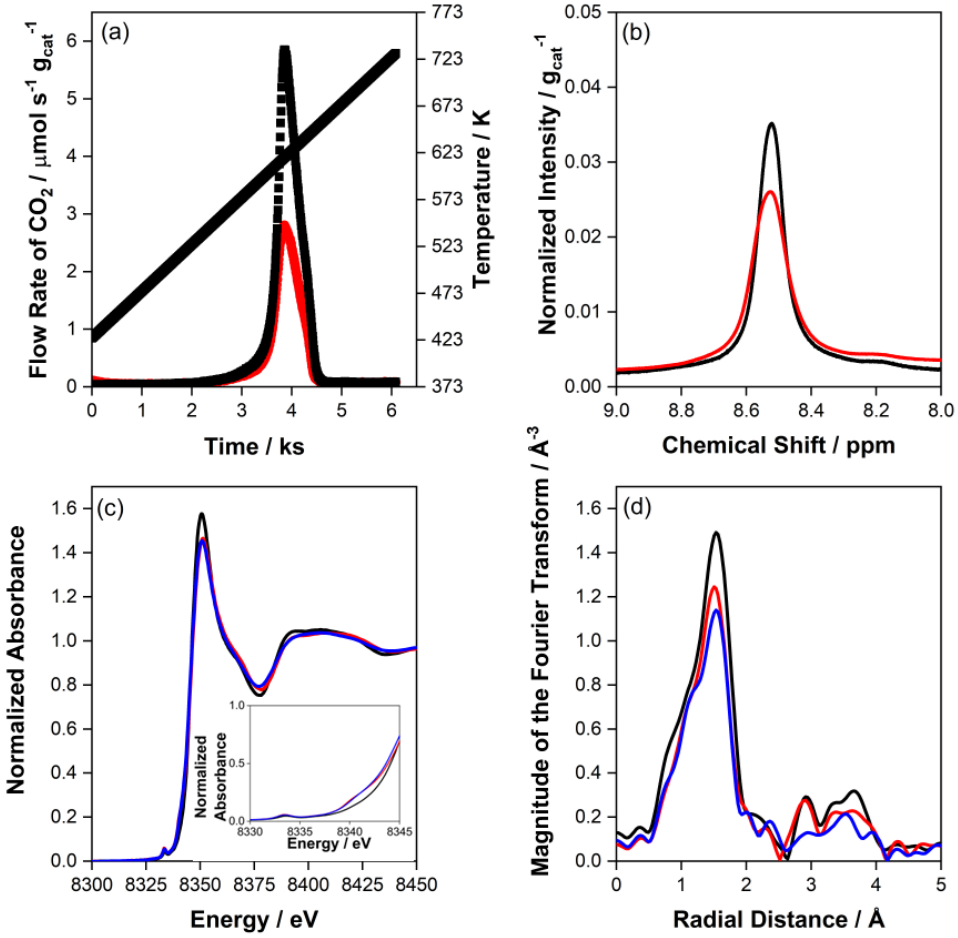

Figure 4.4. (a) TPO profile of 4.6 mg of as synthesized (black) and 3.7 mg of thermally activated (red, 493 K for 4 hours in 0.83 cm^3 s^{-1} of He) Ni-MIL-127 outlining the evolution of normalized amount of CO_2 with the temperature ramped at 0.05 K s^{-1} in 0.83 cm^3 s^{-1} He, 0.17 cm^3 s^{-1} Ar, and 0.17 cm^3 s^{-1} O_2. (b) ^{1}H NMR spectra for 23.2 mg of as synthesized (black) and 17.2 mg of thermally activated (red, 493 K for 4 hours in 0.83 cm^3 s^{-1} of He) Ni-MIL-127 in 1 M NH_4OH/D_2O normalized to 100 μL of acetonitrile. (c) Ni K-edge XANES, with inset showing the pre-edge peaks, and (d) EXAFS data (magnitude of the Fourier transform (k^2-weight)) in the k range of 3.0 $Å^{-1}$ < k < 13.0 $Å^{-1}$ for Ni-MIL-127 as synthesized (black), thermally activated (513 K in 0.25 cm^3 s^{-1} helium, red), at steady state (ambient pressure of 0.14 cm^3 s^{-1} propylene at 513 K after 10 hours, blue).

In conjunction with TPO, we show in Figure 4.4b the ^{1}H nuclear magnetic resonance (NMR) spectra for the digested as synthesized (black) and thermally treated

(red) Ni-MIL-127 in a 1 M solution of NH_4OH/D_2O with 100 μL of acetonitrile as the internal standard. The ABTC linker (8.53 ppm) intensities are normalized by the amount of Ni-MIL-127 and intensity of the internal standard. The chemical shift for the ABTC linker was verified using the pure linker dissolved in NH_4OH/D_2O (Figure 4.15). After integration of the NMR peaks, the number of organic linkers in the as-synthesized Ni-MIL-127 was 2.14 mmol g_{cat}^{-1} while the thermally treated sample was 1.69 mmol g_{cat}^{-1}. This indicates that ~22% of the linkers are lost upon thermal treatment, consistent with our observations from TPO. We attribute a lower absolute value of linkers determined by TPO compared to ^{1}H NMR to plausible incomplete combustion of the ABTC linker, where aromatic fragments (m/z = 78) are observed (Figure 4.17). The TPO data reported in Figure 4.4a and Figure 4.16 for as synthesized and thermally activated Ni-MIL-127 species do not have observable aromatic fragments, but we cannot eliminate the possibility of aromatic fragments being formed during TPO due to incomplete combustion of Ni-MIL-127. Nevertheless, a decrease in carbon content and ABTC linkers of 22% is observed from TPO and ^{1}H NMR, respectively, to suggest linkers are removed from the MOF during thermal treatment.

The stability of the material with incorporation of defects can be verified with PXRD, N_2 isotherms and pore size distributions, and IR spectroscopy (Figure 4.1b, 4.1c, 4.2a, and 4.2b respectively), where the crystallinity, porosity, structural integrity is unchanged.[65,161] After degassing the sample at 393 K and 493 K for 4 hours in vacuum (<100 Pa), a BET surface area of 1003 $m^2 g^{-1}$ and 1551 $m^2 g^{-1}$, respectively, was observed (Table 4.4). This increase in surface area is proposed to be positively correlated with defectivity in MOF materials as seen in UiO-66 and MOF-74 and is consistent with our observations that missing linker defects are engendered upon thermal treatment.[67,162]

Table 4.4. BET surface areas and micropore volumes for Ni-MIL-127 at different temperatures

Sample	BET Surface Area / $m^2 g^{-1}$	Micropore Volume / $cm^3 g^{-1}$
Ni-MIL-127 degassed at 393 K	1003	0.52
Ni-MIL-127 degassed at 493 K	1551	0.69

X-ray absorption spectroscopy (XAS) was used to explore the effect of missing linker defects on the nickel active sites on Ni-MIL-127. Comparing the X-ray absorption near edge structure (XANES) data between the as synthesized and thermally treated sample at 513 K in helium (Figure 4.4c), minimal changes in the absorption edge energies are observed, but variations in the XANES spectra for the as synthesized and thermally treated samples show an increase in the pre-edge shoulder at 8440 eV, a decrease in the white line intensity, and subtle changes in the post-edge XANES spectra for the thermally treated samples. The latter corresponds to changes in the extended X-ray absorption fine structure (EXAFS) spectra for the two states, where a decrease in the amplitude of the oscillations in the EXAFS spectra (Figure 4.5g) and a decrease in the overall magnitude of the first scattering contribution in the Fourier transform of the EXAFS spectrum (Figure 4.4d) is observed when comparing the transformation between the as synthesized and thermally treated samples. The pre-edge feature at 8440 eV (inset of Figure 4.4c) in the thermally treated sample is attributed to a 1s to $4p_z$ transition consistent with 5-coordinate square pyramidal configuration of Ni which arises due to symmetry reduction and a decrease in the inversion center symmetry.[163–165] From EXAFS fitting (Figure 4.5) of the first coordination shell in Figure 4.4d to a NiO species, a decrease in the Ni-O coordination from 6.0 to 5.3 for the as synthesized and thermally treated samples (Table 4.5), respectively, is determined, which suggests an increase in the number of uncoordinated nickel species in the thermally treated samples. This decrease in Ni-O coordination is consistent with the formation of the 5-coordinate signature at 8440 eV (inset of Figure 4.4c). The decrease in the white line intensity and amplitude of the oscillations in the post-edge XANES spectrum are likely due to removal of the ABTC ligands. These XAS results corroborate a decrease in nickel coordination to generate an open coordination site through a missing linker defect, as shown from TPO and ^{1}H NMR results, to facilitate propylene oligomerization on Ni-MIL-127.

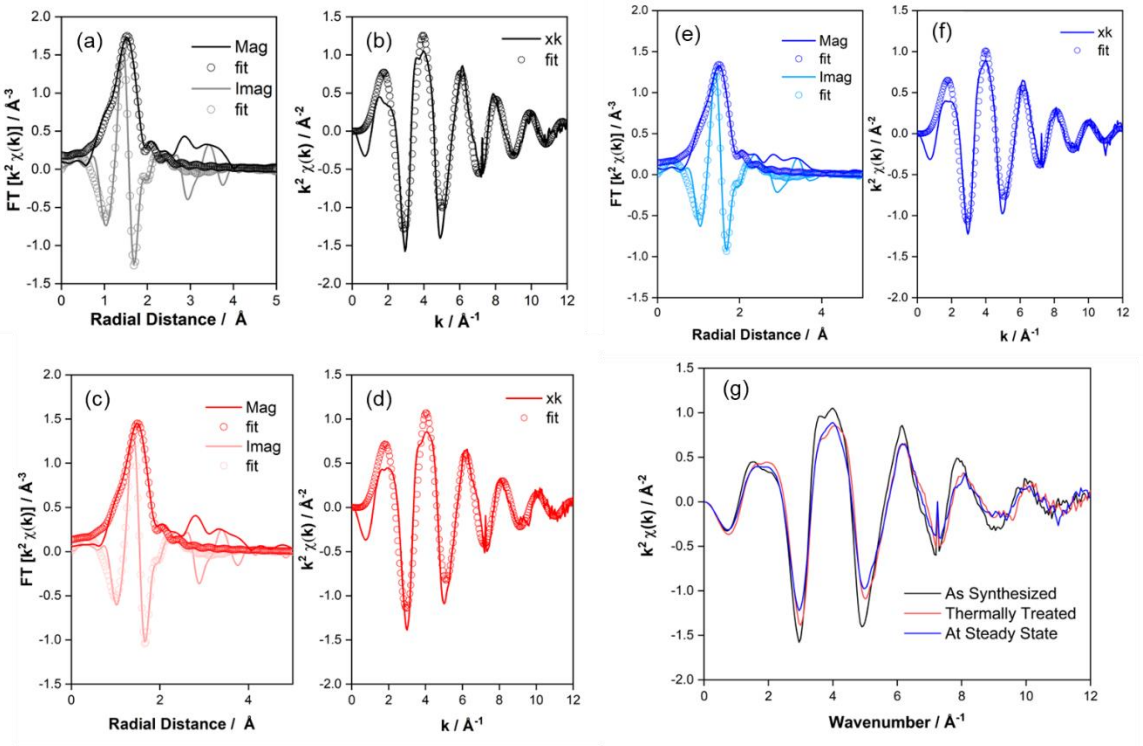

Figure 4.5. k^2-weighted Ni K-edge (a, c, e) Magχ(R) and Imgχ(R) spectra, and (b, d, f) xk plots of as synthesized Ni-MIL-127 (black), thermally treated Ni-MIL-127 at 513 K in 0.16 $cm^3\ s^{-1}$ He (red), and at steady state in at 513 K 0.14 $cm^3\ s^{-1}$ C_3H_6 (blue), respectively, and the corresponding FEFF fits. (g) EXAFS data for Ni-MIL-127 as synthesized (black), thermally activated (513 K in 0.25 $cm^3\ s^{-1}$ helium, red), at steady state (ambient pressure of 0.17 $cm^3\ s^{-1}$ propylene at 513 K after 10 hours, blue)

Table 4.5. Summary of EXAFS fitting parameters for the Ni-O bond in NiO for Ni-MIL-127 at various conditions

Condition	Ni-O Coordination Number	Interatomic distances / Å	σ^2 / 10^{-3} Å^2
As Synthesized (black)	6.0 ± 0.6	2.02 ± 0.01	5.8 ± 1.7
Thermally Treated (red)	5.3 ± 0.7	1.99 ± 0.01	7.2 ± 1.9
At Steady State (blue)	5.2 ± 0.6	2.00 ± 0.01	7.7 ± 2.2

Our goal was to determine the structure of the as synthesized and thermally treated Ni-MIL-127 materials from TPO, ^{1}H NMR, and XAS. We examined the plausibility of the formation of the activated material using density functional theory (DFT) on cluster models with benzene-capped linkers of Ni-MIL-127 as opposed to those with formate-capped

linkers proposed by Barona et al.[155] We propose that the as-synthesized Ni-MIL-127 structure contains four ABTC linkers, one bridging oxo species, and one water molecule as determined from our fitted EXAFS data (Figure 4.6). Based upon our analysis of the material upon thermal treatment where a missing linker defect is generated as shown by TPO and ^{1}H NMR (Figures 4.4a and 4.4b), and no change in formal charge of the nickel is noted from XANES spectra (Figure 4.4c), we surmise that upon thermal treatment, nickel is bound to three ABTC linkers, a bridging oxo species, and an OH^- ligand to maintain the oxidation state of nickel (Figure 4.6). Additionally, from our Fe XANES (Figure 4.7a), the value of the inflection point of the rising edge energy, which has been proposed to correspond with number of Fe species of different oxidation states,[166] at 7125.6 eV (Figure 4.7b) does not change between as synthesized and thermally activated materials. Based on the Fe oxidation state for the as synthesized Ni-MIL-127 from Mössbauer (Figure 4.2c), this suggests that the Fe oxidation state remains as Fe(III) in as synthesized and thermally treated samples. We postulate that because the oxidation state of the Fe atoms remains unchanged as Fe(III) and the nickel atoms remain as Ni(II) after thermal treatment, the missing linker that is generated requires the formation of a hydroxyl species to maintain charge neutrality. Using DFT, the generation of this missing linker defect and the unsaturated Ni-MIL-127 species yields a change in free energy of 82 kJ mol^{-1} at 298 K with respect to the as synthesized Ni-MIL-127 material. However, at the pretreatment temperature at 493 K, the change in free energy to generate the missing linker defect is 25 kJ mol^{-1}. This decrease in free energy is consistent with our observations that it is more favorable to form missing linker defects at higher temperatures.

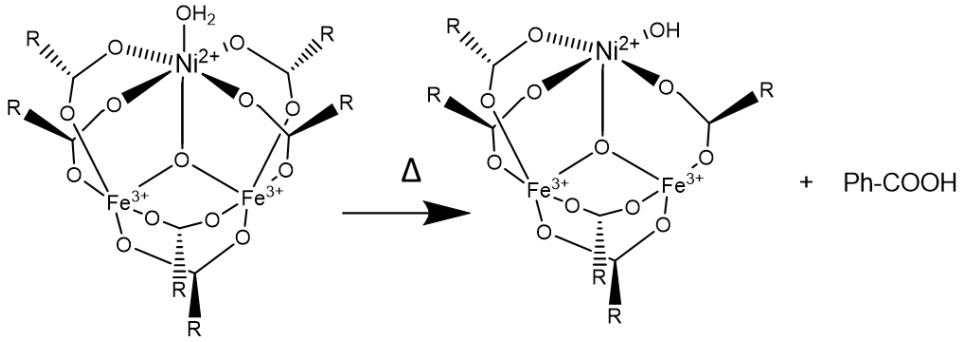

Figure 4.6. Schematic for the proposed Ni-MIL-127 structures upon thermal treatment in helium, where Ph-COOH is an ABTC linker

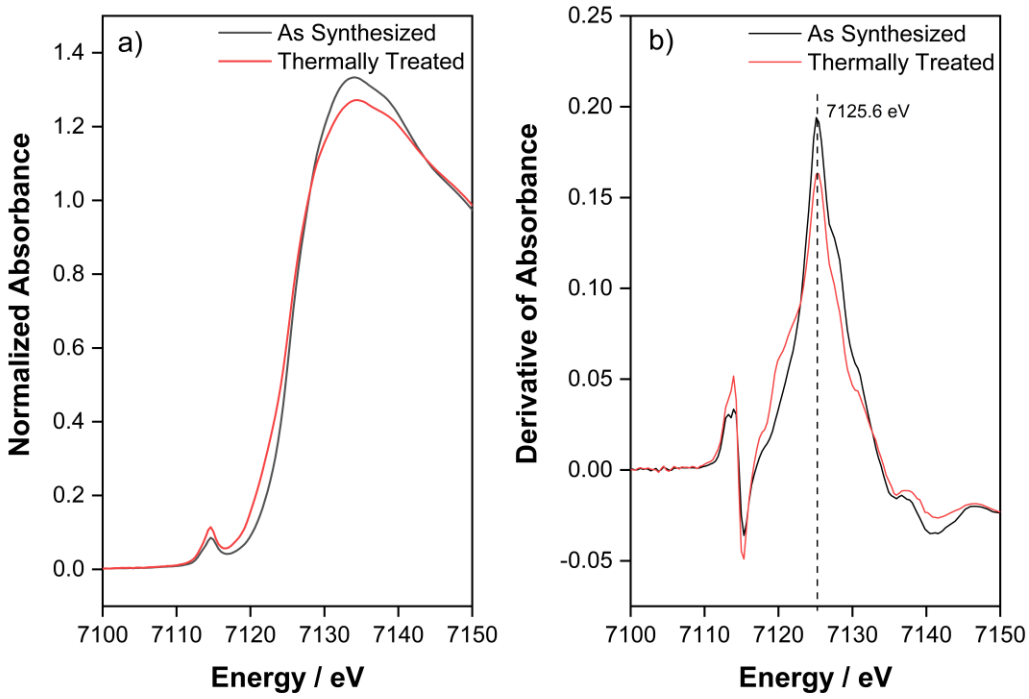

Figure 4.7. (a) Fe K-edge XANES and (b) the first derivative of normalized absorbance for Ni-MIL-127 as synthesized (black), thermally activated (513 K in 0.25 cm^3 s^{-1} helium, red).

The effect of missing linker defects, which engender a coordinately unsaturated nickel site for propylene oligomerization reactivity on Ni-MIL-127, was evaluated by running propylene oligomerization at 433 K and 500 kPa of 0.83 cm^3 s^{-1} of propylene before and after thermal activation in helium at 493 K in 0.83 cm^3 s^{-1}, as shown in Figure 4.8. Without prior thermal activation, propylene oligomerization rates decrease with time

on stream. After thermally treating Ni-MIL-127 at 493 K, a ~4× enhancement in rate is observed at the same reaction conditions, and the catalyst maintains stable propylene oligomerization rates. Thus, we surmise that these missing linker defects are necessary for olefin oligomerization stability in MOFs, as previous work for ethylene and butene dimerization on Ni/UiO-66, a MOF with inherent missing linker defects show stable oligomerization rates,[76,129] while Ni-MOF-74, a MOF that does not have missing linker defects, deactivates with time on stream for propylene oligomerization.[72,163] The stability of Ni-MIL-127 for propylene oligomerization is unique and allows us to probe and enumerate the relevant active sites, measure steady state kinetics and product selectivities, and scrutinize reaction mechanisms for propylene oligomerization.

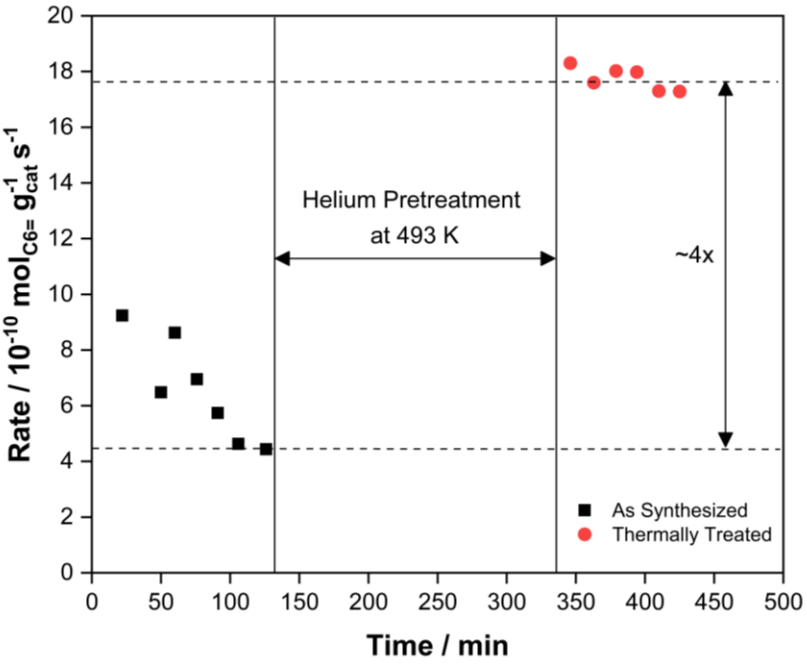

Figure 4.8. Propylene oligomerization rates at 500 kPa and 413 K in 0.83 cm^3 s^{-1} on 21.8 mg of Ni-MIL-127 before and after helium pretreatment at 493 K.

Accessible nickel sites on Ni-MIL-127, generated upon removing linkers, that catalyze propylene oligomerization were enumerated using NO titrations ex-situ and in-situ. The upper bound estimate of nickel active sites was determined ex-situ using low temperature (77 K) infrared (IR) dosing experiments with NO. In Figures 4.9a and 4.9b,

we show the IR spectra of an as synthesized sample after dosing 400 Pa (~4 μmol) and 2 kPa (~20 μmol) of NO on 7.7 mg of Ni-MIL-127. At low NO pressures, we observe a band at 1873 cm^{-1} attributed to Ni(II)-NO.[157] Upon subsequent NO dosing, the Ni(II)-NO band saturates, and another band appears at 1894 cm^{-1}. This band at 1894 cm^{-1} corresponds to a Fe(III)-NO species, which is consistent with the IR frequencies of Fe(III)-NO bands for as synthesized MIL-127 type materials at subambient temperatures[157,167,168] and the oxidation state from Mössbauer spectra we acquired at 25 K (Figure 4.2c) and Fe XANES spectra (Figure 4.7a). The amount of nickel and iron was quantified by integration of band areas upon NO dosing until the bands saturated, as depicted in Figure 4.9c. The Ni(II)-NO and Fe(III)-NO bands saturate after dosing 595 μmol g_{cat}^{-1} and a subsequent 1557 μmol g_{cat}^{-1}, respectively, a cumulative NO dosed of ~2152 μmol g_{cat}^{-1}. This yields a Ni:Fe ratio of 1:2.6, consistent with the Ni:Fe ratio obtained from EDS (Table 4.2, Equation 4.2).

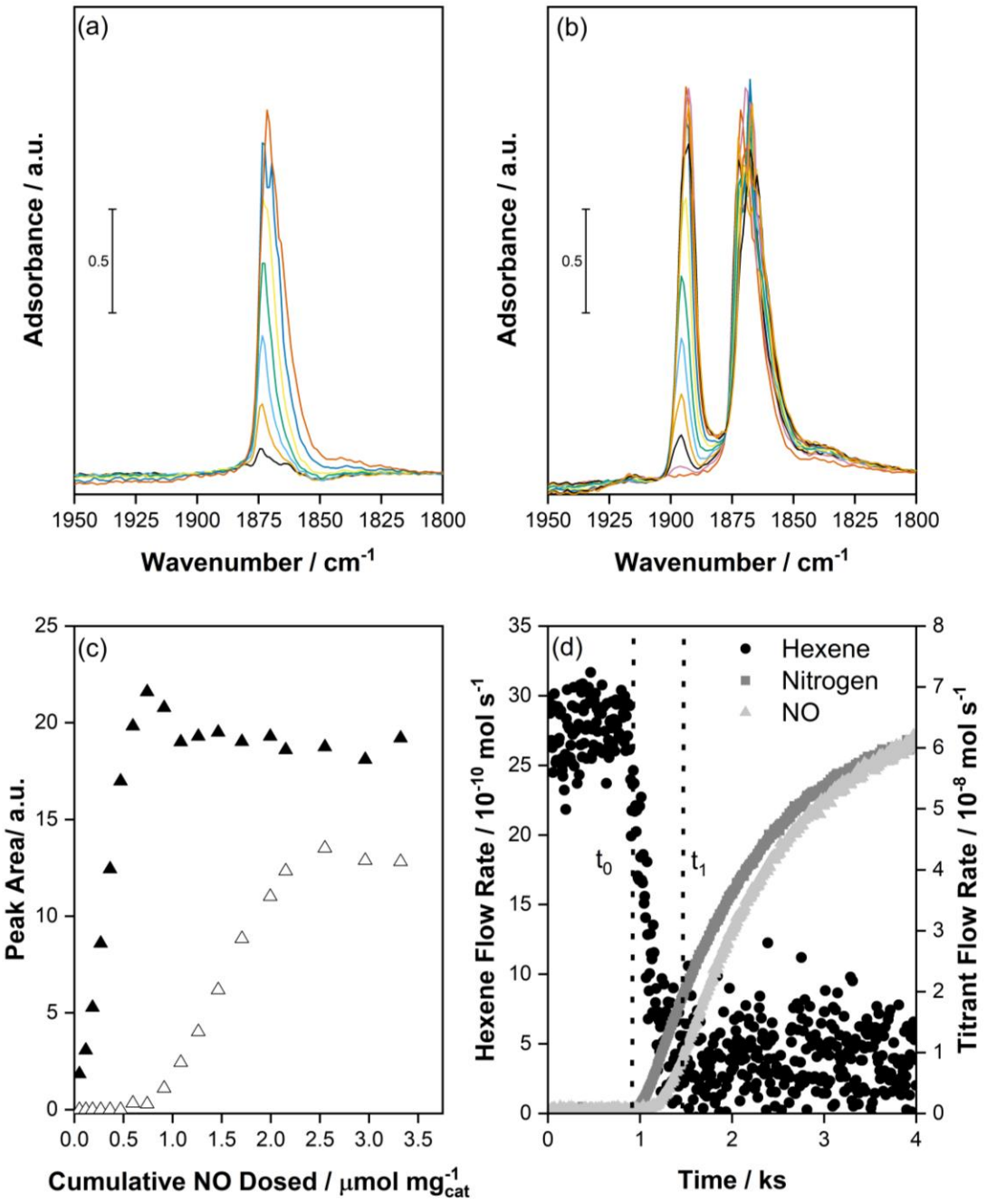

Figure 4.9. IR spectra with cumulative doses of (a) 400 Pa (~4 μmol) and (b) 2 kPa (~20 μmol) of NO with (c) the corresponding plot of the integration of the Ni(II)-NO (▲) and Fe(III)-NO (△) peak areas versus the cumulative amount of NO dosed on 7.7 mg of as synthesized Ni-MIL-127 at 77 K. (d) In-situ NO titration showing a decrease in the rate of hexene formation (●)upon introduction of 0.17 cm^3 s^{-1} of 1% NO (▲) and 99% N_2 (■) in 0.83 cm^3 s^{-1} at a total pressure of 500 kPa at 493 K on 29.8 mg of Ni-MIL-127.

Previous work has reported that various nickel moieties exist and only $(Ni\text{-}OH)^+$ species are active for propylene oligomerization on Ni-Al-MCM-41 at 248 K and 230 kPa.[44,45] Similar observations in MOF systems have been made where not all Ni species are active during ethylene oligomerization in Ni/UiO-66.[76] Thus, we aimed to enumerate the active sites in-situ during propylene oligomerization as shown in Figure 4.9d to accurately normalize reaction rates. Once propylene oligomerizations rates on Ni-MIL-127 reached steady state at 500 kPa and 493 K, a mixture of 1% NO and 99% N_2 was introduced into the propylene feed, and subsequently a decrease in the rate of hexene formation was observed. At t_0, nitrogen achieves breakthrough before NO, as NO titrates nickel active sites and impedes the formation of hexene until t_1. We note that NO continues to have a delayed breakthrough response even after hexene is no longer formed after t_1, as NO titrates the iron in the MOF after nickel is titrated. This phenomenon is consistent with the ex-situ IR data for the as synthesized material presented in Figure 4.9c, where NO titrates nickel active sites before iron. As shown in Figure 4.3, the pure iron analog of Ni-MIL-127 is inactive for propylene oligomerization, and thus, we attribute the decrease in hexene formation to the loss of nickel active sites. The amount of active nickel is quantified by numerical integration between the normalized nitrogen and NO breakthrough curves between time t_0 and t_1.[136,137] An upper bound 371 ± 18 μmol g_{cat}^{-1} of nickel was obtained at various titration conditions (See Section 4.5.3) assuming one NO molecule binds to one nickel. Comparing the amount of NO adsorbed ex-situ on as synthesized samples (Figure 4.9c) and the uptake of NO in in-situ titration experiments to impede hexene formation (Figure 4.9d), ~62% of nickel atoms are active for propylene oligomerization, consistent with the degree of coordination fitted from EXAFS, where ~70% of nickel atoms have an open coordination site (Figure 4.5, Table 4.5).

4.3.2. Propylene Oligomerization Reaction Mechanism and Kinetics

The Ni-MIL-127 precatalyst after thermal activation undergoes an induction period, as shown in Figure 4.1d, to generate the relevant surface Ni species for propylene oligomerization. We propose the initiation mechanism for propylene oligomerization (Figure 4.10) consists of a series of stoichiometric reactions of propylene to form hexadiene

and water which facilitates the formation of a Ni-hydride or Ni-propyl species, similar to the initiation mechanism presented for ethylene and butene oligomerization.[40,41,129] In Figure 4.11a, an increase in propylene pressure from 114 kPa to 500 kPa decreases the induction period from ~170 ks to ~60 ks at 473 K, consistent with previous observations where higher ethylene pressures decrease the duration of the induction period for ethylene oligomerization on Ni/UiO-66.[76] Additionally, an increase in reaction temperature from 473 K to 513 K decreases the induction period from ~170 ks to ~30 ks at 114 kPa, congruous with observations on Ni-Na-X where activating the catalyst at 493 K eliminated the induction period that was observed at 453 K.[35] Hexadiene formation (Figure 4.11b) is also detected during the induction period at 500 kPa and 473 K. These observations imply propylene pressures and reaction temperatures affect the rate at which relevant surface intermediates are formed prior to steady state.

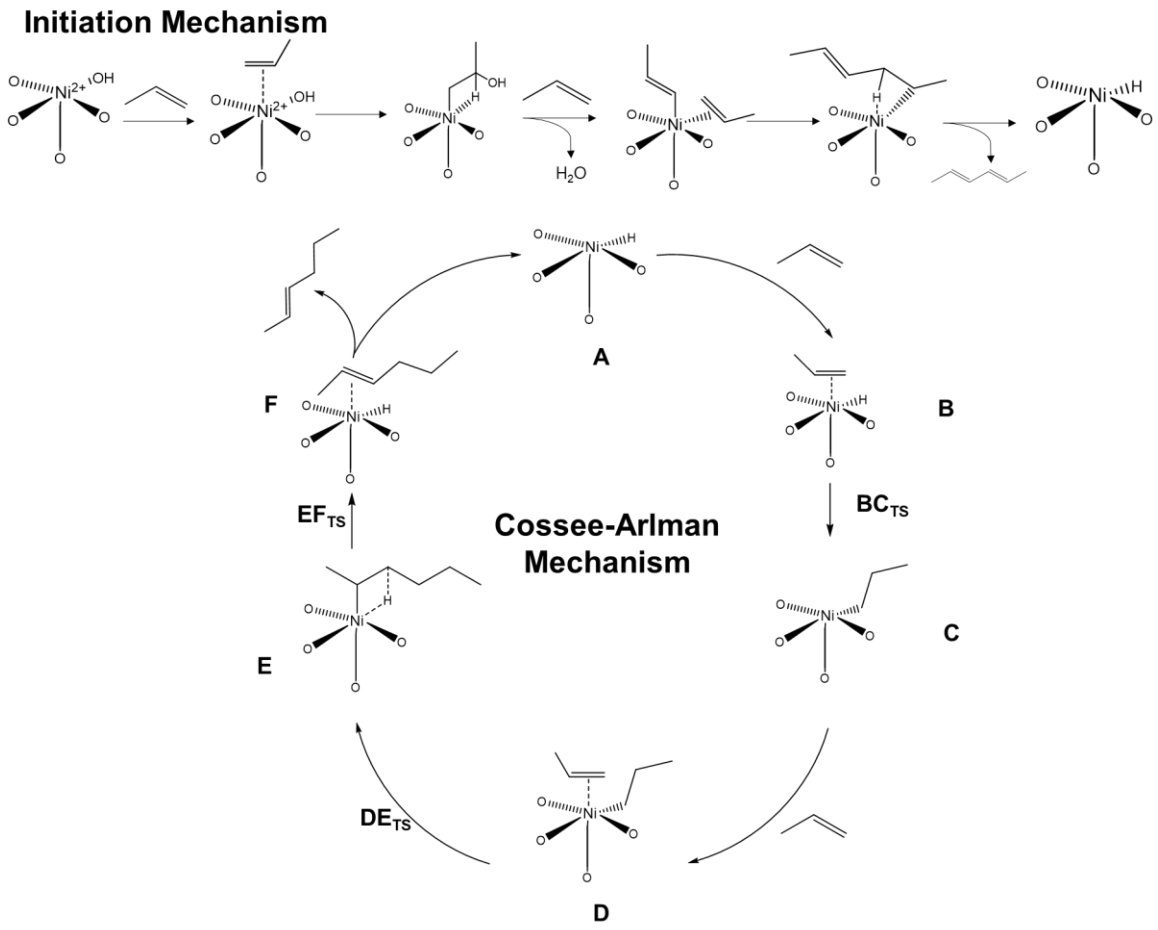

Figure 4.10. Initiation Mechanism and Cossee−Arlman Mechanism for Propylene Oligomerization on Ni-MIL-127. Note the entire node is omitted for clarity

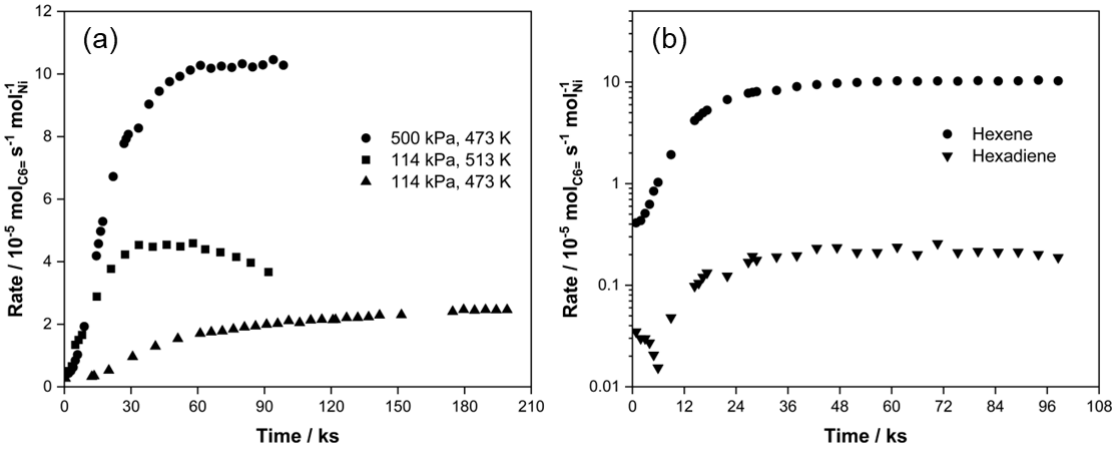

Figure 4.11. Time on stream for propylene oligomerization at (a) 500 kPa and 473 K (●), 114 kPa and 473 K (▲), and 114 kPa and 513 K (■) on Ni-MIL-127 and at (b) 500 kPa and 473 K in 0.83 $cm^3\ s^{-1}$ of propylene showing the production of hexene (●) and hexadiene (▲) on 25.0 mg Ni-MIL-127.

The relevant Ni-propyl species formed during the induction period was examined through steady state kinetics and spectroscopic measurements. Propylene oligomerization is first order in propylene pressure from 5 – 550 kPa on Ni-MIL-127 at 473 K as shown in Figure 4.12a. This suggests that the resting state of the catalyst at steady state is a Ni-propyl species, considering two propylene molecules are required to form hexene. The Ni-propyl surface intermediate was probed with IR spectroscopy after the catalyst reached steady state after exposure to propylene for two days (Figure 4.11a) at 473 K and ambient pressure and subsequently degassing the sample (< 3 Pa). In Figure 4.14, aliphatic C-H bands at 2962 cm^{-1}, 2923 cm^{-1}, and 2867 cm^{-1} are observed,[37] consistent with the presence of a Ni-propyl species that was posited from observed first order reaction kinetics for propylene oligomerization. Subtle differences in the XANES region are observed between the thermally treated samples and the structure at steady state (Figure 4.4c), but the pre-edge peak at 8440 eV persists and suggests a five coordinate nickel species. The EXAFS results for Ni-MIL-127 after thermal treatment and at steady state reported in Figure 4.5g are similar, and the fitting of the first coordination shell (Figure 4.5) shows that, within error, Ni maintains the same coordination (Table 4.5). We note that Ni-C and Ni-O bonds cannot be differentiated, so the loss of an OH^- species and the formation of a propyl ligand cannot

be resolved. However, we surmise that the Ni-OH moiety is removed via migratory insertion of propylene to eliminate water during the induction period[41] and generate the steady state Ni-propyl species (Figure 4.10) which justifies similar coordination and geometries between the two structures.

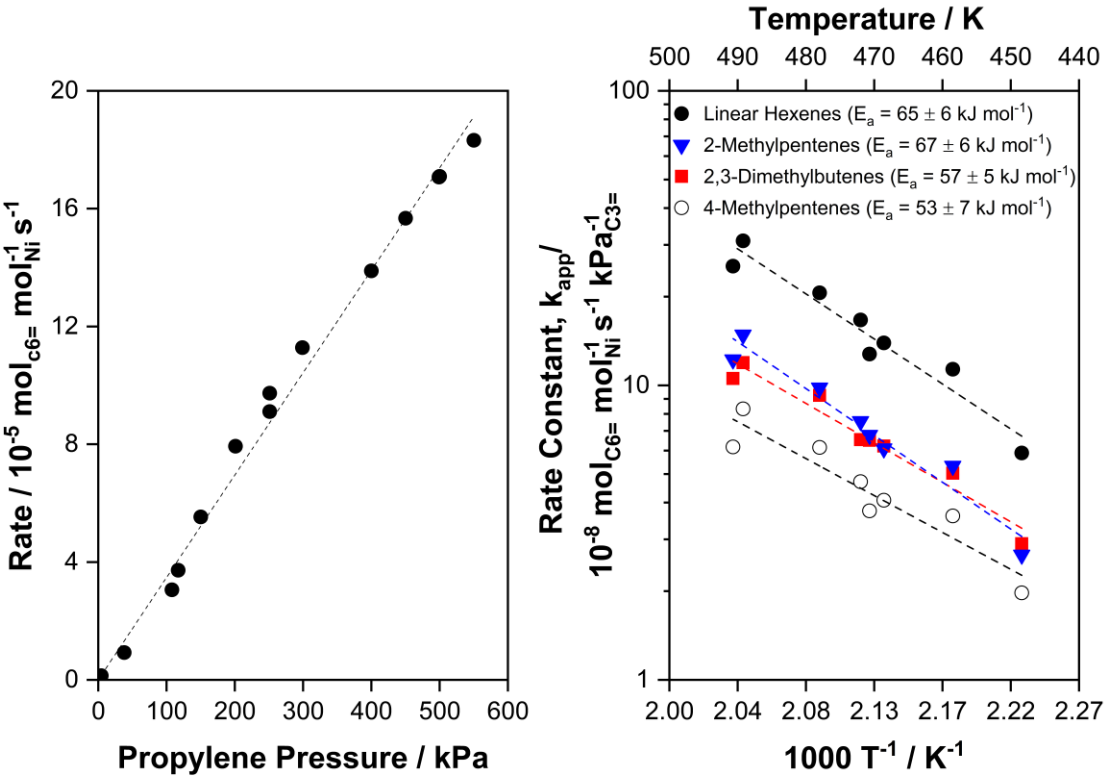

Figure 4.12. (a) Hexene formation rate versus propylene partial pressure (5 – 550 kPa) at 473 K on Ni-MIL-127. (b) Arrhenius plot for propylene oligomerization to form linear hexenes (●), 2-methylpentenes (▼), 2,3-dimethylbutenes (■), and 4-methylpentenes (○) at 500 kPa from 448-493 K for Ni-MIL-127.

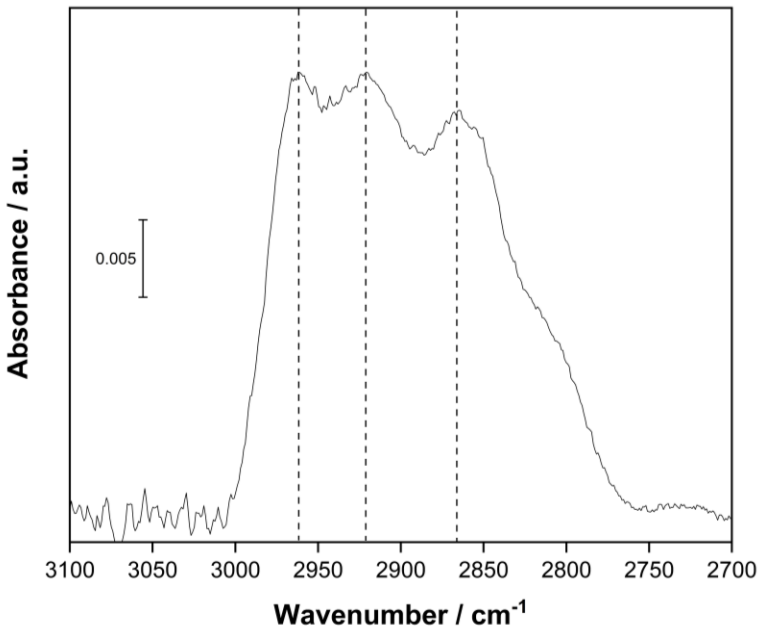

Figure 4.13. The difference IR spectra from 2700-3100 cm^{-1} for Ni-MIL-127 in vacuum (<3 Pa) after exposure to flowing propylene at ambient pressure for 2 days at 473 K. The dotted lines at 2962 cm^{-1}, 2923 cm^{-1}, and 2867 cm^{-1} are presented to show IR bands corresponding to Ni-propyl species

After the relevant Ni-propyl species is formed during the induction period on Ni-MIL-127, olefin oligomerization is proposed in the literature to follow the Cossee-Arlman mechanism on nickel catalysts as presented in Figure 4.10.[31,41,49–51,59,70,80,95,169] Isomers of linear hexenes, 2-methylpentenes, 4-methylpentenes, and 2,3-dimethylbutenes are generated from the Cossee-Arlman cycle by regioselective insertion of adsorbed propylene molecules.[51] Herein, we report the mechanism for the production of linear hexenes while others are reported in Section 4.5.4. The Cossee-Arlman mechanism starts with a nickel hydride species (**A**) that binds to a propylene molecule to give a nickel hydride species with propylene physiosorbed on the surface (**B**). 1,2-Propyl (**C**) or 2,1-propyl species are formed upon migratory insertion (**BC**$_{TS}$) of the hydride species and are the relevant surface species. Another propylene molecule is adsorbed on **C** to generate propylene adsorbed on the Ni-propyl species (**D**). The kinetically relevant 1,2- and 2,1- olefin insertions (**DE**$_{TS}$) proceed on **D** to generate isomeric Ni-hexyl species (**E**).[51] The Ni-hexyl species undergo

β-hydride elimination (**EF**$_{TS}$) to yield physisorbed hexene (**F**) which desorbs to regenerate **A** and produce the respective hexene isomers.

The validity of the Cossee-Arlman mechanism was investigated by comparison between experimental and computed apparent activation energies. An Arrhenius plot presented in Figure 4.12b for linear hexenes, 2-methylpentenes, 4-methylpentenes, and 2,3-dimethylbutenes reveals apparent activation enthalpies of 65.0 ± 5.8 kJ mol^{-1}, 67.3 ± 5.9 kJ mol^{-1}, 53.4 ± 7.2 kJ mol^{-1}, 56.8 ± 4.8 kJ mol^{-1}, respectively, between 448 K – 493 K at 500 kPa on Ni-MIL-127. The measured apparent activation energies for the different hexene isomers are within error of each other, as the product selectivities appear to be invariant with temperature (Figure 4.26). These apparent activation energies are comparable with the activation energies of 58 kJ mol^{-1} and 45 kJ mol^{-1} on Ni/UiO-66 for butene oligomerization and on Ni-Na-X for propylene oligomerization, respectively.[35,129]

Calculated enthalpy and free energy diagrams from DFT with the M06-L functional for linear hexene formation via the Cossee-Arlman mechanism are presented in Figure 4.14 on cluster models of Ni-MIL-127 (S^2=11) at 493 K and 101.3 kPa while the enthalpy and free energy diagrams for the other hexene isomers are presented in Figures 4.36-4.39. The free energy of adsorbing a propylene molecule to generate B is 38 kJ mol^{-1}, akin to ethylene and butene adsorption free energies on Ni/UiO-66 of -17 kJ mol^{-1} and 55 kJ mol^{-1}, respectively. The hydride insertion step (**BC**$_{TS}$), olefin insertion step (**DE**$_{TS}$), and β-hydride elimination step (**EF**$_{TS}$) yield free energy barriers of 17 kJ mol^{-1}, 76 kJ mol^{-1}, and 120 kJ mol^{-1}. The calculated migratory insertion and olefin insertion intrinsic free energies on Ni/UiO-66 for ethylene oligomerization is 22 kJ mol^{-1} and 80 kJ mol^{-1}, respectively, consistent with values reported in Figure 4.14.[76] We note that the barrier for β-hydride elimination of 130 kJ mol^{-1} is higher than what is reported for ethylene and butene oligomerization on Ni/UiO-66.[76,80] We attribute the larger β-hydride elimination barrier of 130 kJ mol^{-1} for linear hexenes due to a combination of the change in spin state found in nickel framework based MOFs[169] and the specific hexene isomer that is produced. Nickel framework-based MOFs, such as Ni-MFU-4l, for olefin oligomerization have been proposed to change spin states along the reaction coordinate[169] while olefin oligomerization

on nickel supported MOFs, such as Ni/UiO-66, do not.[76,129] Ni-MFU-4l yield higher reaction barriers for β-hydride elimination (72 kJ mol^{-1}) for ethylene oligomerization[169] where a change in the triplet to singlet spin state on Ni-MFU-4l along the reaction coordinate was attributed to contribute towards the higher observed barrier on framework-based MOFs for β-hydride elimination. Similarly, a change in spin state is observed for intermediates **E** and **F** to give rise to a higher β-hydride elimination barrier (Table 4.11). Additionally, the β-hydride elimination step, which affects whether internal or terminal alkenes are produced, for the Cossee-Arlman mechanism yield intrinsic free energy barriers of ~130 kJ mol^{-1} and ~60 kJ mol^{-1} for internal and terminal alkenes, respectively (Figure 4.14 and Figures 4.36-4.39). The higher β-hydride elimination barrier of 130 kJ mol^{-1} for 2-hexene presented herein can be ascribed to a change in spin state for this step and the specific structural hexene isomer formed.

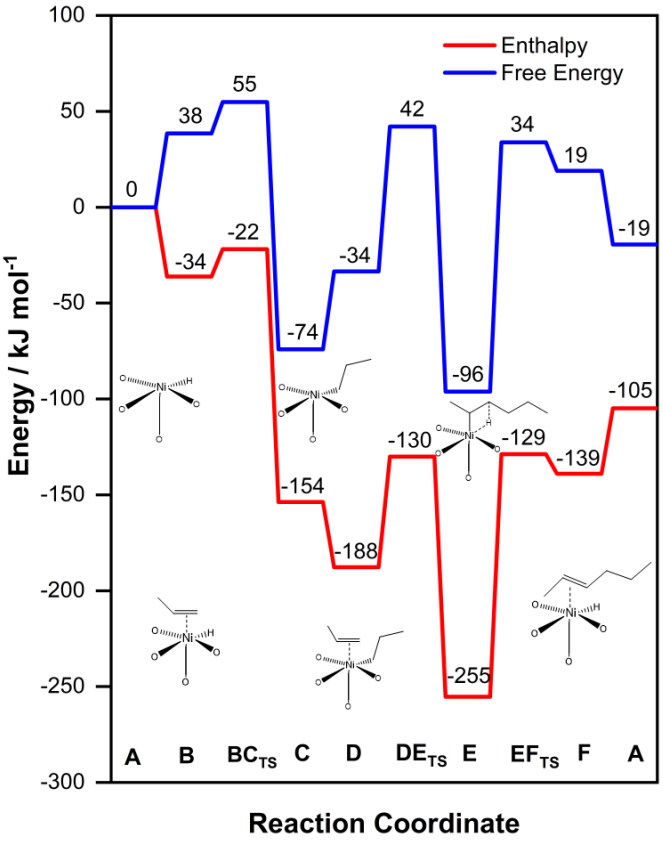

Figure 4.14. Enthalpy (red) and free energy (blue) diagram for the synthesis of linear hexenes via propylene oligomerization through the Cossee−Arlman mechanism for on Ni-

MIL-127 at 473 K and 101.3 kPa. Intermediate structures (S^2=11) are shown along the reaction pathway.

Because of the first order kinetics observed in experimental studies (Figure 4.12a), the resting state of the catalyst is likely the Ni-propyl species (**C**). The kinetically relevant step for the formation of hexenes from **C** is the olefin insertion step (**DE**$_{TS}$) as the apparent free energy barrier is 116 kJ mol^{-1} as opposed to 108 kJ mol^{-1} for the β-hydride elimination step (**EF**$_{TS}$). From the kinetically relevant olefin insertion step (**DE**$_{TS}$) and the most relevant surface Ni-propyl species (**C**) determined from steady state reaction orders and IR and XAS spectroscopy, we obtain calculated apparent activation enthalpies for linear hexenes, 2-methylpentenes, 4-methylpentenes, and 2,3-dimethylbutenes in the range of 24-42 kJ mol^{-1} (Figures 4.36-4.39), somewhat lower than the apparent activation energies of ~53-65 kJ mol^{-1} obtained from experiment. These values are within the 8-23 kJ mol^{-1} error of DFT using the M06-L functional and are consistent with errors found in olefin oligomerization on Ni/UiO-66 and Ni/NU-1000 MOF materials.[76,80,129]

Metallacycle and proton-transfer mechanisms for propylene oligomerization were investigated as alternatives to the Cossee-Arlman mechanism by comparison of expected trends for these alternative mechanisms with experimental observations and by comparison of DFT computed energy barriers for all three mechanisms (Section 4.5.5).[41,53] The metallacycle mechanism (Figure 4.43) on nickel catalysts is characteristic of external activators, successive coordination of two olefin molecules, and a redox reaction on the nickel active site.[11,13,31,41] The observed induction period in the absence of activators (Figure 4.11a), the five-coordinate nickel species after thermal treatment (Table 4.5) unable to directly coordinate two propylene molecules, and a persistent Ni(II) species after thermal treatment and during reaction as indicated from XANES (Figure 4.4c) are incongruous with the metallacycle mechanism for propylene oligomerization on Ni-MIL-127. The proton transfer pathway was scrutinized with DFT calculations (Section 4.5.5, Figure 4.41, Figure 4.42), where the C-H activation step was found to be the kinetically relevant step in our work and previous work for ethylene oligomerization on Ni-SSZ-24 and butene oligomerization on Ni/UiO-66.[41,53,129] The larger intrinsic rate-limiting C-H activation free energy barrier of 191 kJ mol^{-1} for the proton-transfer mechanism (Figure 4.42) is higher

than the intrinsic free energy for the kinetically relevant carbon-carbon coupling step of 76 kJ mol^{-1} for the Cossee-Arlman mechanism (Figure 4.14). These observations and calculations render the Cossee-Arlman mechanism most favorable for propylene oligomerization on Ni-MIL-127 compared to the metallacycle and proton-transfer mechanisms. The Ni-MIL-127 structure, initiation mechanism, and Cossee-Arlman mechanism for propylene oligomerization is consistent with our spectroscopic measurements, observed induction periods, and steady state kinetics.

4.4. Conclusion

Thermal treatment on Ni-MIL-127, which contains a fully coordinated nickel atom in the inorganic node, generates a missing linker defect on nickel to engender a five-coordinate nickel site to facilitate stable propylene oligomerization after undergoing an induction period in the absence of cocatalysts and activators. Transient and steady state rate measurements suggest the induction period is attributed to the formation of the relevant Ni-propyl species at steady state. The steady state Cossee-Arlman mechanism is validated on Ni-MIL-127 for propylene oligomerization by comparison between experimental and computed activation energies. These results demonstrate how the stable Ni-MIL-127 MOF reported herein can be designed to further improve reactivity for olefin oligomerization through a synergy between experiment and theory.

4.5. Supplemental Information

4.5.1. Supplemental Structural and Chemical Characterization of Ni-MIL-127

The ^{1}H NMR spectrum of the ABTC linker dissolved in 1M NH_4OH/D_2O and 100 mm^3 of acetonitrile (2.12 ppm) is presented in Figure 4.15 to validate the peak location (8.53 ppm) of ABTC linkers in Ni-MIL-127 (Figure 4.4b in the main text) with the equation to calculate the moles of ABTC per mass of materials shown in Equation 4.3. The number of linkers per mass of sample was determined from the equation below where the number of nuclei for acetonitrile is 3 while the nuclei for the ABTC is 6, representing the aryl protons. Supplemental TPO for as synthesized and activated Ni-MIL-127 samples are presented in Figure 4.16 and summarized in Table 4.6. Note that the time scale presented in Figure 4.16 are arbitary and do not correspond to a temperature for clarity. Signals for

the incomplete combustion (m/z = 44 and 78) of Ni-MIL-127 are shown in Figure 4.17, where the amount of CO_2 was determined to be 1.83 μmol g_{cat}^{-1}, one order of magnitude less than that observed with complete combustion (Figure 4.16, Figure 4.4a, Table 4.6). Post reaction (500 kPa of 0.83 cm^3 s^{-1} propylene at 473 K) PXRD patterns are reported in Figure 4.18 to show the material maintains crystallinity after reaction.

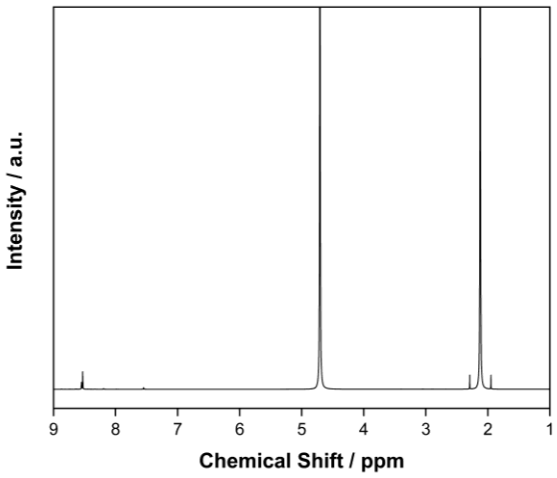

Figure 4.15. ^1H NMR spectra for 4.5 mg of ABTC linker (8.53 ppm) in 100 mm^3 of acetonitrile (2.12 ppm) in 1M NH_4OH/D_2O. The peak at 4.70 ppm is HDO.

$$\frac{\left(\frac{Intensity\ of\ ABTC\ (8.53\ ppm)}{Intensity\ of\ Acetonitrile\ (2.12\ ppm)} * \frac{3}{6}\right) * (100\ mm^3) * \left(\frac{786 * 10^{-6} g}{mm^3}\right)}{(41.05 \frac{g}{mol})(Mass\ of\ Sample)} = \frac{Moles\ of\ ABTC}{Mass\ of\ Sample} \quad \text{Eq. 4.3}$$

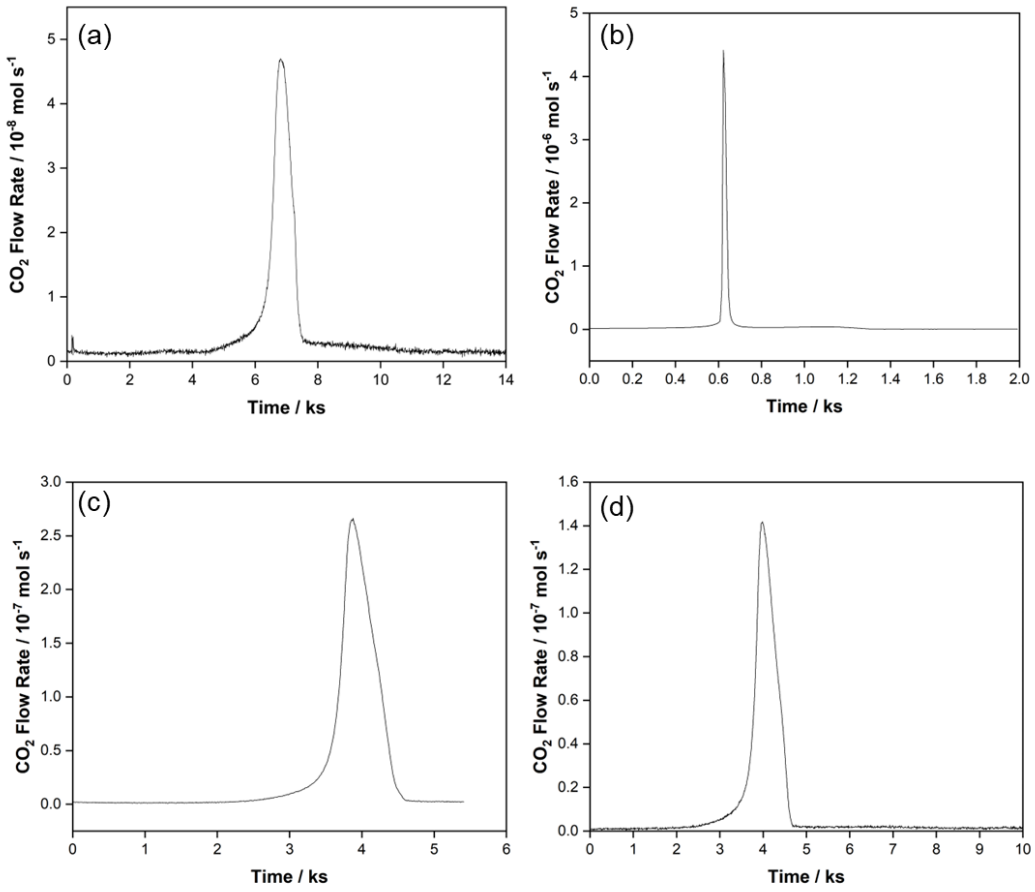

Figure 4.16. TPO for (a) 1.7 mg and (b) 5.1 mg of as synthesized Ni-MIL-127 and (c) 6.6 mg and (d) 3.0 mg of thermally activated (0.83 cm^3 s^{-1} He at 493 K for four hours) Ni-MIL-127 in 0.83 cm^3 s^{-1} He, 0.17 cm^3 s^{-1} Ar, and 0.17 cm^3 s^{-1} O_2 with the temperature ramped at 0.05 K s^{-1}.

Table 4.6. Summary of TPO data for as synthesized and thermally activated Ni-MIL-127

As Synthesized Sample	**Quantity of CO_2 / µmol g_{cat}^{-1}**	**Thermally Activated Sample**	**Quantity of CO_2 / µmol g_{cat}^{-1}**
Figure 4.4a	28.1	Figure 4.4a	18.7
Figure 4.16a	25.3	Figure 4.16c	22.0
Figure 4.16b	32.6	Figure 4.16d	26.7
Average ± S.D	28.7 ± 3.7		22.4 ± 4.0

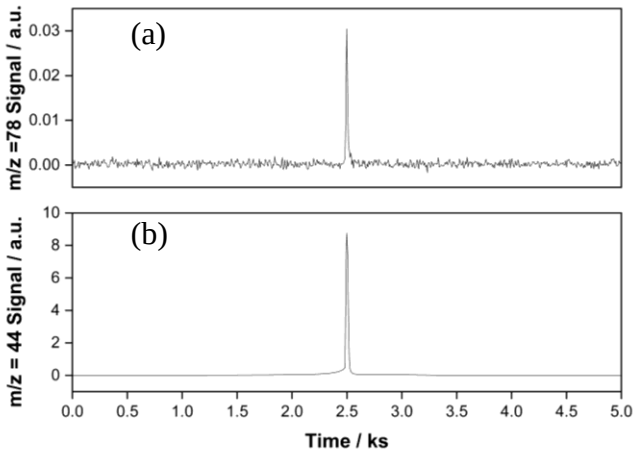

Figure 4.17. TPO signals for (a) m/z = 78 corresponding to aromatic fragments and (b) m/z = 44 corresponding to CO_2 on 6.4 mg of thermally activated (0.83 cm^3 s^{-1} He at 493 K for four hours) Ni-MIL-127 in 0.83 cm^3 s^{-1} He, 0.17 cm^3 s^{-1} Ar, and 0.17 cm^3 s^{-1} O_2 with the temperature ramped at 0.05 K s^{-1}.

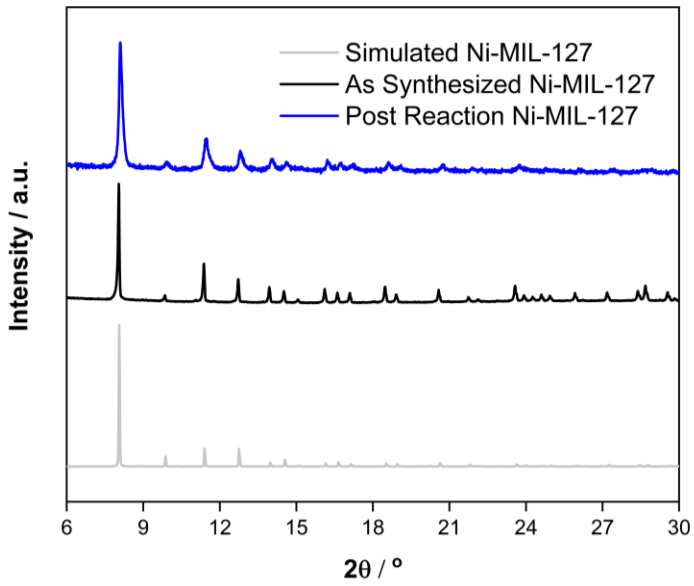

Figure 4.18. Simulated, as synthesized, and post reaction (500 kPa of 0.83 cm^3 s^{-1} propylene at 473 K) PXRD patterns for Ni-MIL-127

4.5.2. Propylene Oligomerization Time on Stream, Selectivities, Kinetics on Ni-MIL-127

The contact time was varied by changing the catalyst mass (5-30 mg) or propylene flow rate (0.083 – 0.83 cm^3 s^{-1}) at 500 kPa and 473 K to probe whether hexene formation

rates were measured in the presence of product inhibition. As seen in Figures 4.19, at low contact times (<1.5 mol_{Ni} s $mol_{C3=}^{-1}$), there is a linear relationship between conversion and contact time. However, at higher contact times, the relationship between conversion and contact becomes nonlinear. Additionally, the hexene formation rate decreases when the propylene flowrate decreases from 0.83 cm^3 s^{-1} to less than 0.17 cm^3 s^{-1}, while the catalyst maintains stability (Figure 4.20). The analysis from Figures 4.19 and 4.20 suggest that at high conversions and contact times, our rates are inhibited by the product. We attempted to probe the product that inhibited hexene reaction rates by cofeeding primary hexene products (Figure 4.21), 1-hexene and 2,3-dimethyl-1-butene, at 25 Pa and a secondary product (Figure 4.22), 1-nonene, at 25 Pa during propylene oligomerization at 500 kPa and 473 K. To avoid possible effects of isomerization,[37] only the formation of 4-methyl-1-pentene was investigated during 1-hexene and 2,3-dimethyl-1-butene cofeeds. We conclude that hexene formation rates do not change with hexene cofeeds as there is no change in reaction rates with or without the cofeed (Figure 4.21). When 1-nonene is cofed, the hexene reaction rate increases after 1-nonene is no longer introduced to the propylene feed (Figure 4.22), indicating that the secondary product inhibits hexene formation on Ni-MIL-127. Our goal was to measure reaction rates and kinetics in the absence of product inhibition, so we opted to measure rates at low conversion (<0.025%) to alleviate the effects of product inhibition. The individual hexene product selectivities are shown in Figure 4.23 and Table 4.7, respectively, and the structural hexene isomer selectivities are shown in Figures 4.24 and Table 4.8, respectively at conversion below 0.025% at 500 kPa propylene and 473 K.

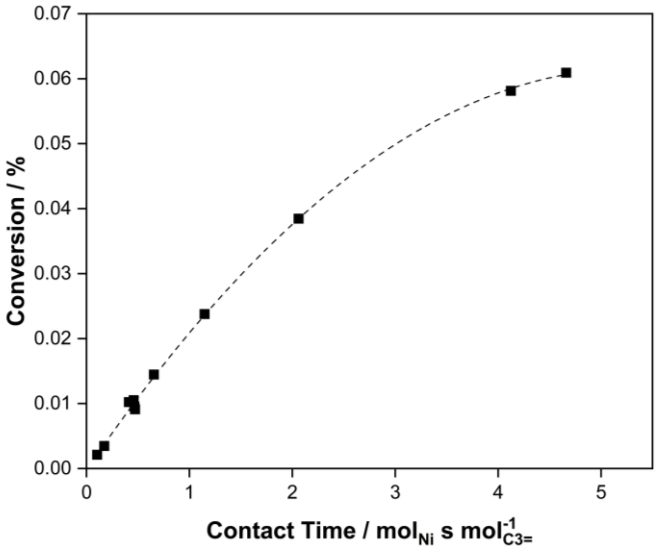

Figure 4.19. Conversion versus contact time for propylene oligomerization at 500 kPa and 473 K on Ni-MIL-127

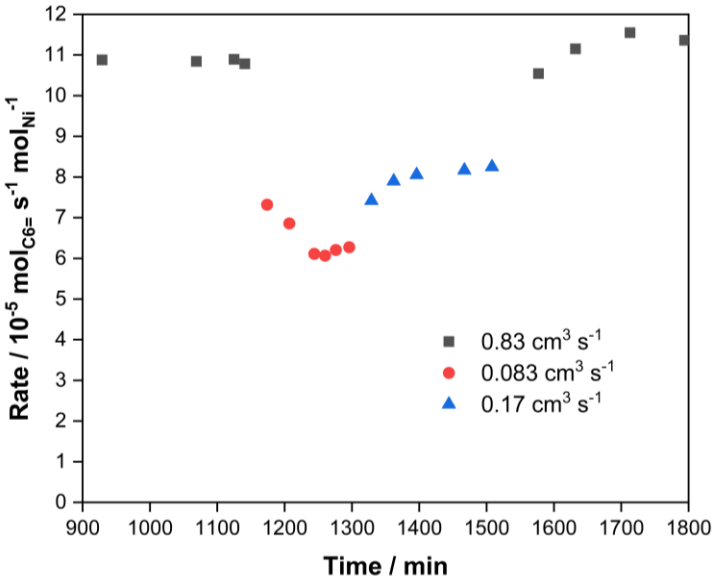

Figure 4.20. Time on stream for propylene oligomerization on 26.3 mg of Ni-MIL-127 at 500 kPa and 473 K after steady state was reached with changing flow rates.

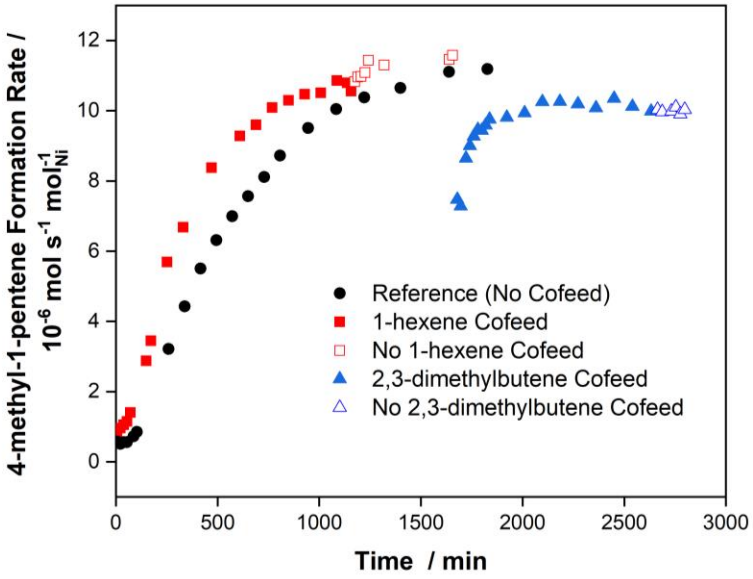

Figure 4.21. Time on stream for 4-methyl-1-pentene formation rates on 23.6 mg of Ni-MIL-127 with 500 kPa of 0.83 cm^3 s^{-1} propylene and 25 Pa 1-hexene (red) or 2,3-dimethylbutene during (filled) or after the cofeed (open). Rates for 4-methyl-1-pentene in the absence of cofeeds on 15.3 mg of Ni-MIL-127 with 0.83 cm^3 s^{-1} propylene at 500 kPa and 473 K is shown as black circles for reference.

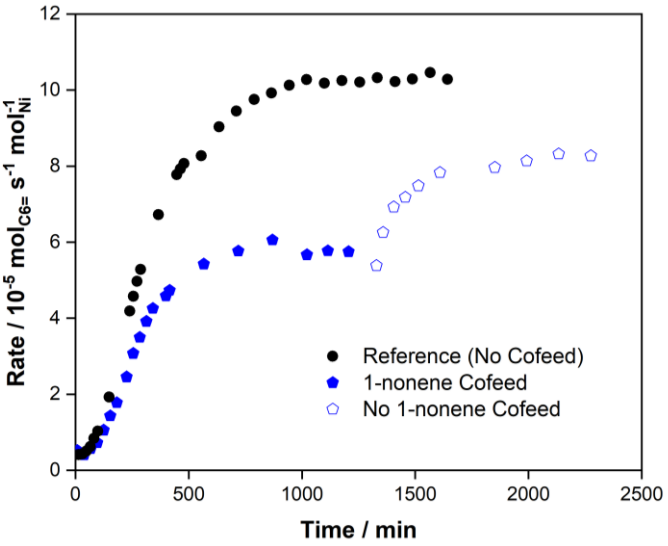

Figure 4.22. Time on stream for hexene formation on 18.8 mg of Ni-MIL-127 with 500 kPa of 0.83 cm^3 s^{-1} propylene and 25 Pa 1-nonene during (filled) or after the cofeed (open). Rates for hexene formation on 25.0 mg of Ni-MIL-127 with 0.83 cm^3 s^{-1} propylene at 500 kPa and 473 K is shown as black circles for reference.

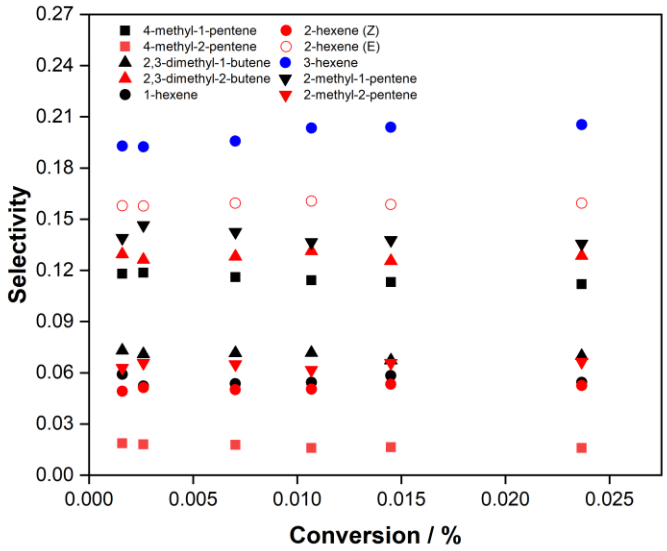

Figure 4.23. Selectivity versus conversion at <0.025% for all observed hexene products for propylene oligomerization on Ni-MIL-127 at 500 kPa and 473 K.

Table 4.7. Tabulated selectivities at 0.025% conversion for all observed hexene products for propylene oligomerization on Ni-MIL-127 at 500 kPa and 473 K.

Product	Selectivity / %
4-methyl-1-pentene	11.2
4-methyl-2-pentene	15.9
2,3-dimethyl-1-butene	7.0
2,3-dimethyl-2-butene	12.9
1-hexene	5.4
2-hexene (Z)	5.2
2-hexene (E)	15.9
3-hexene (E)	20.5
2-methyl-1-pentene	13.6
2-methyl-2-pentene	6.6

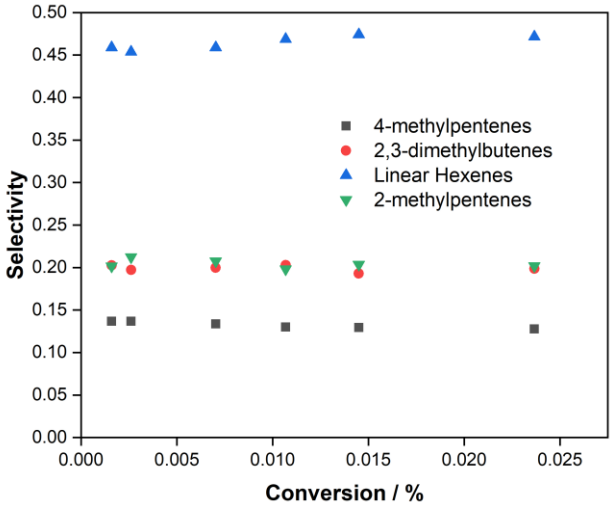

Figure 4.24. Combined selectivity versus conversion at <0.025% for structural hexene isomers for propylene oligomerization on Ni-MIL-127 at 500 kPa and 473 K.

Table 4.8. Tabulated combined selectivities at 0.025% conversion for structural hexene isomers for propylene oligomerization on Ni-MIL-127 at 500 kPa and 473 K.

Product	Selectivity / %
4-methylpentenes	12.8
2,3-dimethylbutenes	19.9
Linear Hexenes	47.1
2-methylpentenes	20.2

In Figures 4.25a and 4.25b, we show time on stream while changing the propylene pressure (108 kPa-550 kPa) and temperature (448 K-493 K), respectively, during propylene oligomerization. We note that the catalyst is stable for up to 108 ks, or 30 hours, unprecedented for propylene oligomerization on heterogeneous nickel-based catalyst at elevated temperatures in the absence of cocatalysts or prior activation in propylene. In Figure 4.26, invariant product selectivity is shown with respect to temperature to suggest that the apparent activation energies of these products are almost identical (Figure 4.12b).

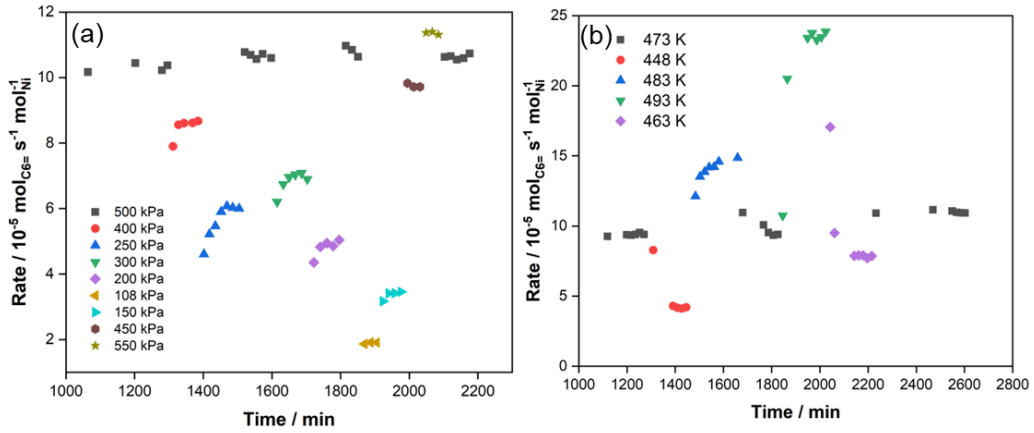

Figure 4.25. Time on stream after the catalyst reached steady state for propylene oligomerization on (a) 5.8 mg of Ni-MIL-127 at various pressures (108 kPa – 550 kPa) at 473 K and (b) 5.6 mg of Ni-MIL-127 at various temperatures (448 K – 493 K) at 500 kPa with 0.83 $cm^3\ s^{-1}$ of propylene.

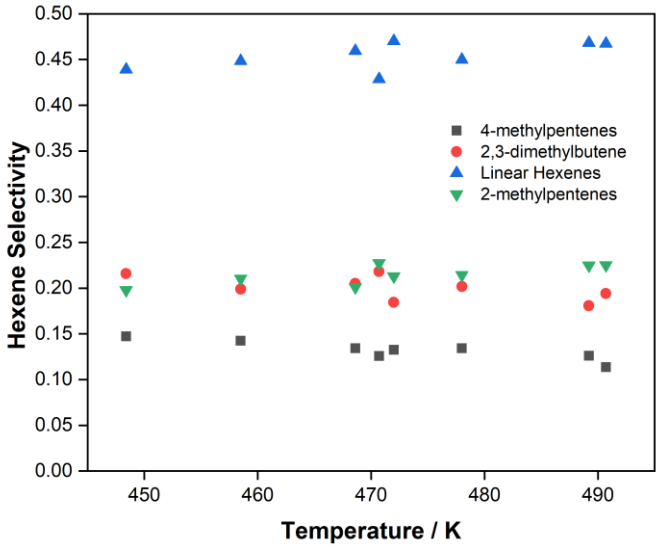

Figure 4.26. Hexene selectivity versus temperature (448 K – 493 K) on 5.6 mg of Ni-MIL-127 with 0.83 $cm^3\ s^{-1}$ of propylene 500 kPa.

4.5.3. Supplemental *in-situ* NO Titrations

This section presents supplemental NO titration experiments at various NO flow rates and catalyst masses summarized in Table 4.9. After the induction period for all catalysts at 500 kPa, and 473 K, the temperature was increased to 493 K to increase the resolution of the hexene signal (m/z = 84). The catalyst was allowed to reach steady state

and then NO was introduced into the propylene feed. The quantification of NO required to titrate active Ni species between t_0 and t_1 and Fe species is achieved by mathematical integration of the normalized N_2 and NO flow rate between t_0 and t_1 and after t_1, respectively. The N_2 flow rate is normalized as N_2 concentration was 99 times greater than that of NO.

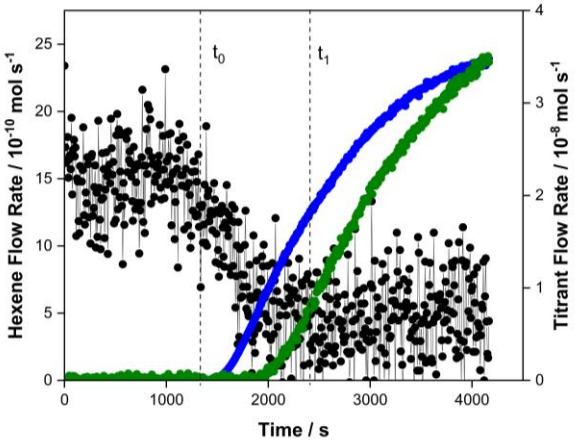

Figure 4.27. Hexene (●), normalized N_2 (●), and NO (●) flowrates during in-situ NO titration for propylene oligomerization 500 kPa total pressure, 0.83 cm^3 s^{-1} propylene, 0.083 cm^3 s^{-1} N_2, and 0.83 mm^3 s^{-1} NO. Total flow: 0.92 cm^3 s^{-1} at 493 K. Catalyst weight: 15.6 mg Ni-MIL-127

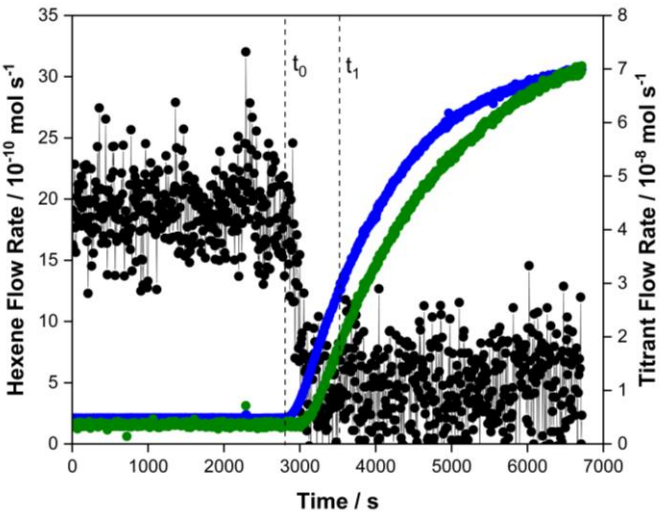

Figure 4.28. Hexene (●), normalized N_2 (●), and NO (●) flowrates during in-situ NO titration for propylene oligomerization 500 kPa total pressure, 0.83 cm^3 s^{-1} propylene, 0.16 cm^3 s^{-1} N_2, and 1.6 mm^3 s^{-1} NO. Total flow: 1 cm^3 s^{-1} at 493 K. Catalyst weight: 18.4 mg Ni-MIL-127

Table 4.9. Summary of in-situ NO titrations at 500 kPa and 493 K on Ni-MIL-127

Sample	NO Flow Rate / nmol s^{-1}	Catalyst Loading / mg	Ni sites / µmol g_{cat}^{-1}	Fe sites / µmol g_{cat}^{-1}
Figure 4.9d	34.8	15.6	383	990
Figure 4.27	69.6	18.4	378	1330
Figure 4.28	69.6	29.8	350	1083
Average ± S.D.			**371 ± 18**	**1152 ± 203**

4.5.4. Cossee-Arlman Mechanism and DFT Cluster Models and Calculations

In this section, we present the steady state Cossee-Arlman mechanism showing the pathways for different hexene isomers proposed on nickel-based MOFs which correspond to 2,1 or 1,2 insertions of the propylene molecule on the nickel active site (Figures 4.29-4.32).[51] These pathways were used to calculate energy barriers to compare with those obtained from experiment (Figure 4.12b). The chain transfer pathway (**OP_{TS}**), which has been proposed in favor of the β-hydride elimination step (**EF_{TS}**) for some diamine nickel complexes for ethylene polymerization,[124] is presented in Figure 4.33.

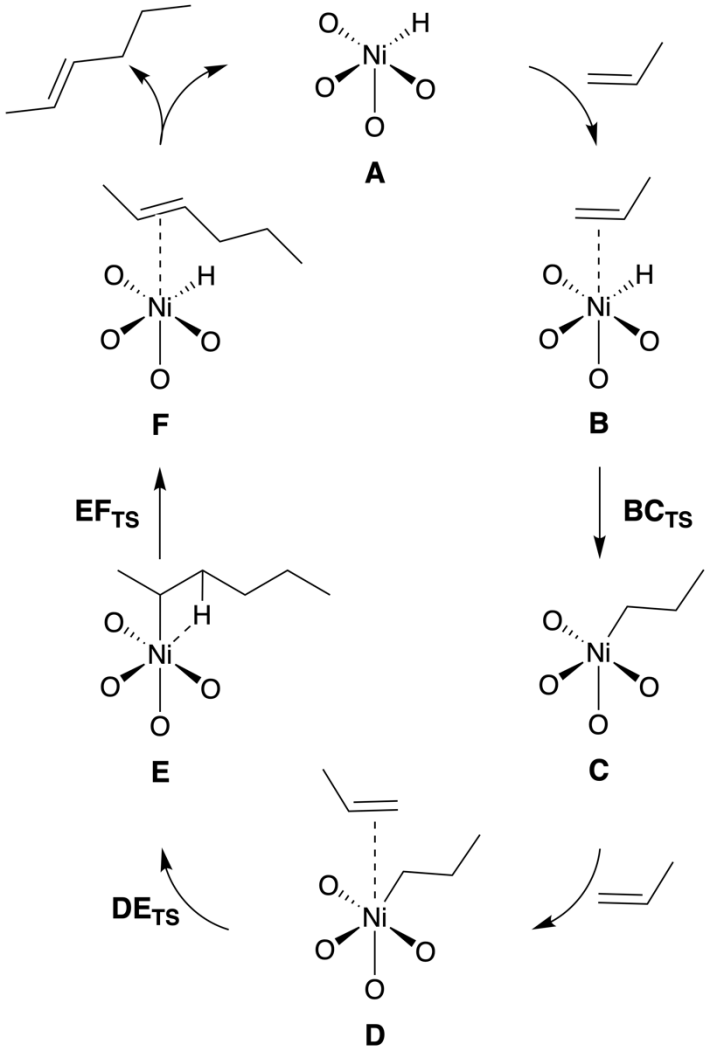

Figure 4.29. Pathway for the formation of linear hexene through [1,2]-hydride insertion followed by [2,1]-C-C insertion in the Cossee-Arlman mechanism.

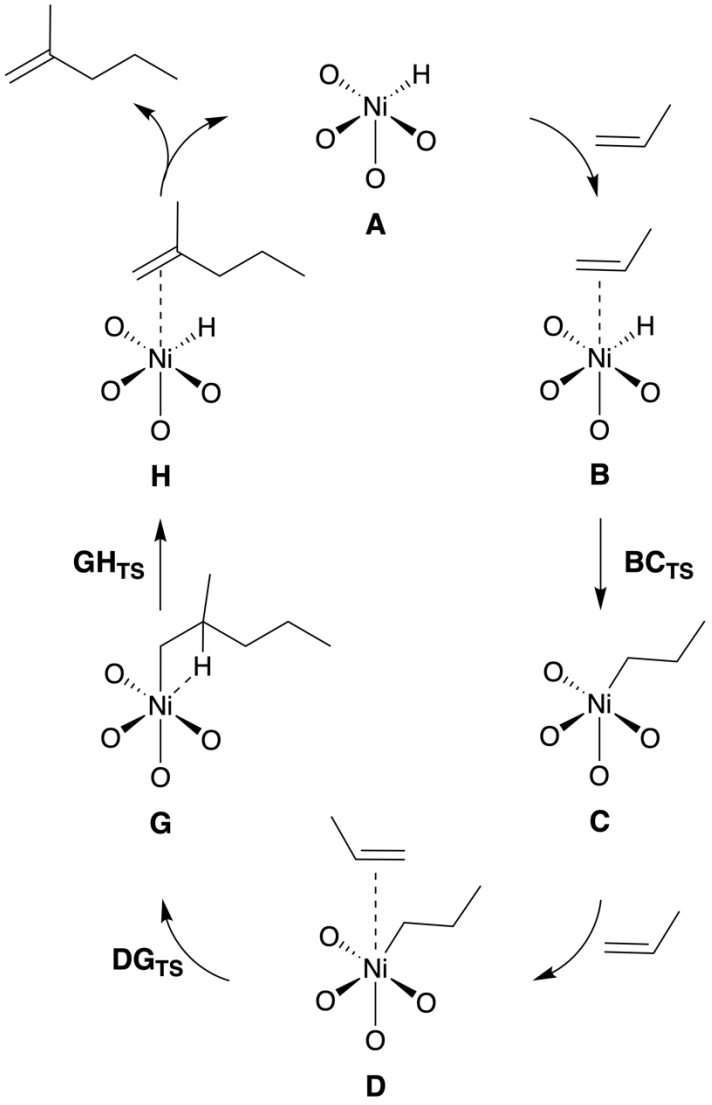

Figure 4.30. Pathway for the formation of 2-methylpentene through [1,2]-hydride insertion followed by [1,2]-C-C insertion in the Cossee-Arlman mechanism.

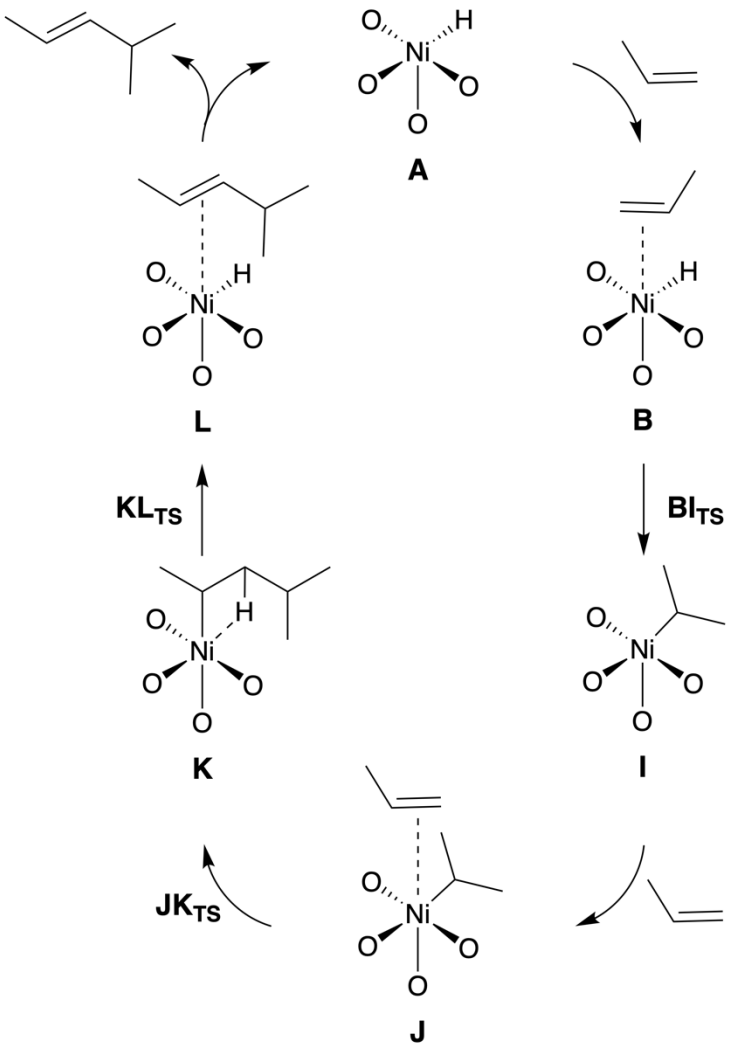

Figure 4.31. Pathway for the formation of 4-methylpentene through [2,1]-hydride insertion followed by [2,1]-C-C insertion in the Cossee-Arlman mechanism.

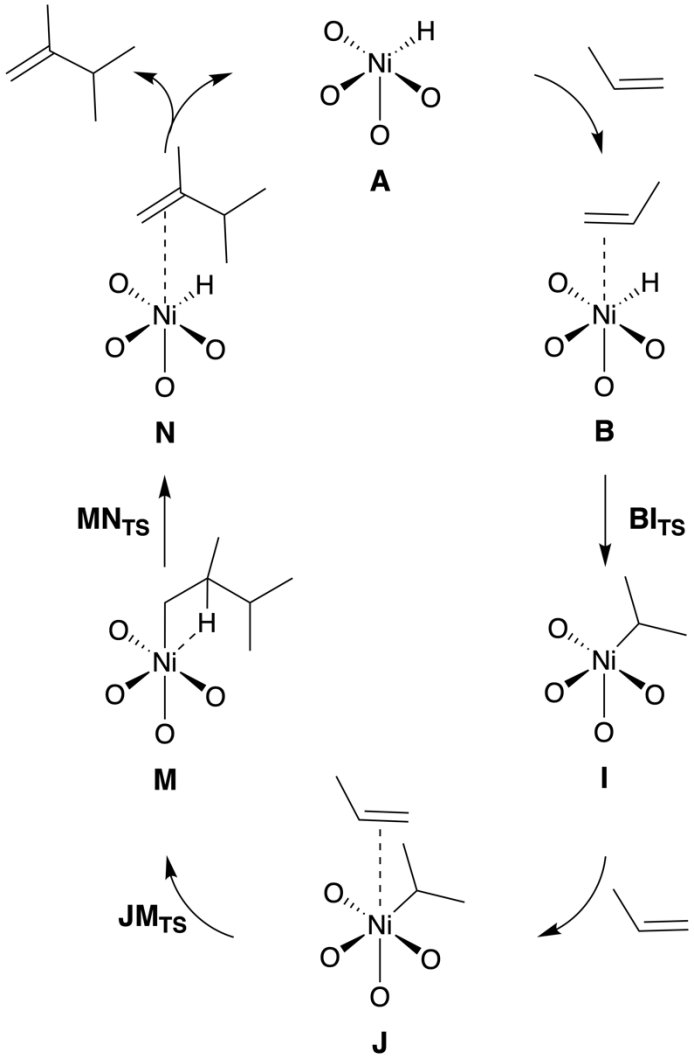

Figure 4.32. Pathway for the formation of 2,3-dimethylbutene through [2,1]-hydride insertion followed by [1,2]-C-C insertion in the Cossee-Arlman mechanism.

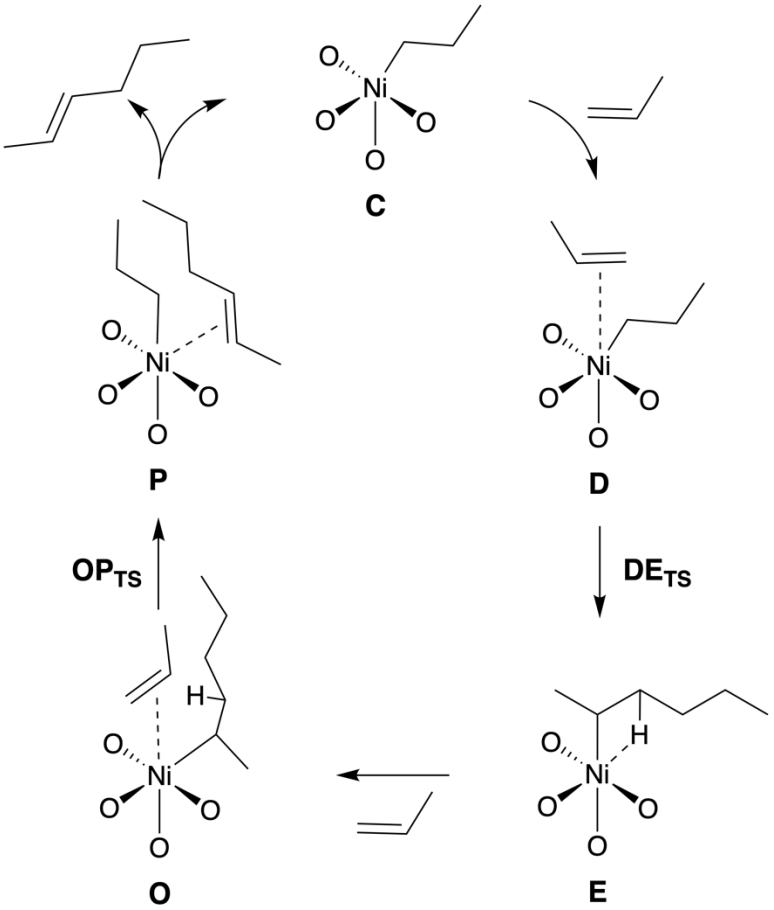

Figure 4.33. Pathway for the formation of linear hexene through [2,1]-C-C insertion followed by [1,2]-chain transfer to adsorbed propylene in the Cossee-Arlman mechanism.

Below, we present the various cluster models obtained and modified from Barona et al.[155] for Ni-MIL-127 which were used for subsequent DFT calculations for thermal activation of the MOF material and the Cossee-Arlman mechanism for propylene oligomerization (Figure 4.34).

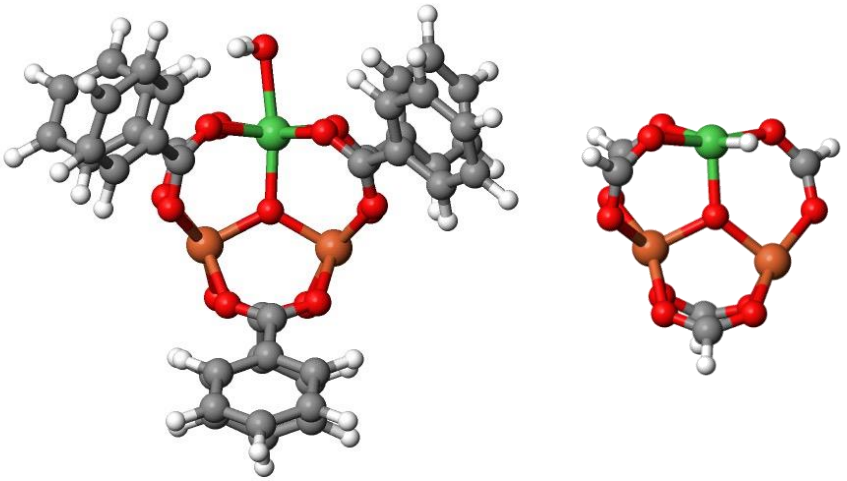

Model I *Model II*

Figure 4.34. Cluster models used in density functional theory (DFT) calculations. Benzene-capped model (*Model I*) to investigate the plausibility of linker decarboxylation, and formate-capped model (*Model II*) to investigate the Cossee-Arlman mechanism for propylene dimerization. Color code: Ni (green), Fe (orange), O (red), C (grey), and H (white).

The thermal treatment of Ni-MIL-127 was postulated to induce one missing linker defect per [$Fe_2Ni(\mu_3\text{-}O)$] of the MOF as evidenced from temperature programmed oxidation (TPO), ^1H nuclear magnetic resonance (NMR), and X-ray adsorption spectroscopy (XAS) measurements (Figure 4.10). We used KS-DFT calculations on benzene-capped clusters of Ni-MIL-127 (Figure 4.34, Model I) to further verify the plausibility of linker decarboxylation (Figure 4.35). The creation of a single missing linker defect proceeds with a free energy change of 82 kJ mol^{-1} at 298 K which decreases to 25 kJ mol^{-1} at 493 K (Table 4.10), consistent with the observation that creation of missing linker defects is favored at higher temperatures.

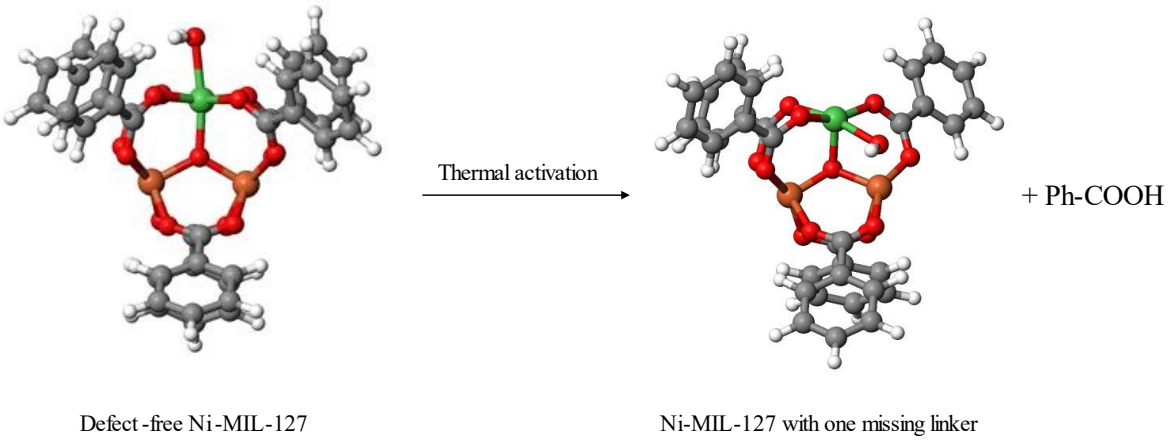

Figure 4.35. Investigation of missing linker defects postulated to be created upon thermal activation in Ni-MIL-127 using KS-DFT on benzene-capped cluster model (Model I) of the MOF. Ph-COOH denotes ABTC linker represented as benzene-COOH linkers in the cluster model. Color code: Ni (green), Fe (orange), O (red), C (grey), and H (white).

Table 4.10. DFT-based plausibility of the creation of missing linker defects upon thermal activation of Ni-MIL-127 at 101.3 kPa. Values are reported using the $2S + 1 = 13$ spin state for the defect-free and missing linker-defect containing MOF node which was found to be the most stable spin state.

Temperature	**ΔH / kJ mol^{-1}**	**ΔG / kJ mol^{-1}**
298 K	168	82
493 K	175	25

The free energy and enthalpy diagrams for propylene oligomerization on Ni-MIL-127 at 473 K and 101.3 kPa corresponding to Figures 4.29-4.33 are reported in Figures 4.36-4.40, respectively. The apparent activation energy for linear hexenes, 2-methylpentenes, 4-methylpentenes, and 2,3-dimethylbutenes were calculated from the difference in enthalpy between the Ni-propyl species and the carbon-carbon coupling steps (**C** and **DE$_{TS}$**, **C** and **DG$_{TS}$**, **I** and **JK$_{TS}$**, **I** and **JM$_{TS}$**, respectively) to yield apparent activation energies of 24 kJ mol^{-1}, 30 kJ mol^{-1}, 28 kJ mol^{-1}, and 42 kJ mol^{-1}, respectively.

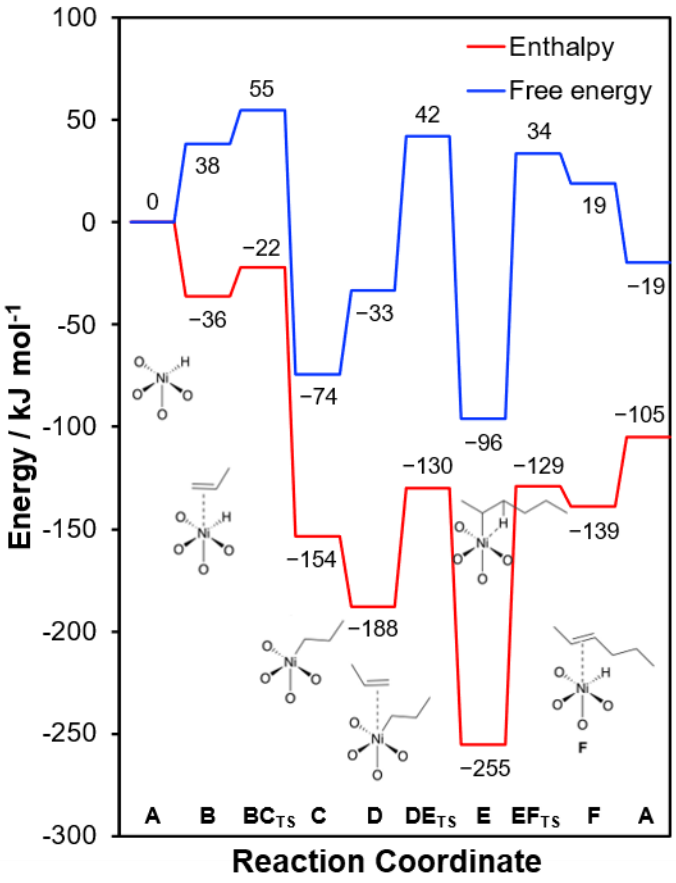

Figure 4.36. Enthalpy (red) and free energy (blue) diagram for dimerization of propylene to linear hexene following the Cossee-Arlman mechanism (Figure 4.29) calculated using the M06-L density functional on cluster model (*Model II*) of Ni-MIL-127 at 473 K and 101.3 kPa.

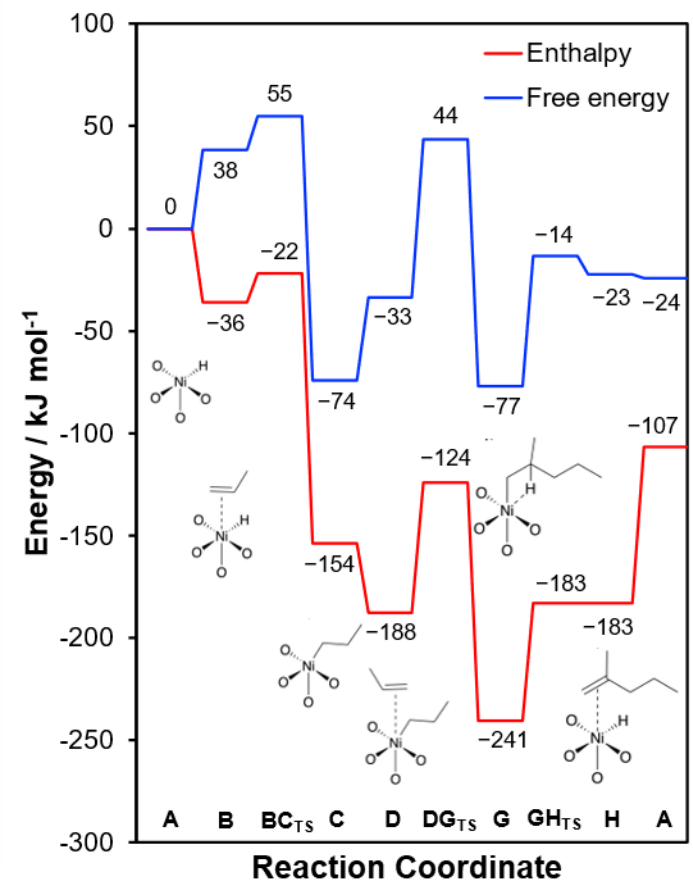

Figure 4.37. Enthalpy (red) and free energy (blue) diagram for dimerization of propylene to 2-methylpentene following the Cossee-Arlman mechanism (Figure 4.30) calculated using the M06-L density functional on cluster model (*Model II*) of Ni-MIL-127 at 473 K and 101.3 kPa.

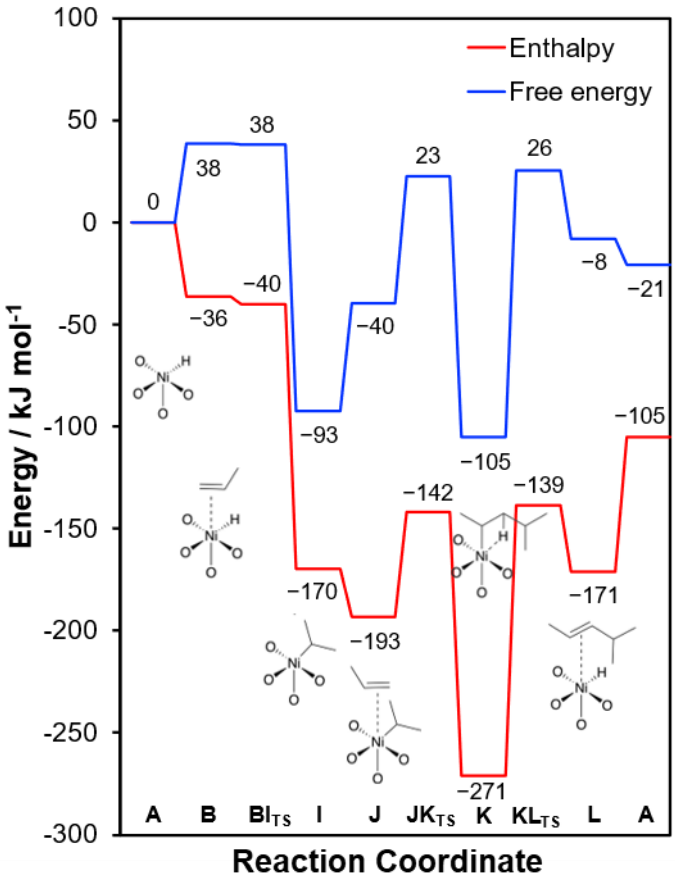

Figure 4.38. Enthalpy (red) and free energy (blue) diagram for dimerization of propylene to 4-methylpentene following the Cossee-Arlman mechanism (Figure 4.31) calculated using the M06-L density functional on cluster model (*Model II*) of Ni-MIL-127 at 473 K and 101.3 kPa.

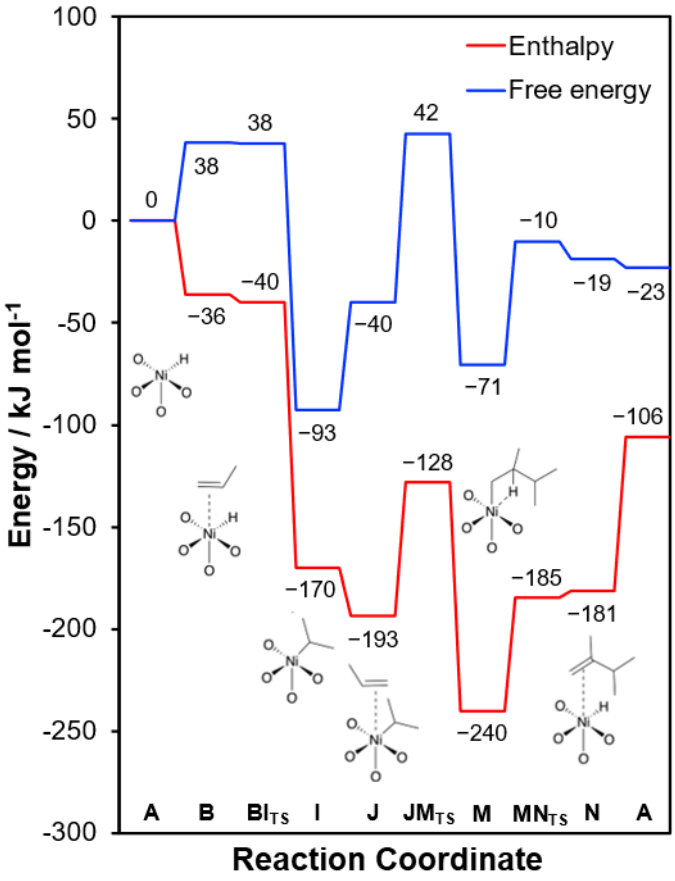

Figure 4.39. Enthalpy (red) and free energy (blue) diagram for dimerization of propylene to 2,3-dimethylbutene following the Cossee-Arlman mechanism (Figure 4.32) calculated using the M06-L density functional on cluster model (*Model II*) of Ni-MIL-127 at 473 K and 101.3 kPa.

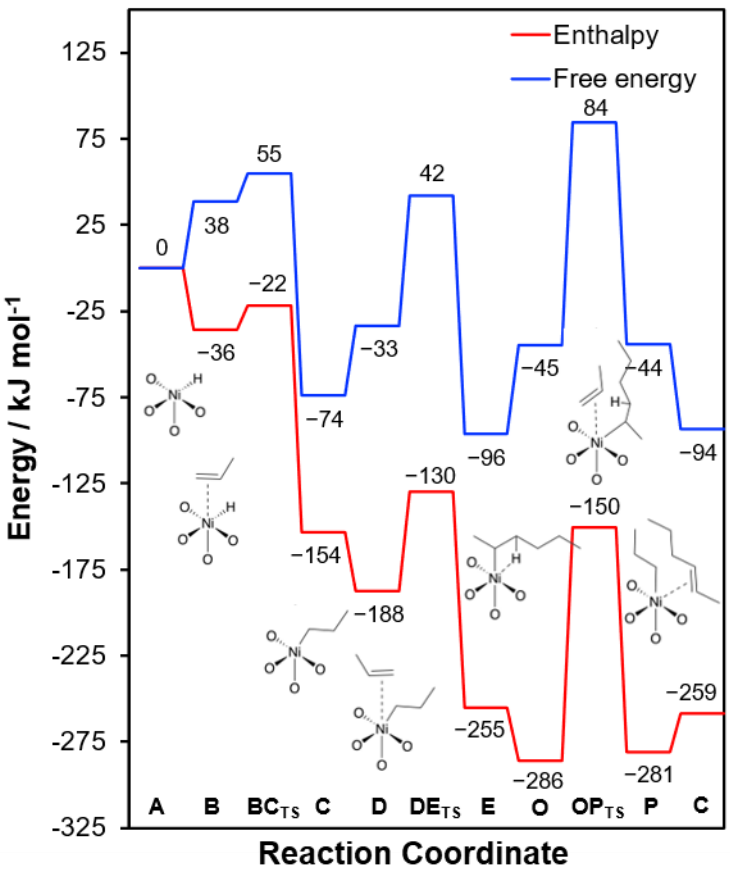

Figure 4.40. Enthalpy (red) and free energy (blue) diagram for dimerization of propylene to linear hexene following the [2,1]-C-C insertion and subsequent [1,2]-chain transfer to adsorbed propylene (Figure 4.33) calculated using the M06-L density functional on cluster model (*Model II*) of Ni-MIL-127 at 473 K and 101.3 kPa.

4.5.5. Proton Transfer and Metallacycle Mechanisms

Alternative to the hydride-mediated Cossee-Arlman mechanism for propylene oligomerization for linear hexene formation, a proton transfer (Phillips-type) reaction mechanism occurring on the Ni center of the nodes of Ni-MIL-127 (intermediate **PA**) was also investigated (Figure 4.41) with the reaction energy diagram presented in Figure 4.42. This mechanism proceeds with propylene adsorption on the vacant axial site of Ni centers of the MOF node (intermediate **PB**). The adsorbed propylene undergoes a C-H activation step ($\Delta G^{\neq} = 183$ kJ mol^{-1}) to transfer the proton to a hydroxyl ligand resulting in the formation of a Ni-propenyl intermediate (intermediate **PC**) and a water molecule. Subsequently, the adsorption of a second propylene molecule on the Ni center is assisted

by the simultaneous shuttle of the water molecule to the adjacent Fe center of the bimetallic node (intermediate **PD**). The adsorbed propylene molecule undergoes a C-C insertion step with the Ni-propenyl intermediate ($\Delta G^{\neq} = 48$ kJ mol^{-1}) to form a Ni-hexenyl intermediate (intermediate **PE**) with a vacant site on the Ni center. The water molecule is shuttled back to the vacant site of the Ni center (intermediate **PF**). The Ni-hexenyl intermediate then undergoes a proton transfer step ($\Delta G^{\neq} = 85$ kJ mol^{-1}) with the aqua ligand to form hexene adsorbed on the Ni center (intermediate **PG**). Desorption of the hexene product regenerates the active site for the next catalytic cycle. The C-H activation step is the rate-limiting step owing to its largest intrinsic free energy barrier along the reaction cycle, consistent with our previous investigation for 1-butene dimerization on isolated Ni(OH) centers of Ni/UiO-66 catalyst[129] and for ethylene oligomerization on Ni-SSZ-24 catalysts.[41] The computed first-order apparent activation barrier for this mechanism ($\Delta H^{\neq,app} = 112$ kJ mol^{-1}) is higher than that computed for propylene oligomerization following the Cossee-Arlman mechanism ($\Delta H^{\neq,app} = 24$ kJ mol^{-1}) and that measured experimentally (65.0 ± 5.8 kJ mol^{-1}). Additionally, the larger intrinsic rate-limiting free energy barrier of 191 kJ mol^{-1} for the proton-transfer mechanism compared to the intrinsic free energy for the kinetically relevant carbon-carbon coupling step of 76 kJ mol^{-1} for the Cossee-Arlman mechanism renders the Cossee-Arlman mechanism most favorable for propylene oligomerization.

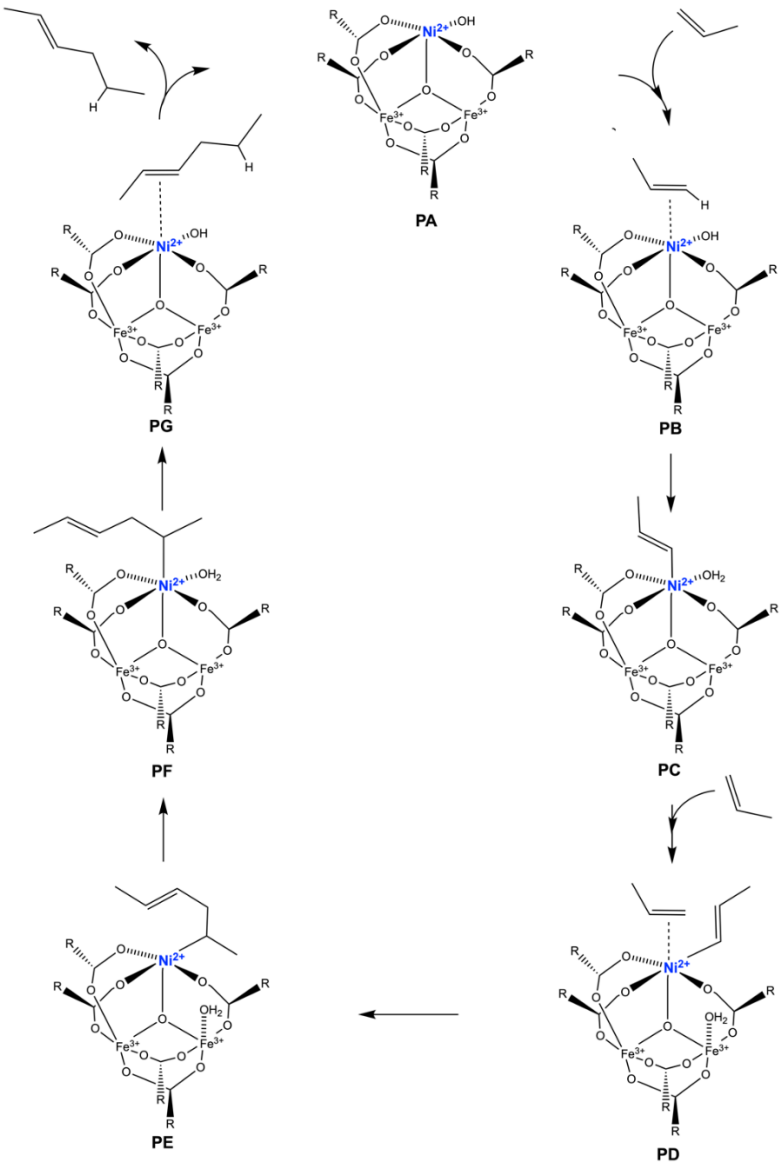

Figure 4.41. Proton transfer mechanism for propylene oligomerization to linear hexenes on Ni-MIL-127.

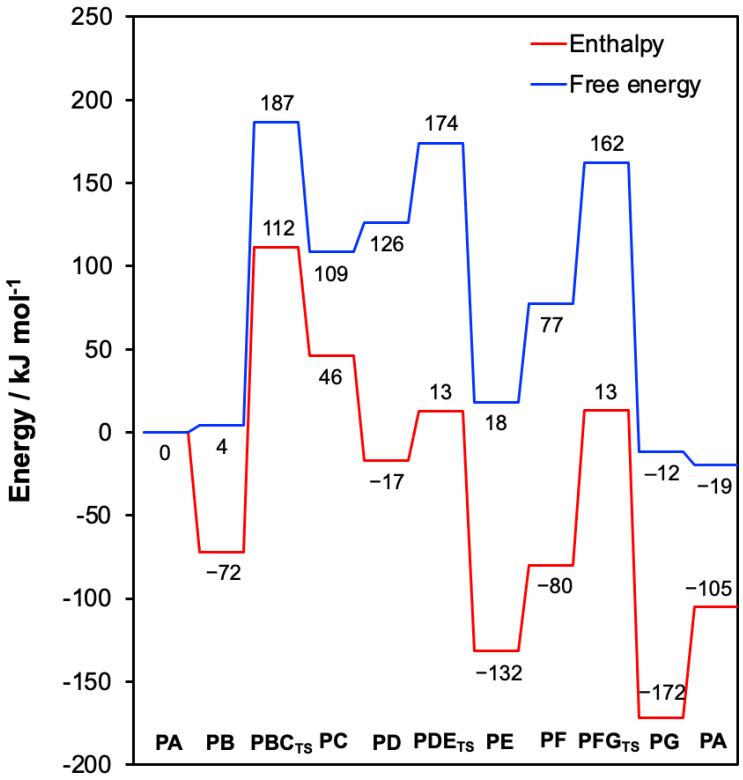

Figure 4.42. Enthalpy (red) and free energy (blue) diagram for the synthesis of linear hexenes via propylene oligomerization through the proton-transfer mechanism on Ni-MIL-127 at 473 K and 101.3 kPa. The most stable intermediates found along the (S^2 = 13) and (S^2 = 11) potential energy surface are shown.

In addition to our DFT calculations, the observed first order kinetics is not consistent with spectroscopic evidence. The proton transfer mechanism would suggest that **PA**, a Ni(OH) center, is the most abundant surface intermediate given observed first order kinetics. The difference IR spectrum from 2700-3100 cm^{-1} for Ni-MIL-127 in vacuum (<3 Pa) after exposure to flowing propylene at ambient pressure for 2 days at 473 K is presented in Figure 4.13 shows bands at 2962 cm^{-1}, 2923 cm^{-1}, and 2867 cm^{-1} which are attributed to aliphatic C-H bands.[37] These bands are neither consistent with the Ni(OH) center nor alkenyl intermediates in the proton transfer mechanism shown in Figure 4.41. These bands are consistent with the Ni-propyl intermediate, which we attribute as most abundant surface intermediate for the Cossee-Arlman mechanism, and thus, we discount the plausibility of the proton-transfer mechanism on Ni-MIL-127 for propylene oligomerization.

The other mechanism for olefin oligomerization on nickel-based catalysts is the metallacycle mechanism (Figure 4.43), which has mostly been proposed on homogeneous nickel-based catalysts, excluding the SHOP catalyst for ethylene oligomerization.[11] The metallacycle mechanism is characteristic of external activators, successive coordination of two olefin molecules, and a redox reaction on the nickel active site.[11,13,31,41] We note that the Ni-MIL-127 described herein does not use external activators during propylene oligomerization as an induction period is observed. Because the thermally activated material is a 5-coordinate nickel species (Table 4.5), successive coordination of two olefin molecules on the nickel center is improbable to allow for the metallacycle mechanism. From our in-situ XANES during propylene oligomerization (Figure 4.4c), the oxidation state of nickel remains as +2 compared to the thermally treated sample and no redox reaction is observed. The Cossee-Arlman mechanism for propylene oligomerization on Ni-MIL-127 is consistent with our experimental observations of the induction period in the absence of external activators that is required to form a nickel-propyl and then subsequent insertion of another propylene molecule, and a nickel oxidation state that remains as +2 throughout the reaction.[31,41]

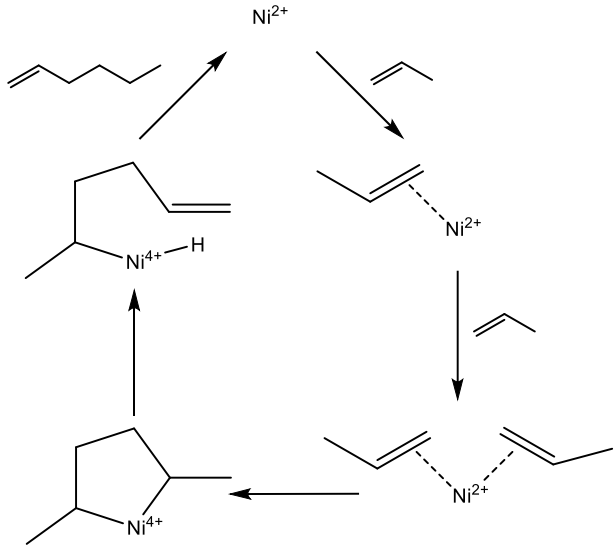

Figure 4.43 Metallacycle mechanism for propylene oligomerization to linear hexenes on nickel-based catalysts.

4.5.6. Tabulated data for the computed thermodynamic energies calculated using DFT

Table 4.11. Tabulated data of the absolute and relative electronic energies (E), enthalpies (H) and Gibbs free energies (G) at 473 K and 101.3 kPa for all DFT-optimized structures and their corresponding spin state and deviation in S^2 value. In cases where multiple spin states are reported for a given species, the spin state highlighted in blue was used as the most stable spin state for that species.

Structure	**$2S + 1$**	**Deviation in S^2**	***E* / Hartree**	***H* / Hartree**	***G* / Hartree**	**ΔE / kJ mol^{-1}**	**ΔH / kJ mol^{-1}**	**ΔG / kJ mol^{-1}**
Generation of a single missing linker defect upon thermal activation of Ni-MIL127 at 298 K								
Ph-COOH	1	0.0000	- 420.642663	- 420.505213	- 420.602477	-	-	-
Defect-free node	13	0.0001	-6708.083275	-6707.394499	-6707.528640	0.0	0.0	0.0
	11	0.0044	-6708.063125	-6707.374595	-6707.508465	52.9	52.3	53.0
Node with single missing linker	13	0.0001	-6287.379259	-6286.811348	-6286.929839	161.1	167.7	82.4
	11	0.0008	-6287.341966	-6286.773234	-6286.892964	259.0	267.8	179.2
Generation of a single missing linker defect upon thermal activation of Ni-MIL127 at 493 K								
Ph-COOH	1	0.0000	- 420.642663	- 420.505213	- 420.602477	-	-	-
Defect-free node	13	0.0001	-6708.083275	-6707.317426	-6707.635820	0.0	0.0	0.0
	11	0.0044	-6708.063125	-6707.297514	-6707.615468	52.9	52.3	53.4
Node with single missing linker	13	0.0001	-6287.379259	-6286.745761	-6287.023899	161.1	174.5	24.8
	11	0.0008	-6287.341966	-6286.707807	-6286.987792	259.0	274.1	119.6
Propylene dimerization to linear hexene following the Cossee-Arlman mechanism								
propylene	1	0.0000	- 117.799298	- 117.709775	- 117.763850	-	-	-
A	13	0.0002	-5057.690037	-5057.539251	-5057.678477	54	51	42
	11	0.0008	-5057.710519	-5057.558523	-5057.694391	0	0	0
B	13	0.0001	-5175.524840	-5175.282042	-5175.443589	-39	-36	38
	11	0.0025	-5175.509966	-5175.268507	-5175.434175	0	-1	63
BC_{TS}	13	0.0002	-5175.499091	-5175.258017	-5175.419075	28	27	103
	11	0.0021	-5175.517592	-5175.276633	-5175.437342	-20	-22	55
C	13	0.0002	-5175.550737	-5175.303856	-5175.468632	-107	-93	-27
	11	0.0013	-5175.574319	-5175.326827	-5175.486471	-169	-154	-74
D	13	0.0003	-5293.364333	-5293.025310	-5293.220253	-145	-124	5
	11	0.0020	-5293.390342	-5293.049597	-5293.234839	-213	-188	-33

DE_{TS}	13	0.0006	-5293.346935	-5293.009204	-5293.195486	-99	-82	70
	11	0.0029	-5293.367577	-5293.027624	-5293.206064	-153	-130	42
E	13	0.0002	-5293.400950	-5293.059529	-5293.245105	-241	-214	-60
	11	0.0052	-5293.417378	-5293.075299	-5293.258738	-284	-255	-96
EF_{TS}	13	0.0002	-5293.341197	-5293.005527	-5293.188532	-84	-72	88
	11	0.0022	-5293.362398	-5293.027128	-5293.209232	-140	-129	34
F	13	0.0001	-5293.368494	-5293.031003	-5293.214868	-156	-139	19
	11	0.0026	-5293.353951	-5293.017815	-5293.205357	-118	-104	44
linear hexene	1	0.0000	-235.642952	-235.459516	-235.535111	-	-	-
Propylene dimerization to 2-methylpentene following the Cossee-Arlman mechanism (Note: Only new intermediates and transition states are reported; the most stable spin sate for each type of species determined above were investigated)								
DG_{TS}	11	0.0021	-5293.364799	-5293.025303	-5293.205450	-146	-124	44
G	11	0.0025	-5293.411809	-5293.069770	-5293.251438	-270	-241	-77
GH_{TS}	11	0.0008	-5293.385311	-5293.047804	-5293.227237	-200	-183	-14
H	13	0.0001	-5293.370105	-5293.033594	-5293.217276	-160	-146	13
	11	0.0008	-5293.386624	-5293.047875	-5293.230685	-203	-183	-23
2-methyl pentene	1	0.0000	-235.644122	-235.460151	-235.537002	-	-	-
Propylene dimerization to 4-methylpentene following the Cossee-Arlman mechanism (Note: Only new intermediates and transition states are reported; the most stable spin sate for each type of species determined above were investigated)								
BI_{TS}	11	0.0024	-5175.524534	-5175.283510	-5175.443733	-39	-40	38
I	11	0.0017	-5175.580289	-5175.332981	-5175.493516	-185	-170	-93
J	11	0.0041	-5293.392094	-5293.051750	-5293.237200	-218	-193	-40
JK_{TS}	11	0.0053	-5293.371151	-5293.032080	-5293.213405	-163	-142	23
K	11	0.0018	-5293.422969	-5293.081341	-5293.262215	-299	-271	-105
KL_{TS}	11	0.0024	-5293.366403	-5293.030883	-5293.212374	-150	-139	26
L	13	0.0001	-5293.365462	-5293.028100	-5293.211330	-148	-131	28
	11	0.0009	-5293.382594	-5293.043215	-5293.225139	-193	-171	-8
4-methyl pentene	1	0.0000	-235.643826	-235.459920	-235.536511	-	-	-
Propylene dimerization to 2,3-dimethylbutene following the Cossee-Arlman mechanism (Note: Only new intermediates and transition states are reported; the most stable spin sate for each type of species determined above were investigated)								
JM_{TS}	11	0.0038	-5293.365864	-5293.026780	-5293.205921	-149	-128	42
M	11	0.0014	-5293.410973	-5293.069502	-5293.248965	-267	-240	-71
MN_{TS}	11	0.0011	-5293.385735	-5293.048394	-5293.226056	-201	-185	-10
N	13	0.0001	-5293.368518	-5293.031477	-5293.212527	-156	-140	25
	11	0.0009	-5293.386131	-5293.047143	-5293.229287	-202	-181	-19

2,3-dimethyl butene	1	0.0000	-235.643390	-235.459525	-235.535661	-	-	-
Propylene dimerization to linear hexene following the C-C insertion step and subsequent chain transfer to adsorbed propylene (Note: Only new intermediates and transition states are reported)								
O	13	0.0003	-5411.212790	-5410.779033	-5410.992709	-274	-239	-18
	11	0.0045	-5411.231791	-5410.796726	-5411.002915	-324	-286	-45
OP_{TS}	11	0.0294	-5411.172904	-5410.745132	-5410.953829	-169	-150	84
P	11	0.0027	-5411.229555	-5410.794940	-5411.002719	-318	-281	-44
Propylene dimerization to linear hexene following the proton transfer mechanism								
PA	13	0.0001	-5133.010734	-5132.850233	-5132.991598	0	0	0
	11	0.0061	-5132.989609	-5132.829222	-5132.970436	55	55	56
PB	13	0.0001	-5250.840613	-5250.587425	-5250.753936	-80	-72	4
	11	0.0054	-5250.829203	-5250.576163	-5250.745987	-50	-42	25
PBC_{TS}	13	0.0002	-5250.736689	-5250.489704	-5250.661950	193	185	245
	11	0.001	-5250.764947	-5250.517529	-5250.684366	118	112	187
PC	13	0.0001	-5250.795572	-5250.542756	-5250.713146	38	45	111
	11	0.0011	-5250.796221	-5250.542512	-5250.714109	36	46	109
PD	13	0.0002	-5368.610207	-5368.264913	-5368.461516	-2	13	152
	11	0.001	-5368.622625	-5368.276314	-5368.471206	-35	-17	126
PDE_{TS}	13	0.0003	-5368.579461	-5368.236320	-5368.428968	78	88	237
	11	0.0015	-5368.609946	-5368.264889	-5368.453016	-2	13	174
PE	13	0.0003	-5368.644225	-5368.297293	-5368.494606	-92	-72	65
	11	0.0025	-5368.667811	-5368.319967	-5368.512483	-154	-132	18
PF	13	0.0003	-5368.630110	-5368.283470	-5368.480616	-55	-36	102
	11	0.0035	-5368.647761	-5368.300250	-5368.489875	-101	-80	77
PFG_{TS}	13	0.0003	-5368.605190	-5368.264808	-5368.457468	11	13	162
	11	0.0023	-5368.592437	-5368.250841	-5368.437751	44	50	214
PG	13	0.0001	-5368.683179	-5368.335135	-5368.523776	-194	-172	-12
	11	0.0057	-5368.671395	-5368.323511	-5368.515789	-163	-141	9

Chapter 5. Olefin Oligomerization at Subambient Temperatures

5.1. Introduction

The utility of nickel-based heterogeneous catalysts formulated to mimic the Shell Higher Olefin Process catalyst, a homogeneous nickel catalyst, to selectively form linear alpha olefins (LAOs) during ethylene oligomerization has been limited by rapid deactivation due to the formation of higher molecular weight carbonaceous oligomers or of bridging nickel-alkene species that block the active site.[5,19,46,131] The former has been evidenced by dissolving Ni-H-Beta after reaction in HF while the latter was postulated from a hyperbolic decay of oligomerization reactivity and density functional theory (DFT) calculations.[32,46,72,131,170] Catalyst deactivation convolutes the ability to probe the active sites, kinetics, and mechanism for olefin oligomerization. Only four cases in the literature have reported nickel-based heterogeneous catalysts that are stable for olefin oligomerization in the absence of cocatalysts and the reaction conditions for these four studies are summarized in Table 5.1: (1) Ni/UiO-66, a zirconium oxide based MOF with nickel supported on the inorganic node through a missing benzene dicarboxylic (BDC) acid linker defect, active for ethylene oligomerization,[76] (2) Ni-UiO-67-bpy, an isoreticular MOF to UiO-66 with mixed linkers of biphenyl-dicarboxylic (bpdc) acid and bipyridine (bpy) with nickel supported on the bpy linker,[171] active for ethylene oligomerization, (3) Ni-MIL-127, a bimetallic nickel and iron oxo-trimer MOF with azobenzene tetracarboxylic acid (ABTC) linkers, active for propylene oligomerization,[77] and (4) Ni-MCM-41, a mesoporous Ni-based aluminosilicate, active for ethylene, propylene, and 1-butene oligomerization.[44,45] The former three studies on MOFs are investigated at elevated temperatures (> 473 K) and pressures (> 500 kPa) but have turnover frequencies several orders of magnitude lower than MOFs that use cocatalysts during the reaction; Ni-MFU-4l, the most active heterogeneous catalyst reported in the literature, uses methylaluminoxane (MAO) activators and has an ethylene oligomerization rate of 41,500 $mol_{C4=}$ mol_{Ni}^{-1} h^{-1} at 5 MPa and 298 K.[49] Ni-MCM-41 has obtained similar reaction rates for ethylene oligomerization as Ni-MFU-4l at 38,900 $mol_{C4=}$ mol_{Ni}^{-1} h^{-1} at subambient temperatures (258 K) and elevated pressures (3 MPa).

Table 5.1. Summary of stable olefin oligomerization catalysts reported in the literature and their process conditions, rates, and linear dimer selectivities.

Catalyst	Ni Content / wt%	Olefin	Pressure / kPa	Temperature / K	TOF / mol mol_{Ni}^{-1} hr^{-1}	Linear Dimer Selectivity	Reference
Ni/UiO-66	2.5	Ethylene	500	473	25.2	90%	[76]
Ni-UiO-67-bpy	1.1	Ethylene	2600	523	16.4	99%	[171]
Ni-MIL-127	3.8	Propylene	500	473	0.6	51%	[77]
Ni-MCM-41	0.2	Ethylene	3000	258	38,900	91%	[44]
Ni-MCM-41	0.2	Propylene	230	248	1,200	54%	[45]
Ni-MCM-41	0.2	1-Butene	55	248	350	N/A	[45]

The stability of Ni-MCM-41 was only observed at subambient temperatures (<258 K) for olefin oligomerization, as the catalyst deactivated at elevated temperatures (> 448 K).[42,44,45,83] This phenomenon was attributed to the formation of intrapore liquids in the pores of Ni-MCM-41 during olefin oligomerization at subambient temperatures and elevated pressures where intrapore liquids have been proposed to solvate transition state structures to preferentially desorb dimers over propagating oligomer chain growth, which is postulated to cause deactivation.[44,45] The extent of filling of intrapore liquid alkenes in the pores of the material at various temperatures and pressures was determined using nitrogen isotherms and the Barret-Joyner-Halenda (BJH) equation and was validated by showing that large pore (3.5 ± 2.5 nm) Ni-MCM-41 deactivated at higher pressures (<1.5 MPa) while small pore (1.7 ± 0.5 nm) Ni-MCM-41 deactivated at lower pressures (<1.1 MPa) at 248 K for ethylene oligomerization, as more alkene molecules are required to fill larger pores of the catalyst to promote desorption of the resulting product.[44,45,172] This method of forming an intrapore liquid in the pores to mitigate catalyst deactivation has also been shown in aldol condensation reactions on anatase TiO_2 catalysts in the presence of nonpolar liquids, which was proposed to also solvate the transition state and promote desorption over carbon-carbon coupling reactions.[173]

In contrast, studies to eliminate catalyst deactivation using microporous zeolitic materials such as Ni-Beta and Ni-FAU were unable to demonstrate that intrapore liquids could attenuate catalyst deactivation at 248 K and 2.4 MPa of ethylene.[42] The authors proposed that the smaller micropores in zeolites restrict the coordination and confinement of ethylene molecules in the pores, which inhibits the ability for ethylene molecules to form

adsorbed multilayers to interact with the pore surfaces, and thus form an intrapore liquid in the pore.[42,174] As a result, the loosely bound ethylene molecules would not effectively solvate the transition state, which would not promote desorption of 1-butene.[42] Hence, it was postulated that microporous materials cannot solvate olefin molecules and prevent deactivation during oligomerization while mesoporous materials could condense an intrapore liquid.

Zeolites have smaller pores (<1 nm) than metal organic frameworks (MOFs), which have pore sizes >1 nm,[63,175] which provide a greater ability for olefin molecules to bind to the active site within the pores of the MOF to promote stable olefin oligomerization. MOF structures have been shown to be dynamic in nature with the inorganic node and organic linker exhibiting structural flexibility in the presence of various adsorbed molecules as shown in gas separation studies.[176,177] Molecular dynamic simulations with UiO-66 show up to a 20% increase in uptake of different molecules at 298 K with a flexible MOF structure compared to rigid MOF structures at 77 K.[178–180] We hypothesized that the larger pore sizes in MOFs and the flexibility of the MOF structure allows the material to adsorb more olefin molecules and could enable the formation of an intrapore liquid to facilitate stable olefin oligomerization.

In this work, we attempted to alleviate catalyst deactivation on Ni-MOF-74 or Ni-CPO-27, a nickel framework-based catalyst which has been previously shown to deactivate with time on stream for ethylene and propylene oligomerization at 453 K,[72] for ethylene and propylene oligomerization by forming an intrapore liquid at subambient temperatures and elevated pressures. For ethylene oligomerization, the catalyst deactivated at 258 K regardless of ethylene partial pressure (1100 – 2900 kPa) but was stable at 243 K while the catalyst was stable for propylene oligomerization at 273 K despite changes in relative propylene pressure (200 – 500 kPa). These observations suggest that the formation of intrapore liquids do not mitigate catalyst deactivation in Ni-MOF-74. At these conditions, low conversion data on Ni-MOF-74 for ethylene oligomerization was obtained to show that 1-butene selectivity (>92% selectivity) was higher than those at elevated temperatures and pressures to validate that 1-butene is a primary product for dimerization and 2-butenes

are formed via isomerization and reinsertion of 1-butene, consistent with the Cossee-Arlman mechanism.

5.2. Experimental Methods

5.2.1. Synthesis of MOFs[15]

Ni-MOF-74 was synthesized following a modified procedure reported in the literature.[181–183] A solution of 743 mg of 2,5-dihydroxyterephthalic acid (Alfa Aesar, 97%, 3.75 mmol) in 12.5 cm^3 of THF (Sigma-Aldrich, 99.9%) and a solution 1.87 g of nickel(II) acetate tetrahydrate (Acros Organics, 100%) in 12.5 cm^3 of HPLC grade water (Fisher Chemical) were individually sonicated until the solids were completely dissolved. The acid solution was added to the aqueous solution in a 50 cm^3 Teflon lined inset. The inset was put into the autoclave, sealed, and reacted for 3 days at 383 K in a preheated oven. The product was vacuum filtered and washed three times with ~50 cm^3 of HPLC grade water. The final product was dried at 363 K in an oven for 24 hours.

5.2.2. Catalytic Testing

Ni-MOF-74 (5 - 1000 mg) was packed between two quartz wool plugs (Technical Glass Products). The free volume in the reactor tube was filled with quartz rods (3 mm O.D.; Technical Glass Products) to prevent any vertical displacement of the catalyst bed. The tubular reactor was then placed inside a resistively heated furnace (Applied Test Systems). The temperature was measured and regulated using a K-type thermocouple (Omega) wrapped around the periphery of the stainless-steel reactor with the tip placed at the center of the catalyst bed and an electronic controller (Watlow), respectively. The catalyst was pretreated in helium (Matheson, 99.997%, 0.83 $cm^3\ s^{-1}$) from ambient temperature to 473 K (0.08 $K\ s^{-1}$) for 4 hours and then cooled to reaction temperature (298-473 K) if the reaction temperature was >298 K or to ambient temperature (~298 K) if the reaction temperature was <298 K in flowing helium (Matheson, 99.997%, 0.83 $cm^3\ s^{-1}$). For subambient reaction temperatures (243-298 K), the flow of liquid nitrogen was controlled with a needle valve and fed through a brass tube inserted inside the resistively heated furnace with the electronic controller regulating the reaction temperature. Ethylene

[15] Ni-MOF-74 was synthesized by Caleb Lavallee at the University of Minnesota

(Matheson, 99.999%, 0.083-83 $cm^3\ s^{-1}$) or propylene (Matheson, 99.87%, 0.083-83 $cm^3\ s^{-1}$) was introduced to the reactor with flow controlled by mass flow controllers (Brooks 5850E Series). The gas-phase pressure (500 – 3000 kPa) was measured using a pressure transducer (Omega) placed upstream of the reactor and controlled using a back-pressure regulator (TESCOM Series 44-2300) placed downstream of the reactor. The composition of the reactor effluent was quantified using a gas chromatograph (Agilent GC 7890A) equipped with a dimethylpolysiloxane HP-1 column (50 m × 320 μm × 0.52 μm) connected to a flame ionization detector (FID). The saturation pressures to determine the relative olefin pressures was calculated using Equation 5.1

$$\log\left(\frac{P_{sat}}{0.1322}\right) = \frac{-0.2185 * A}{T} + B \qquad \text{(Eq.5.1)}$$

where P_{sat} is in kPa and T is in Kelvin with the values of A and B given in Table 5.2 with the valid temperature ranges.[184]

Table 5.2. Parameters for A and B in Equation 5.1 and their valid temperature ranges.

Molecule	A	B	Temperature Range / K
Ethylene	3453.7	7.298306	104.7 – 281.9
Propylene	4697.4	7.39391	141.1 – 358.0

5.2.3. Powder X-Ray Diffraction (PXRD)[16]

PXRD patterns were collected over a 2θ range of 5-50° at 0.01° resolution with a Smartlab SE (Rigaku) diffractometer with Cu-Kα radiation (λ=1.54414 Å).

5.2.4. N_2 Isotherms[17]

Nitrogen adsorption isotherms were measured at 77 K using an ASAP 2020 surface area and porosity analyzer (Micromeritics) after removing water by degassing the samples at <150 Pa at 473 K for four hours. Surface areas were determined by fitting a Langmuir isotherm between P/P_0 values of 0.05 and 0.30.

[16] PXRD was collected by Caleb Lavallee at the Characterization Facility at the University of Minnesota
[17] N_2 isotherms were collected by Caleb Lavallee at the University of Minnesota

5.2.5. NO Titration with Infrared Spectroscopy

Ni-MOF-74 was diluted and physically mixed with $CaCO_3$ (Neta Scientific, 99.995%) in 1:4.5 ratio by mass. Wafers of the diluted MOF sample (~16 mg) for infrared (IR) spectroscopy were pressed (<1.4 MPa) and placed in a quartz IR cell with KBr (Sigma-Aldrich) windows. Spectra from 400-4000 cm^{-1} at a resolution of 2 cm^{-1} with an average of 32 scans were measured with a Nicolet 6700 spectrometer. The sample was heated in an IR cell from ambient temperature to 473 K (0.067 K s^{-1}) in flowing helium (Matheson, 99.997%) and held for 2 hours at 473 K. After 2 hours, vacuum (<3 Pa) was pulled on the sample and the spectra were collected. Nitric oxide (Matheson, CP Grade) was dosed from a 23.71 cm^3 dosing volume after the pressure stabilized after each dose, and the pressure was monitored with a pressure transducer (Kurt J. Lesker).

5.2.6. X-Ray Absorption Spectroscopy (XAS)[18]

All XAS spectra were collected at beamline 4-1 at Stanford Synchrotron Radiation Light source (SSRL). All experiments were carried out in transmission mode and with a water cooled double-crystal monochromator with Si (220) crystals. Six inch long, nitrogen-filled, ion chambers, operated with an 1800 VDC bias, were used to measure the relative intensity of the X-ray beam before and after the sample, and before and after the reference foil. A Ni foil located downbeam of the sample was used as an internal reference to calibrate the photon energy of each spectrum. The as-synthesized Ni-MOF-74 was diluted with SiO_2 in a 1:1 ratio by mass to obtain a total absorption length of 2.5, determined at 50 eV above the Ni K-edge. The sample (~4 mg mixed) was loaded in an *in-situ* XAS cell[134] forming an approximately 1 cm long catalyst bed located in between two quartz wool plugs inside the 1 mm OD, 0.96 mm ID, quartz capillary.

Extended X-ray absorption fine structure (EXAFS) spectra at the Ni-K edge (8333 eV) were collected for the as-synthesized sample in helium (0.16 cm^3 s^{-1}) at 298 K. X-ray absorption near edge structure (XANES) spectra were collected while the temperature was ramped at 0.05 K s^{-1} until 393 K and held for 1 hours where EXAFS spectra for the Ni-K

[18] XAS spectra were collected in collaboration with Adam Hoffman, Jiyun Hong, Jorge Perez-Aguilar, and Simon R. Bare at SSRL.

edge were obtained. Each XANES and EXAFS spectrum took approximately 5 and 15 minutes, respectively, to collect.

5.3. Results and Discussion

5.3.1. Characterization of Ni-MOF-74 and the Nickel Active Site

Ni-MOF-74 ($[Ni_2(dhtp)(H_2O)_2]\cdot 8H_2O$) is a honeycomb MOF structure with intersections of the honeycombs connected with one-dimensional helical chains formed by nickel-oxygen coordinated octahedra and the adjacent honeycombs connected by the organic linker, as shown in Figure 5.1a.[182,185] The PXRD and N_2 isotherms are reported below in Figure 5.1b and Figure 5.1c to confirm the crystallinity and porosity of Ni-MOF-74, respectively. The BET surface area and micropore volume of Ni-MOF-74 was 743 m^2 g^{-1} and 0.41 cm^3 g^{-1}, respectively. The surface area of the MOF is lower than what is generally reported in the literature, which has a range of 780 – 1400 m^2 g^{-1}.[183,186–188] The pore size distribution is shown in Figure 5.1d with an average pore size of 1.94 nm from the BJH desorption isotherm.

The number of framework nickel atoms were enumerated with ex-situ titrations with IR spectroscopy. The IR spectra of Ni-MOF-74 is shown in Figure 5.2a after cumulative amount of 106 µmol of NO was dosed onto the sample. A peak at 1847 cm^{-1} is observed after dosing NO into the IR cell at 473 K. This peak corresponds to a Ni(II)-NO adduct, which was reported previously in an experiment with dosing NO onto Ni-MOF-74 at room temperature to 10 Pa.[163] We note the peak at 1874 cm^{-1} corresponds to gas phase NO that is not absorbed on the surface. The amount of nickel was quantified assuming one NO molecule binds to one nickel atom and by integration of band areas upon NO dosing until the band at 1847 cm^{-1} saturated, as depicted in Figure 5.2b. The Ni(II)-NO band saturates at ~5500 µmol g^{-1} of NO dosed, which is in good agreement with an expected NO dosed of ~5800 µmol g^{-1} for the dehydrated Ni-MOF-74.

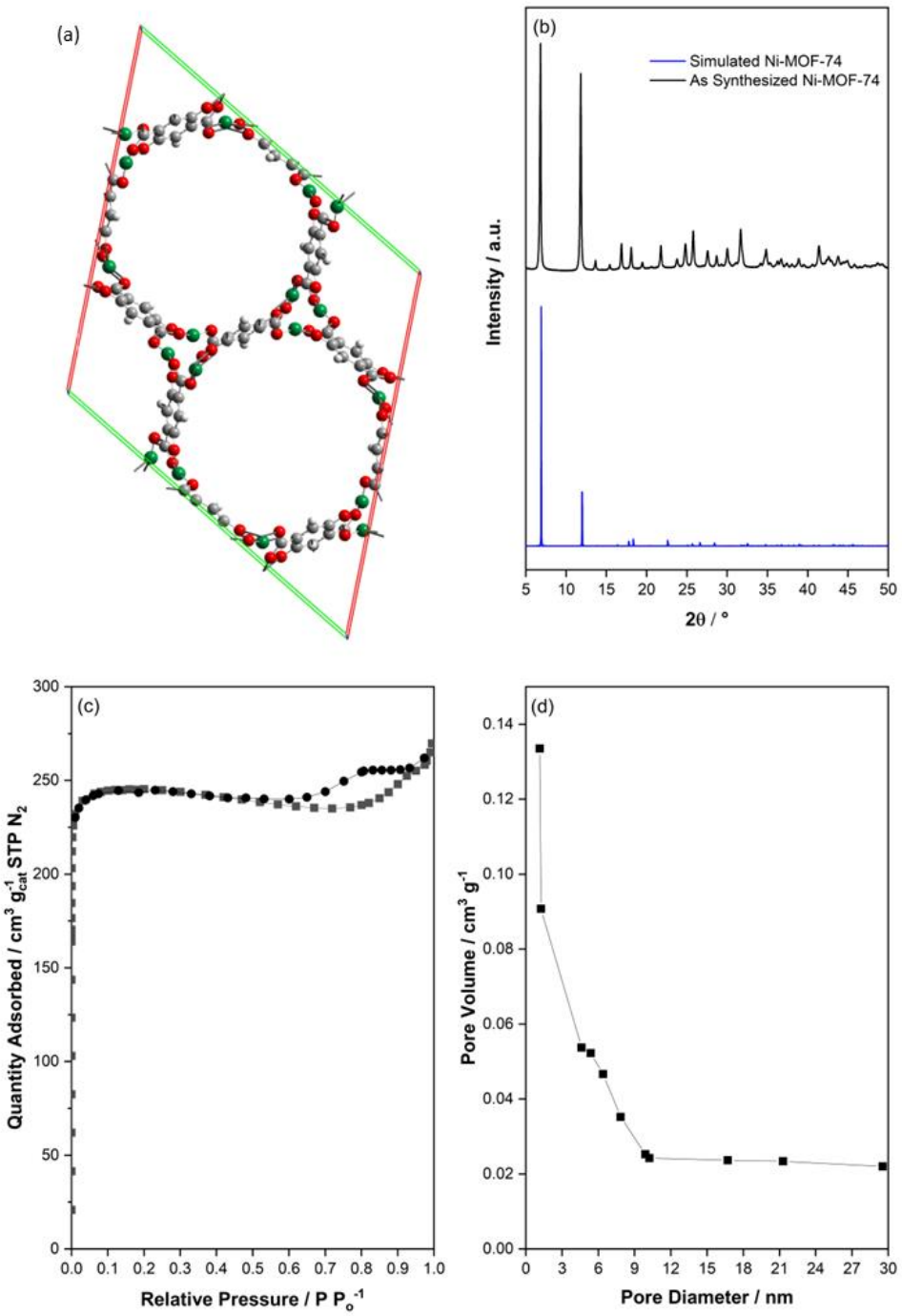

Figure 5.1. (a) Bidimensional representation of dehydrated Ni-MOF-74 with carbon, hydrogen, oxygen, and nickel in grey, red, white, and green respectively. (b) PXRD pattern of simulated[189] (blue) and as synthesized (black) Ni-MOF-74. (c) N_2 isotherm and (d) pore size distribution of Ni-MOF-74.

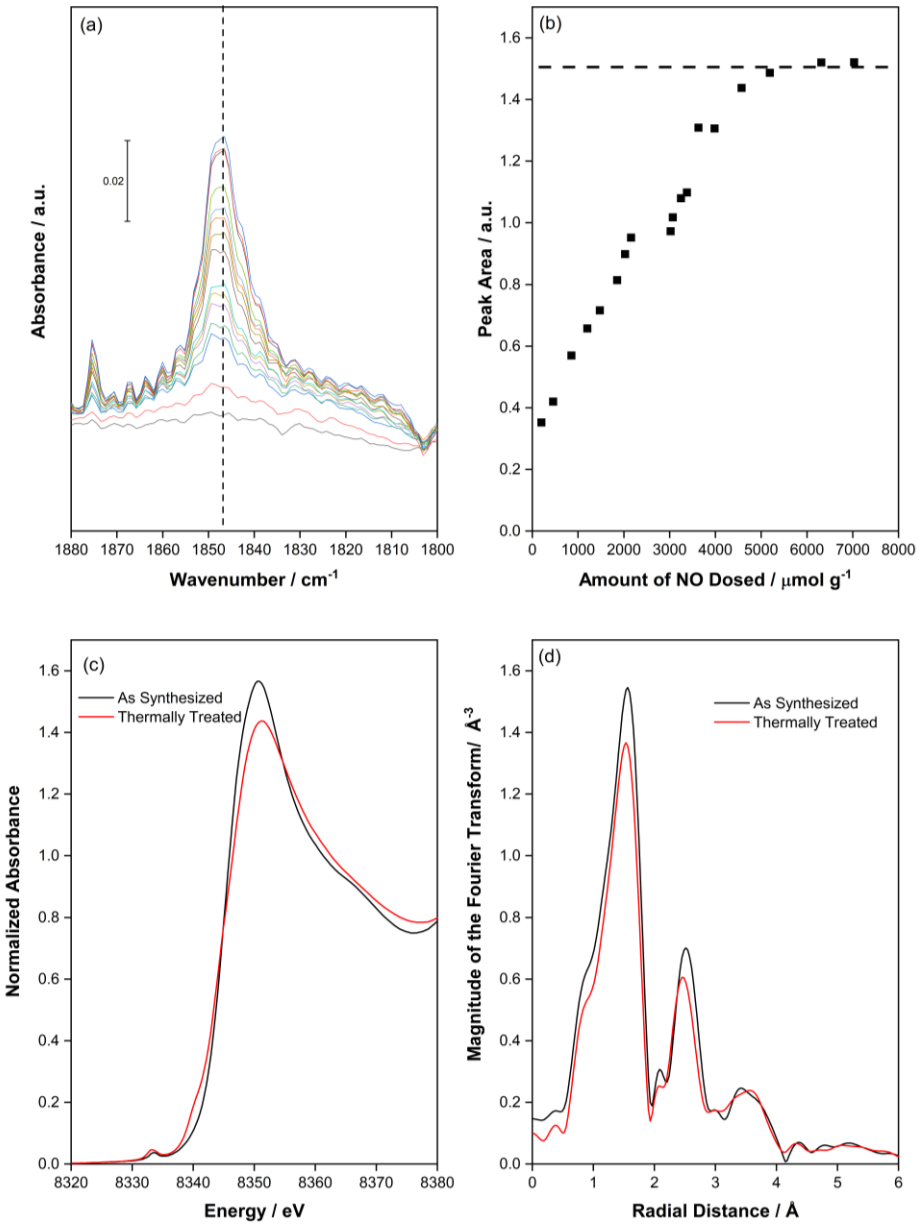

Figure 5.2. (a) IR spectra with a cumulative dose of 106 μmol of NO and (b) the corresponding plot of the integration of the Ni(II)-NO peak areas versus the cumulative amount of NO dosed on 16.4 mg pellet of 18% Ni-MOF-74 and 82% $CaCO_3$ by weight at 473 K. of as synthesized Ni-MIL-127 at 77 K. (c) Ni K-edge XANES and (d) EXAFS data (magnitude of the Fourier transform (k^2-weight)) in the k range of 3.0 $Å^{-1} < k < 12.6$ $Å^{-1}$ for Ni-MOF-74 as synthesized (black) and thermally activated (493 K in 0.16 cm^3 s^{-1} helium, red)

The speciation and coordination of nickel on Ni-MOF-74 was examined with XAS as synthesized and after thermal pretreatment at 473 K in helium, which was also studied previously by Bordiga et al.[163] From the XANES region as shown in Figure 5.2c, the main observations are described: (1) the peak at 8333.3 eV shifts to 8332.9 eV and increases in intensity from the as synthesized to thermally treated sample. (2) A new band at 8339.6 eV appears in the thermally treated sample. (3) There is no change in the rising edge energy between the two samples, and (4) the feature at 8350.6 eV decreases in intensity and blueshifts to 8351.1 eV from the as synthesized to thermally treated sample. The redshift of the pre-edge peak at 8332.9 eV corresponds to a 1s to 3d electronic transition which corresponds to a loss in an inversion center.[163] The formation of the band at 8339.6 eV corresponds to a 1s to $4p_z$ transition which is indicative of a symmetry reduction. The two observations suggest the nickel species is an octahedral-like geometry and changes to a square-pyramidal-like geometry after thermal activation.[163–165] The same rising edge energy between the samples suggests that there is no change in oxidation state after thermally treating the samples to suggest that nickel is in the 2+ oxidation state, consistent with the Ni(II) species observed from ex-situ NO titrations in Figure 5.2a. The decrease in the white line intensity indicates a decrease in the coordination of the nickel atom. In the EXAFS region of Ni-MOF-74 in Figure 5.2d, the first coordination shell at 1.56 Å corresponds to a Ni-O scattering path and decreases in intensity,[163] consistent with the loss of coordination evinced from the decrease in white line intensity in the XANES analysis. The peak from 2.1 – 2.9 Å decreases in intensity and corresponds to the second coordination shell and was attributed to Ni-Ni and Ni-C scattering paths, which could not be deconvoluted previously.[163] From IR spectroscopy and XAS, the precatalyst contains ~5500 μmol g^{-1} nickel active sites with an oxidation state of 2+ in square-pyramidal-like geometry.

5.3.2. Investigation of Olefin Oligomerization Activity, Stability, and Selectivity on Ni-MOF-74 at Subambient Temperatures

Time on stream for ethylene and propylene oligomerization in the absence of cocatalysts on Ni-MOF-74 is shown in Figure 5.3a at an elevated temperature of 453 K and 500 kPa of olefin. At the elevated temperature, an induction period is observed, and

the catalyst deactivates immediately after the rate reaches a maximum, consistent with prior reports of Ni-MOF-74 for ethylene and propylene oligomerization at the same reaction conditions reported here.[72] The induction period and deactivation is attributed to a stoichiometric reaction to generate the catalytically relevant Ni-alkyl species and to the production of longer chain molecular weight hydrocarbons, respectively.[72] Operation at subambient temperatures, 243 K for ethylene ($P_i/P_{i,sat}$ = 0.90) and 273 K for propylene ($P_i/P_{i,sat}$ = 0.87), show stable oligomerization rates, as shown in Figure 5.3. Rates at these subambient conditions are 10^3 – 10^4 lower than those reported at elevated temperatures. These results seem to suggest that lower temperatures mitigate catalyst deactivation for olefin oligomerization.

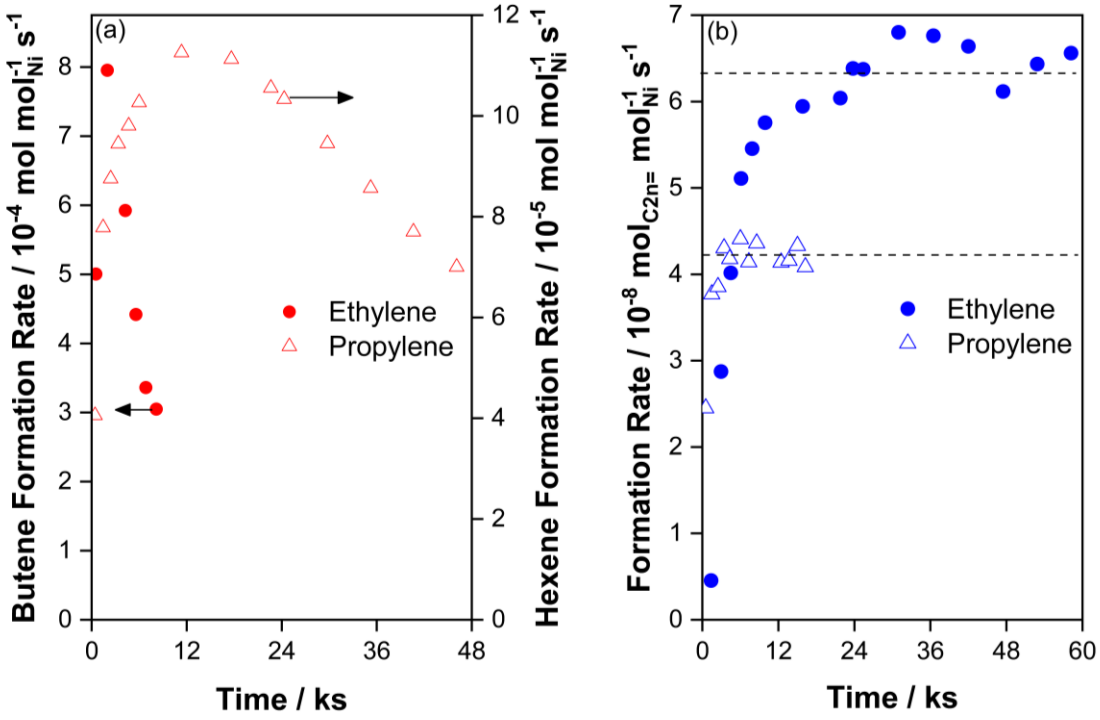

Figure 5.3. Butene and hexene formation rates for ethylene (●) and propylene (△) oligomerization at (a) 500 kPa and 473 K (red) on 11.1 and 12.2 mg, respectively, of Ni-MOF-74 and at (b) elevated relative olefin pressures, ($P_i/P_{i,sat}$),(blue) of 0.90 (243 K and 1807 kPa) and 0.87 (273 K and 500 kPa), respectively, on 51.2 mg and 66.3 mg, respectively, of Ni-MOF-74

The hypothesis that formation of intrapore liquids eliminates catalyst deactivation was scrutinized by changing relative olefin pressures. Capillary condensation was postulated on Ni-Beta at relative ethylene pressures > 0.51 with 1.2-1.5 nm pores and on Ni-MCM-41 at relative ethylene pressures > 0.65 with 3-5 nm pores as pore size is inversely related to the capillary condensation pressure which was estimated from the Kelvin equation.[42,44,45] With an intermediate pore size between Ni-Beta and Ni-MCM-41 on Ni-MOF-74 (~1.9 nm), we hypothesized an intrapore liquid would form at relative olefin pressures ($P_i/P_{i,sat}$) > 0.7. Ethylene oligomerization rates at 258 K and pressures of 2294 kPa and 1099 kPa, corresponding to relative ethylene pressures of 0.73 and 0.35, respectively, on Ni-MOF-74 are shown in Figure 5.4a. At both process conditions, the catalyst deactivates with time on stream with the condition at higher relative ethylene pressures deactivating more quickly, suggesting that the formation of intrapore liquids in Ni-MOF-74 do not eliminate deactivation. To further probe capillary condensation and its effect on catalyst stability, propylene oligomerization at 500 kPa and 207 kPa at 273 K, corresponding to relative propylene pressures of 0.87 and 0.36, was studied as shown in Figure 5.4b. The catalyst appeared to be stable at both conditions, even at the lower relative propylene pressure of 0.36, suggesting that changes in the relative olefin pressures and the formation of intrapore liquids do not affect catalyst deactivation.

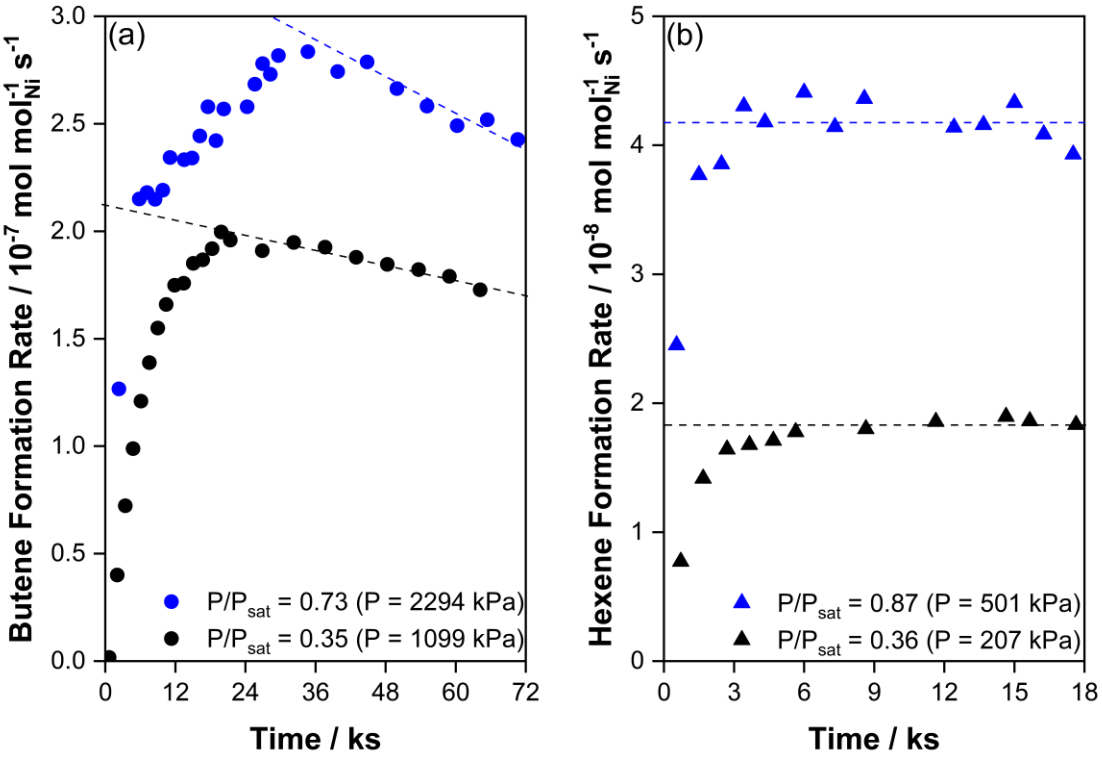

Figure 5.4. (a) Butene formation rates for ethylene oligomerization (●) at high (blue) and low (black) relative ethylene pressures of 0.73 and 0.35 at 258 K and hexene formation rates for propylene oligomerization (▲) at high (blue) and low (black) relative propylene pressures of 0.87 and 0.36 at 273 K on Ni-MOF-74

From observations in Figure 5.4, we posit that lower temperatures do not generate intrapore liquids that promote desorption of products to prevent oligomer chain growth but lengthen the induction period for olefin oligomerization. This hypothesis is consistent with the observation during olefin oligomerization on Ni/UiO-66,[76] Ni-MIL-127,[77] and Ni-Na-X,[35] which reported temperature-dependent induction periods prior to steady state. By just observation of reaction rates, the induction period and steady state could not be deconvoluted at subambient temperatures. As shown in Figure 5.3b and Figure 5.4a at the same ethylene partial pressures of 0.73, catalyst deactivation is observed at 258 K and 2294 kPa but deactivation is not observed at 243 K and 1512 kPa. Thus, we posit that deactivation is not observed at the lower temperature (243 K) because the induction period is extended, resulting in the appearance of stable reaction rates. Additionally, deactivation

is faster at higher pressures, as shown in Figure 5.4a, which is consistent with formation of larger hydrocarbons to cause catalyst deactivation as the rate of chain growth for oligomerization will increase due to the increased rate of dimer formation from higher reactant pressures.[46] Therefore, subambient temperatures and operating at high relative olefin pressures does not form an intrapore liquid in Ni-MOF-74 that stabilizes the catalyst but increases the duration of the initiation period prior to steady state and promotes catalyst deactivation at higher pressures at the same subambient temperature.

We note that the claim of catalyst stability in previous studies for olefin oligomerization was only valid for ~300 minutes, or 18 ks, on stream, at one process condition at a subambient temperature and elevated pressure, and the catalyst was not tested for stability at longer lifetimes.[42,44,45] Propylene oligomerization at 500 kPa and 273 K, corresponding to relative propylene pressures of 0.87, is shown for a longer time on stream (1300 minutes or 78 ks) in Figure 5.5. At times less than 18 ks as shown in Figure 5.3b and Figure 5.5, the catalyst is presumably at steady state, but the catalyst starts to deactivate at ~27 ks (450 minutes) with observable deactivation thereafter. From these findings, we presume that the stable rates initially observed are a combination of the induction period and catalyst deactivation, and that subambient temperatures and elevated pressures do not enable stable oligomerization rates at longer times on stream nor the formation of a psuedoliquid in the pores of the catalyst, which was examined by changing relative olefin pressures. The inability for Ni-MOF-74 (~1.94 nm pores) to form a psuedoliquid in the pores may arise from the inaccuracies of the BJH formalism and Kelvin equation to estimate pore sizes in microporous materials, which was also hypothesized on Ni-Beta (1.1 – 1.3 nm) and Ni-FAU (1.2 – 1.7 nm) materials that both deactivated at a relative ethylene pressure of 0.84 at 258 K.[42,174]

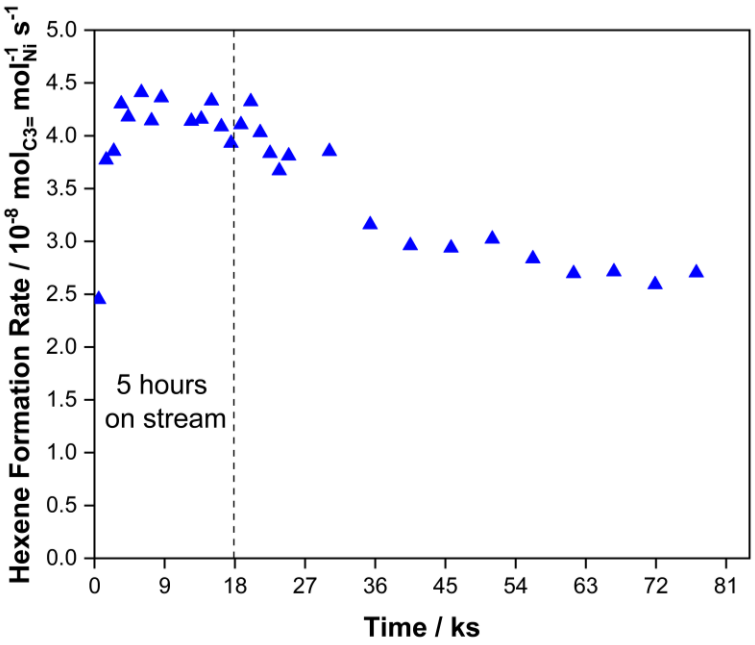

Figure 5.5. Propylene oligomerization at relative propylene pressures of 0.87 and 0.36 at 273 K on Ni-MOF-74.

On Ni-MOF-74, a unique feature of running ethylene oligomerization reactions is the high selectivity toward the linear alpha olefin (LAO), 1-butene. In Figure 5.6, rates and selectivity with time on stream during ethylene oligomerization at 500 kPa and 473 K and at 1512 kPa and 243 K are presented (P/P_{sat} = 0.73). At the elevated temperature of 473 K, deactivation is observed with a decrease in 1-butene selectivity and an increase in selectivity toward 2-butene and hexenes. This observation is consistent with the hypothesis that internal alkenes are isomerized from terminal alkenes to promote the growth of higher molecular weight carbon chains, which led to the hypothesis that intrapore liquids promote desorption of 1-butene to prevent deactivation.[37,44,45] At low temperatures of 243 K and elevated pressures of 1512 kPa, the only product observed is 1-butene at 100% selectivity at a conversion of 0.001% at all times on stream on Ni-MOF-74, unprecedented in the literature. Ethylene oligomerization with Ni-MIL-127 at subambient temperatures shown in Figure 5.9, also shows 100% selectivity toward 1-butene at 0.0006% conversion. While the rates of reaction for both catalysts are low, no other nickel formulations have reported 100% selectivity toward 1-butene during ethylene oligomerization. On Ni/UiO-66 at the same conversion on Ni-MOF-74, 1-butene selectivities during ethylene oligomerization at

500 kPa and 473 K is ~50%.[76] On Ni-MCM-41 during ethylene oligomerization at 1500 kPa and 243 K, the same process conditions as Ni-MOF-74 reported herein for ethylene oliugomerization, at ~3 - 5 % conversion, 1-butene selectivities of ~96% were reported and extrapolated to 0% conversion to surmise that 1-butene is the primary product during ethylene oligomerization.[44]

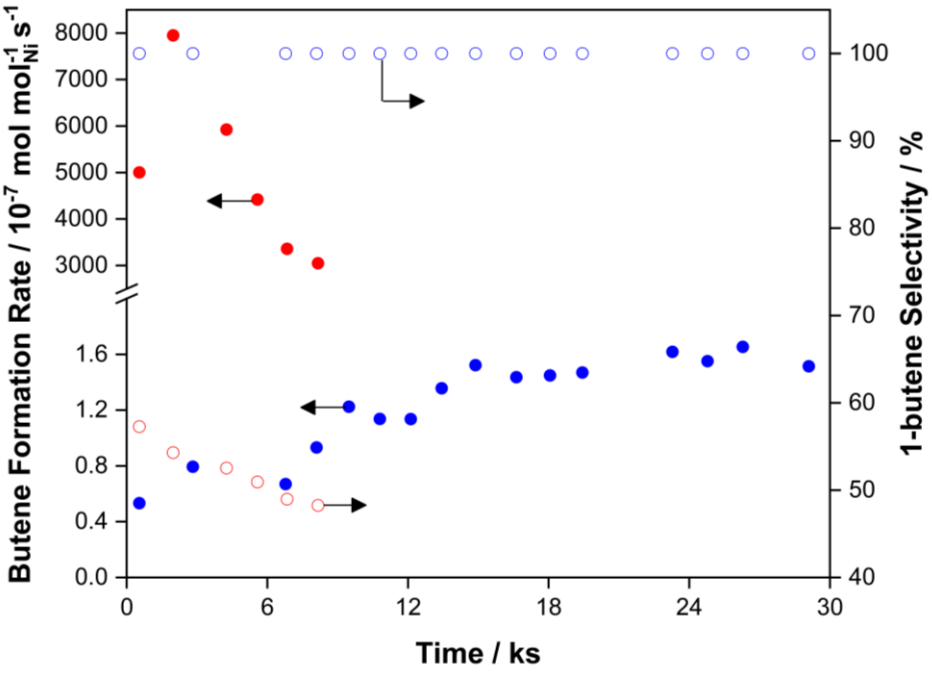

Figure 5.6. Butene formation rates (filled) and 1-butene selectivities (open) at 500 kPa and 473 K (red) and at 1512 kPa and 243 K (blue) on Ni-MOF-74.

We attempted to exploit low conversion data at subambient temperatures to understand the rank of the products observed during ethylene oligomerization.[190] In Figure 5.7, selectivity versus conversion is shown for ethylene oligomerization at 258 K at 2294 kPa and 1099 kPa (P/P_{sat} of 0.73 and 0.36 respectively). In all cases, the catalysts deactivated with time on stream (Figure 5.4a) and only selectivity-conversion data up to the maximum rate and conversions are shown in Figure 5.7. At low conversions, the only product observed is 1-butene, consistent with the selectivity observed at 243 K to suggest that 1-butene is the only primary product during ethylene oligomerization. At higher conversions, 2-butenes (cis-2-butene and trans-2-butene) and hexenes are formed, indicating that these species are formed from 1-butene. Additionally, the selectivity of 2-

butenes remains constant while the selectivity toward hexenes increases with a decreasing selectivity toward 1-butene at increasing conversions, in line with the mechanistic proposal that 2-butene is formed via isomerization and hexenes are formed via chain propagation of 1-butene and ethylene.

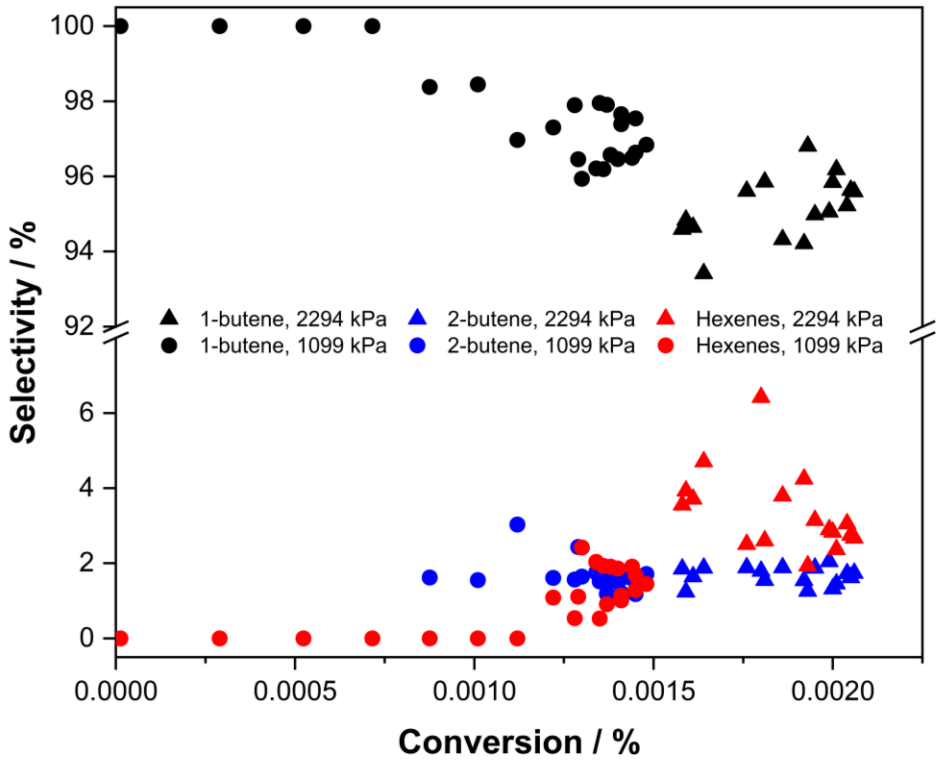

Figure 5.7. Selectivity versus conversion showing 1-butene (black), 2-butene (blue) and hexenes (red) at 2294 kPa (▲) and 1099 kPa (●) at 258 K on Ni-MOF-74.

Based on observations in Figure 5.7, we describe a mechanistic sequence for isomerization of 1-butene to 2-butene for ethylene oligomerization on Ni-MOF-74. The production of solely LAOs is evidence for the metallacycle mechanism,[17,81,82] but at higher conversions in our data, 2-butenes are observed. The presence of internal alkenes was postulated as evidence for the coordination-insertion mechanism (Figure 5.8a), also known as the Cossee-Arlman mechanism, which arises from reinsertion of 1-butene on the beta carbon on ***F*** and subsequent β-hydride elimination from ***G*** to make ***H***. [31,46,78,79] In contrast, internal alkenes cannot form in the metallacycle mechanism (Figure 5.8b) as 1-butene, which is formed from a Ni-butenyl intermediate (***M***) via reductive elimination, does not

reinsert, as the mechanism is characterized by successive coordination of olefin molecules to produce ***I*** and ***J*** and subsequent carbon coupling to form a metallacyclopentane intermediate (***L***). We note that chain growth to make hexenes from coupling of ethylene and 1-butene can occur in both mechanisms, and the production of hexenes cannot be used to solely implicate either mechanism. However, the change in selectivity from 1-butene to 2-butene as conversion increases is unique to low temperature (< 258 K) ethylene oligomerization to show that 1-butene is the primary product and 2-butene is formed from the reinsertion and isomerization of 1-butene, which is consistent with the Cossee-Arlman mechanism.

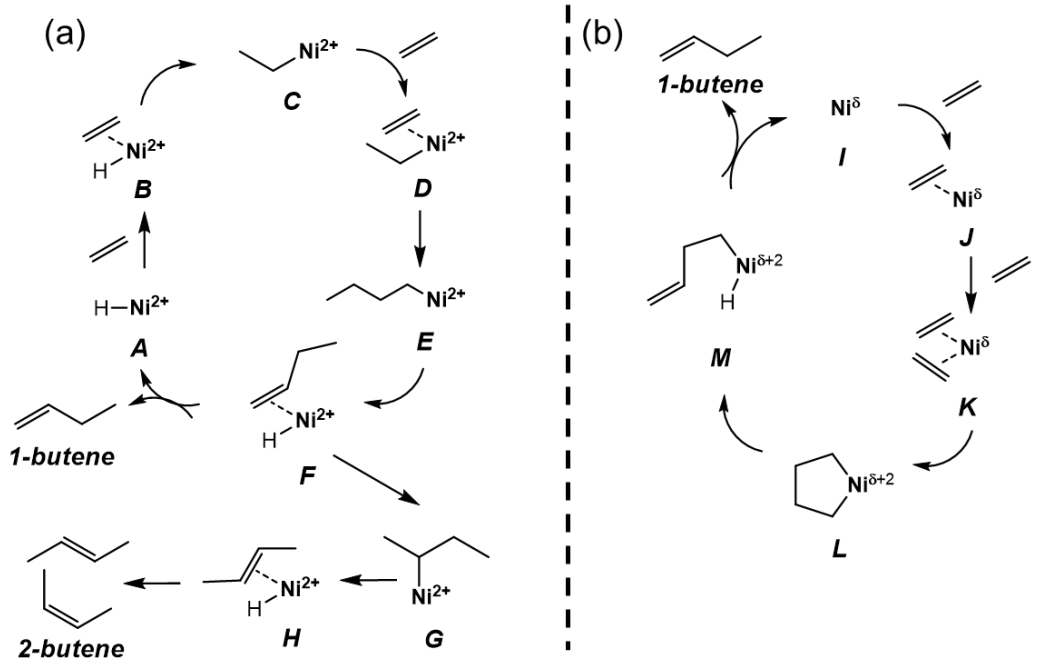

Figure 5.8. (a) Cossee-Arlman showing the reinsertion of 1-butene and (b) metallacycle mechanism on nickel catalysts for ethylene oligomerization.

5.4. Conclusion

In summary, deactivation during ethylene and propylene oligomerization at subambient temperatures and elevated pressures is observed on Ni-MOF-74 irrespective of plausible capillary condensation within the pores of the material. We surmise that the subambient temperatures and elevated olefin pressures proposed to facilitate the formation of intrapore liquids elongates the induction period and promotes the generation of larger chain hydrocarbons which cause deactivation, respectively. Low conversion data at these

process conditions show that 1-butene is the primary product, and at higher conversions, 2-butene and hexenes are formed from reinsertion and β-hydride elimination and from carbon chain coupling of ethylene and 1-butene, respectively. The production of the former is consistent with the Cossee-Arlman mechanism which is characterized by insertions of olefin molecules on the nickel active site.

5.5. Supplemental Information

We attempted to study the stability of Ni-MIL-127 during ethylene oligomerization at subambient temperatures and elevated pressures with the catalysts described in Chapter in Chapter 4, respectively.[77] On Ni-MIL-127, the catalyst was reported to be stable for propylene oligomerization, but it deactivated with time on stream for ethylene oligomerization at 473 K and 500 kPa as shown in Figure 5.9. Similar to Ni-MOF-74, the selectivity to 1-butene decreases with time on stream and increases in 2-butene and hexene selectivity is observed. At 258 K and 2286 kPa (P/P_{sat} = 0.73), Ni-MIL-127 deactivated with time on stream but was 100% selective toward 1-butene at 0.0006% conversion. Subambient temperatures which were postulated to form intrapore liquids that mitigated deactivation did not prevent catalyst deactivation in Ni-MIL-127, similar to the observation of catalyst deactivation at subambient temperatures on Ni-MOF-74 during ethylene oligomerization.

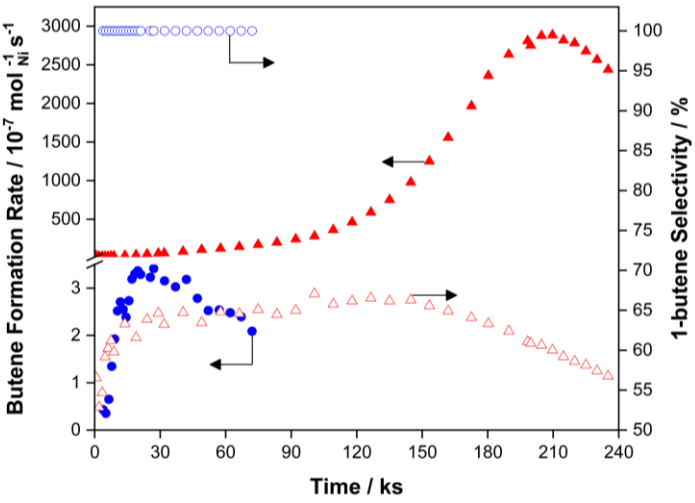

Figure 5.9. Butene formation rates (filled) and 1-butene selectivities (open) at 500 kPa and 473 K (red) and at 2286 kPa and 258 K (blue) on Ni-MIL-127.

References

(1) McFarland, E. Unconventional Chemistry for Unconventional Natural Gas. *Science*. 2012, pp 341–342. https://doi.org/10.1126/science.1226840.

(2) Torres Galvis, H. M.; De Jong, K. P. Catalysts for Production of Lower Olefins from Synthesis Gas: A Review. *ACS Catal.* **2013**, *3* (9), 2130–2149. https://doi.org/10.1021/cs4003436.

(3) Forestière, A.; Olivier-Bourbigou, H.; Saussine, L. Oligomérisation Des Mono-Oléfines Par Des Catalyseurs Homogènes. *Oil Gas Sci. Technol.* **2009**, *64* (6), 649–667. https://doi.org/10.2516/ogst/2009027.

(4) Vogt, E. T. C.; Weckhuysen, B. M. Fluid Catalytic Cracking: Recent Developments on the Grand Old Lady of Zeolite Catalysis. *Chem. Soc. Rev.* **2015**, *44* (20), 7342–7370. https://doi.org/10.1039/c5cs00376h.

(5) Nicholas, C. P. Applications of Light Olefin Oligomerization to the Production of Fuels and Chemicals. *Appl. Catal. A Gen.* **2017**, *543* (June), 82–97. https://doi.org/10.1016/j.apcata.2017.06.011.

(6) Lappin, G. R.; Nemec, L. H.; Sauer, J. D.; Wagner, J. D. Olefins, Higher 1. *Kirk-Othmer Encycl. Chem. Technol.* **2010**, 1–20.

(7) Kissin, Y. V. Polymers of Higher. *Kirk-Othmer Encycl. Chem. Technol.* **2015**, 1–27.

(8) Agapie, T. Selective Ethylene Oligomerization: Recent Advances in Chromium Catalysis and Mechanistic Investigations. *Coord. Chem. Rev.* **2011**, *255* (7–8), 861–880. https://doi.org/10.1016/j.ccr.2010.11.035.

(9) Elvira O., Greiner Camara, Y. I. Chemical Economics Handbook: Linear Alpha-Olefins (681.5030). **2010**, 78.

(10) Olivier-Bourbigou, H.; Breuil, P. A. R.; Magna, L.; Michel, T.; Espada Pastor, M. F.; Delcroix, D. Nickel Catalyzed Olefin Oligomerization and Dimerization. *Chem. Rev.* **2020**, *120* (15), 7919–7983. https://doi.org/10.1021/acs.chemrev.0c00076.

(11) Bryliakov, K. P.; Antonov, A. A. Recent Progress of Transition Metal Based Catalysts for the Selective Dimerization of Ethylene. *J. Organomet. Chem.* **2018**, *867*, 55–61. https://doi.org/10.1016/j.jorganchem.2018.03.021.

(12) Skupińska, J. Oligomerization of α-Olefins to Higher Oligomers. *Chem. Rev.* **1991**, *91* (4), 613–648. https://doi.org/10.1021/cr00004a007.

(13) McGuinness, D. S.; Suttil, J. A.; Gardiner, M. G.; Davies, N. W. Ethylene Oligomerization with Cr-NHC Catalysts: Further Insights into the Extended Metallacycle Mechanism of Chain Growth. *Organometallics* **2008**, *27* (16), 4238–4247. https://doi.org/10.1021/om800398e.

(14) Keim, W. Oligomerization of Ethylene to α-Olefins: Discovery and Development of the Shell Higher Olefin Process (SHOP). *Angew. Chemie - Int. Ed.* **2013**, *52* (48),

12492–12496. https://doi.org/10.1002/anie.201305308.

(15) Keim, W. Nickel: An Element with Wide Application in Industrial Homogeneous Catalysis. *Angew. Ch* **1990**, *29*, 235–244.

(16) McGuinness, D. S. Olefin Oligomerization via Metallacycles: Dimerization, Trimerization, Tetramerization, and Beyond. *Chem. Rev.* **2011**, *111* (3), 2321–2341. https://doi.org/10.1021/cr100217q.

(17) Speiser, F.; Braunstein, P.; Saussine, L. Catalytic Ethylene Dimerization and Oligomerization: Recent Developments with Nickel Complexes Containing P,N-Chelating Ligands. *Acc. Chem. Res.* **2005**, *38* (10), 784–793. https://doi.org/10.1021/ar050040d.

(18) Kuhn, P.; Sémeril, D.; Matt, D.; Chetcuti, M. J.; Lutz, P. Structure-Reactivity Relationships in SHOP-Type Complexes: Tunable Catalysts for the Oligomerisation and Polymerisation of Ethylene. *Dalt. Trans.* **2007**, No. 5, 515–528. https://doi.org/10.1039/b615259g.

(19) Finiels, A.; Fajula, F.; Hulea, V. Nickel-Based Solid Catalysts for Ethylene Oligomerization-a Review. *Catal. Sci. Technol.* **2014**, *4* (8), 2412–2426. https://doi.org/10.1039/c4cy00305e.

(20) Ipatieff, V. N. Catalytic Polymerization of Gaseous Olefins by Liquid Phosphoric Acid: I. Propylene. *Ind. Eng. Chem.* **1935**, *27* (9), 1067–1069. https://doi.org/10.1021/ie50309a024.

(21) Coetzee, J. H.; Mashapa, T. N.; Prinsloo, N. M.; Rademan, J. D. An Improved Solid Phosphoric Acid Catalyst for Alkene Oligomerization in a Fischer-Tropsch Refinery. *Appl. Catal. A Gen.* **2006**, *308*, 204–209. https://doi.org/10.1016/j.apcata.2006.04.023.

(22) Lallemand, M.; Rusu, O. A.; Dumitriu, E.; Finiels, A.; Fajula, F.; Hulea, V. NiMCM-36 and NiMCM-22 Catalysts for the Ethylene Oligomerization: Effect of Zeolite Texture and Nickel Cations/Acid Sites Ratio. *Appl. Catal. A Gen.* **2008**, *338* (1–2), 37–43. https://doi.org/10.1016/j.apcata.2007.12.024.

(23) Egloff, G. Polymer Gasoline. *Ind. Eng. Chem.* **1925**, *28* (12), 1461–1467.

(24) Ipatieff, V. N.; Corson, B. B.; Egloff, G. Polymerization, a New Source of Gasoline. *Ind. Eng. Chem. Res.* **1935**, *1077* (3), 1077–1081.

(25) Morrell, J. C. Polymerization Catalyst Comprising Phosphoric Acid and Siliceous Materials. 3, 1962.

(26) Zhang, J.; Yan, Y.; Chu, Q.; Feng, J. Solid Phosphoric Acid Catalyst for Propene Oligomerization: Effect of Silicon Phosphate Composition. *Fuel Process. Technol.* **2015**, *135*, 2–5. https://doi.org/10.1016/j.fuproc.2014.09.007.

(27) Quann, R. J.; Green, L. A.; Tabak, S. A.; Krambeck, F. J. Chemistry of Olefin

Oligomerization over ZSM-5 Catalyst. *Ind. Eng. Chem. Res.* **1988**, *27* (4), 565–570. https://doi.org/10.1021/ie00076a006.

(28) Vernuccio, S.; Bickel, E. E.; Gounder, R.; Broadbelt, L. J. Propene Oligomerization on Beta Zeolites: Development of a Microkinetic Model and Experimental Validation. *J. Catal.* **2021**, *395*, 302–314. https://doi.org/10.1016/j.jcat.2021.01.018.

(29) Wilshier, K. G. Propene Oligomerization over H-ZSM-5 Zeolite. *Stud. Surf. Sci. Catal.* **1988**, *36* (C), 621–625. https://doi.org/10.1016/S0167-2991(09)60559-0.

(30) Bellussi, G.; Mizia, F.; Calemma, V.; Pollesel, P.; Millini, R. Oligomerization of Olefins from Light Cracking Naphtha over Zeolite-Based Catalyst for the Production of High Quality Diesel Fuel. *Microporous Mesoporous Mater.* **2012**, *164*, 127–134. https://doi.org/10.1016/j.micromeso.2012.07.020.

(31) Joshi, R.; Zhang, G.; Miller, J. T.; Gounder, R. Evidence for the Coordination-Insertion Mechanism of Ethene Dimerization at Nickel Cations Exchanged onto Beta Molecular Sieves. *ACS Catal.* **2018**, *8* (12), 11407–11422. https://doi.org/10.1021/acscatal.8b03202.

(32) Henry, R.; Komurca, M.; Ganjkhanlou, Y.; Brogaard, R. Y.; Lu, L.; Jens, K.-J.; Berlier, G.; Olsbye, U. Ethene Oligomerization on Nickel Microporous and Mesoporous-Supported Catalysts: Investigation of the Active Sites. *Catal. Today* **2018**, *299*, 154–163.

(33) Moussa, S.; Concepción, P.; Arribas, M. A.; Martínez, A. Nature of Active Nickel Sites and Initiation Mechanism for Ethylene Oligomerization on Heterogeneous Ni-Beta Catalysts. *ACS Catal.* **2018**, *8* (5), 3903–3912. https://doi.org/10.1021/acscatal.7b03970.

(34) Martínez, A.; Arribas, M. A.; Concepción, P.; Moussa, S. New Bifunctional Ni-H-Beta Catalysts for the Heterogeneous Oligomerization of Ethylene. *Appl. Catal. A Gen.* **2013**, *467*, 509–518. https://doi.org/10.1016/j.apcata.2013.08.021.

(35) Mlinar, A. N.; Baur, G. B.; Bong, G. G.; Getsoian, A.; Bell, A. T. Propene Oligomerization over Ni-Exchanged Na-X Zeolites. *J. Catal.* **2012**, *296*, 156–164. https://doi.org/10.1016/j.jcat.2012.09.010.

(36) Mlinar, A. N.; Ho, O. C.; Bong, G. G.; Bell, A. T. The Effect of Noncatalytic Cations on the Activity and Selectivity of Nickel-Exchanged Xzeolites for Propene Oligomerization. *ChemCatChem* **2013**, *5* (10), 3139–3147. https://doi.org/10.1002/cctc.201300232.

(37) Ehrmaier, A.; Liu, Y.; Peitz, S.; Jentys, A.; Chin, Y. H. C.; Sanchez-Sanchez, M.; Bermejo-Deval, R.; Lercher, J. Dimerization of Linear Butenes on Zeolite-Supported Ni 2+. *ACS Catal.* **2019**, *9* (1), 315–324. https://doi.org/10.1021/acscatal.8b03095.

(38) Ehrmaier, A.; Peitz, S.; Sanchez-Sanchez, M.; Bermejo-Deval, R.; Lercher, J. On

the Role of Co-Cations in Nickel Exchanged LTA Zeolite for Butene Dimerization. *Microporous Mesoporous Mater.* **2019**, *284* (March), 241–246. https://doi.org/10.1016/j.micromeso.2019.03.047.

(39) Ling, Y.; Chen, X.; Meng, J.; Liang, C. Identification of Uniform High-Density Isolated Ni Active Sites on LTA Zeolite for Propylene Dimerization. *Appl. Catal. A Gen.* **2022**, *640* (March), 118661. https://doi.org/10.1016/j.apcata.2022.118661.

(40) Brogaard, R. Y.; Kømurcu, M.; Dyballa, M. M.; Botan, A.; Van Speybroeck, V.; Olsbye, U.; De Wispelaere, K. Ethene Dimerization on Zeolite-Hosted Ni Ions: Reversible Mobilization of the Active Site. *ACS Catal.* **2019**, *9* (6), 5645–5650. https://doi.org/10.1021/acscatal.9b00721.

(41) Brogaard, R. Y.; Olsbye, U. Ethene Oligomerization in Ni-Containing Zeolites: Theoretical Discrimination of Reaction Mechanisms. *ACS Catal.* **2016**, *6* (2), 1205–1214. https://doi.org/10.1021/acscatal.5b01957.

(42) Caulkins, R.; Joshi, R.; Gounder, R.; Ribeiro, F. H. Effects of Ethene Pressure on the Deactivation of Ni-Zeolites During Ethene Oligomerization at Sub-Ambient Temperatures. *ChemCatChem* **2022**, *14* (1). https://doi.org/10.1002/cctc.202101478.

(43) Mlinar, A. N.; Shylesh, S.; Ho, O. C.; Bell, A. T. Propene Oligomerization Using Alkali Metal- and Nickel-Exchanged Mesoporous Aluminosilicate Catalysts. *ACS Catal.* **2014**, *4* (1), 337–343. https://doi.org/10.1021/cs4007809.

(44) Agirrezabal-Telleria, I.; Iglesia, E. Stabilization of Active, Selective, and Regenerable Ni-Based Dimerization Catalysts by Condensation of Ethene Withinordered Mesopores. *J. Catal.* **2017**, *352*, 505–514. https://doi.org/10.1016/j.jcat.2017.06.025.

(45) Agirrezabal-Telleria, I.; Iglesia, E. Mechanistic Insights and Consequences of Intrapore Liquids in Ethene, Propene, and Butene Dimerization on Isolated Ni2+ Sites Grafted within Aluminosilicate Mesopores. *J. Catal.* **2020**, *389*, 690–705. https://doi.org/10.1016/j.jcat.2020.06.038.

(46) Joshi, R.; Saxena, A.; Gounder, R. Mechanistic Insights into Alkene Chain Growth Reactions Catalyzed by Nickel Active Sites on Ordered Microporous and Mesoporous Supports. *Catal. Sci. Technol.* **2020**, *10* (21), 7101–7123. https://doi.org/10.1039/d0cy01186j.

(47) Busatta, C. A.; Mignoni, M. L.; de Souza, R. F.; Bernardo-Gusmão, K. Nickel Complexes Immobilized in Modified Ionic Liquids Anchored in Structured Materials for Ethylene Oligomerization. *Appl. Sci.* **2018**, *8* (5), 1–12. https://doi.org/10.3390/app8050717.

(48) Ganjkhanlou, Y.; Berlier, G.; Groppo, E.; Borfecchia, E.; Bordiga, S. In Situ Investigation of the Deactivation Mechanism in Ni-ZSM5 During Ethylene Oligomerization. *Top. Catal.* **2017**, *60* (19–20), 1664–1672. https://doi.org/10.1007/s11244-017-0845-6.

(49) Metzger, E. D.; Brozek, C. K.; Comito, R. J.; Dinca, M. Selective Dimerization of Ethylene to 1-Butene with a Porous Catalyst. *ACS Cent. Sci.* **2016**, *2* (3), 148–153. https://doi.org/10.1021/acscentsci.6b00012.

(50) Metzger, E. D.; Comito, R. J.; Hendon, C. H.; Dincă, M. Mechanism of Single-Site Molecule-like Catalytic Ethylene Dimerization in Ni-MFU-4l. *J. Am. Chem. Soc.* **2017**, *139* (2), 757–762. https://doi.org/10.1021/jacs.6b10300.

(51) Comito, R. J.; Metzger, E. D.; Wu, Z.; Zhang, G.; Hendon, C. H.; Miller, J. T.; Dincă, M. Selective Dimerization of Propylene with Ni-MFU-4l. *Organometallics* **2017**, *36* (9), 1681–1683. https://doi.org/10.1021/acs.organomet.7b00178.

(52) Metzger, E. D.; Comito, R. J.; Wu, Z.; Zhang, G.; Dubey, R. C.; Xu, W.; Miller, J. T.; Dinca, M. Highly Selective Heterogeneous Ethylene Dimerization with a Scalable and Chemically Robust MOF Catalyst. *ACS Sustain. Chem. Eng.* **2019**, *7* (7), 6654–6661. https://doi.org/10.1021/acssuschemeng.8b05703.

(53) Bernales, V.; League, A. B.; Li, Z.; Schweitzer, N. M.; Peters, A. W.; Carlson, R. K.; Hupp, J. T.; Cramer, C. J.; Farha, O. K.; Gagliardi, L. Computationally Guided Discovery of a Catalytic Cobalt-Decorated Metal-Organic Framework for Ethylene Dimerization. *J. Phys. Chem. C* **2016**, *120* (41), 23576–23583. https://doi.org/10.1021/acs.jpcc.6b07362.

(54) Canivet, J.; Aguado, S.; Schuurman, Y.; Farrusseng, D. MOF-Supported Selective Ethylene Dimerization Single-Site Catalysts through One-Pot Postsynthetic Modification. *J. Am. Chem. Soc.* **2013**, *135* (11), 4195–4198. https://doi.org/10.1021/ja312120x.

(55) Arrozi, U. S. F.; Bon, V.; Kutzscher, C.; Senkovska, I.; Kaskel, S. Towards Highly Active and Stable Nickel-Based Metal-Organic Frameworks as Ethylene Oligomerization Catalysts. *Dalt. Trans.* **2019**, *48* (10), 3415–3421. https://doi.org/10.1039/c8dt03866j.

(56) Brozek, C. K.; Dincă, M. Cation Exchange at the Secondary Building Units of Metal-Organic Frameworks. *Chem. Soc. Rev.* **2014**, *43* (16), 5456–5467. https://doi.org/10.1039/c4cs00002a.

(57) Li, Z.; Peters, A. W.; Liu, J.; Zhang, X.; Schweitzer, N. M.; Hupp, J. T.; Farha, O. K. Size Effect of the Active Sites in UiO-66-Supported Nickel Catalysts Synthesized: Via Atomic Layer Deposition for Ethylene Hydrogenation. *Inorg. Chem. Front.* **2017**, *4* (5), 820–824. https://doi.org/10.1039/c7qi00056a.

(58) Li, Z.; Schweitzer, N. M.; League, A. B.; Bernales, V.; Peters, A. W.; Getsoian, A. B.; Wang, T. C.; Miller, J. T.; Vjunov, A.; Fulton, J. L.; et al. Sintering-Resistant Single-Site Nickel Catalyst Supported by Metal-Organic Framework. *J. Am. Chem. Soc.* **2016**, *138* (6), 1977–1982. https://doi.org/10.1021/jacs.5b12515.

(59) Liu, J.; Ye, J.; Li, Z.; Otake, K. I.; Liao, Y.; Peters, A. W.; Noh, H.; Truhlar, D. G.; Gagliardi, L.; Cramer, C. J.; et al. Beyond the Active Site: Tuning the Activity and

Selectivity of a Metal-Organic Framework-Supported Ni Catalyst for Ethylene Dimerization. *J. Am. Chem. Soc.* **2018**, *140* (36), 11174–11178. https://doi.org/10.1021/jacs.8b06006.

(60) Goetjen, T. A.; Zhang, X.; Liu, J.; Hupp, J. T.; Farha, O. K. Metal-Organic Framework Supported Single Site Chromium(III) Catalyst for Ethylene Oligomerization at Low Pressure and Temperature. *ACS Sustain. Chem. Eng.* **2019**, *7* (2), 2553–2557. https://doi.org/10.1021/acssuschemeng.8b05524.

(61) Islamoglu, T.; Goswami, S.; Li, Z.; Howarth, A. J.; Farha, O. K.; Hupp, J. T. Postsynthetic Tuning of Metal-Organic Frameworks for Targeted Applications. *Acc. Chem. Res.* **2017**, *50* (4), 805–813. https://doi.org/10.1021/acs.accounts.6b00577.

(62) Mihet, M.; Grad, O.; Blanita, G.; Radu, T.; Lazar, M. D. Effective Encapsulation of Ni Nanoparticles in Metal-Organic Frameworks and Their Application for CO2 Methanation. *Int. J. Hydrogen Energy* **2019**, *44* (26), 13383–13396. https://doi.org/10.1016/j.ijhydene.2019.03.259.

(63) Valtchev, V.; Mintova, S. 1. Zeolites and MOFs? Dare to Know Them! *Zeolites Met. Fram.* **2019**, 13–24. https://doi.org/10.1515/9789048536719-002.

(64) Ren, J.; Ledwaba, M.; Musyoka, N. M.; Langmi, H. W.; Mathe, M.; Liao, S.; Pang, W. Structural Defects in Metal–Organic Frameworks (MOFs): Formation, Detection and Control towards Practices of Interests. *Coord. Chem. Rev.* **2017**, *349*, 169–197. https://doi.org/10.1016/j.ccr.2017.08.017.

(65) Yang, D.; Gates, B. C. Catalysis by Metal Organic Frameworks: Perspective and Suggestions for Future Research. *ACS Catal.* **2019**, *9* (3), 1779–1798. https://doi.org/10.1021/acscatal.8b04515.

(66) Svane, K. L.; Bristow, J. K.; Gale, J. D.; Walsh, A. Vacancy Defect Configurations in the Metal-Organic Framework UiO-66: Energetics and Electronic Structure. *J. Mater. Chem. A* **2018**, *6* (18), 8507–8513. https://doi.org/10.1039/c7ta11155j.

(67) Shearer, G. C.; Chavan, S.; Bordiga, S.; Svelle, S.; Olsbye, U.; Lillerud, K. P. Defect Engineering: Tuning the Porosity and Composition of the Metal-Organic Framework UiO-66 via Modulated Synthesis. *Chem. Mater.* **2016**, *28* (11), 3749–3761. https://doi.org/10.1021/acs.chemmater.6b00602.

(68) Sannes, D. K.; Øien-Ødegaard, S.; Aunan, E.; Nova, A.; Olsbye, U. Quantification of Linker Defects in UiO-Type Metal-Organic Frameworks. *Chem. Mater.* **2023**, *35*, 3793–3800. https://doi.org/10.1021/acs.chemmater.2c03744.

(69) Chung, Y. G.; Haldoupis, E.; Bucior, B. J.; Haranczyk, M.; Lee, S.; Zhang, H.; Vogiatzis, K. D.; Milisavljevic, M.; Ling, S.; Camp, J. S.; et al. Advances, Updates, and Analytics for the Computation-Ready, Experimental Metal-Organic Framework Database: CoRE MOF 2019. *J. Chem. Eng. Data* **2019**, *64* (12), 5985–5998. https://doi.org/10.1021/acs.jced.9b00835.

(70) Bernales, V.; Ortuño, M. A.; Truhlar, D. G.; Cramer, C. J.; Gagliardi, L. Computational Design of Functionalized Metal-Organic Framework Nodes for Catalysis. *ACS Cent. Sci.* **2018**, *4* (1), 5–19. https://doi.org/10.1021/acscentsci.7b00500.

(71) Odoh, S. O.; Cramer, C. J.; Truhlar, D. G.; Gagliardi, L. Quantum-Chemical Characterization of the Properties and Reactivities of Metal-Organic Frameworks. *Chem. Rev.* **2015**, *115* (12), 6051–6111. https://doi.org/10.1021/cr500551h.

(72) Mlinar, A. N.; Keitz, B. K.; Gygi, D.; Bloch, E. D.; Long, J. R.; Bell, A. T. Selective Propene Oligomerization with Nickel(II)-Based Metal-Organic Frameworks. *ACS Catal.* **2014**, *4* (3), 717–721. https://doi.org/10.1021/cs401189a.

(73) Cossee, P. On the Reaction Mechanism of the Ethylene Polymerization with Heterogeneous Ziegler-Natta Catalysts. *Tetrahedron Lett.* **1960**, *1* (38), 12–16. https://doi.org/10.1016/S0040-4039(01)99340-2.

(74) Cossee, P. Ziegler-Natta Catalysis I. Mechanism of Polymerization of α-Olefins with Ziegler-Natta Catalysts. *J. Catal.* **1964**, *3* (1), 80–88. https://doi.org/10.1016/0021-9517(64)90095-8.

(75) Arlman, E. J.; Cossee, P. Ziegler-Natta Catalysis III. Stereospecific Polymerization of Propene with the Catalyst System TiCl3AlEt3. *J. Catal.* **1964**, *3* (1), 99–104. https://doi.org/10.1016/0021-9517(64)90097-1.

(76) Yeh, B.; Vicchio, S. P.; Chheda, S.; Zheng, J.; Schmid, J.; Löbbert, L.; Bermejo-Deval, R.; Gutiérrez, O. Y.; Lercher, J. A.; Lu, C. C.; et al. Site Densities, Rates, and Mechanism of Stable Ni/UiO-66 Ethylene Oligomerization Catalysts. *J. Am. Chem. Soc.* **2021**, *143* (48), 20274–20280. https://doi.org/10.1021/jacs.1c09320.

(77) Yeh, B.; Chheda, S.; Prinslow, S. D.; Hoffman, A. S.; Hong, J.; Perez-Aguilar, J. E.; Bare, S. R.; Lu, C. C.; Gagliardi, L.; Bhan, A. Structure and Site Evolution of Framework Ni Species in MIL-127 MOFs for Propylene Oligomerization Catalysis. *J. Am. Chem. Soc.* **2023**, *145* (6), 3408–3418. https://doi.org/10.1021/jacs.2c10551.

(78) Escobar, M. A.; Trofymchuk, O. S.; Rodriguez, B. E.; Lopez-Lira, C.; Tapia, R.; Daniliuc, C.; Berke, H.; Nachtigall, F. M.; Santos, L. S.; Rojas, R. S. Lewis Acid Enhanced Ethene Dimerization and Alkene Isomerization - ESI-MS Identification of the Catalytically Active Pyridyldimethoxybenzimidazole Nickel(II) Hydride Species. *ACS Catal.* **2015**, *5* (12), 7338–7342. https://doi.org/10.1021/acscatal.5b02003.

(79) Killian, C. M.; Johnson, L. K.; Brookhart, M. Preparation of Linear α-Olefins Using Cationic Nickel(II) α-Diimine Catalysts. *Organometallics* **1997**, *16* (10), 2005–2007. https://doi.org/10.1021/om961057q.

(80) Ye, J.; Gagliardi, L.; Cramer, C. J.; Truhlar, D. G. Computational Screening of MOF-Supported Transition Metal Catalysts for Activity and Selectivity in Ethylene Dimerization. *J. Catal.* **2018**, *360*, 160–167.

https://doi.org/10.1016/j.jcat.2017.12.007.

(81) Grubbs, H.; Miyashita, A. The Metallacyclopentane-Olefin Interchange Reaction. *J.C.S. Chem. Comm.* **1977**, *63* (864), 864–865.

(82) Grubbs, H.; Miyashita, A. Metallacyclopentanes as Catalysts for the Linear and Cyclodimerization of Olefins. *J. Am. Chem. Soc.* **1978**, *100* (23), 7416–7418.

(83) Andrei, R. D.; Popa, M. I.; Fajula, F.; Hulea, V. Heterogeneous Oligomerization of Ethylene over Highly Active and Stable Ni-AlSBA-15 Mesoporous Catalysts. *J. Catal.* **2015**, *323*, 76–84. https://doi.org/10.1016/j.jcat.2014.12.027.

(84) Andrei, R. D.; Popa, M. I.; Fajula, F.; Cammarano, C.; Al Khudhair, A.; Bouchmella, K.; Mutin, P. H.; Hulea, V. Ethylene to Propylene by One-Pot Catalytic Cascade Reactions. *ACS Catal.* **2015**, *5* (5), 2774–2777. https://doi.org/10.1021/acscatal.5b00383.

(85) Lacarriere, A.; Robin, J.; Świerczyński, D.; Finiels, A.; Fajula, F.; Luck, F.; Hulea, V. Distillate-Range Products from Non-Oil-Based Sources by Catalytic Cascade Reactions. *ChemSusChem* **2012**, *5* (9), 1787–1792. https://doi.org/10.1002/cssc.201200092.

(86) Ghosh, A. K.; Kevan, L. Electron Spin Resonance Studies of Ethylene Dimerization Catalyzed by Nickel Species on Y Zeolites. *J. Phys. Chem.* **1990**, *94* (7), 3117–3121. https://doi.org/10.1021/j100370a068.

(87) Elev, I. V.; Shelimov, B. N.; Kazansky, V. B. The Role of Ni+ Ions in the Activity of NiCaY Zeolite Catalysts for Ethylene Dimerization. *J. Catal.* **1984**, *89* (2), 470–477. https://doi.org/10.1016/0021-9517(84)90323-3.

(88) Lallemand, M.; Finiels, A.; Fajula, F.; Hulea, V. Nature of the Active Sites in Ethylene Oligomerization Catalyzed by Ni-Containing Molecular Sieves: Chemical and IR Spectral Investigation. *J. Phys. Chem. C* **2009**, *113* (47), 20360–20364. https://doi.org/10.1021/jp9082932.

(89) Jaegers, N. R.; Iglesia, E. Theoretical Assessment of the Mechanism and Active Sites in Alkene Dimerization on Ni Monomers Grafted onto Aluminosilicates: (Ni-OH)+ Centers and C-C Coupling Mediated by Lewis Acid-Base Pairs. *J. Am. Chem. Soc.* **2022**. https://doi.org/10.1021/jacs.2c13487.

(90) Chevreau, H.; Permyakova, A.; Nouar, F.; Fabry, P.; Livage, C.; Ragon, F.; Garcia-Marquez, A.; Devic, T.; Steunou, N.; Serre, C.; et al. Synthesis of the Biocompatible and Highly Stable MIL-127(Fe): From Large Scale Synthesis to Particle Size Control. *CrystEngComm* **2016**, *18* (22), 4094–4101. https://doi.org/10.1039/c5ce01864a.

(91) Mol, J. C. Industrial Applications of Olefin Metathesis. *J. Mol. Catal. A Chem.* **2004**, *213* (1), 39–45. https://doi.org/10.1016/j.molcata.2003.10.049.

(92) Katz, M. J.; Brown, Z. J.; Colón, Y. J.; Siu, P. W.; Scheidt, K. A.; Snurr, R. Q.;

Hupp, J. T.; Farha, O. K. A Facile Synthesis of UiO-66, UiO-67 and Their Derivatives. *Chem. Commun.* **2013**, *49* (82), 9449–9451. https://doi.org/10.1039/c3cc46105j.

(93) Shannon, S.; Goodwin, J. G. Characterization of Catalytic Surfaces by Isotopic-Transient Kinetics during Steady-State Reaction. *Chem. Rev.* **1995**, *95*, 677–695.

(94) Wang, Z.; Schmalbach, K. M.; Combs, R. L.; Chen, Y.; Penn, R. L.; Mara, N. A.; Stein, A. Effects of Phase Purity and Pore Reinforcement on Mechanical Behavior of NU-1000 and Silica-Infiltrated NU-1000 Metal-Organic Frameworks. *ACS Appl. Mater. Interfaces* **2020**, *12* (44), 49971–49981. https://doi.org/10.1021/acsami.0c12877.

(95) Ye, J.; Gagliardi, L.; Cramer, C. J.; Truhlar, D. G. Single Ni Atoms and Ni4 Clusters Have Similar Catalytic Activity for Ethylene Dimerization. *J. Catal.* **2017**, *354*, 278–286. https://doi.org/10.1016/j.jcat.2017.08.011.

(96) Abdel-Mageed, A. M.; Rungtaweevoranit, B.; Parlinska-Wojtan, M.; Pei, X.; Yaghi, O. M.; Jürgen Behm, R. Highly Active and Stable Single-Atom Cu Catalysts Supported by a Metal-Organic Framework. *J. Am. Chem. Soc.* **2019**, *141* (13), 5201–5210. https://doi.org/10.1021/jacs.8b11386.

(97) Planas, N.; Mondloch, J. E.; Tussupbayev, S.; Borycz, J.; Gagliardi, L.; Hupp, J. T.; Farha, O. K.; Cramer, C. J. Defining the Proton Topology of the Zr6-Based Metal-Organic Framework NU-1000. *J. Phys. Chem. Lett.* **2014**, *5* (21), 3716–3723. https://doi.org/10.1021/jz501899j.

(98) Zhao, Y.; Truhlar, D. G. A New Local Density Functional for Main-Group Thermochemistry, Transition Metal Bonding, Thermochemical Kinetics, and Noncovalent Interactions. *J. Chem. Phys.* **2006**, *125* (19), 1–18. https://doi.org/10.1063/1.2370993.

(99) Frisch, M. J.; Rucks, G. W.; Schlegel, H. B.; Scuseria, G. E.; Robb, M. A. Cheeseman, J. R. Scalmani, G.; Barone, V.; Petersson, G. A.; Nakatsuji, H.; Li, X.; Caricato, M.; et al. Gaussian 16. Gaussian Inc.: Wallingford, CT 2016.

(100) Weigend, F.; Ahlrichs, R. Balanced Basis Sets of Split Valence, Triple Zeta Valence and Quadruple Zeta Valence Quality for H to Rn: Design and Assessment of Accuracy. *Phys. Chem. Chem. Phys.* **2005**, *7* (18), 3297–3305. https://doi.org/10.1039/b508541a.

(101) Weigend, F. Accurate Coulomb-Fitting Basis Sets for H to Rn. *Phys. Chem. Chem. Phys.* **2006**, *8* (9), 1057–1065. https://doi.org/10.1039/b515623h.

(102) Andrae, D.; Häußermann, U.; Dolg, M.; Stoll, H.; Preuß, H. Energy-Adjusted Ab Initio Pseudopotentials for the Second and Third Row Transition Elements. *Theor. Chim. Acta* **1990**, *77* (2), 123–141. https://doi.org/10.1007/BF01114537.

(103) Grundner, S.; Markovits, M. A. C.; Li, G.; Tromp, M.; Pidko, E. A.; Hensen, E. J.

M.; Jentys, A.; Sanchez-Sanchez, M.; Lercher, J. A. Single-Site Trinuclear Copper Oxygen Clusters in Mordenite for Selective Conversion of Methane to Methanol. *Nat. Commun.* **2015**, *6* (May), 1–9. https://doi.org/10.1038/ncomms8546.

(104) Paolucci, C.; Parekh, A. A.; Khurana, I.; Di Iorio, J. R.; Li, H.; Albarracin Caballero, J. D.; Shih, A. J.; Anggara, T.; Delgass, W. N.; Miller, J. T.; et al. Catalysis in a Cage: Condition-Dependent Speciation and Dynamics of Exchanged Cu Cations in Ssz-13 Zeolites. *J. Am. Chem. Soc.* **2016**, *138* (18), 6028–6048. https://doi.org/10.1021/jacs.6b02651.

(105) Getman, R. B.; Xu, Y.; Schneider, W. F. Thermodynamics of Environment-Dependent Oxygen Chemisorption on Pt(111). *J. Phys. Chem. C* **2008**, *112* (26), 9559–9572. https://doi.org/10.1021/jp800905a.

(106) Soon, A.; Todorova, M.; Delley, B.; Stampfl, C. Surface Oxides of the Oxygen Copper System Precursors to the Bulk Oxide Phase. *Surf. Sci.* **2007**, *601*, 5809–5813.

(107) Ochterski, J. W. *Thermochemistry in Gaussian*; 2000.

(108) Ribeiro, R. F.; Marenich, A. V.; Cramer, C. J.; Truhlar, D. G. Use of Solution-Phase Vibrational Frequencies in Continuum Models for the Free Energy of Solvation. *J. Phys. Chem. B* **2011**, *115* (49), 14556–14562. https://doi.org/10.1021/jp205508z.

(109) Mcbride, J.; Gordon, S. *Computer Program for Calculation of Complex Chemical Equilibrium Compositions and Applications II. Users Manual and Program Description*; 1996. https://doi.org/10.4324/9781315886411-23.

(110) Lym, J.; Wittreich, G. R.; Vlachos, D. G. A Python Multiscale Thermochemistry Toolbox (PMuTT) for Thermochemical and Kinetic Parameter Estimation. *Comput. Phys. Commun.* **2020**, *247*, 106864. https://doi.org/10.1016/j.cpc.2019.106864.

(111) Li, G.; Vassilev, P.; Sanchez-Sanchez, M.; Lercher, J. A.; Hensen, E. J. M.; Pidko, E. A. Stability and Reactivity of Copper Oxo-Clusters in ZSM-5 Zeolite for Selective Methane Oxidation to Methanol. *J. Catal.* **2016**, *338*, 305–312. https://doi.org/10.1016/j.jcat.2016.03.014.

(112) Cavka, J. H.; Jakobsen, S.; Olsbye, U.; Guillou, N.; Lamberti, C.; Bordiga, S.; Lillerud, K. P. A New Zirconium Inorganic Building Brick Forming Metal Organic Frameworks with Exceptional Stability. *J. Am. Chem. Soc.* **2008**, *130* (42), 13850–13851. https://doi.org/10.1021/ja8057953.

(113) Shearer, G. C.; Chavan, S.; Ethiraj, J.; Vitillo, J. G.; Svelle, S.; Olsbye, U.; Lamberti, C.; Bordiga, S.; Lillerud, K. P. Tuned to Perfection: Ironing out the Defects in Metal-Organic Framework UiO-66. *Chem. Mater.* **2014**, *26* (14), 4068–4071. https://doi.org/10.1021/cm501859p.

(114) Biswas, S.; Van Der Voort, P. A General Strategy for the Synthesis of Functionalised UiO-66 Frameworks: Characterisation, Stability and CO2 Adsorption Properties. *Eur. J. Inorg. Chem.* **2013**, No. 12, 2154–2160.

https://doi.org/10.1002/ejic.201201228.

(115) Trickett, C. A.; Gagnon, K. J.; Lee, S.; Gándara, F.; Bürgi, H. B.; Yaghi, O. M. Definitive Molecular Level Characterization of Defects in UiO-66 Crystals. *Angew. Chemie - Int. Ed.* **2015**, *54* (38), 11162–11167. https://doi.org/10.1002/anie.201505461.

(116) Nguyen, H. G. T.; Schweitzer, N. M.; Chang, C. Y.; Drake, T. L.; So, M. C.; Stair, P. C.; Farha, O. K.; Hupp, J. T.; Nguyen, S. T. Vanadium-Node-Functionalized UiO-66: A Thermally Stable MOF-Supported Catalyst for the Gas-Phase Oxidative Dehydrogenation of Cyclohexene. *ACS Catal.* **2014**, *4* (8), 2496–2500. https://doi.org/10.1021/cs5001448.

(117) Goetjen, T. A.; Zhang, X.; Liu, J.; Hupp, J. T.; Farha, O. K. Metal-Organic Framework Supported Single Site Chromium(III) Catalyst for Ethylene Oligomerization at Low Pressure and Temperature. *ACS Sustain. Chem. Eng.* **2019**, *7* (2), 2553–2557. https://doi.org/10.1021/acssuschemeng.8b05524.

(118) Kandiah, M.; Nilsen, M. H.; Usseglio, S.; Jakobsen, S.; Olsbye, U.; Tilset, M.; Larabi, C.; Quadrelli, E. A.; Bonino, F.; Lillerud, K. P. Synthesis and Stability of Tagged UiO-66 Zr-MOFs. *Chem. Mater.* **2010**, *22* (24), 6632–6640. https://doi.org/10.1021/cm102601v.

(119) Valenzano, L.; Civalleri, B.; Chavan, S.; Bordiga, S.; Nilsen, M. H.; Jakobsen, S.; Lillerud, K. P.; Lamberti, C. Disclosing the Complex Structure of UiO-66 Metal Organic Framework: A Synergic Combination of Experiment and Theory. *Chem. Mater.* **2011**, *23* (7), 1700–1718. https://doi.org/10.1021/cm1022882.

(120) Foley, B. L.; Johnson, B. A.; Bhan, A. A Method for Assessing Catalyst Deactivation: A Case Study on Methanol-to-Hydrocarbons Conversion. *ACS Catal.* **2019**, *9* (8), 7065–7072. https://doi.org/10.1021/acscatal.9b01106.

(121) Razdan, N. K.; Kumar, A.; Foley, B. L.; Bhan, A. Influence of Ethylene and Acetylene on the Rate and Reversibility of Methane Dehydroaromatization on Mo/H-ZSM-5 Catalysts. *J. Catal.* **2020**, *381*, 261–270. https://doi.org/10.1016/j.jcat.2019.11.004.

(122) Platero-Prats, A. E.; League, A. B.; Bernales, V.; Ye, J.; Gallington, L. C.; Vjunov, A.; Schweitzer, N. M.; Li, Z.; Zheng, J.; Mehdi, B. L.; et al. Bridging Zirconia Nodes within a Metal-Organic Framework via Catalytic Ni-Hydroxo Clusters to Form Heterobimetallic Nanowires. *J. Am. Chem. Soc.* **2017**, *139* (30), 10410–10418. https://doi.org/10.1021/jacs.7b04997.

(123) Ittel, S. D.; Johnson, L. K.; Brookhart, M. Late-Metal Catalysts for Ethylene Homo- and Copolymerization. *Chem. Rev.* **2000**, *100* (4), 1169–1203. https://doi.org/10.1021/cr9804644.

(124) Musaev, D. G.; Morokuma, K. Theoretical Studies of the Mechanism of Ethylene Polymerization Reaction Catalyzed by Diimine-M(II) (M = Ni, Pd and Pt) and Ti-

and Zr-Chelating Alkoxides. *Top. Catal.* **1999**, *7* (1–4), 107–123. https://doi.org/10.1023/a:1019147313488.

(125) Zhao, Y.; González-Garda, N.; Truhlar, D. G. Benchmark Database of Barrier Heights for Heavy Atom Transfer, Nucleophilic Substitution, Association, and Unimolecular Reactions and Its Use to Test Theoretical Methods. *J. Phys. Chem. A* **2005**, *109* (9), 2012–2018. https://doi.org/10.1021/jp045141s.

(126) Wang, Y.; Jin, X.; Yu, H. S.; Truhlar, D. G.; He, X. Revised M06-L Functional for Improved Accuracy on Chemical Reaction Barrier Heights, Noncovalent Interactions, and Solid-State Physics. *Proc. Natl. Acad. Sci. U. S. A.* **2017**, *114* (32), 8487–8492. https://doi.org/10.1073/pnas.1705670114.

(127) Piccini, G.; Alessio, M.; Sauer, J. Ab-Initio Calculation of Rate Constants for Molecule-Surface Reactions with Chemical Accuracy. *Angew. Chemie - Int. Ed.* **2016**, *55* (17), 5235–5237. https://doi.org/10.1002/anie.201601534.

(128) Yeh, B.; Chheda, S.; Zheng, J.; Schmid, J.; Löbbert, L.; Bermejo-deval, R.; Gutiérrez, O. Y.; Lercher, J. A.; Gagliardi, L.; Bhan, A. Validation of the Cossee–Arlman Mechanism for Propylene Oligomerization on Ni/UiO-66. *Catal. Sci. Technol.* **2023**. https://doi.org/10.1039/d3cy00570d.

(129) Zheng, J.; Löbbert, L.; Chheda, S.; Khetrapal, N.; Schmid, J.; Alberto Gaggioli, C.; Yeh, B.; Bermejo-Deval, R.; Kishan Motkuri, R.; Balasubramanian, M.; et al. Metal-Organic Framework Supported Single-Site Nickel Catalysts for Butene Dimerization. *J. Catal.* **2022**, *413*, 176–183. https://doi.org/10.1016/j.jcat.2022.06.019.

(130) Löbbert, L.; Chheda, S.; Zheng, J.; Khetrapal, N.; Schmid, J.; Zhao, R.; Gaggioli, C. A.; Camaioni, D. M.; Bermejo-Deval, R.; Gutiérrez, O. Y.; et al. Influence of 1-Butene Adsorption on the Dimerization Activity of Single Metal Cations on UiO-66 Nodes. *J. Am. Chem. Soc.* **2023**, *145* (2), 1407–1422. https://doi.org/10.1021/jacs.2c12192.

(131) Hulea, V.; Fajula, F. Ni-Exchanged AlMCM-41 - An Efficient Bifunctional Catalyst for Ethylene Oligomerization. *J. Catal.* **2004**, *225* (1), 213–222. https://doi.org/10.1016/j.jcat.2004.04.018.

(132) Xu, Z.; Zhao, D.; Chada, J. P.; Rosenfeld, D. C.; Rogers, J. L.; Hermans, I.; Huber, G. W. Olefin Conversion on Nitrogen-Doped Carbon-Supported Cobalt Catalyst: Effect of Feedstock. *J. Catal.* **2017**, *354*, 213–222. https://doi.org/10.1016/j.jcat.2017.08.019.

(133) Jonathan, A.; Eagan, N. M.; Bruns, D. L.; Stahl, S. S.; Lanci, M. P.; Dumesic, J. A.; Huber, G. W. Ethylene Oligomerization into Linear Olefins over Cobalt Oxide on Carbon Catalyst. *Catal. Sci. Technol.* **2021**, *11* (10), 3599–3608. https://doi.org/10.1039/d1cy00207d.

(134) Hoffman, A. S.; Singh, J. A.; Bent, S. F.; Bare, S. R. In Situ Observation of Phase

Changes of a Silica- Supported Cobalt Catalyst for the Fischer–Tropsch Process by the Development of a Synchrotron- Compatible in Situ/Operando Powder X-Ray Diffraction Cell. *J. Synchrotron Radiat.* **2018**, *25* (6), 1673–1682. https://doi.org/10.1107/S1600577518013942.

(135) Edward P. Hunter; Sharon G. Lias. Proton Affinity Evaluation. In *NIST Chemistry WebBook, NIST Standard Reference Database Number 69*; P.J. Linstrom, W.G. Mallard, Eds.; National Institute of Standards and Technology: Gaithersburg MD, 20899.

(136) Afrin, S.; Bollini, P. Beyond Upper Bound Estimates of Active Site Densities in Heterogeneous Catalysis: A Note on the Critical Role of Titrant Pressure. *J. Catal.* **2022**, *413*, 76–80. https://doi.org/10.1016/j.jcat.2022.06.006.

(137) Lee, W. S.; Kumar, A.; Wang, Z.; Bhan, A. Chemical Titration and Transient Kinetic Studies of Site Requirements in Mo2C-Catalyzed Vapor Phase Anisole Hydrodeoxygenation. *ACS Catal.* **2015**, *5* (7), 4104–4114. https://doi.org/10.1021/acscatal.5b00713.

(138) Canivet, J.; Vandichel, M.; Farrusseng, D. Origin of Highly Active Metal-Organic Framework Catalysts: Defects? Defects! *Dalt. Trans.* **2016**, *45* (10), 4090–4099. https://doi.org/10.1039/c5dt03522h.

(139) Sholl, D. S.; Lively, R. P. Defects in Metal-Organic Frameworks: Challenge or Opportunity? *J. Phys. Chem. Lett.* **2015**, *6* (17), 3437–3444. https://doi.org/10.1021/acs.jpclett.5b01135.

(140) Hall, J. N.; Bollini, P. Structure, Characterization, and Catalytic Properties of Open-Metal Sites in Metal Organic Frameworks. *React. Chem. Eng.* **2019**, *4* (2), 207–222. https://doi.org/10.1039/c8re00228b.

(141) Kirchon, A.; Feng, L.; Drake, H. F.; Joseph, E. A.; Zhou, H. C. From Fundamentals to Applications: A Toolbox for Robust and Multifunctional MOF Materials. *Chem. Soc. Rev.* **2018**, *47* (23), 8611–8638. https://doi.org/10.1039/c8cs00688a.

(142) Liu, S.; Zhang, Y.; Han, Y.; Feng, G.; Gao, F.; Wang, H.; Qiu, P. Selective Ethylene Oligomerization with Chromium-Based Metal-Organic Framework MIL-100 Evacuated under Different Temperatures. *Organometallics* **2017**, *36* (3), 632–638. https://doi.org/10.1021/acs.organomet.6b00834.

(143) Drake, H. F.; Day, G. S.; Vali, S. W.; Xiao, Z.; Banerjee, S.; Li, J.; Joseph, E. A.; Kuszynski, J. E.; Perry, Z. T.; Kirchon, A.; et al. The Thermally Induced Decarboxylation Mechanism of a Mixed-Oxidation State Carboxylate-Based Iron Metal-Organic Framework. *Chem. Commun.* **2019**, *55* (85), 12769–12772. https://doi.org/10.1039/c9cc04555d.

(144) Vermoortele, F.; Bueken, B.; Le Bars, G.; Van De Voorde, B.; Vandichel, M.; Houthoofd, K.; Vimont, A.; Daturi, M.; Waroquier, M.; Van Speybroeck, V.; et al. Synthesis Modulation as a Tool to Increase the Catalytic Activity of Metal-Organic

Frameworks: The Unique Case of UiO-66(Zr). *J. Am. Chem. Soc.* **2013**, *135* (31), 11465–11468. https://doi.org/10.1021/ja405078u.

(145) Vermoortele, F.; Vandichel, M.; Van De Voorde, B.; Ameloot, R.; Waroquier, M.; Van Speybroeck, V.; De Vos, D. E. Electronic Effects of Linker Substitution on Lewis Acid Catalysis with Metal-Organic Frameworks. *Angew. Chemie - Int. Ed.* **2012**, *51* (20), 4887–4890. https://doi.org/10.1002/anie.201108565.

(146) Liu, Y.; Klet, R. C.; Hupp, J. T.; Farha, O. Probing the Correlations between the Defects in Metal-Organic Frameworks and Their Catalytic Activity by an Epoxide Ring-Opening Reaction. *Chem. Commun.* **2016**, *52* (50), 7806–7809. https://doi.org/10.1039/c6cc03727e.

(147) Gadipelli, S.; Guo, Z. Postsynthesis Annealing of MOF-5 Remarkably Enhances the Framework Structural Stability and CO2 Uptake. *Chem. Mater.* **2014**, *26* (22), 6333–6338. https://doi.org/10.1021/cm502399q.

(148) Simons, M. C.; Vitillo, J. G.; Babucci, M.; Hoffman, A. S.; Boubnov, A.; Beauvais, M. L.; Chen, Z.; Cramer, C. J.; Chapman, K. W.; Bare, S. R.; et al. Structure, Dynamics, and Reactivity for Light Alkane Oxidation of Fe(II) Sites Situated in the Nodes of a Metal-Organic Framework. *J. Am. Chem. Soc.* **2019**, *141* (45), 18142–18151. https://doi.org/10.1021/jacs.9b08686.

(149) Simons, M. C.; Prinslow, S. D.; Babucci, M.; Hoffman, A. S.; Hong, J.; Vitillo, J. G.; Bare, S. R.; Gates, B. C.; Lu, C. C.; Gagliardi, L.; et al. Beyond Radical Rebound: Methane Oxidation to Methanol Catalyzed by Iron Species in Metal-Organic Framework Nodes. *J. Am. Chem. Soc.* **2021**, *143* (31), 12165–12174. https://doi.org/10.1021/jacs.1c04766.

(150) Yang, D.; Bernales, V.; Islamoglu, T.; Farha, O. K.; Hupp, J. T.; Cramer, C. J.; Gagliardi, L.; Gates, B. C. Tuning the Surface Chemistry of Metal Organic Framework Nodes: Proton Topology of the Metal-Oxide-Like Zr6 Nodes of UiO-66 and NU-1000. *J. Am. Chem. Soc.* **2016**, *138* (46), 15189–15196. https://doi.org/10.1021/jacs.6b08273.

(151) Dhakshinamoorthy, A.; Alvaro, M.; Chevreau, H.; Horcajada, P.; Devic, T.; Serre, C.; Garcia, H. Iron(Iii) Metal-Organic Frameworks as Solid Lewis Acids for the Isomerization of α-Pinene Oxide. *Catal. Sci. Technol.* **2012**, *2* (2), 324–330. https://doi.org/10.1039/c2cy00376g.

(152) Feng, D.; Wang, K.; Wei, Z.; Chen, Y. P.; Simon, C. M.; Arvapally, R. K.; Martin, R. L.; Bosch, M.; Liu, T. F.; Fordham, S.; et al. Kinetically Tuned Dimensional Augmentation as a Versatile Synthetic Route towards Robust Metal-Organic Frameworks. *Nat. Commun.* **2014**, *5*, 1–8. https://doi.org/10.1038/ncomms6723.

(153) Ravel, B.; Newville, M. ATHENA, ARTEMIS, HEPHAESTUS: Data Analysis for X-Ray Absorption Spectroscopy Using IFEFFIT. *J. Synchrotron Radiat.* **2005**, *12* (4), 537–541. https://doi.org/10.1107/S0909049505012719.

(154) Cairns, R. W.; Ott, E. X-Ray Studies of the System Nickel-Oxygen-Water. I. Nickelous Oxide and Hydroxide. *J. Am. Chem. Soc.* **1933**, *55* (2), 527–533. https://doi.org/10.1021/ja01329a013.

(155) Barona, M.; Ahn, S.; Morris, W.; Hoover, W.; Notestein, J. M.; Farha, O. K.; Snurr, R. Q. Computational Predictions and Experimental Validation of Alkane Oxidative Dehydrogenation by Fe2M MOF Nodes. *ACS Catal.* **2020**, *10* (2), 1460–1469. https://doi.org/10.1021/acscatal.9b03932.

(156) Ortuño, M. A.; Bernales, V.; Gagliardi, L.; Cramer, C. J. Computational Study of First-Row Transition Metals Supported on MOF NU-1000 for Catalytic Acceptorless Alcohol Dehydrogenation. *J. Phys. Chem. C* **2016**, *120* (43), 24697–24705. https://doi.org/10.1021/acs.jpcc.6b06381.

(157) Wongsakulphasatch, S.; Nouar, F.; Rodriguez, J.; Scott, L.; Guillouzer, C. Le; Devic, T.; Horcajada, P.; Greneche, J.-M.; Llewellyn, P. L.; Vimont, Alexandre; et al. Direct Accessibility of Mixed-Metal (III/II) Acid Sites through the Rational Synthesis of Porous Metal Carboxylates. *Chem. Commun.* **2015**, *51*, 3664–3671. https://doi.org/10.1039/Mo.

(158) Fang, Y.; Banerjee, S.; Joseph, E. A.; Day, G. S.; Bosch, M.; Li, J.; Wang, Q.; Drake, H.; Ozdemir, O. K.; Ornstein, J. M.; et al. Incorporating Heavy Alkanes in Metal–Organic Frameworks for Optimizing Adsorbed Natural Gas Capacity. *Chem. - A Eur. J.* **2018**, *24* (64), 16977–16982. https://doi.org/10.1002/chem.201804012.

(159) An, J. R.; Wang, Y.; Dong, W. W.; Gao, X. J.; Yang, O. Y.; Liu, Y. L.; Zhao, J.; Li, D. S. Efficient Visible-Light Photoreduction of CO2 to CH4 over an Fe-Based Metal-Organic Framework (PCN-250-Fe3) in a Solid-Gas Mode. *ACS Appl. Energy Mater.* **2022**, *5* (2), 2384–2390. https://doi.org/10.1021/acsaem.1c03868.

(160) Drake, H. F.; Xiao, Z.; Day, G. S.; Vali, S. W.; Chen, W.; Wang, Q.; Huang, Y.; Yan, T. H.; Kuszynski, J. E.; Lindahl, P. A.; et al. Thermal Decarboxylation for the Generation of Hierarchical Porosity in Isostructural Metal-Organic Frameworks Containing Open Metal Sites. *Mater. Adv.* **2021**, *2* (16), 5487–5493. https://doi.org/10.1039/d1ma00163a.

(161) Atzori, C.; Shearer, G. C.; Maschio, L.; Civalleri, B.; Bonino, F.; Lamberti, C.; Svelle, S.; Lillerud, K. P.; Bordiga, S. Effect of Benzoic Acid as a Modulator in the Structure of UiO-66: An Experimental and Computational Study. *J. Phys. Chem. C* **2017**, *121* (17), 9312–9324. https://doi.org/10.1021/acs.jpcc.7b00483.

(162) Wu, D.; Yan, W.; Xu, H.; Zhang, E.; Li, Q. Defect Engineering of Mn-Based MOFs with Rod-Shaped Building Units by Organic Linker Fragmentation. *Inorganica Chim. Acta* **2017**, *460*, 93–98. https://doi.org/10.1016/j.ica.2016.07.022.

(163) Bonino, F.; Chavan, S.; Vitillo, J. G.; Groppo, E.; Agostini, G.; Lamberti, C.; Dietzel, P. D. C.; Prestipino, C.; Bordiga, S. Local Structure of CPO-27-Ni Metallorganic Framework upon Dehydration and Coordination of NO. *Chem. Mater.* **2008**, *20* (15),

4957–4968. https://doi.org/10.1021/cm800686k.

(164) Colpas, G. J.; Maroney, M. J.; Bagyinka, C.; Kumar, M.; Willis, W. S.; Suib, S. L.; Baidya, N.; Mascharak, P. K. X-Ray Spectroscopic Studies of Nickel Complexes, with Application to the Structure of Nickel Sites in Hydrogenases. *Inorg. Chem.* **1991**, *30* (5), 920–928. https://doi.org/10.1021/ic00005a010.

(165) Alwis, K. H. K. L.; Ingham, B.; Mucalo, M. R.; Kappen, P.; Glover, C. An X-Ray Absorption Spectroscopy Investigation of the Coordination Environment of Electrogenerated Ni(Ii)-Pseudohalide Complexes Arising from the Anodic Polarization of Ni Electrodes in DMSO Solutions of NCO-, NCS- and NCSe- Ions. *RSC Adv.* **2015**, *5* (20), 15709–15718. https://doi.org/10.1039/c4ra14940h.

(166) Wilke, M.; Farges, F.; Petit, P. E.; Brown, G. E.; Martin, F. Oxidation State and Coordination of Fe in Minerals: An Fe K-XANES Spectroscopic Study. *Am. Mineral.* **2001**, *86* (5–6), 714–730. https://doi.org/10.2138/am-2001-5-612.

(167) Eubank, J. F.; Wheatley, P. S.; Lebars, G.; McKinlay, A. C.; Leclerc, H.; Horcajada, P.; Daturi, M.; Vimont, A.; Morris, R. E.; Serre, C. Porous, Rigid Metal(III)-Carboxylate Metal-Organic Frameworks for the Delivery of Nitric Oxide. *APL Mater.* **2014**, *2* (124112), 1–10. https://doi.org/10.1063/1.4904069.

(168) Vitillo, J. G.; Gagliardi, L. Thermal Treatment Effect on CO and NO Adsorption on Fe(II) and Fe(III) Species in Fe3O-Based MIL-Type Metal-Organic Frameworks: A Density Functional Theory Study. *Inorg. Chem.* **2021**, *60* (16), 11813–11824. https://doi.org/10.1021/acs.inorgchem.1c01044.

(169) Mancuso, J. L.; Gaggioli, C. A.; Gagliardi, L.; Hendon, C. H. Singlet-to-Triplet Spin Transitions Facilitate Selective 1-Butene Formation during Ethylene Dimerization in Ni(II)-MFU-4 L. *J. Phys. Chem. C* **2021**, No. 125, 22036–22043. https://doi.org/10.1021/acs.jpcc.1c07658.

(170) Saxena, A.; Joshi, R.; Seemakurthi, R. R.; Koninckx, E.; Broadbelt, L. J.; Gounder, R. Effect of Nickel Active Site Density on the Deactivation of Ni-Beta Zeolite Catalysts during Ethene Dimerization. *ACS Eng. Au* **2022**, *2*, 12–16. https://doi.org/10.1021/acsengineeringau.1c00014.

(171) Mustafa, K.; Lazzarini, A.; Kaur, G.; Borfecchia, E.; Sigurd, Ø. Ø.; Gianolio, D.; Bordiga, S.; Petter, K.; Olsbye, U. Co-Catalyst Free Ethene Dimerization over Zr-Based Metal-Organic Framework (UiO-67) Functionalized with Ni and Bipyridine. *Catal. Today* **2021**, *369* (March 2020), 193–202. https://doi.org/10.1016/j.cattod.2020.03.038.

(172) Barrett, E. P.; Joyner, L. G.; Halenda, P. P. The Determination of Pore Volume and Area Distributions in Porous Substances. I. Computations from Nitrogen Isotherms. *J. Am. Chem. Soc.* **1951**, *73* (1), 373–380. https://doi.org/https://doi.org/10.1021/ja01145a126.

(173) Kadam, S. A.; Hwang, A.; Iglesia, E. Consequences of Intrapore Liquids on

Reactivity, Selectivity, and Stability for Aldol Condensation Reactions on Anatase TiO2 Catalysts. *ChemCatChem* **2022**, *14* (13). https://doi.org/10.1002/cctc.202200059.

(174) Haynes, J. M. Pore Size Analysis According to the Kelvin Equation. *Matériaux Constr.* **1973**, *6* (3), 209–213. https://doi.org/10.1007/BF02479035.

(175) Feng, L.; Wang, K. Y.; Lv, X. L.; Yan, T. H.; Zhou, H. C. Hierarchically Porous Metal-Organic Frameworks: Synthetic Strategies and Applications. *Natl. Sci. Rev.* **2020**, *7* (11), 1743–1758. https://doi.org/10.1093/nsr/nwz170.

(176) Bo, U.; Barth, B.; Paula, C.; Kuhnt, A.; Schwieger, W.; Mundstock, A.; Caro, J.; Hartmann, M. Ethene / Ethane and Propene / Propane Separation via the Olefin and Paraffin Selective Metal − Organic Framework Adsorbents CPO-27 and ZIF - 8. *Langmuir* **2013**, *29*, 8592−8600. https://doi.org/dx.doi.org/10.1021/la401471g.

(177) Fairen-Jimenez, D.; Moggach, S. A.; Wharmby, M. T.; Wright, P. A.; Parsons, S.; Düren, T. Opening the Gate: Framework Flexibility in ZIF-8 Explored by Experiments and Simulations. *J. Am. Chem. Soc.* **2011**, *133* (23), 8900–8902. https://doi.org/10.1021/ja202154j.

(178) Shukla, P. B.; Johnson, J. K. Impact of Loading-Dependent Intrinsic Framework Flexibility on Adsorption in UiO-66. *J. Phys. Chem. C* **2022**, *126* (41), 17699–17711. https://doi.org/10.1021/acs.jpcc.2c04629.

(179) Yang, Q.; Wiersum, A. D.; Jobic, H.; Guillerm, V.; Serre, C.; Llewellyn, P. L.; Maurin, G. Understanding the Thermodynamic and Kinetic Behavior of the CO 2/CH4 Gas Mixture within the Porous Zirconium Terephthalate UiO-66(Zr): A Joint Experimental and Modeling Approach. *J. Phys. Chem. C* **2011**, *115* (28), 13768–13774. https://doi.org/10.1021/jp202633t.

(180) Yang, Q.; Jobic, H.; Salles, F.; Kolokolov, D.; Guillerm, V.; Serre, C.; Maurin, G. Probing the Dynamics of CO2 and CH4 within the Porous Zirconium Terephthalate UiO-66(Zr): A Synergic Combination of Neutron Scattering Measurements and Molecular Simulations. *Chem. - A Eur. J.* **2011**, *17* (32), 8882–8889. https://doi.org/10.1002/chem.201003596.

(181) Dietzel, P. D. C.; Johnsen, R. E.; Fjellvåg, H.; Bordiga, S.; Groppo, E.; Chavan, S.; Blom, R. Adsorption Properties and Structure of CO2 Adsorbed on Open Coordination Sites of Metal-Organic Framework Ni2(Dhtp) from Gas Adsorption, IR Spectroscopy and X-Ray Diffraction. *Chem. Commun.* **2008**, No. 41, 5125–5127. https://doi.org/10.1039/b810574j.

(182) Dietzel, P. D. C.; Johnsen, R. E.; Blom, R.; Fjellvåg, H. Structural Changes and Coordinatively Unsaturated Metal Atoms on Dehydration of Honeycomb Analogous Microporous Metal-Organic Frameworks. *Chem. - A Eur. J.* **2008**, *14* (8), 2389–2397. https://doi.org/10.1002/chem.200701370.

(183) Dietzel, P. D. C.; Besikiotis, V.; Blom, R. Application of Metal-Organic

Frameworks with Coordinatively Unsaturated Metal Sites in Storage and Separation of Methane and Carbon Dioxide. *J. Mater. Chem.* **2009**, *19* (39), 7362–7370. https://doi.org/10.1039/b911242a.

(184) Schlessinger, G. G. Vapor Pressures, Critical Temperatures and Critical Pressures of Organic Compounds. In *Handbook of Chemistry and Physics*; 1979; pp D152–D153.

(185) Rosi, N. L.; Kim, J.; Eddaoudi, M.; Chen, B.; O'Keeffe, M.; Yaghi, O. M. Rod Packings and Metal-Organic Frameworks Constructed from Rod-Shaped Secondary Building Units. *J. Am. Chem. Soc.* **2005**, *127* (5), 1504–1518. https://doi.org/10.1021/ja045123o.

(186) Das, A. K.; Vemuri, R. S.; Kutnyakov, I.; McGrail, B. P.; Motkuri, R. K. An Efficient Synthesis Strategy for Metal-Organic Frameworks: Dry-Gel Synthesis of MOF-74 Framework with High Yield and Improved Performance. *Sci. Rep.* **2016**, *6* (February), 1–7. https://doi.org/10.1038/srep28050.

(187) Bae, Y. S.; Liu, J.; Wilmer, C. E.; Sun, H.; Dickey, A. N.; Kim, M. B.; Benin, A. I.; Willis, R. R.; Barpaga, D.; LeVan, M. D.; et al. The Effect of Pyridine Modification of Ni-Dobdc on Co2 Capture under Humid Conditions. *Chem. Commun.* **2014**, *50* (25), 3296–3298. https://doi.org/10.1039/c3cc44954h.

(188) Lee, D. J.; Li, Q.; Kim, H.; Lee, K. Preparation of Ni-MOF-74 Membrane for CO 2 Separation by Layer-by-Layer Seeding Technique. *Microporous Mesoporous Mater.* **2012**, *163*, 169–177. https://doi.org/10.1016/j.micromeso.2012.07.008.

(189) Butler, K. T.; Hendon, C. H.; Walsh, A. Electronic Chemical Potentials of Porous Metal-Organic Frameworks. *J. Am. Chem. Soc.* **2014**, *136* (7), 2703–2706. https://doi.org/10.1021/ja4110073.

(190) Bhore, N. A.; Klein, M. T.; Bischoff, K. B. The Delplot Technique: A New Method for Reaction Pathway Analysis. *Ind. Eng. Chem. Res.* **1990**, *29* (2), 313–316. https://doi.org/10.1021/ie00098a025.